Understanding deformation patterns of rocks and characterizing their relationship to subduction interface processes and rheology at different depths (10-60 km)

Dissertation

zur Erlangung des Grades eines
Doktors der Naturwissenschaften (Dr. rer. nat.)

am Fachbereich Geowissenschaften
der Freien Universität Berlin

vorgelegt von

Paraskevi Io Ioannidi

Berlin, 2020

Erstgutachter: Prof. Dr. Onno Oncken

Zweitgutachterin: Prof. Dr. Laetitia Le Pourhiet

Tag der Disputation: 08/06/2020

Erklärung

nach §7 (4) der Promotionsordnung des Fachbereichs Geowissenschaften and der Freien Universität Berlin:

Hiermit erkläre ich, dass die vorliegende Dissertation ohne unzulässige Hilfe Dritter und ohne Benutzung anderer als der angegebenen Literatur angefertigt wurde. Die Stellen der Arbeit, die anderen Werken wörtlich oder inhaltlich entnommen sind, wurden durch entsprechende Angaben der Quellen kenntlich gemacht. Diese Arbeit hat in gleicher oder ähnlicher Form noch keiner Prüfungsbehörde vorgelegen.

Berlin, März 2020

Acknowledgements

First of all, I would like to thank my advisors, Prof. Onno Oncken, Dr. Samuel Angiboust, Prof. Laetitia Le Pourhiet and Prof. Philippe Agard, for helping me carry out the present thesis. Their immense knowledge, motivation and patience have been essential throughout this academic journey. In particular, I want to express my gratiude to Prof. Onno Oncken and Dr. Samuel Angiboust for believing in me and trusting me with this project. Prof. Oncken, I have benefited greatly from your broad, encompassing view of lithosphere dynamics; each meeting was training me on seeing the bigger picture. Samuel, you guided me well throughout this research and you were always there to discuss any doubts I had. Thank you for your patience. Laetitia, I am grateful to you for introducing me to the beautiful world of computational rheology, for helping me grasp difficult concepts, and for inspiring me to continue in numerical modelling. Philippe, I wish to express my gratitude to you for creating this great project called "ZIP", that enabled me to carry out this doctoral thesis, for giving me encouragement during my research, and for believing in me.

Moreover, I want to thank Dr. Erik Rybacki for patiently discussing with me rheology and flow laws. I also want to acknowledge technical support from Regina Prero, Nicolai Klitshcer, Manuel Dziggel, and Oona Apppelt, who facilitated various aspects of my research, from logistics to sample preparation, graphic design, and micro-analyses. Moreover,Franziska Alberg, I will forever be in your debt. You have been a sunshine in the section, the person that finds a way to solve everything and thinks of our needs before they appear.

Furthermore, I want to thank all my friends and colleagues at GFZ and especially my great office-mate Ehsan, for being patient with me, supporting me and sharing his tea almost every afternoon. Christian, I appreciate the evenings playing pool and discussing (my) PhD worries. Silvia, thank you for checking in on me regularly. To Isabel, Vasso S., Felix, Malte, Armin, and all my colleagues, thank you for making me feel part of the section. I am deeply grateful to Iskander, for always being available to answer my numerical questions, for discussing patiently my models and for introducing me to the best band in the world. I am also thankful to all the lovely people from my step-section 4.2 and their friends: Livia, Audrey, Johannes, Stephan, Valerian, Lea, Amandine, thank you for including me in your beautiful group. Special thanks go to Bernhard for, among others, helping me out with my German abstract and the German tax system.

Of course, I could not forget the ZIP-fellows. I am thankful to all "ZIPPIES", for scientific discussions but most importantly for the wonderful moments we shared in 2 continents and

almost 10 countries together. My heartfelt thanks particularly to Léa Bayettamou for her constant care and love, to Michele for his extreme support, to Gian Maria for all our trips and Greek conversations, and to Casper for joining me in field trips and inviting me to ETH. Friends from ISTeP, Guillaume, Mathieu, and Tan thank you for making each of my stays in Paris wonderful.

I am also grateful to all my friends in Berlin/Potsdam for making my everyday life happy and fulfilling. Katerina, you have been an anchor, your equanimity has been inspiring to me, and I am glad you moved to Berlin. Miss Betty, you and your minions have been the best flatmates I could ever imagine; you turned the flat into a Pallas-home. Miss Anna, thank you for being there in hard times, teasing me and and not ever loosing your smile. I am grateful also to my friend and colleague Spiros Olivotos, for assisting me in the field, for sharing his lunch time with me and for being a true friend outside the office. Annoula ζωάκι, miss Mary, Ana, and my dear Heike our schedules may have been conflicting, but your support and care were always present. Jacqueline, you have always been a dear and a pleasure to talk to. Ronako, Manonaki, and Evaki, I am happy we have once shared the flat, academic concerns and advice. Stelios, we embarked on this trip together, we are travelling to different places now, but you have always believed in me and that was a driving force, thank you.

Friends from Greece, you have always given me your long-distance support. My high-school best friends, Yvoni and Afroditi, my university friends Foteini, Vassilis and Christos, you have all been important parts of my life and I am grateful for your support all these years. My heartfelt thanks also to Kostas, for his encouragement and for giving me the opportunity to make one of my dreams come true: a road-trip in amazing New Zealand. Natassa, and your beautiful daughters, Iris and Christina, you are like family to me. The way you see me and my academic journey infuses me with even more enthusiasm about what I do.

Last but not least, I would like to thank my family for always supporting and pushing me forward. Μαμά, thank you for inspiring me to be an independent person and to go after my dreams. Μπαμπά, thank you for being the person I can count on the most when decisions seem hard. Anastasia, thank you for your inspiring geo-scientific interest, since ever! Γιαγιά Βούλα, σε ευχαριστώ για την αγάπη και την περηφάνεια σου όλα αυτά τα χρόνια. I love you all.

Abstract

Subduction zones are naturally complex systems, with much of their deformation being accommodated along the interface between two tectonic plates. Hence, the physical nature and the rheology of the subduction interface play an important role in the deformation, degree of locking, and slip processes during convergence, as well as large scale subduction dynamics. Over the last two decades, different slip patterns have been recognized by geodetic and seismic techniques, such as slow slip events and episodic tremor and slip, the physics behind which still evade us. Since direct observations along an active subduction interface are not feasible, field examples of exhumed zones can provide important insight into the nature of such transient events. Concurrently, most field outcrops suggest that the subduction interface is rather heterogeneous, comprising different units that deform following various patterns. However, these units are often too small to be resolved in a large-scale geodynamic model and are, therefore, not taken into account in such models. Outcrop-scale numerical experiments can be combined with natural structural observations from outcrops in order to refine the rheologies used in large geodynamic models. Here, methods ranging from field, petrological and geochronological observations on exhumed rocks to outcrop-scale numerical simulations are deployed, in order to investigate the rheology of the plate interface, the deformation mechanisms and the timing of deformation.

The European Alps are a great natural laboratory exposing an almost continuous subduction interface allowing for the study of deformation processes from shallow to deeper segments (from ca. 10 km to ca. 45 km depth). Here, a network of fossil subduction plate interfaces preserved in the Central Alps (Val Malenco, N Italy) is used as a proxy to study such processes on subducting continental slices (the Margna and Sella nappes), at depths corresponding to the former brittle-ductile transition. This network of shear zones comprises mostly mylonites and schists but also rare foliated cataclasites, with different generations of micas and garnet locally overgrowing resorbed pre-Alpine cores. Thermodynamic modelling points to peak burial deformation conditions of ∼0.9 GPa and 350°-400°C, at ca. 30 km depth. Rb/Sr geochronology on marbles yields an age of 48.9 ± 0.9 Ma, while a wide range of both Rb/Sr and $^{40}Ar/^{39}Ar$ apparent ages is obtained from deformed orthogneisses and micaschists embracing 87-44 Ma, due to incomplete recrystallization. Based on pressure-temperature, structural and geochronological observations, the studied shear zones last equilibrated at depths downdip of the seismogenic zone in an active subduction zone setting. Fluids contribute to the bulk rheology of this interface by enhancing pressure-solution creep which prevails in the microstructural record. This

study suggests that this system of shear zones represents deformation conditions along the subduction interface(s) in the transition zone below the seismogenic zone during active subduction, where transient slip is found.

Other exhumed subduction interfaces exhibit block-in-matrix characteristics, termed mélanges, the block concentration of which can affect their bulk rheology. To investigate this, synthetic models are created, with different proportions of strong blocks within a weak matrix, and compared to exhumed natural mélange outcrops. 2D Finite Element visco-plastic models in simple shear are used to determine the effective rheological parameters of such a two-phase medium, comprising blocks of basalt within a wet quartzitic matrix. Models and their structures are treated as scale-independent and self-similar. Therefore, field geometries are upscaled to km-scale models, compatible with large-scale, geodetic and seismic observations. Outcrops of mélanges, as well as of other units deformed during subduction suggest that deformation is mainly taken up by dissolution-precipitation creep. However, flow laws for dissolution-precipitation creep are not well-established experimentally and scarcely used in large-scale numerical models. To make the results of this study comparable to and usable by numerical studies, dislocation creep is assumed to be the governing flow law for both phases (basalt and wet quartz). Finally, effective rheological estimates for a natural subduction interface are provided. The results suggest that block concentration affects deformation and strain localization, with the effective dislocation creep parameters (A, n, and Q) varying between the values of the strong and the weak phase, when both phases deform viscously. However, as the contribution of brittle deformation of the basaltic blocks increases, the value of the stress exponent, n, can exceed that of the purely strong phase. Using these effective parameters as input into seismic cycle models could help evaluate the possible effect of field heterogeneities on the slip behaviour of the plate interface.

In summary, the heterogeneity of the subduction interface plays an important role in the degree of localization and rheology of the plate interface. Mixed brittle-ductile deformation is common in subducted rocks and might give rise to different kinematic behaviours. Re-assessing fabrics in exhumed rocks with respect to their (relevant) timing, spatial distribution, as well as cross-cutting relationships of individual fabric features is essential for linking kinematic far-field observations to the physics of deformation processes acting upon the interface. Finally, incorporating the results of small-scale numerical studies in large-scale geodynamic models may help improve our understanding of the mechanical behaviour of the plate interface, including transient or aseismic slip phenomena, which may control the recurrence of megathrust ruptures

in active subduction systems.

(**German version of the abstract can be found in Appendix C**.)

Dedication

To Elias, Anastasia, Iris, and Γιαγιά Βούλα.

« Πάντα ῥεῖ. »

Ηράκλειτος (Πλάτων, Κρατύλος, 339-340 π.Χ.)

« Everything flows. »

Heraclitus (Plato, Cratylus, 339-340 B.C.)

Contents

List of Tables

List of Figures

Chapter 1

Introduction

1.1 Plate tectonics

Plate tectonics theory, stemming itself from the concepts of continental drift proposed in the beginning of the 20th century by Alfred Wegener, was introduced more than 50 years ago, in an attempt to reconcile different tectonic processes taking place on and within the Earth (e.g., Wilson, 1965; Morgan, 1968; McKenzie and Parker, 1967). Based on this theory, the Earth's surface is divided in large, thin and relatively rigid lithospheric plates, comprising the crust and the upper part of the mantle. The boundaries of these plates are categorized, with respect to their relevant movements, in (Fig. 1.1):

- convergent boundaries, in which the involved lithospheric plates move towards each other. This results in either continental collisional zones (e.g., in the Alps during Tertiary times, Schmid et al., 1996; Dal Piaz, 2001), or in subduction of the (usually oceanic) plate (e.g., in the Andes, Allmendinger and Gubbels, 1996; Allmendinger et al., 1997; Lamb and Hoke, 1997; Elger et al., 2005; Oncken et al., 2006; Barnes and Ehlers, 2009; Carrapa et al., 2011).

- divergent boundaries, along which the plates move apart and new oceanic crust is produced (e.g., the Mid-Atlantic Ridge Vine and Matthews, 1963; Frey et al., 1974; White, 1984; Cannat, 1995)

- transform boundaries, in which the two plates slide past each other (e.g., the Alpine Fault

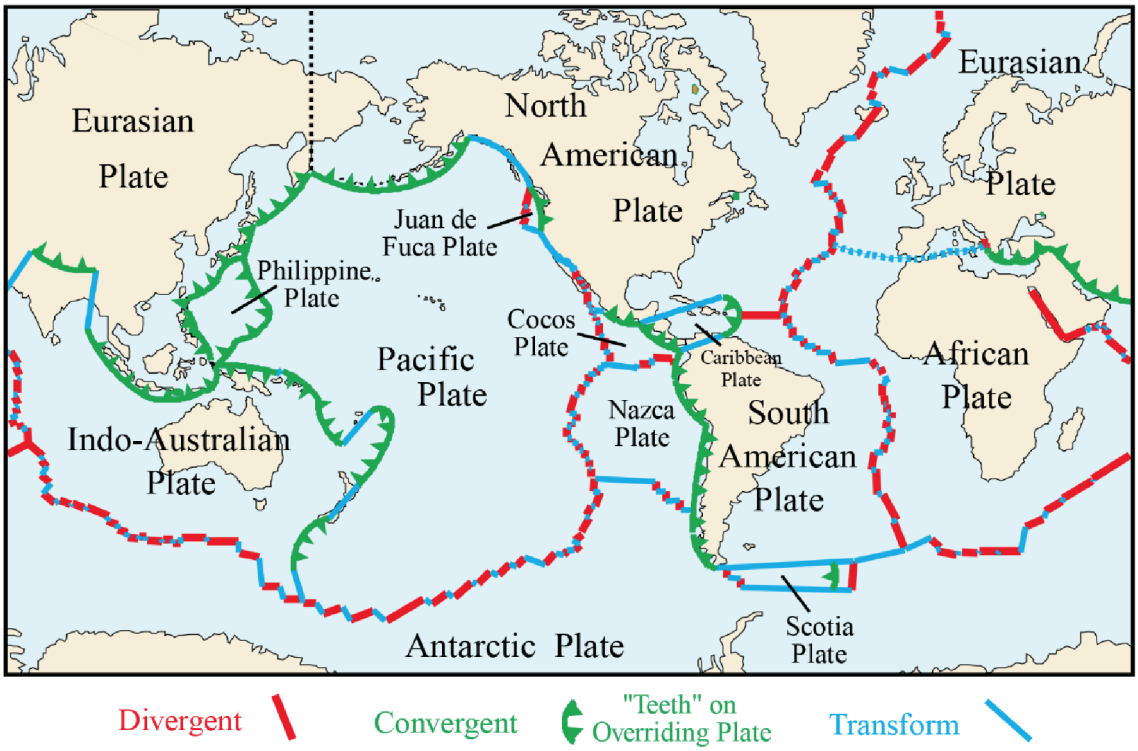

Figure 1.1: Map of plate tectonics, with representation of the different plates and divergent (red), convergent (green) and transform (blue) plate boundaries. From USGS.

in New Zealand and the San Andreas Fault in USA, Wellman and Willett, 1942; Mount and Suppe, 1987; Sylvester, 1988; Teyssier and Tikoff, 1998).

Amongst the above features, subduction zones constitute the largest physical and chemical system within Earth (Stern, 2002). They host the largest earthquakes that have ever been recorded (Mw $>$ 9.0, e.g., the 1964 Alaska, 1969 Valdivia, 2004 Sumatra, and 2011 Tohoku-Oki earthquakes) and release 95% of all seismic moment on Earth. They are also key structures in recycling of material and fluids from the Earth's surface to its interior and vice versa (e.g., Tatsumi, 1989; Philippot, 1993; Hacker et al., 2003a,b; Zack and John, 2007; Hacker, 2008; John et al., 2012; Scambelluri et al., 2004).

Most commonly, the subducting slab is composed of lithospheric mantle, oceanic crust and a sedimentary cover, e.g., in Chile where the Nazca oceanic plate subducts beneath the South American continental plate, or in the Mariana islands, where the oceanic Pacific plate descends beneath the also oceanic Philippine micro-plate. However, subduction of continental slivers has also been reported (e.g., in the European Alps, Ernst, 1971; Chopin, 1984; Marchant and Stampfli, 1997; Hacker et al., 2000; Ye et al., 2000a,b; Babist et al., 2006, and Chapter 1.2.4).

1.2 State of the art on subduction zone dynamics

The past decades, advances in remote monitoring techniques (e.g., seismic imaging techniques, high-resolution locations of earthquakes, dense and precise GPS and InSAR measurements) have enhanced our knowledge on short-term mechanical coupling, kinematics, and stress release along subduction zones (Peng and Gomberg, 2010, and references therein). A kinematic segmentation of subduction zones has emerged from the identification of transient slip patterns in currently active subduction zones, such as slow slip events (SSE), episodic tremor and slip (ETS) and very low frequency (VLF) earthquakes (e.g., Ito and Obara, 2006; Liu and Rice, 2007; Audet et al., 2009; Peng and Gomberg, 2010; Obara and Kato, 2016; Gao and Wang, 2017, and Fig. 1.2). Concurrently, a rheological segmentation has been suggested for fossil subduction zones around the world, based on microstructural deformation patterns observed in exhumed rocks. Linear pressure-solution creep has been reported for high P/T conditions along the subduction interface (e.g., Bachmann et al., 2009b) and up to eclogite conditions (e.g., Stöckhert, 2002; Wassmann and Stöckhert, 2013a). Pseudotachylytes coincide spatially with the temperature conditions characterizing the seismogenic zone of paleo-subduction in the Alps (Bachmann et al., 2009b), while at temperatures $> 350°C$, power-law creep controls the deformation of quartzofeldspathic rocks (Shimizu, 1995; Angiboust et al., 2014). However, pseudotachylytes have also been reported at paleo-depths where viscous deformation by dislocation creep was active in the rocks (Lin et al., 2003; Austrheim and Andersen, 2004; Lin et al., 2005; Behr and Platt, 2011; White, 2012; Menant et al., 2018, and references therein), as well as in cool and wet metasedimentary rocks (Rowe et al., 2005; Bjørnerud, 2010; Meneghini et al., 2010).

It is evident that a rheological as well as kinematic segmentation exists along the subduction interface, which is controlled by several factors. Below I discuss some of these factors, such as the rheology of the plate interface and the effect of fluids; I also introduce the essential concepts of seismic cycle and subduction of continental slivers.

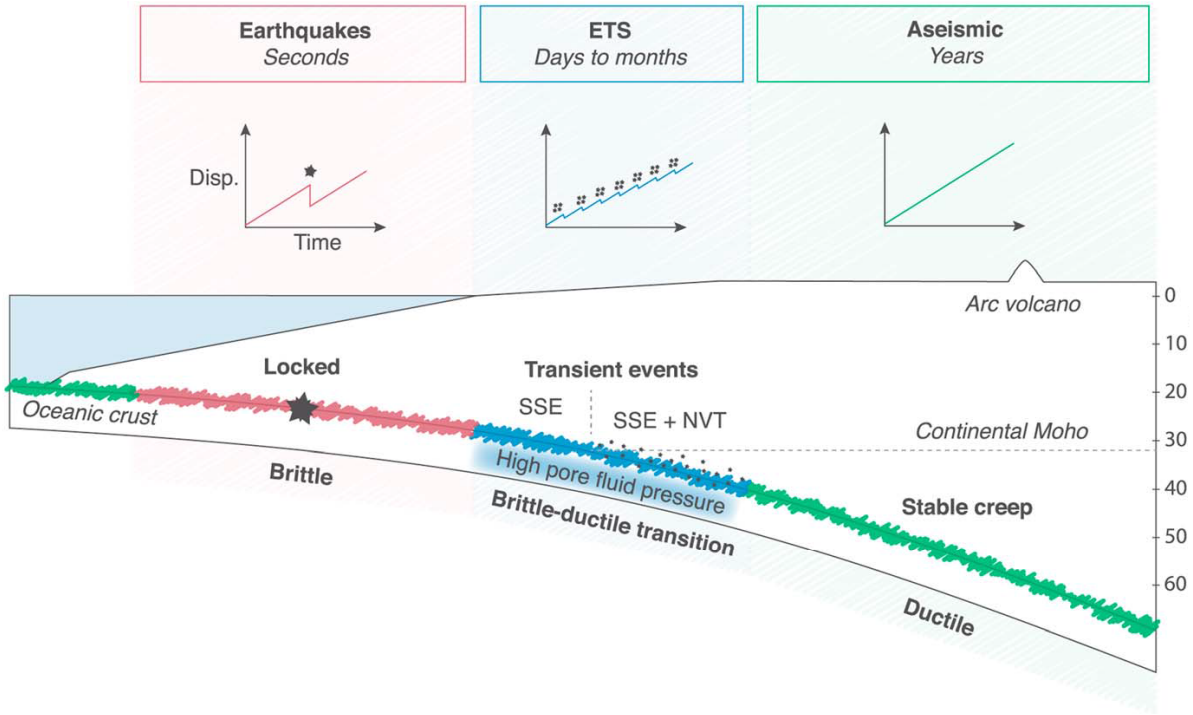

Figure 1.2: Kinematic and rheological segmentation along the subduction interface. Upper graph shows figurative displacement versus time diagram for the three domains (from Dragert et al., 2004; Bernaudin and Gueydan, 2018). Lower graph depicts locked domain with red (black star represents earthquakes), transient events domain with blue (ETS, nonvolcanic tremor (NVT) as black points), and stable slip domain in green, along a subduction plate interface (modified from Peng and Gomberg, 2010). The light blue area indicates high pore fluid pressure inferred from v_P/v_S data (Audet et al., 2009; Peacock et al., 2011). Modified from (Bernaudin and Gueydan, 2018).

1.2.1 Seismic cycle

As the downgoing slab subducts beneath the overriding plate, some portions of their interface slide freely past each other, while others remain locked due to mechanical coupling, resulting in accumulation of stresses and storage of elastic deformation within and adjacent to their interface. After a certain threshold value of stresses is reached, the stresses and stored elastic energy are released by sudden slip and de-coupling of the interface, often followed by a phase of postseismic relaxation. The process involving stress built-up, sudden release and postseismic deformation is termed "seismic cycle" (e.g., Wang, 2007) and can be described in the frame of the elastic-rebound theory (Reid, 1911). The time during radiation of elastic energy and stress release is called *coseismic* and is followed by a transient *postseismic* relaxation period. Finally, the period between two consecutive characteristic seismic events constitutes the *interseismic*

period (upper panel of Fig. 1.2). The latter stage is characterized by the slow accumulation of elastic strain along the locked patch(es) of the subduction megathrust. This stage lasts until the abrupt seismic rupture. During the coseismic phase, unstable slip occurs within a typical depth range between 5 and 45 km along the subduction interface, called the seismogenic coupling zone (e.g., Tichelaar and Ruff, 1993) and causes interplate earthquakes. The updip and downdip limits of this zone are controlled by several factors such as lithology, temperature, fluid pressure and percolation, stress accumulation, serpentinization and dehydration reactions (e.g., Oleskevich et al., 1999; Peacock and Hyndman, 1999; Saffer and Tobin, 2011). It is suggested that these limits are not sharp but rather mark a transitional regime between frictional and viscous failure (e.g., Wang and Hu, 2006; Fagereng and Cooper, 2010; Marone and Richardson, 2010).

Postseismic deformation follows the occurrence of a earthquake and may last for the next hours, months or even years. During this postseismic phase, crustal and mantle rocks affected by the earthquake adapt to the coseismic deformation imposed (Scholz, 1998; Wang et al., 2012). The two widely accepted relaxation processes during postseismic deformation are afterslip, namely decaying slip at the fault, and viscoelastic relaxation in crust and mantle. Afterslip acts as a slow continuation of the earthquake localized along the fault, while viscoelastic relaxation acts on large volumes of the mantle and lower crust (Bürgmann and Dresen, 2008; Wang et al., 2012). During the coseismic and postseismic stages, the viscosity of the mantle is time-dependent: it decreases during the earthquake and then increases during the postseismic period (Pollitz, 2003; Freed and Bürgmann, 2004; Bürgmann and Dresen, 2008; Wang et al., 2012).

1.2.2 Fluids

Fluids enter the system of a subduction zone either as water within the porosity of sediments and crust, or as bound water within the crystal lattice of hydrous minerals. They are released initially during compaction and later on during dehydration reactions, as the rocks (sediments and crust) get progressively buried and heated (e.g., Saffer and Tobin, 2011).

Common sources of fluids include dehydration of clay and opal minerals (e.g., Bruce, 1984; Bethke, 1986; Bekins et al., 1994; Spinelli and Saffer, 2004), compaction of sediments and the transition from shale to schist (Bailey et al., 1964; Fyfe et al., 1978; Kerrick and Connelly, 2001),

basalt pore collapse and dehydration of zeolite to greenschist (Peacock and Hyndman, 1999; Kerrick and Connolly, 2001; Hacker et al., 2003a; Hacker, 2008). During the above processes, pore pressures rise, fluids are expelled and may either migrate updip along the plate interface or towards the overlying forearc crust. In the latter case, they can either remain present as a free fluid phase or be consumed by retrograde (hydration) reactions (Peacock, 2009). Variations in the permeability and composition of sediments and crust, mainly due to their porosity and/or content of hydrous minerals, play a pivotal role in the mechanical and geochemical behaviour of the interface (e.g., Kerrick and Connelly, 2001; Hacker, 2008; Saffer and Tobin, 2011, and Fig. 1.2).

A convenient way of parameterizing the content of fluids along the subduction interface is the pore fluid ratio, λ. It is the ratio of pore fluid pressure over the lithostatic pressure of the rocks; it ranges from 0 for dry conditions to 1 for fluids reaching lithostatic pressures, while a value of ~ 0.4 reflects hydrostatic conditions. The effect of fluids within a subduction zone system is manifold. They can promote frictional sliding of rocks at depths and temperatures where normally viscous creep would is expected (e.g., Gao and Wang, 2017). Moreover, they play a role in the periodicity of transient slip event: during coseismic rupture and related crack/vein opening, pore fluid pressures locally drop thus enabling rapid fluid percolation and crystallization of minerals from supersaturated solutions. This crack sealing can lead to reduction of permeability and new build-up of quasi-lithostatic pore fluid pressures (Wassmann and Stöckhert, 2013b). Seismological studies suggest that the plate interface maintains low permeabilities in the downdip transition zone, thus enabling the existence of high pore fluid pressures which in turn favour decoupling and steady slip instead of slip at seismic rates (e.g., Audet et al., 2009; Peacock et al., 2011; Moreno et al., 2014).

Fluid percolation has been linked to the variability, in space and time, of kinematics and slip mechanisms observed along subduction interfaces (e.g., Ito et al., 2007; Peacock et al., 2011; Saffer and Tobin, 2011, and Fig. 1.2). These fault slip behaviours vary from postseismic afterslip, to slow slip events (SSE), very low-frequency earthquakes (VLFE) and episodic tremor and slip (ETS) (e.g., Kodaira et al., 2004; Ito and Obara, 2006; Liu and Rice, 2007; Audet et al., 2009; Obana and Kodaira, 2009; Bedford et al., 2013). Field, as well as geophysical observations in several subduction zones suggest high pore fluid ratios along the subduction interface (e.g.,

Seno, 2009; Fagereng and Cooper, 2010; Moreno et al., 2014; Angiboust et al., 2015) and a distribution that may vary from moderate to extreme overpressures (Saffer and Tobin, 2011, and references therein). For instance, very high, possibly near-lithostatic pore fluid pressures have been invoked as a geological condition promoting episodic tremor and slip (ETS) (Liu and Rice, 2009; Matsuzawa et al., 2010; Johnson et al., 2013; Audet and Kim, 2016).

1.2.3 Subduction interface rheology

Much of the aforementioned processes that take place during convergence and subsequent subduction are accommodated by deformation along the interface of the involved plates (e.g., Kirby, 1983; Scambelluri and Philippot, 2001; Hacker et al., 2003a; Wada et al., 2008; Guillot et al., 2009; Bebout and Penniston-Dorland, 2016; Agard et al., 2018). However, in spite of the large amount of kinematic observations currently available (e.g., from GPS, InSAR, and seismological data), the mechanical properties and mechanisms responsible for locking and the rheology of the interface are still largely elusive. In order to assess these properties in active subduction interfaces, one must look into the rock record of exhumed suture zones (see also Grigull et al., 2012; Wassmann and Stöckhert, 2013b; Agard et al., 2018).

The thickness of the plate interface is estimated to vary from a few centimeters at shallow depths (e.g., Saffer and Tobin, 2011; Vannucchi et al., 2012; Rowe et al., 2013) to some kilometers at deeper parts (e.g., Agard et al., 2016). A recent compilation by Agard et al. (2018) suggests an average thickness smaller than ∼300 m. The plate interface is intrinsically weak, with low (< 35 MPa) shear stresses acting upon it (Bird, 1978; Magee and Zoback, 1993; Zhong, Shijie and Gurnis, 1994; Wang and Nieh, 1995; Springer, 1999; Currie et al., 2002; Grevemeyer et al., 2003; Seno, 2009; Luttrell et al., 2011; Duarte et al., 2015, e.g.,). However, due to mechanical coupling of the plates, it is possible that stresses are periodic built up during the interseismic period and suddenly released in the form of earthquakes. Important factors that affect the coupling of the interface are the lithology, geometry, thickness, lubrication of the interface, its rheology and how these vary with depth. Notably, strong mechanical coupling is favoured when rheologies on both sides of the plate interface are similar.

Agard et al. (2018) introduced the concept of "coupled thickness" of the interface, for the cases when mechanical coupling between the downgoing slab and the overriding plate is strong; it is

the width that accommodates the strain and includes part of the upper plate, the plate interface and any décollement within the slab. The (coupled or not) thickness of the interface is an important parameter, since it controls the strain rate under which deformation will be accommodated: for a given convergence velocity, a thinner interface will localize more deformation compared to a thicker one ($\dot{\varepsilon} = velocity/width$).

A useful parameter for describing the rheology of the subduction interface is the effective viscosity, which, by definition, is sensitive to changes in the strain rate ($\dot{\eta} = \tau/(2\dot{\varepsilon})$). As such, the effective viscosity of the interface strongly depends on the dominant/faster mechanism accommodating deformation, which often experiences changes with depth (e.g., Stöckhert, 2002; Wassmann and Stöckhert, 2013b; Agard et al., 2018). An introduction to the most common deformation mechanisms and equivalent flow laws of rocks is given in Chapter 1.3, while Chapter 3 gives an overview of the most commonly observed mechanisms at exhumed subduction zones.

Brittle fracturing and ductile shearing are competing mechanisms responsible for coupling and de-coupling of the interface. From ample field observations it is evident that the subduction interface is far from homogeneous (e.g., Vannucchi et al., 2008; Bachmann et al., 2009b; Fagereng and Cooper, 2010; Grigull et al., 2012; Vannucchi et al., 2012; Rowe et al., 2013; Angiboust et al., 2015). This heterogeneity implies deformation within the interface at different strain rates and therefore some of its components might show brittle behavior, while others may deform viscously (e.g., Fagereng and Cooper, 2010; Vannucchi et al., 2010; Angiboust et al., 2015).

1.2.4 Subduction of continental slivers

While subduction of oceanic lithosphere is more common, slivers of continental crust and their sedimentary covers can also be subducted at different depths and either get scraped off and exhumed from shallow (e.g., Cowan, 1978) or intermediate depths (100-200 km) as high pressure (HP) and ultra-high pressure (UHP) rocks (Liou et al., 1994; Coleman and Wang, 1995; Ernst and Liou, 1999; Chopin, 2003; Hacker et al., 2000; Ye et al., 2000a,b), or consumed in the mantle (e.g., von Huene and Scholl, 1991).

When subducted slivers make their way back to the surface, they allow the study of deformation processes once acting on the rocks, such as observed in the Alps (e.g., Philippot, 1990; Wheeler, 1991; Handy et al., 1999; Angiboust et al., 2015). In the case that the slivers are composed of basement units, analogue models and field observations suggest that deformation of these slivers is mainly localized at their boundaries, while internally they seem more coherent and undeformed (Bialas et al., 2011; Angiboust et al., 2014; Ioannidi et al., 2020). Most of their deformation is taken up by dissolution precipitation creep and veining at shallow levels, gradually giving over to crystal plastic deformation (dislocation creep) as pressures and temperatures increase. Chapter 4 presents in detail petrological and geochronological work carried out in Central Alps, where continental slivers were once part of the subduction interface.

1.3 Deformation mechanisms

Natural crystals contain defects in their lattice, such as vacancies, interstitial defects, substitutions and screw or edge dislocations, which accommodate strain during viscous deformation (Figure 1.3). To describe the relation between the stress exerted on a material and the strain rate at which it deforms, constitutive equations of the following form have been invoked from experimental studies:

$$\dot{\varepsilon} = A\sigma^n d^{-m} f_{H_20}^r exp(\frac{-Q+pV}{RT}) \tag{1.1}$$

where $\dot{\varepsilon}$ is the strain rate, A a material constant, σ the stress, n the stress exponent, d the grain size in μm, m the grain size exponent, f_{H_20} is the water fugacity, r the fugacity exponent, Q the activation energy, p the applied pressure, V the activation volume, R the molar gas constant, and T the absolute temperature. Depending on the deformation mechanism, the flow law describes a *Newtonian* (*linear* behavior with n=1) or a *non-Newtonian* material (*power-law* behavior, $n > 1$).

The most commonly studied deformation mechanisms on rocks are dislocation, diffusion and (dis-)solution precipitation creep and are presented below.

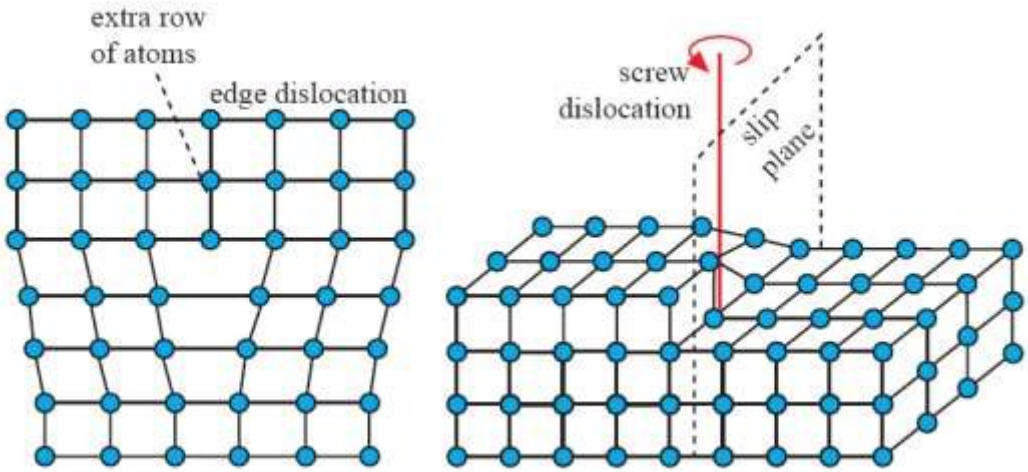

Figure 1.3: Description of defects in the crystal lattice.

1.3.1 Dislocation creep

Dislocation creep is a thermally activated process wherein dislocations move through the crystal lattice (e.g., Cohen, 1999). Strain rate increases exponentially with stress giving a grain size insensitive, power-law flow. The relationship between stress and strain rate is given by Eq. 1.1 when $m = 0$. Due to lack of activation volume data and fugacity, it is common that the dislocation creep flow law is written as:

$$\dot{\varepsilon} = A\sigma^n exp(\frac{-Q}{RT}) \tag{1.2}$$

It is the most studied and commonly used flow law for geodynamic modelling and includes several accompanying mechanisms: a producing mechanism (dislocation glide or climb), a recovery mechanism (dislocation climb or grain boundary migration) and a number of dynamic recrystallization mechanisms (e.g., bulging, subgrain rotation, grain boundary migration) which can accompany deformation, all in the dislocation creep regime (e.g., Guillope and Poirier, 1979; Drury and Urai, 1990). Evidence for deformation under dislocation creep observed in the microscale include undulose extinction, deformation lamellae and potentially lattice preferred orientation (LPO).

Of particular geologic interest is the use of the recrystallized grain size of particular minerals as a paleopiezometer (e.g., Kohlstedt and Weathers, 1980; Ord and Christie, 1984). In such cases, the size of the recrystallized grains is measured and the differential stresses responsible

for this deformation are estimated. The most prominent paleopiezometer is that of quartz (e.g., Twiss, 1977; Hirth and Tullis, 1992; Stipp et al., 2002, 2010; Cross and Skemer, 2017) and to a lesser extent of calcite (Schmid et al., 1980; Rutter, 1995; Barnhoorn et al., 2004). Some other minerals for which paleopiezometry may be applied are olivine (Van der Wal et al., 1993; Jung and Karato, 2001a,b) and feldspar (Post and Tullis, 1999).

1.3.2 Diffusion creep

The second most studied deformation mechanism of rocks is linear diffusion creep, during which vacancies in the crystal lattice are diffused in the rock. Two fundamental mechanisms exist that accommodate this diffusion in crystalline rocks. When the mechanism is characterized by diffusion of vacancies within the crystal, then it is called Nabarro-Herring creep or volume/bulk diffusion and it is given by equation:

$$\dot{\varepsilon_C} = A_{NH}\frac{\sigma\Omega}{RT}\frac{Dv}{d^2} \tag{1.3}$$

In the case when diffusion concentrates along grain boundaries, it is accommodated by diffusion of vacancies in the crystal lattice along grain boundaries (Knipe, 1989; Wheeler, 1992) and it is called Coble creep. The flow law for Coble creep is given by Eq. 1.4 and 1.5 (see p. 65 in Passchier and Trouw, 2005, for parameters):

$$\dot{\epsilon_C} = A_C\frac{\sigma\Omega}{RT}\frac{\delta}{d^3}D_{GB} \tag{1.4}$$

$$\dot{\varepsilon} = A_c\frac{\mu V D_G W}{RTd^3}(\sigma/\mu)e^{\frac{-H_G}{RT}} \tag{1.5}$$

At lower temperatures, Coble creep is faster and hence the dominant mechanism with respect to Nabarro-Herring, since diffusivity at grain boundaries is higher than diffusivity within the crystal.

Diffusion creep is an efficient mechanism of viscous deformation when diffusional distances are small (a few microns on the microscale) and the temperature is relatively high (more than half the melting temperature, T_m, of the material). In the presence of fluids, however, deformation

by diffusion creep is possible even at low temperatures, if the rate of dissolution and precipitation is fast enough (see the following paragraph for details). At lower temperatures and in absence of a fluid phase, diffusional deformation becomes idle and dislocation mechanisms take over (Raj and Chyung, 1981).

1.3.3 Dissolution-precipitation creep

Studies have pointed out the importance of dissolution-precipitation creep in the deformation of rocks (e.g., Wheeler, 1992; Grigull et al., 2012; Gratier et al., 2013; Wassmann and Stöckhert, 2013b; Reber and Pec, 2018, see also Chapter 3). It is a stress-driven mass-transfer mechanism especially effective in the presence of fluids (Coble, 1963), that can take place under much smaller stresses than dislocation creep (Ilic and Hackl, 2005). In the presence of circulating fluids and above-hydrostatic pressures, material is dissolved from high normal stress areas of minerals and transferred through the fluid, which later deposits the dissolved material in zones of lower normal stresses (pores, veins etc). The grains appear little deformed internally and the areas of lower stresses are denoted by pressure-solution seams (porosity which has later been filled up by the dissolved material). Dissolution precipitation creep is a diffusional mechanism, with diffusion being driven by the gradient in normal tractions at grain boundaries (Robin, 1978; Raj, 1982). One of the forms it is commonly expressed by is Eq. 1.1, when $n = 1$ and $m > 0$.

As it is a multi-stage series process (first dissolution of solid phase, then transport of matter through the liquid phase, and finally precipitation of matter (Raj and Chyung, 1981; Raj, 1982)), the deformation kinetics of a crystal-liquid aggregate would be dominated by the slowest of the processes: the interfacial process would control the kinetics at lower temperatures and for finer grain sizes, while the transport process would take over at higher temperatures and/or larger grain sizes (Wang and Raj, 1984).

This mechanism is also facilitated by fractures: as fluid pathways open during fracturing, diffusion of matter becomes more efficient. On the other hand, progressive healing of fractures leads to gradual deceleration of diffusion. Therefore, when fracturing activates pressure-solution, the process instead of defining a steady-state deformation mechanism tends to be cyclic: fracturing

accommodates the creep rate, fracture sealing progressively reduces this rate (e.g Gratier et al., 1999, 2013).

1.3.4 Other mechanisms

The aforementioned deformation mechanisms are the most commonly thermally activated mechanisms observed in exhumed rocks and those that control their bulk rheology. However, other important mechanisms have also been observed, such as Peierls creep, grain boundary sliding, superplasticity, and brittle creep, briefly presented below.

Peierls creep, also called low-temperature plasticity, refers to deformation occurring at low temperatures and high stresses (e.g., Frost and Ashby, 1982; Kameyama et al., 1999). As a dislocation moves within a crystal, it slides along the lattice creating a frictional resistance, called Peierls stress. This is essentially the stress needed to move a dislocation in a crystal without the help of thermal activation. It is an intrinsic property of the material (Karato, 2008; Goryaeva et al., 2015) and depends also on the temperature. A Peierls flow law has the following form:

$$\dot{\varepsilon} = A_p \sigma^2 (\frac{\sigma}{\sigma_p}) exp(\frac{-Q_p}{RT}) \tag{1.6}$$

where σ_p is the resistance to glide and is composed of an intrinsic Peierls stress and a grain size sensitive stress. The rate of deformation for Peierls creep is more sensitive to stress but less sensitive to temperature than the power-law creep (compare Eq. 1.6 to Eq. 1.1). Peierls creep is an important mechanisms, since it limits the strength of the lithosphere at high deviatoric stresses by reducing the pressure dependence of the strength and by decreasing the ability of the lithosphere to localize strain at high strain rates. As seen from Figure 1.4, there is small dependency of the Peierls mechanism on pressure and temperature. Therefore, in geodynamic modelling this mechanism can often be approximated by a maximum cutoff stress (e.g., Tackley, 1998; Kameyama et al., 1999; Watremez et al., 2013; May et al., 2015).

Grain boundary sliding (GBS) describes the translation of grains past each other, a process also including shear displacement localized in the boundary and/or within the crystal lattice adjacent to the boundary (Raj and Ashby, 1971). However, since grain boundaries are never

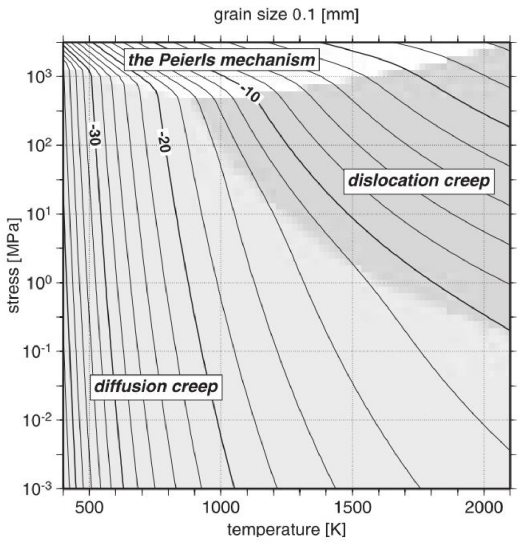

Figure 1.4: Deformation mechanism map calculated for grain size of 0.1 mm. In the light shaded area, deformation occurs mainly by diffusion creep, while in the darker shaded area, deformation occurs mainly by power-law creep. White region indicates that Peierls creep is dominant. Solid curves are lines of constant strain rate and the numbers attached to each contour indicate the logarithm of the strain rate (in s^{-1}). From Kameyama et al. (1999).

plane in the microscale, sliding can only operate in the presence of other accommodating mechanisms, such as diffusion or dislocation creep (e.g., Stevens, 1972; Burov, 2011). GBS is a highly nonlinear mechanism, operating at high stresses. When assisted by diffusion at grain boundaries, it is a high temperature mechanism (Boullier and Gueguen, 1975) that is able to accommodate high strains. However, GBS can also act parallel to dislocation creep. It is, therefore, difficult to identify and study experimentally GBS as a dominant mechanism (Stevens, 1972; Drury, 2005).

Another mechanism used to define deformation of fine-grained alloys up to very high strains without boudinage is superplasticity (e.g., Zelin and Mukherjee, 1994; Kaibyshev et al., 1998). It has also been observed in rocks (e.g., Schmid, 1982; Poirier, 1985; Rutter et al., 1994; Hoshikuma, 1996; Boullier and Gueguen, 1998) and it refers to very fine-grained aggregates (1-10 μm) of equidimensional grains, which have been deformed to very high strain without developing a strong shape- or lattice-preferred orientation. Grain boundary sliding is often the accommodating mechanism and is active only at very small grain sizes (Boullier and Gueguen, 1975; Allison et al., 1979; Schmid, 1982; Van Der Pluijm, 1991; Rutter et al., 1994). In general, superplasticity is a high temperature/low stress mechanism, independent of slip system. It is mostly observed in mafic rocks corresponding to mantle depths (Boullier and Gueguen, 1975).

All the above mentioned mechanisms describe time dependent deformation processes in rocks which, despite localization, do not lose cohesion nor continuity. However, laboratory experiments have demonstrated that rocks can also fail by static fatigue at stresses significantly lower than their short term failure strength (e.g., Kranz, 1979; Carter et al., 1981; Kranz et al., 1982; Baud and Meredith, 1997; Heap et al., 2009, 2011). This corresponds to a brittle, time-dependent mechanism called brittle creep (Brantut et al., 2012). The main underlying mechanism behind it is the propagation of sub-critical cracks via stress corrosion in a statically loaded rock, below the critical stress intensity factor (Brantut et al., 2012). During stress corrosion, the amplified stresses at the crack tip preferentially activate chemical reactions in which chemical bonds, such as the silicon-oxygen bonds in a water-quartz system, are broken (e.g., Michalske and Freiman, 1982). The minimum strain rate during this secondary creep is well approximated by a law of the form:

$$\dot{\varepsilon} \propto exp(\frac{-H}{RT})[1 - k\frac{\sigma_{peak} - \sigma_1}{K_{IC}/\sqrt{\pi\alpha}}]^{n+1} \tag{1.7}$$

where k is a non dimensional numerical factor, σ_{peak} is the maximum stress which corresponds to the short term strength of the material in the original Ashby and Sammis (1990) approach, σ_1 is the maximum principal stress, K_{IC} is the critical mode I stress sensitivity factor (or the fracture toughness of the material), α is the radius of the microcrack and n is the stress corrosion index, giving the overall stress sensitivity.

This mechanism implies an offset in the strength of porous rocks, for typical tectonic rates ($10^{-15}s^{-1}$). However, in porous rocks, brittle creep and dissolution-precipitation creep are two competitive mechanisms (Brantut et al., 2012; Reber and Pec, 2018). The transition from the first to the second occurs with increasing depth and decreasing strain rates, with brittle creep being a higher stress-lower temperature phenomenon, relative to the latter.

At this point, it is important to note that brittle fracturing/deformation plays a crucial role under high velocities and/or low temperatures, since it is an obvious mechanism underlying earthquake slip. However, as both the petrological and the modelling part of this study mainly focus on viscous deformation and deal with brittle failure in a complementary way, it is not further elaborated here. The reader is prompted to the relevant, extensive reviews concerning

the rock record under brittle deformation by Niemeijer et al. (2012) and Rowe et al. (2015).

1.3.5 Complex flow laws

Although the previously mentioned flow laws account for one type of deformation mechanism being active at a time, more than one mechanisms can be active simultaneously in a rock. The rheology of an aggregate is, therefore, dependent on the collective deformation of the constituent minerals (e.g., White et al., 1980; Handy, 1990; Platt, 2015). Below, some of the most common complex viscous flow laws are summarized.

Complex flow laws can either account for the bulk rheology of a polyphase aggregate (e.g., Handy, 1990; Tullis et al., 1991; Huet et al., 2014; Platt, 2015) or for different deformation mechanisms acting simultaneously in the same phase (e.g., Fukuda et al., 2018; Tokle et al., 2019). Handy (1990) proposed three basic types of polymineralic deformation: (1) a load-bearing framework that contains only a small amount of weak phase, (2) isolated inclusions of a strong phase within a weaker matrix and (3) an aggregate of phases that have relatively low strength contrasts. Strain partitioning in a polyphase aggregate allows expressing the bulk strength of a rock as a function of its strain rate, temperature and the volume proportions and rheological properties of its constituent minerals.

Tullis et al. (1991) performed numerical experiments on monomineralic aggregates of clinopyroxene and plagioclase in the dislocation creep regime and found that the aggregate strength is primarily affected by volume fraction, and lies between the bounds set by the end-member flow laws and those set by assumptions of uniform stress (equivalent to a Voigt bound) and uniform strain rate (equivalent to a Reuss bound).

Xiao et al. (2002) experimentally deformed quartz-anorthite aggregates in the diffusion creep regime and found that the bulk strength increases with increasing content of quartz particles which act as almost rigid inclusions. Creep data from triaxial tests at 300 MPa pressure indicate that the bulk deformation closely follows the isostress bound up to 50 wt% quartz. Similarly, Dimanov and Dresen (2005) investigated the bulk strength and rheology of a composite medium of anorthite and diopside. They found that, in general, the strength of the composite increases with increasing diopside content whilst still remaining in the isostress and isostrain bounds. The

value of the n exponent for the two-phase aggregate is between 3 and 5, depending again on the diopside content, and the activation energies are either close to or those of the end-members.

Dresen and Evans (2008) investigated the effect of a second (Si- or Al-rich) phase within fine-grained marbles in the strength of the aggregate. They found that the presence of a strong phase lowers the pressure needed for the transition from the brittle to the viscous regime relevant to the pure phase. They also concluded that the deformation resistance of the two-phase aggregate is consistently higher than that of the single phase.

Huet et al. (2014) provided a theoretical mixing law for estimating the bulk rheology of a multi-phase aggregate deforming by power-law creep. Their models are based on a minimization of the mechanical power dissipated in the rock during deformation, and the bulk creep parameters, as well as the calculated viscosities provide a good fit with two-phase experimental data. Finally, Platt (2015) examined deformation of fine-grained sheared bands of quartz-feldspar and olivine-orthopyroxene, under diffusion and dislocation creep, and proposed bulk flow laws for such ultramylonites using an appropriate mixing law.

Concerning the effect of two different mechanisms acting simultaneously on the same phase, Fukuda et al. (2018) suggested a composite flow law for wet quartz encompassing the effect of both nonlinear stress dependency and grain size, reflected upon the values of the stress dependency and grain size ($n = 1.7$ and $m = 0.51$, respectively). Moreover, Tokle et al. (2019) recently reviewed published flow laws on wet quartzite and found two distinct trends, one with high stress sensibility ($n = 4$) and one with low stress sensibility ($n = 2.7$). This correlation could be because of a change in the slip system of quartz; alternatively, dislocation accommodated grain boundary sliding (disGBS) microstructures could be indicative of deformation conditions between $n = 4$ and $n = 2.7$, suggesting a rheological model for quartz similar to that proposed of ice and olivine.

1.3.6 Competition between flow laws

Since high-temperature deformation mechanisms act in parallel, it is possible that more than one are active at the same time. In such a case, the bulk creep behaviour is controlled by the fastest mechanism (Kameyama et al., 1999; Bürgmann and Dresen, 2008).

Of the parameters controlling the transition from one deformation mechanism to another, temperature and grain size are the dominant. The former crudely controls the transition from the brittle to the viscous regime. It is, therefore, crucial to establish a realistic temperature gradient with depth, in order to obtain a better constrained strength of the lithosphere. Grain size plays also a major role in the deformation of a polycrystalline aggregate (Schmid et al., 1977; Behrmann, 1983). Diffusion creep and grain boundary sliding are favoured by small grain sizes, since diffusion paths are relatively short. The presence of a second phase might inhibit grain growth, resulting in enhancing the process (Kruse and Stünitz, 1999; Newman et al., 1999; Krabbendam et al., 2003). Concerning the effect of stresses, diffusion creep is dominant at low differential stresses, while dislocation creep takes up at higher stresses. Finally, at very high deviatoric stresses (e.g., >500 MPa for olivine), Peierls creep becomes dominant (Kameyama et al., 1999).

1.4 Brittle-Ductile Transition

Traditionally, the lithosphere has been divided in an strong, brittle layer overlying a weak, ductile one (e.g., Scholz, 1998). There exists, therefore, a transition depth above which failure of rocks happens because of fracturing, while below this zone rocks fail by ductile flow (Ranalli, 1995). The depth at which the brittle-ductile transition occurs is dependent on several factors such as lithology, water content, pressure and temperature conditions, and strain rate. It is commonly given in the form of a rheological profile with depth, or else a strength envelope (Fig. 1.5), calculated for a specific pore fluid pressure, and strain rate and accounting for one or more of the deformation mechanism presented in Chapter 1.3.

The transition from brittle to ductile deformation, however, is not a sharp boundary, but rather gradual one. Brittle and viscous deformation mechanisms can act simultaneously, giving rise to a mixed macroscopic mode of deformation (e.g., Reber and Pec, 2018), termed semi-brittle flow. This mode of deformation is common at different observation scales. At the microscale, it has been recognized at naturally (Debat et al., 1978; Tullis, 1979; Simpson, 1985) and experimentally deformed rocks (e.g., Jordan, 1987; Ji and Zhao, 1994; Ji et al., 2000; Herrmann et al., 2019). Similar semi-brittle behaviour has been also observed for granular

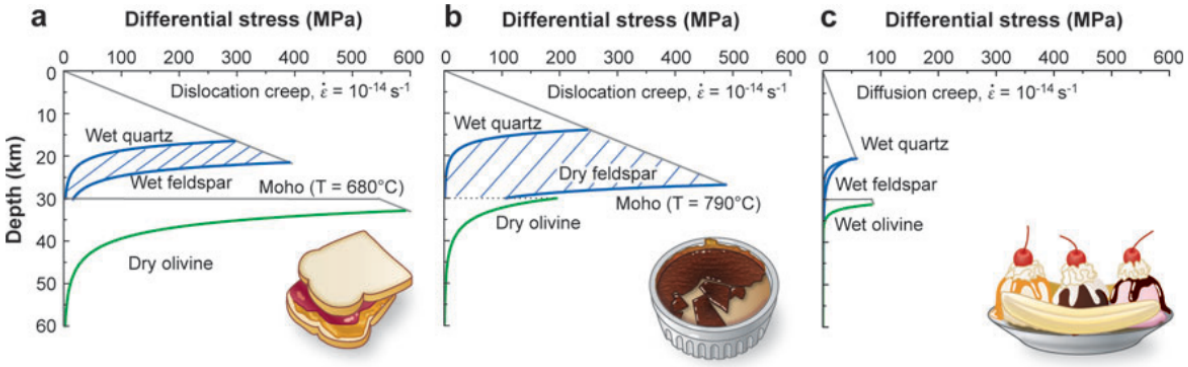

Figure 1.5: Schematic view of proposed models of strength through continental lithosphere. In the upper crust, frictional strength increases with pressure and depth. In panels (a) and (b) coefficient of friction following Byerlee's law and hydrostatic fluid pressure (ratio of pore pressure to lithostatic pressure $\lambda = 0.4$) are assumed in strike-slip kinematics. In panel (c), high pore fluid pressure ($\lambda = 0.9$) causes low friction. (a) Jelly sandwich strength envelope. (b) Créme brûlée model. (c) Banana split model. From Bürgmann and Dresen (2008).

materials in analogue experiments (Reber et al., 2014, 2015) and in small- and large-scale numerical experiments (Jammes et al., 2015; Jammes and Lavier, 2016).

1.5 Field examples

1.5.1 The Alps

The natural laboratory chosen to investigate deformation during subduction of continental slivers are the Central Alps (black square in Fig. 1.6). A detailed discussion about the geology, paleogeography and geodynamic evolution of this part of the Alps can be found in Chapter 4. Here, a brief overview of the study area, the main units that comprise it and their evolution in time are given.

The Alps are the result of the final collision between the European and Adriatic plates, which succeeded the subduction and accretion of the oceanic (Penninic) domains formerly occupying those plates. Before their convergence, the Alpine domain was already thinned, due to Jurassic east-west rifting (e.g., Eberli, 1988; Froitzheim, 1988), which resulted in a southeastward motion of Africa and Asia and assisted the opening of the Piemonte-Liguria Ocean (Laubscher and Bernoulli, 1977; Frisch, 1979; Froitzheim and Manatschal, 1996). This phase caused the most distal part of the Apulian continental margin to stretch and thin, leading to the formation of

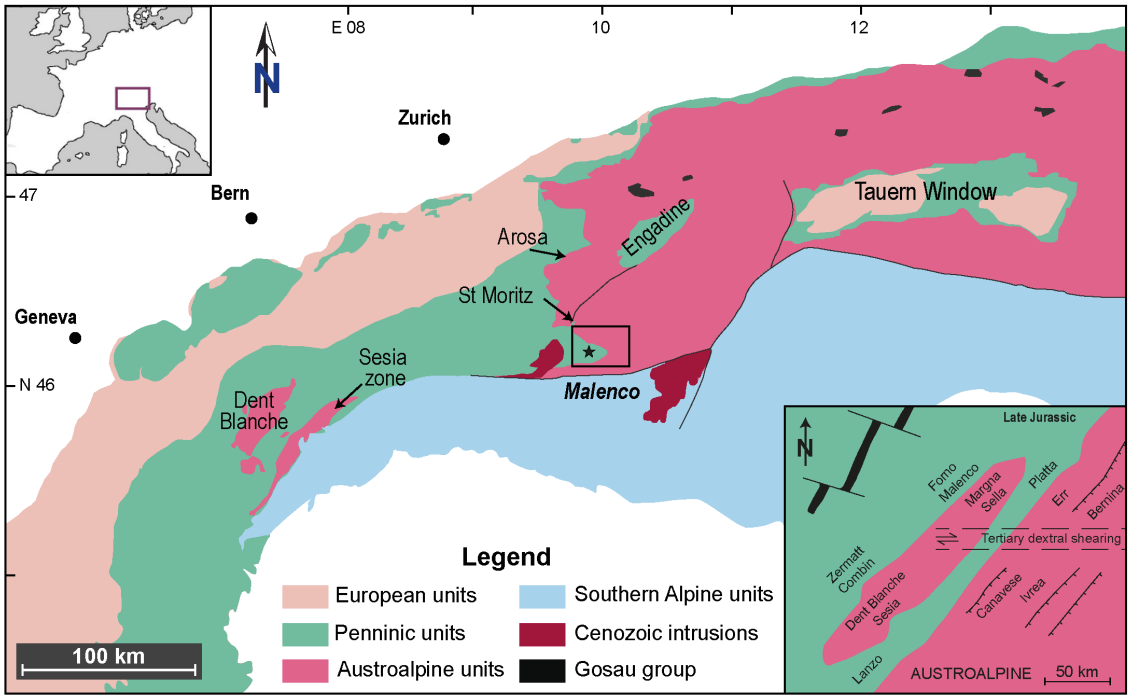

Figure 1.6: Geological map of the Western and Central Alps showing the location of the Austroalpine nappes with respect to surrounding tectonic units. The studied area is located in the black box in the Val Malenco region. Inset: Paleogeographic reconstruction along the NW margin of the Apulian plate. Dent Blanche, Sesia, Margna, and Sella nappes are interpreted as extensional allochthons derived from the Apulian margin (modified from Froitzheim and Manatschal, 1996).

extensional allochthons, such as the Margna and Sella Nappes, resting on top of exposed sub-continental mantle represented in the study area by the Malenco (ultra-)mafics (e.g., Hermann and Müntener, 1996, see also inset of Fig. 1.6).

Two Alpine orogenic phases, an early Cretaceous and a Tertiary one occurred. During the first stage, east- to southeastward subduction took place (e.g., Schmid et al., 2004), associated with top-W and locally top-SW and top-NW stacking (e.g., Froitzheim et al., 1994; Handy, 1996). The Tertiary stage is characterized by a change in the direction of convergence to N-S, with subsequent top-N thrusting and closure of the Tethys oceanic domain between the European and Adriatic plates (Froitzheim et al., 1994; Handy, 1996; Schmid et al., 2004).

The base of the Austroalpine nappes in Central and Western Alps (Dent Blanche) has been proposed by Bachmann et al. (2009b) and Angiboust et al. (2015), respectively, as a field analogue for the roof of an ancient subduction interface. Nonetheless, the southern end of the Austroalpine complex in the Central Alps (Malenco region) has up to now not been studied in

the frame of the subduction interface model, despite its potential importance as the missing element linking the depths of the Arosa-Engadine units (10-20 km) in Central Alps and Dent Blanche-Sesia massifs (40-60 km) in Western Alps.

The study area is placed in Val Malenco, N Italy, close to the border with Eastern Switzerland and geotectonically belongs to the Central Alps (black square in Fig. 1.6). The main units consist of the continental Austroalpine slivers of Margna and Sella Nappes, sandwiched between the structurally higher, also Austroalpine, Bernina Nappe and the lower Malenco serpentinites. They comprise mostly mica-rich gneisses and schists and are overlain by narrow bands of Mesozoic marbles and dolomites (Guntli and Liniger, 1989; Liniger and Nievergelt, 1990; Hermann and Müntener, 1992; Trommsdorff et al., 1993; Bissig and Hermann, 1999; Mohn et al., 2011).

1.5.2 Mélange outcrops

A particular type of subduction interface is a mélange; it is a zone of finite, mappable thickness (e.g., 1:25,000 or less; Agard et al., 2018), comprising mixed continental and oceanic blocks within an often sedimentary matrix (e.g., Cowan, 1978; Cloos, 1983; Shreve and Cloos, 1986; Ring et al., 1988). Localities where these subduction mélange formations have been reported include, among others, the Arosa Mélange in Central Alps (e.g., Ring et al., 1988; Bachmann et al., 2009b), the Franciscan Mélange in California (e.g., Hsü, 1968; Blake and Jones, 1974; Wakabayashi, 1992), the Chrystalls Beach in New Zealand (e.g., Nelson, 1982; Fagereng and Cooper, 2010), the Ghost Rocks Formation in Kodiak Island, Alaska (Meneghini et al., 2010) and the Mugi Mélange in SW Japan (e.g., Kumon, 1981; Kimura and Mukai, 1991).

Field observations suggest different deformation for blocks and matrix: the former appear either strain free or fractured, while matrix deformation attests mainly to dissolution-precipitation creep (e.g., Bachmann et al., 2009b; Fagereng and Cooper, 2010; Fagereng, 2011; Grigull et al., 2012) and locally dislocation creep. The percentage of blocks with respect to the matrix can play an essential role in the bulk deformation of this two-phase medium. It ranges typically from 5% to 50%, although higher concentrations have also been observed (Grigull et al., 2012). The co-existence of sealed veins and pervasive viscous microstructures implies fluctuations between brittle and ductile behavior, possibly due to changes in pore fluid pressures.

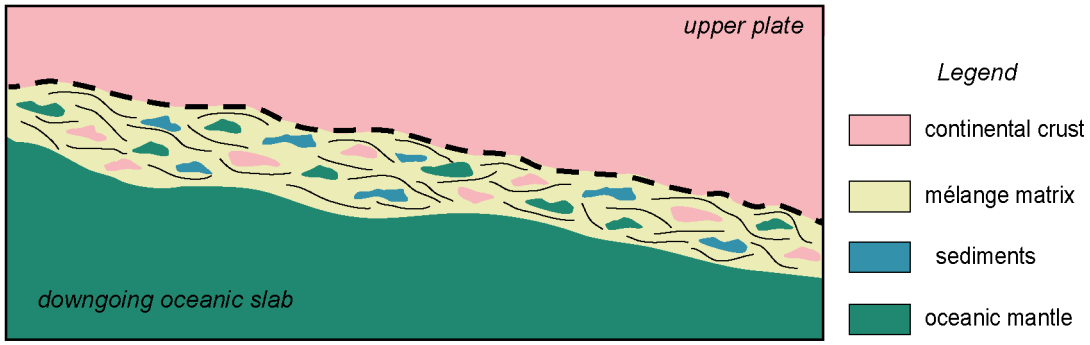

Figure 1.7: Schematic representation of a subduction mélange.

Chapter 5 presents this case study, which involves digitizing exhumed mélange outcrops from Chrystalls Beach in New Zealand (e.g., Nelson, 1982; Fagereng and Cooper, 2010), the Mugi Mélange in SW Japan (e.g., Kumon, 1981; Kimura and Mukai, 1991) and the Schistes Lustrés, in Western Alps (Lemoine et al., 1984; Agard et al., 2002), and calculating their effective rheology.

1.6 Aim and open questions

This thesis has been undertaken in the frame of European Marie Curie Initial Training Network (ITN) "Zooming In between Plates (ZIP)". The ZIP project focused on three main research goals: (1) determining the plate interface dimensions, geometry, and physical properties, (2) modelling time-integrated material fluxes, and (3) constraining how rock rheologies control seismicity, mega-earthquake nucleation, and rupture propagation. The present contribution tackles different aspects of deformation processes along a subduction interface from shallow (10 km) to intermediate (60 km) depths. The main questions addressed here are:

- What are the characteristic deformation mechanisms, along a subduction interface, as these are reported at exhumed suture zones? Can these mechanisms be connected with seismic and aseismic slip patterns remotely recorded along active subduction zones? How is the rheology of a subduction interface commonly simulated in geodynamic models?

An intrinsic part of the above posed questions is the study of exhumed rocks that once formed part of the subduction interface. Therefore, I examined the southern end of the Austroalpine

complex in Central Alps (Malenco region) comprising slivers deformed at ca. 30 km depth, in the frame of the Alpine subduction interface. This area is potentially the missing element linking deformation patterns in depths of the Arosa-Engadine units (10-20 km) in Central Alps and Dent Blanche-Sesia massifs (40-60 km) in Western Alps. This study aims to answer to the following questions:

- What is the characteristic deformation along the subduction interface during subduction of continental slivers and what is its timing? Can deformation fabrics and their timing elucidate active deformation conditions of the transition zone, at the downdip end of the seismogenic zone?

The final major set of questions that this thesis tackles is related to the deformation of the interface, in the case of a subduction mélange. In particular:

- What is the effective rheology of a subduction interface, in the special case that it is not a homogeneous medium, but rather characterized by a block-in-matrix geometry? How does the concentration of blocks affect the bulk deformation of the mélange? Can the effective rheology of a mixed material reflect small-scale complexities, rendering it thus useful for implementation in large-scale geodynamic models?

All the above questions are tackled individually in the main chapters of the thesis (Chapters 3, 4 and 5, respectively).

1.7 Scope of the thesis

The aim of the thesis is to review and investigate how deformation is taken up by the rock record along a subduction zone interface and what its effective rheology is. Two case studies are considered, the first concerning deformation of exhumed continental slivers, the second a generic mélange unit; these questions are tackled with two different approaches. The first includes field work, as well as petrological observations and geochronological analyses of exhumed continental slivers in the Central Alps. The results of this study are presented in Chapter 4: **"Deformation along the roof of a fossil subduction interface in the transition zone**

below seismogenic coupling: The Austroalpine case and new insights from the Malenco Massif (Central Alps)". It is published in the Journal *Geosphere* as:

Ioannidi, P.I., Angiboust, S., Oncken, O., Agard, P., Glodny, J., and Sudo, M., 2020, Deformation along the roof of a fossil subduction interface in the transition zone below seismogenic coupling: The Austroalpine case and new insights from the Malenco Massif (Central Alps): Geosphere, v. 16, no. X, p. 1-23, https://doi.org/10.1130/GES02149.1.

Samuel Angiboust and Onno Oncken designed the project. Paraskevi Io Ioannidi made substantial contribution to the field work, data analysis, $^{40}Ar/^{39}Ar$ dating and their interpretation and prepared the draft of the manuscript. Samuel Angiboust performed a major part of the thermodynamic modelling and contributed to the draft and the field work. Onno Oncken and Philippe Agard took part in the field work, discussion and interpretation of the data. Johannes Glodny and Masafumi Sudo performed geochronology and contributed to the discussion and interpretation of age data.

The second approach includes the numerical study of a subduction mélange, where strong basaltic blocks are embedded within a quartzitic matrix. The study focuses mainly on the effect of block concentrations on the effective rheology of the mélange, assuming the rheology of each material is characterized by brittle failure and dislocation creep. From literature review as well as the aforementioned in the Central Alps, field observations point to dissolution-precipitation creep as the dominant deformation mechanism for a quartz- and phyllosilicate-rich matrix (Bachmann et al., 2009b; Fagereng and Cooper, 2010; Fagereng, 2011; Grigull et al., 2012; Wassmann and Stöckhert, 2013b); however, the detailed processes of this deformation mechanism are not well constrained yet (see also Wallace et al., 2012). Moreover, most numerical simulations use dislocation creep to model large scale subduction zone processes. Using dislocation creep in our models makes our models comparable to large scale modelling studies. Moreover, dislocation creep is usually active at higher stresses; therefore, by using this mechanism instead of a dissolution-precipitation or diffusion creep law, and our results can be seen as placing an upper limit for the stresses (Stöckhert, 2002; Wallace et al., 2012), or a lower limit for the strain rates. This work is presented in Chapter 5: **"Effective rheology of a two-phase subduction shear zone: insights from numerical simple shear experiments and implications for subduction zone interfaces"** and is currently submitted at *EPSL*

as:

Ioannidi, P.I., Le Pourhiet, L., Agard, P., Angiboust, A., Oncken, O., Effective rheology of a two-phase subduction shear zone: insights from numerical simple shear experiments and implications for subduction zone interfaces.

Laetitia Le Pourhiet and Paraskevi Io Ioannidi designed the project. Paraskevi Io Ioannidi designed and processed the models, calculated the effective rheology and wrote the draft of the manuscript. Laetitia Le Pourhiet supervised the numerics of the study. Philippe Agard, Onno Oncken and Samuel Angiboust provided the field examples modelled and insight into deformation processes of natural rocks. All co-authors contributed to the discussion and interpretation of the results.

Finally, I summarize the most commonly observed deformation mechanisms along exhumed subduction interfaces and their interpretation in the frame of actively recorded deformation, such as episodic tremor and slip (ETS) and slow slip events (SSEs). I additionally discuss the most common numerical implementations for modelling the rheology of a subducting slab and their limitations. The results are presented in Chapter 3: **"Viscous deformation mechanisms along the subduction interface"**.

Chapter 2

Methods

Different methods were used in this study and are shortly presented here. Estimation of P-T conditions, thermodynamic modelling, as well as isotopic analyses of Rb/Sr and Ar/Ar comprise the methods employed for the field data. Additionally, the Finite Element Method (FEM) was applied in order to investigate the rheological properties of a subduction mélange. Some of the presently mentioned methods are also presented in Chapters 4 and 5, since these form parts of one accepted and one submitted publication.

2.1 Field work

Three field campaigns were undertaken in the area of Val Malenco, North Italy, during the summer months of 2015 and 2016. The aim of these campaigns was to identify deformation patterns at various scales and collect samples. These samples, obtained exclusively from the continental slivers and sediments described in the area, were used to perform petrological, geochemical and geochronological analyses. In total, more than twenty samples were collected and twelve were analyzed, in order to characterize the textures and the type of micro-scale deformation and also to constrain the P-T-t evolution of the study area.

2.2 P-T estimates

Pressure and temperature conditions as well as the metamorphic grade of the studied rocks can be inferred partly by micro-scale observations of their mineralogical composition and microstructures. For instance, deformation patterns, such as brittle failure or recrystallization due to subgrain rotation or bulging of quartz and feldspar can pinpoint to a range of temperatures under which this deformation occurred.

Moreover, the mineral parageneses, as well as the presence and/or chemical composition of some characteristic minerals can provide information for the P-T conditions of the rock. Such a mineral is phengite, an Al-rich mica and intermediate member of the muscovite-celadonite solid solution. The phengite content of metamorphic white micas and its potential use as geobarometer has been the subject of many studies (e.g., Velde, 1965; Frey et al., 1983; Massonne and Schreyer, 1987). In the presence of the requisite mineral assemblage (K-feldspar, quartz and phlogopite or another trioctahedral mica), the use of phengite as a geobarometer lies in the Tschermak (or phengite) substitution:

$$(Mg, Fe^{2+})^{[VI]} + Si^{[IV]} \leftrightarrow Al^{[VI]} + Al^{[IV]} \tag{2.1}$$

which corresponds to the transformation, with increasing pressure, of muscovite (left hand-side) to celadonite (right hand-side). Massonne and Schreyer (1987) report that, after a series of reproducible experiments, an increase in the phengite Si-content pfu (per formula unit) was observed with increasing pressure, whereas increasing temperature had the inverse effect on the Si-content. In absence of well-studied natural samples bearing the limiting mineral assemblage, the results should be used to determine only the minimum pressure under which the phengite formed.

2.3 EPM analyses

EPM analyses were performed with a JEOL-JXA 8230 probe at GFZ Potsdam, under common analytical conditions (15 kV, 20 nA, wavelength-dispersive spectroscopy mode), using a 10

μm diameter beam. The following standards were used for calibration: orthoclase(Al, Si, K), fluorite (F), rutile (Ti), Cr_2O_3 (Cr), wollastonite (Ca), tugtupite (Cl), albite (Na), MgO (Mg), Fe_2O_3 (Fe), rhodonite (Mn). Samples of micaschists and (ortho- and para-)gneisses were analyzed from both the Margna and Sella units. The analyses focused on phengite and, to a lesser extent, on amphibole composition of 8 samples. The Si-content (pfu) of phengites (Ph) and the related content of the celadonite (Cel) endmember, $K(Mg,Fe^{2+})AlSi_4O_{10}(OH)_2$, are used here as an indicator of relative pressure changes (Massonne and Schreyer, 1987). High silica regions of phengite correlate with lower aluminum contents and can be an indicator of relatively higher pressure conditions.

2.4 Rb/Sr geochronology

Rubidium/Strontium geochronological analysis were performed on four mica-rich mylonites and one impure meta-carbonatic rock from the study area in Val Malenco, C. Alps, in order to obtain their Alpine metamorphic ages.

Rubidium (Rb), an alkaline metal that occurs in two natural isotopes, ^{85}Rb and ^{87}Rb, often substitutes potassium in K-bearing minerals, such as micas and K-feldspar, due to their similar ionic radius (1.46 Å and 1.33 Å, respectively). Similarly, strontium (Sr), an earth alkaline metal, can substitute calcium in Ca-rich minerals, such as calcite, plagioclase, apatite (ionic radius 1.13 Å for Sr and 0.99 Å for Ca). Sr has four naturally occurring isotopes, ^{84}Sr, ^{86}Sr, ^{87}Sr and ^{88}Sr.

^{87}Sr is produced by the radioactive decay of ^{87}Rb. The Rb/Sr dating method is based on this decay, which happens along with the emission of a β^- particle (β-decay). The half-life time of ^{87}Rb is 48.8 Ga.

The isotope composition of a mineral after t time is calculated by the decay equation:

$$\frac{^{87}Sr}{^{86}Sr}(t) = (\frac{^{87}Sr}{^{86}Sr})(t_0) + \frac{^{87}Rb}{^{86}Sr}(e^{\lambda t} - 1) \tag{2.2}$$

where $^{87}Sr/^{86}Sr(t_0)$ is the initial isotope composition at t_0 time and λ is the international decay constant with a value of 1.42×10^{-11} a^{-1}. The ratio $^{87}Sr/^{86}Sr$ is measured directly from the

mass spectrometer and the ratio $^{87}Rb/^{86}Sr$ by isotope dilution using an isotope tracer. The initial isotope composition in time t_0 and the term $(e^{\lambda t} - 1)$ remain unknown; thus, at least two analyses of the same sample are needed in order to solve Eq. 2.2 with two unknowns. It is evident that the more minerals measured in the same sample, the more accurate the calculated age will be. Typically, diagrams are produced with $^{87}Rb/^{86}Sr$ in the x-axis and $^{87}Sr/^{86}Sr$ in the y-axis. In the case where all data points fall on the same line, the slope of this regression line gives the age of the sample and is called an *isochron*. Besides the regression line, the mean standard weighted deviation (MSWD) is calculated, which is an indication of the quality of the data. It is important to note that a geologically meaningful age can be obtained only if the mineral system has remained closed with respect to Rb and Sr.

For details concerning the Rb/Sr isotope system of white mica as well as sample preparation techniques and analysing procedure, the reader is prompted to Chapter 4.

2.5 Ar/Ar geochronology

Two mica-rich samples from the Val Malenco, C. Alps, were analysed, the first using bulk mineral separates $^{40}Ar/^{39}Ar$ dating, the second by in-situ $^{40}Ar/^{39}Ar$ UV laser ablation. $^{40}Ar/^{39}Ar$ dating is a version of K-Ar dating, established by Merrihue and Turner (1966) and is based on the decay of the naturally occurring ^{40}K to ^{40}Ar.

Potassium (K) has three naturally occurring isotopes, ^{39}K, ^{40}K and ^{41}K, of which ^{40}K is radioactive. Argon, which is a noble gas, also has three naturally occurring isotopes, ^{36}Ar, ^{38}Ar and ^{40}Ar. In this method, the sample is irradiated in a nuclear reactor and transforms some of its ^{39}K to ^{39}Ar. ^{39}Ar is radioactive and decays back to ^{39}K with a half life time of 269 years. Since an $^{40}Ar/^{39}Ar$ analysis usually takes less than six months, the amount of ^{39}Ar is assumed constant for the analysis period and can be found by:

$$^{39}Ar =^{39} K\Delta t \int_{\min e}^{\max e} \phi_e \sigma_e de \tag{2.3}$$

where t is time, ϕ_e is the flux of density of neutrons with energy, e, and σ_e is the capture cross section of ^{39}K for neutrons of e energy.

Additionally, potassium's radioactive isotope, ^{40}K, decays to ^{40}Ca and to ^{40}Ar by β^- decay, β^+ decay and by electron capture. The proportion of all potassium isotopes is homogeneous through time on Earth, with known abundances. Argon, on the other hand, is variable in isotopic composition, due to its production (^{40}Ar*) during irradiation of ^{40}K:

$$^{40}Ar^* = \frac{\lambda}{\lambda_\epsilon}{}^{40}K(e^{-\lambda t} - 1) \tag{2.4}$$

where λ is the total decay of ^{40}K and λ_ϵ the decay constant of ^{40}Ar.

The atmospheric argon is isotopically homogeneous, with known abundances (see Lee et al., 2006). The basic age equation is obtained from Eq. 2.4:

$$t = \frac{1}{\lambda} ln[\frac{^{40}Ar^*}{^{40}K}\frac{\lambda}{\lambda_\epsilon} + 1] \tag{2.5}$$

where t is the time since the closure of the system (in this case recrystallization). The ratio ^{39}K/^{40}K is effectively constant and therefore the ratio ^{40}Ar*/^{40}K is proportional to the ratio of the argon isotopes ^{40}Ar/^{39}Ar. The fact that the half life of ^{39}Ar is 269 years makes it easy to correct for its effect, since the time between irradiation and analysis is much smaller (typically less than six months).

Using the dimensionless irradiation-related parameter, J, Eq. 2.5 can be re-written as:

$$t = \frac{1}{\lambda ln}[J\frac{^{40}Ar^*}{^{39}Ar} + 1] \tag{2.6}$$

The above method gives the advantage that both K and Ar are measured simultaneously on the same aliquot of sample. This provides greater internal precision and facilitates the analysis of very small and heterogeneous samples. Moreover, this method does not require absolute values of the argon isotopes. Rather it entails isotope ratios between naturally occurring isotopes and the isotopes ^{39}Ar and ^{37}Ar produced by reactor irradiation, which have half lives of 269 years and 34.95 days, respectively. For details concerning the sample preparation techniques and analysing procedure of the ^{40}Ar/^{39}Ar analysis, the reader is prompted to Chapter 4.

2.6 X-Ray Fluorescence Spectrometry (XRF)

Major (wt% oxide) and trace (ppm) elements whole-rock analyses of samples were performed by X-Ray Fluorescence (XRF) at GFZ Potsdam. During X-ray fluorescence analysis, the samples are crushed with a steel jaw crusher, milled until a powdered material (grain size $< 63\mu$m) is obtained and fused to a glass disc. The powdered samples and two Fluxana-samples are dried at $\sim 100°C$, weighed and melted on different heaters at temperatures between 400-1150°C. The melt is then quenched to a glass disc and analyzed. Concentrations were calculated using PANalytical AXIOS Advanced wavelength dispersive XRF spectrometer.

2.7 Thermodynamic modelling

In geoscience, thermodynamic modelling is used to determine thermodynamic equilibria of mineral reactions between different solid and fluid phases. One common approach is finding the compositions and amounts of the relevant mineral phases that are minimizing the Gibbs energy, G, of a system, at constant pressure and temperature. The Gibbs energy can be given in its integrated form for constant pressure and temperature by:

$$G = H - TS \tag{2.7}$$

where H and S are the system's enthalpy and entropy, respectively and T the temperature. Phase diagrams and pseudosections were created using the Gibbs energy minimization software `Perple_X` (Connolly, 2005).

2.8 Finite Element Modelling

In Chapter 5, Finite Element (FE) numerical analysis is applied, in order to investigate the effective rheology of mélange units undergoing subduction.

FE analysis is based on subdividing the computational domain (the model) into smaller, simpler parts called *finite elements*. In each of these elements, the simple governing equations of the

problem are solved, using some necessary initial values (boundary conditions). Only the basic concepts relevant to this study are mentioned in the following section.

The equations commonly solved for lithospheric-scale problems are (1) the conservation of momentum, in which the inertial forces can be ignored for slow, lithospheric-scale deformations, resulting in the Stokes equation:

$$\frac{\partial \sigma_{ij}}{\partial x_j} - \frac{\partial P}{\partial x_i} + \rho g_i = 0 \tag{2.8}$$

(2) the conservation of mass or equation of continuity, which for the common assumption of incompressible flow can be written as:

$$\frac{\partial u_i}{\partial x_i} = 0 \tag{2.9}$$

and (3) the conservation of energy or heat, which re-written for simplification as the temperature equation is the following:

$$\frac{\partial T}{\partial t} + \mathbf{u}\nabla T = \nabla\dot{(}k\nabla T) \tag{2.10}$$

The above partial differential equations are solved in the nodes of each finite element. The shape of these elements depends on the geometry of the model/problem to be solved. In this study, rectangular elements were used.

For details concerning the governing equations, mesh, and boundary conditions used for the FE modelling, the reader is prompted to Chapter 5.

Chapter 3

Viscous deformation mechanisms along the subduction interface

3.1 Introduction

Most of the deformation during convergence and subsequent subduction is accommodated by processes along the interface of the involved plates (e.g., Kirby, 1983; Scambelluri and Philippot, 2001; Hacker et al., 2003a; Wada et al., 2008; Guillot et al., 2009; Rowe et al., 2013; Bebout and Penniston-Dorland, 2016; Agard et al., 2018). Direct observations of exhumed subduction suture zones can shed light on deformation processes and slip during subduction (see also Bachmann et al., 2009b; Fagereng and Cooper, 2010; Meneghini et al., 2010; Grigull et al., 2012; Rowe et al., 2013; Wassmann and Stöckhert, 2013b; Angiboust et al., 2014; Agard et al., 2018; Locatelli et al., 2018). Such fossil subduction zones are preserved and outcropping, among others, in the European Alps, in the Shimanto belt in Japan, in the Tian Shan complex in China etc.

The thickness of the plate interface plays a crucial role in the distribution (or localization) of deformation and it is estimated to vary from a few centimeters at shallow depths (e.g., Saffer and Tobin, 2011; Vannucchi et al., 2012; Rowe et al., 2013) to some kilometers at deeper parts (e.g., Agard et al., 2016). A recent compilation by Agard et al. (2018) suggests an average thickness smaller than ∼300 m. The subduction interface is a rather heterogeneous medium (e.g., Vannucchi et al., 2008; Bachmann et al., 2009b; Fagereng and Cooper, 2010; Grigull

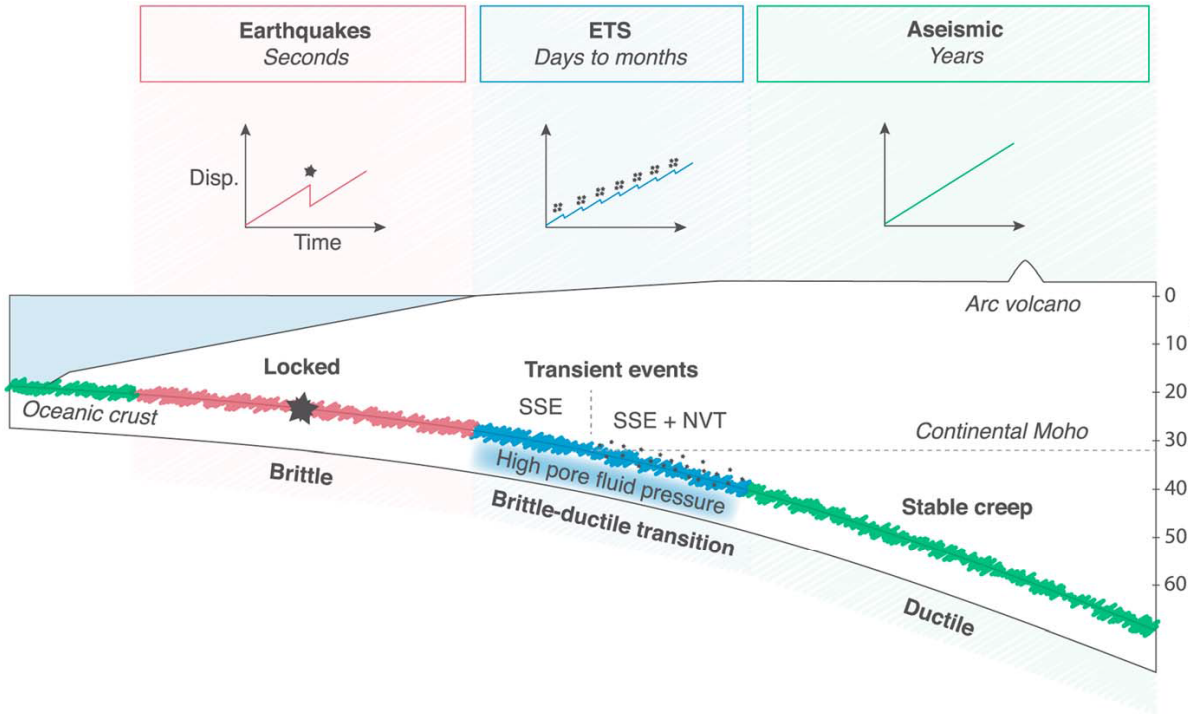

Figure 3.1: Kinematic and rheological segmentation along the subduction interface. Upper graph shows figurative displacement versus time diagram for the three domains (from Dragert et al., 2004; Bernaudin and Gueydan, 2018). Lower graph depicts locked domain with red (black star represents earthquakes), transient events domain with blue (ETS, nonvolcanic tremor (NVT) as black points), and stable slip domain in green, along a subduction plate interface (modified from Peng and Gomberg, 2010). The light blue area indicates high pore fluid pressure inferred from v_P/v_S ratio data (Audet et al., 2009; Peacock et al., 2011). Modified from (Bernaudin and Gueydan, 2018).

et al., 2012; Vannucchi et al., 2012; Rowe et al., 2013; Angiboust et al., 2015). This implies that deformation within it occurs at different strain rates and, therefore, some of its components might show brittle behavior, while others may deform viscously (e.g., Fagereng and Cooper, 2010; Vannucchi et al., 2010; Angiboust et al., 2015).

Deformation mechanisms, such as dislocation and diffusion creep and grain boundary sliding, can act competitively at a range of temperatures and strain rates, while brittle creep takes up deformation at high stresses and low temperatures (see Reber and Pec, 2018, for a comparison). These mechanisms can either act individually or in parallel and are primarily a function of pressure, temperature, strain rate and grain size. As a result, the classic view of a seismogenic zone bounded updip and downdip by stable areas that are creeping (e.g. Sibson, 1984; Scholz, 1998) is substituted by a more complex segmentation, as attested by both field observations (e.g., Bachmann et al., 2009b; Fagereng and Cooper, 2010; Rowe et al., 2013; Wassmann and

Stöckhert, 2013b) and remote sensing techniques (seismicity and GPS data) (e.g., Audet et al., 2009; Obara and Kato, 2016).

A similar kinematic and rheological segmentation has emerged the past two decades from advances in remote sensing and seismological techniques (e.g. Audet et al., 2009; Peng and Gomberg, 2010; Saffer and Tobin, 2011; Audet and Kim, 2016; Obara and Kato, 2016; Gao and Wang, 2017; Audet and Schaeffer, 2018). It is based on the continuous spectrum of slip that ranges between the traditional end-members of seismic and aseismic slip and includes (transient) slip patterns, such as slow slip events (SSEs) and transient episodic tremor and slip (ETS) (e.g Kodaira et al., 2004; Ito and Obara, 2006; Audet et al., 2009; Obana and Kodaira, 2009; Saffer and Tobin, 2011; Obara and Kato, 2016). Mechanically, this segmentation suggests that some of these events are possibly associated with mixed frictional-viscous processes, intermediate between stick-slip and steady creep.

Linking these far-field observations to micromechanical deformation models can help us better understand and constrain kinematic observations with respect to the actual mechanics of such observations. The rheological behaviour of important rock-forming minerals, such as calcite, quartz, feldspar, pyroxene, olivine, and garnet have been extensively tested (e.g., Herwegh et al., 2005; Bürgmann and Dresen, 2008; Karato, 2008); however, other important minerals (such as phyllosilicates, amphiboles, and calcsilicates), as well as aggregates of aforementioned minerals are poorly constrained. Another caveat is the fact that extrapolation of creep parameters is necessary, in order to relate experimental results to strain rates, temperatures and stresses relevant for geologic (time-)scales. However, if the deformation mechanisms are similar, these extrapolations are valid, (Dimanov and Dresen, 2005).

Numerical models, on the other hand, often "rely" on these extrapolations for calculating the strength of the rocks they simulate. However, due to computational and/or resolution limitations, they often use either a monomineralic flow law, or only one creep law for what is usually a more complex material. Below I summarize the most common, naturally observed deformation mechanisms along a subduction interface and their inferred connection to kinematic deformation recorded in active subduction zones. I also present the most used numerical implementations for modelling the rheology of a subducting slab and discuss their limitations. Notably, the newly discovered slip patterns are only briefly discussed, since it is beyond the

scope of this chapter to give a detailed overview.

3.2 General deformation mechanisms and their constitutive laws

During viscous processes, deformation is mainly accommodated by movements of defects in the crystal lattice of minerals, as well as by material transport in a fluid phase. The most commonly observed viscous deformation mechanisms in exhumed suture zones are dislocation and dissolution-precipitation creep.

At low stresses, diffusion creep is usually the main accommodating mechanism. Strain rates depend on grain sizes and also linearly on stresses. A special case of diffusion creep is dissolution-precipitation creep, a stress-driven mass-transfer mechanism, especially effective in the presence of fluids (e.g., Coble, 1963; Wheeler, 1992; Gratier et al., 2013). In the presence of circulating fluids and above-hydrostatic pressures, solid material is dissolved from high normal stress areas of minerals and transferred through the fluid, which later deposits the dissolved material in zones of lower normal stresses (Fig. 3.2a). The grains appear little deformed internally and the areas of lower stresses are denoted by pressure-solution seams (porosity which has later been filled up by the dissolved material). One of the forms it is most commonly expressed by is:

$$\dot{\varepsilon} = A_{diff}\sigma d^{-m} exp(\frac{-Q}{RT}) \tag{3.1}$$

where $\dot{\varepsilon}$ is the strain rate, A a material constant, σ the stress, d the grain size, m the grain size exponent, Q the activation energy, R the molar gas constant, and T the absolute temperature. For a review on dissolution-precipitation creep see Gratier et al. (2013).

As stresses get higher, dislocation creep takes over. It is the mostly studied deformation mechanism in experiments and also the most commonly used in geodynamic modelling. It is a thermally activated process, during which dislocations move through the crystal lattice (Fig. 3.2b). Strain rate is proportional to stress with a stress exponent often between 2 and 5, and shows no dependence on grain size. Several relationships have been proposed to describe the dependence

of strain-rate on stress under dislocation creep. The most common is:

$$\dot{\varepsilon} = A_{disl}\sigma^n exp(\frac{-Q}{RT}) \tag{3.2}$$

where $\dot{\varepsilon}$ is the strain rate, A a material constant, σ the stress, n the stress exponent, Q the activation energy, R the molar gas constant, and T the absolute temperature.

Two more mechanisms of interest for exhumed subduction zones and geodynamic modelling are Peierls creep and grain boundary sliding. The former describes low-temperature plasticity and depends on the frictional resistance of dislocations, as they move through the lattice (Frost and Ashby, 1982; Kameyama et al., 1999; Karato, 2008; Goryaeva et al., 2015). It is an important mechanism, since it limits the strength of the lithosphere at high deviatoric stresses. Grain boundary sliding, on the other hand, occurs when grains move past each other, along with shear displacement at the boundary and/or within the crystal lattice adjacent to the boundary (Raj and Ashby, 1971). It happens exclusively in the presence of other accommodating mechanisms, such as diffusion or dislocation creep (e.g., Stevens, 1972; Burov, 2011).

3.3 Deformation mechanisms on rocks of a subduction interface

The aforementioned viscous deformation mechanisms responsible for rock deformation in subduction zones are largely dependent on lithology, water content, strain rate, and regional pressure and temperature conditions, or depth. A potential bias emerges from field observations, as rock clusters point to preferential exhumation depths of 30 and 80 km, and possibly 55-60 km (Agard et al., 2018).

Generally, dislocation creep accommodates deformation when stresses are higher (Stöckhert, 2002), while the co-existence of high pressures and a fluid phase along the subduction interface enhance the solubility of minerals (e.g., Manning, 1994; Shen and Keppler, 1997; Stöckhert, 2002), resulting in dissolution-precipitation creep or grain boundary sliding accommodated by dissolution-precipitation creep (e.g. Stöckhert, 2002; Bachmann et al., 2009b; Fagereng and Cooper, 2010; Grigull et al., 2012; Kimura et al., 2012; Wallace et al., 2012; Angiboust et al.,

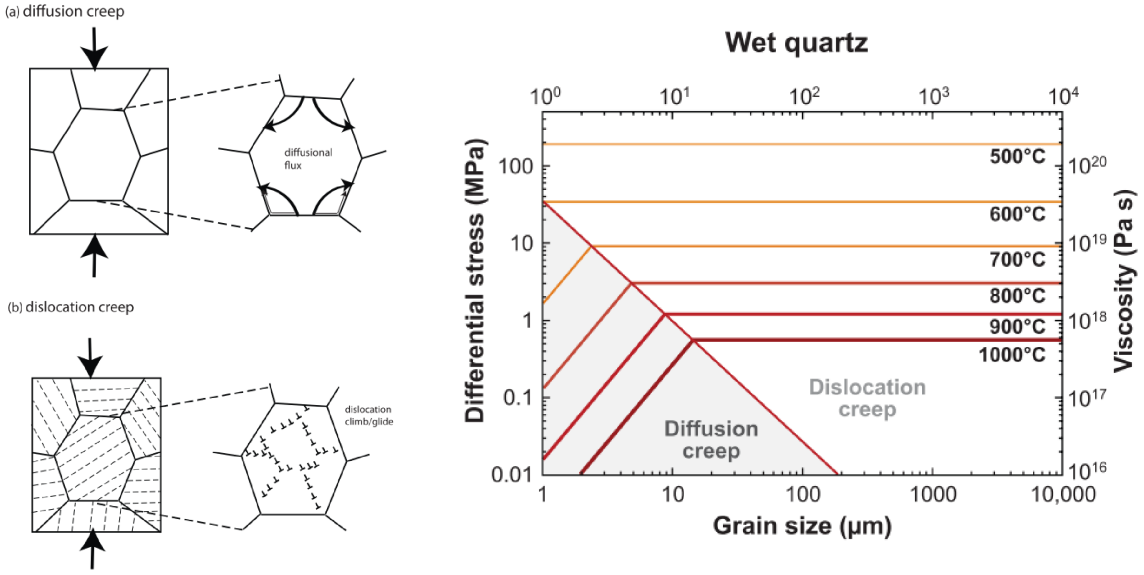

Figure 3.2: Left: Cartoons illustrating physical processes of plastic deformation. (a) Diffusion creep. When grain boundaries are weak, grain-boundary sliding occurs upon applying a stress. This leads to the variation in the normal stress at grain boundaries with different orientation, which in turn causes the concentration gradient in vacancies. Diffusive mass transport occurs due to this concentration gradient in vacancies that leads to plastic deformation. Diffusional mass transport relaxes stress concentration, and steady-state creep occurs corresponding to the steady-state relaxed stress distribution. Diffusional mass transport occurs both inside of grains and along grain-boundaries. (b) Dislocation creep. Crystal dislocations are generated in a crystal and the propagation of crystal dislocations results in finite strain of a crystal. Dislocations move only along certain crystallographic orientations. Therefore plastic deformation by dislocation motion is anisotropic. From Karato (2013); Right: Deformation mechanism map for wet quartz (Rutter and Brodie, 2004a,b), for a strain rate of $10^{-12}s^{-1}$ and a rock density of 2.8 gr/cm^3. From Bürgmann and Dresen (2008).

2015). An extensive report on individual deformation mechanisms and their microscale evidence on rocks is given by Passchier and Trouw (2005), and a possible visualization of a subduction interface based on exhumed fossil subduction zones is given by Agard et al. (2018). Below we focus on deformation patterns on exhumed rocks that formed part of a subduction zone (interface).

The Mugi mélange, part of the Shimanto Belt in SW Japan, consists of a mixture of basalt, chert and shale slivers wrapped within a highly sheared black shale matrix. The inferred maximum temperature of > 150°C (Kimura et al., 2012, and references therein) corresponds to the upper thermal limit of the seismogenic zone (Oleskevich et al., 1999). The fabrics differ between the sheared matrix and the basaltic blocks: pressure-solution, mineral preferred orientation and flattening during shear characterize the matrix (Fig. 3.3a), while (ultra)cataclastic deformation prevails in the competent basaltic blocks, with only scarce evidence of pressure-solution. The

Makimine mélange, another mélange unit of the accretionary Shimanto belt, comprises ocean plate stratigraphy (mudstones, basalt, tuff and turbidites) and has experienced metamorphism at $10 - 15$ km, depth with a maximum temperature of $300° - 350°$C (Ujiie et al., 2018, and references therein). A common feature is the co-existence of mineralized veins and relatively pervasive viscous fabrics, implying locally elevated fluid pressures and increased viscous strains, respectively.

The Chrystalls Beach Complex, an accretionary mélange within the Otago Schist in New Zealand, formerly occupied part of the seismogenic zone and formed under peak metamorphic conditions of > 0.55 GPa and $\sim 300°$ (Fagereng and Cooper, 2010; Fagereng, 2011). Bi-modal deformation fabrics are observed, too, with chert and basalt blocks exhibiting brittle structures while the phyllitic matrix shows evidence of viscous shearing. The overall deformation points to a mixed continuous-discontinuous behavior: continuous matrix fabrics accounting for aseismic flow abut more competent areas of localized seismic and/or aseismic slip (Fagereng and Cooper, 2010). Different deformation mechanisms described at the microscale by Fagereng (2011), imply transient, locally elevated fluid pressures.

Close to Arosa, in Central Alps, rock fabrics at shallow paleodepths ($10 - 15$ km) point to deformation by dissolution-precipitation creep along the subduction interface, with an upper temperature limit of $\sim 150°$C (Bachmann et al., 2009b). In the Engadine Window, temperatures approach 300°C, as dislocation creep and mylonitization occur in the basement rocks above the subduction shear zones (Bachmann et al., 2009b). In Val Malenco, also in Central Alps, at slightly greater depths (corresponding to 0.9 GPa and $\sim 400°$C), Ioannidi et al. (2020) reported widespread pressure-solution fabrics on greenschist facies felsic rocks along with semi-brittle and brittle networks (Fig. 3.3B). Further deep, in the Dent Blanche Thrust in Western Alps (peak metamorphic conditions of $1.1 - 1.3$ GPa and $400 - 500°$C, at ca. 35 km), a cataclastic matrix is cemented and reworked by dissolution-precipitation creep induced foliation after cataclasis (Angiboust et al., 2015, Fig. 3.3D). Microstructural observations suggest cross-cutting relationships between brittle and viscous deformation: cataclasis overprinting foliated cataclasites and dissolution-precipitation creep overprinting cataclasis. The same ages and PT-conditions found for both mechanisms indicate a co-existence or cyclic change of different deformation conditions.

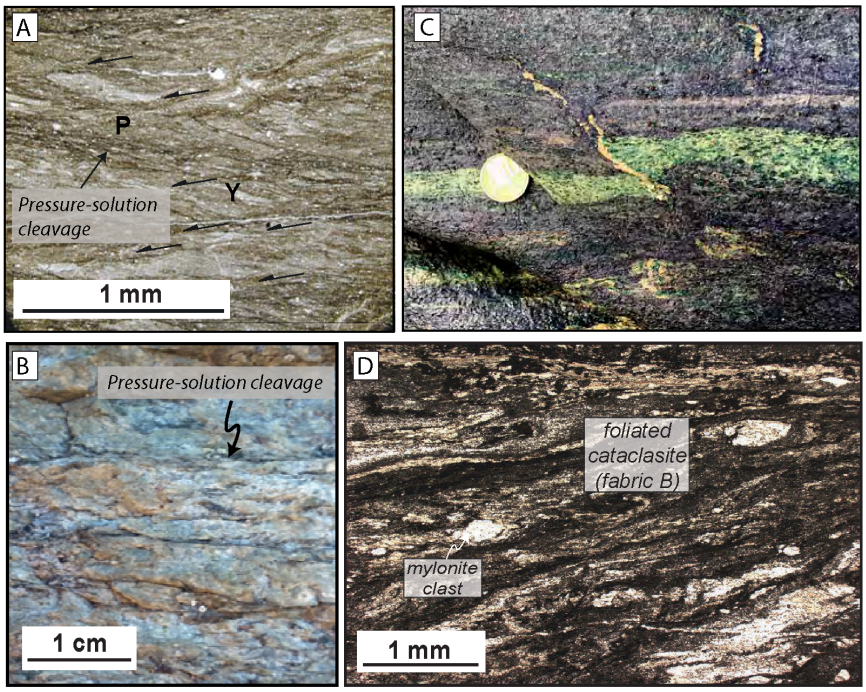

Figure 3.3: (A) Photomicrograph of shale matrix from the Mugi Mélange. Systematic Y-P fabrics and pressure-solution cleavages are well developed. From Kitamura et al. (2005). (B) Close-up hand specimen picture showing the presence of dark pressure-solution planes. From Ioannidi et al. (2020). (C) Thrust-sense dilational shear fracture filled with quartz offsetting a foliation omphacite-rich band and merging into viscous shear in surrounding blueschist. From (Behr et al., 2018). (D) Optical microscope view showing a foliated cataclasite matrix where various-sized fragments of the previous mylonite are floating (fabric B). Note the abundance of dark fringes lining the foliation pointing to the presence of pressure-solution deformation processes. From Angiboust et al. (2015).

Eclogites from the Monviso ophiolite preserve textural evidence for multiple brecciation under eclogite-facies conditions, from outcrop to thin section scale (Locatelli et al., 2018, 2019). It is one of the few localities that record intermediate depth seismicity and associated pulsed fluid flow (Angiboust et al., 2011; Locatelli et al., 2018). Healed fractures within garnet crystals are interpreted to represent successive periods of brittle and ductile deformation during prograde subduction of the ophiolite, with these cycles occurring on the order of 2 Myr or less (Broadwell et al., 2019).

Finally, in the Cycladitic Blueschist Unit in Syros, formed under peak metamorphic conditions of $1.2 - 1.4$ GPa and $450 - 500°$, viscous dislocation creep is reported in the blueschists (Behr et al., 2018). However, the co-existence of blueschists with eclogite facies rocks that deform by brittle fracturing and veining (Fig. 3.3C) suggests a strong rheological contrast (Behr et al., 2018), which may produce combined brittle-viscous shearing.

Interestingly, in the presented field examples, all viscous deformation fabrics are accompanied by features of brittle faulting. This co-existence of seemingly refuting deformation fabrics on the same rock (Fagereng and Cooper, 2010; Kimura et al., 2012; Angiboust et al., 2015) or on different rocks in close vicinity to each other (Behr et al., 2018), such as (hydro)fracturing alongside dissolution-precipitation or dislocation creep, points to unstable deformation conditions. It is known, for instance, that dissolution-precipitation creep during the interseismic period favors compaction of pores and accounts for aseismic creep (Zhao et al., 2002; Bachmann et al., 2009b; Gratier et al., 2011). However, the efficiency of this mechanism depends on the diffusion distances. For large distances, this mechanism cannot accommodate the imposed strain rate and therefore, small seismic ruptures might take over (Gratier et al., 2011). Additionally, brittle and viscous deformation do not act at the same time scales. Fracturing is favoured at fast strain rates and short time scales, whereas viscous deformation takes place at much longer time scales, possibly because it is governed by stress-driven diffusive mass transfer (Gratier et al., 2013). From the rock record, a segmentation of the subduction interface with depth is evident.

A growing body of field studies points to a close relationship between fabrics and remotely recorded slip. In the Chrystalls Beach complex, Fagereng and Cooper (2010) suggested partitioning of seismic and aseismic slip, depending on the volumes of blocks and matrix. Matrix-dominated regions would predominantly deform aseismically, exhibiting distributed deformation, while block dominated regions would show localized seismic and/or aseismic slip. Angiboust et al. (2015) suggested multiple switches between brittle and ductile deformation fabrics, most likely connected to unstable conditions of transient slip near the downdip limit of the seismogenic zone, due to either afterslip or slow slip phenomena. Moreover, the strong rheological contrast between the blueschist and eclogitic units in Syros may produce coupled brittle-viscous deformation, therefore resembling possibly deep episodic tremor and slip (Behr et al., 2018). In the Makimine mélange, mineralized veins, which are evidence for locally elevated pore fluid pressures, and the relatively intense viscous fabrics, suggest frictional-viscous deformation at high strain rates. Ujiie et al. (2018) suggest that the geophysically observed signature of the deformation studied in the Makimine mélange may be transient slow slip faster than plate motion rates (SSEs), accompanied by localized frictional failure (tremor containing LFEs).

All the above observations suggest that deformation mechanisms along the plate interface switch from ductile to brittle and vice versa over (short) periods of time. These changes are not only a function of pressure and temperature, but also of rheological heterogeneities along the interface, fluid content and (transient) strain rates. Following up on these observations, models have focused lately on modelling such processes in the small-scale in which they are observed (Fagereng and Den Hartog, 2017; Webber et al., 2018; Beall et al., 2019; French and Condit, 2019, and present work shown in Chapter 5). These studies are discussed briefly at the end of Chapter 3.5.

3.4 Deformation in relation to geophysical/geodetic observations

The rheological segmentation of subduction zones has also emerged from records of high-sensitivity networks (e.g Obara, 2002; Rogers and Dragert, 2003), which revealed a continuous spectrum of slip patterns along subduction zones, ranging from seismic to aseismic slip (e.g. Peng and Gomberg, 2010; Gao and Wang, 2017, and references therein). Such patterns include weak vibrations accompanied by aseismic slip, the coupled phenomena being referred to as episodic tremor and slip (ETS), and seismic signals of low and very low frequency events (LFEs, Katsumata and Kamaya (2003); Shelly et al. (2006) and VLFs, Obara and Ito (2005); Ito et al. (2009)). These weak seismic events have been identified in Japan, Cascadia, Central California, Mexico, and Costa Rica (e.g., Husker et al., 2012; Hyndman et al., 2015; Wang and Tréhu, 2016; Obara, 2011).

Gao and Wang (2017) recently suggested a rheological segmentation of the megathrust and a unifying model that explains the relationship between the seismogenic zone and the ETS zone in terms of alternating frictional and viscous behaviours of the fault zone (Fig. 3.4). The spatial ocurrence of ETS possibly marks a transition from unstable (seismogenic) to stable (creep) slip. It has also been suggested that the updip and downdip limits of the seismogenic zone could be marked by slow-slip phenomena. This continuum of slip is driven by the inherent properties of the fault surface (Peng and Gomberg, 2010). Detailed overviews for these slip patterns are given by Peng and Gomberg (2010) and Gao and Wang (2017).

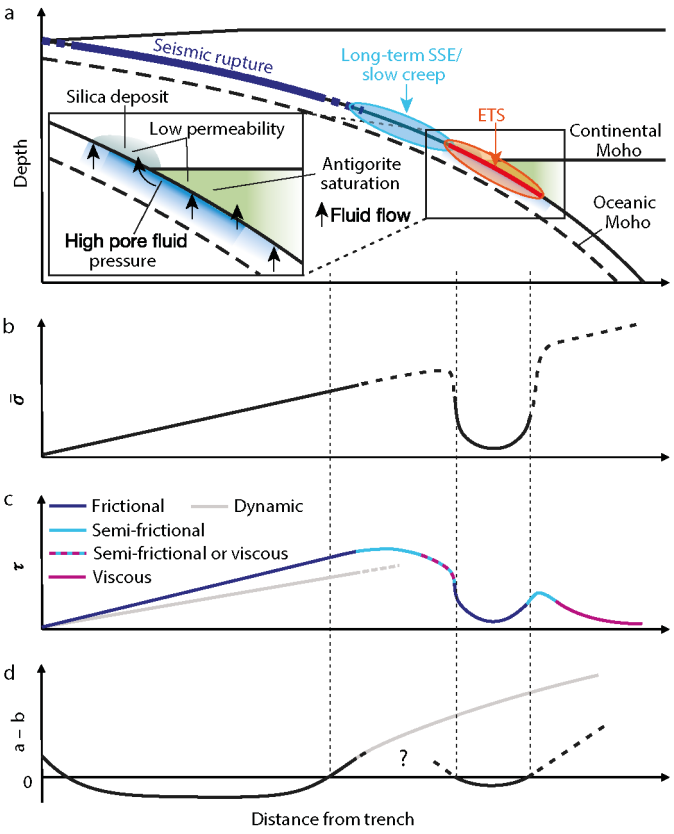

Figure 3.4: Schematic illustration of fault stress and slip phenomena for subduction zones that produce great earthquakes and ETS. (a) Downdip variations in slip behaviour and relationship of ETS with the mantle wedge corner (MWC). The inset shows the inferred hydrogeological conditions around the MWC. (b) Inferred effective normal stress σ along fault. (c) Resultant shear stress τ along fault and rheological behaviour. The dynamic stress is responsible for frictional heating. The deeper part of the segment between the two frictional segments may be either semi-frictional or viscous depending on the thermal regime. (d) A hypothesized scenario of friction parameter (a - b) distribution that can facilitate ETS. The question mark indicates that the relevance of the parameter in this segment is unclear. The grey line represents the usually assumed distribution. In b and d, segments that are not purely frictional are dashed. From Gao and Wang (2017).

3.5 Use of viscous rheology in subduction zone modelling

In (elasto-)visco-plastic models, the yield stress of a rock is described by its frictional and viscous strengths, which depend on the surrounding conditions. Rate- and state-friction laws (e.g., Dieterich, 1978; Ruina, 1983; Scholz, 2002) have been invoked widely to model dynamic rupture of both normal earthquakes (e.g., Rice et al., 2001; Noda and Lapusta, 2013) and slow slip events (Liu and Rice, 2005, 2007; Rubin, 2008; Segall and Bradley, 2012). Other studies, tackling the generation of slow slip events, account for frictional heterogeneities on a fault by

invoking brittle patches embedded within a surrounding linearly viscous fault surface (e.g., Ando et al., 2010; Nakata et al., 2011; Beall et al., 2019). Since different flow laws give different viscosity estimates, the initial viscosity approximation implemented in a model exerts some control on the resulting strength. As (rate- and state-) friction laws are not the scope of this study, we rather focus on how viscous deformation is most often implemented in (elasto-)visco-plastic numerical simulations.

Usually, the viscosity of a rock is approximated in two ways: 1) by a fixed Newtonian viscosity (e.g Kaus and Podladchikov, 2006; Herrendörfer et al., 2015), or 2) by an effective viscosity based on experimentally derived flow laws (e.g. Regenauer-Lieb et al., 2001; Gerya et al., 2002; Yamato et al., 2007; Babeyko and Sobolev, 2008; Angiboust et al., 2012; Van Dinther et al., 2013; Ruh et al., 2015; Sobolev and Muldashev, 2017). Although there is a plethora of these flow laws in literature, most numerical studies use relatively simple rheologies, due to additional assumptions and uncertainties inserted by more complex laws.

Dislocation creep is the most commonly used flow law for crustal and mantle rheologies in subduction modelling (e.g. Gerya et al., 2002; Babeyko and Sobolev, 2008; Wallace et al., 2012; Van Dinther et al., 2013; Ruh et al., 2015; Sobolev and Muldashev, 2017), while a weak subduction interface (or channel) has been approximated by an empirically weakened dislocation creep flow law for quartzite (e.g. Babeyko and Sobolev, 2008). By using dislocation creep, which requires generally higher stresses than dissolution-precipitation and diffusion creep, the estimated viscous strength is overestimated; thus, one can consider this as maximum viscous strength (Stöckhert, 2002; Wallace et al., 2012).

Dissolution-precipitation creep is often approximated by diffusion creep, especially when the former is controlled by dissolution along grain boundaries (e.g., Karato, 2013; Klinge et al., 2015). However, including dissolution-precipitation creep is a complicated task (e.g. Wallace et al., 2012), due to the strong interaction between stress state and diffusional flux (see Raj and Ashby, 1971; Karato, 2013). However, it is considered in some models (e.g. Sobolev and Muldashev, 2017). Finally, the Peierls mechanism is often approximated by a single value of maximum cutoff stresses (e.g. Tackley, 1998; Watremez et al., 2013; May et al., 2015), in order to limit unrealistically high deviatoric stresses.

Large-scale studies that have used a bulk flow law instead of a monomineralic one are scarce.

Pérez-Gussinyé et al. (2006) have used a composite flow law for the crust consisting of 50% dry quartz and 50% anorthosite, in accordance to the numerical estimations of Tullis et al. (1991) for a composite material. However, their study focused on rifted margins and the continent-ocean-transition.

The reason large geodynamic models do not usually take into consideration such heterogeneities is due to resolution limitations. A more realistic way of treating the rheology of the plate interface is to focus instead on small-scale studies that are able to model heterogeneities, both in terms of composition and rheological behaviour. Webber et al. (2018) used a composite matrix rheology involving linear dissolution-precipitation creep in phyllosilicates (Niemeijer and Spiers, 2005; den Hartog et al., 2013; Fagereng and Den Hartog, 2017) and non-linear dislocation creep, in order to investigate stress and strain transients in the Chrystalls Beach mélange. Their high block concentration model produces a cycling behaviour and mixed brittle-viscous deformation.

In addition, Beall et al. (2019) studied the effective rheology of a generalized mélange unit as a function of block concentration and strain, assuming constant linear rheologies and constant stress boundary conditions. They concluded that, in cases where clasts constitute $< 50\%$ of the total volume, deformation within the mélange is governed by that of the weak matrix; however, when concentrations of the strong phase are higher, viscosity can increase up to more than 10 times, due to clast interactions. Chapter 5 also focuses on the effective rheology of a a similar setup (subduction mélange). By using nonlinear viscosities and kinematic simple shear conditions, effective creep parameters for viscous and brittle-viscous deformation for different block concentrations are provided. Bulk viscosity depends on block concentration, when this exceeds 50%. Moreover, bulk viscosity is nonlinear, even during mixed brittle-viscous deformation of the mélange.

Finally, French and Condit (2019) studied strain partitioning along an exhumed subduction interface, using as their case study the lithologic units observed in the Arosa Zone, C. Alps (Bachmann et al., 2009b; Jaeckel et al., 2018). By employing different experimentally derived laws for viscous creep, rate- and state-friction, and varying pore fluid pressures, they investigate the conditions under which aseismic creep and SSEs might occur in the different units that constitute part of the subduction interface.

3.6 Reconciling natural, experimental and numerical observations

Subduction zones are naturally complex systems, with variable strain rates acting along their interfaces and with large heterogeneity in their initial configuration (rock properties, water content, thermal gradients, stage of seismic cycle etc). Both from far-field and rock observations, it is evident that a sharp segmentation along a subduction zone is not realistic. Absence of frictional heating and the presence of frictional-viscous deformation fabrics, acting preferentially on rheologically different rocks, might be indications for transient slip events being recorded on the rocks in a subduction zone regime.

Re-assessing fabrics in exhumed rocks with respect to their (relevant) timing, spatial distribution and cross-cutting relations is essential for linking kinematic far-field observations to the physics of the broad spectrum of slip phenomena. With accumulated evidence from different fields and their combined interpretation, flow laws can also be better constrained. Such flow laws might incorporate dissolution-precipitation and dislocation creep (e.g., Wheeler, 1992; Gratier et al., 2013; Fukuda et al., 2018), mixing laws for polymineralic assemblages (e.g., Tullis et al., 1991; Huet et al., 2014) or account for mixed semi-brittle deformation (e.g., Reber et al., 2014, 2015), similar to the ones reported in subduction zones. Finally, incorporating the results of small-scale numerical studies to large-scale geodynamic models may help better understand some aspects of transient slip patterns.

Chapter 4

Deformation along the roof of a fossil subduction interface in the transition zone below seismogenic coupling: The Austroalpine case and new insights from the Malenco Massif (Central Alps)

Note

This chapter is a reformatted version of a paper with the same title published in *Geosphere*, in the special issue Subduction Top to Bottom 2.

Abstract

A network of fossil subduction plate interfaces preserved in the Central Alps (Val Malenco, N Italy) is herein used as a proxy to study deformation processes related to subduction and subsequent underplating of continental slices (in particular the Margna and Sella nappes) at depths reported to in the former brittle-ductile transition. Field observations, microfabrics, and mapping revealed a network of shear zones comprising mostly mylonites and schists but also

rare foliated cataclasites. These shear zones are either located at the contacts of the two nappes or within the boundaries of the Sella unit. Microprobe results point to two different white mica generations, with higher-pressure (Si-rich) phengites rimming lower-pressure (Si-poor) phengites. Garnet is locally observed overgrowing resorbed pre-Alpine cores. Pressure-temperature estimates based on pseudosection modeling point to peak burial deformation conditions of ~ 0.9 GPa and 350°-400°C, at ca. 30 km depth. Rb/Sr geochronology on marbles deformed during the Alpine event yields an age of 48.9 $\pm$ 0.9 Ma, whereas due to incomplete recrystallization, a wide range of both Rb/Sr and $^{40}Ar/^{39}Ar$ apparent ages is obtained from deformed orthogneisses and micaschists, embracing 87-44 Ma.

Based on our pressure-temperature, structural and geochronological observations, the studied shear zones last equilibrated at depths downdip of the seismogenic zone in an active subduction zone setting. We integrate these new results in the frame of previous studies on other segments of the same Alpine paleosubduction interface, and we propose that this system of shear zones represents deformation conditions along the subduction interface(s) in the transition zone below the seismogenic zone during active subduction.

4.1 Introduction

Subduction zones commonly evidence strong interplate coupling and large magnitude earthquakes in the seismogenic zone (e.g., Hyndman et al., 1997; Conrad et al., 2004; Heuret and Lallemand, 2005). Investigating deformation processes taking place along and in the vicinity of their interface can shed light on properties such as the distribution of seismicity or the effective rheology along the interface (e.g., Stöckhert, 2002; Herrendörfer et al., 2015). Exhumed suture zones are important targets since they enable a direct insight on ancient subduction settings and provide opportunities to access the long-term record of subduction zone deformation (e.g., Ernst and Dal Piaz, 1978; Platt, 1986; Stöckhert, 2002; Agard et al., 2018). Metamorphic rocks from ancient sutures may yield information on how rock fabrics evolve with depth from shallow brittle seismogenic faults (Sibson, 2013; Yamaguchi et al., 2014; Saffer and Wallace, 2015) to deeper tremorgenic regions and beyond (Angiboust et al., 2015; Obara and Kato, 2016; Webber et al., 2018). While the shallow segments of the plate interface have been extensively

documented thanks to a wealth of well-exposed key localities (Kitamura et al., 2005; Vannucchi et al., 2008; Bachmann et al., 2009b; Rowe et al., 2013), our understanding of deeper deformation processes (20-40 km depth) is hampered by the scarcity of direct observations on localities devoid of exhumation-related tectonic imprint. Even rarer is the natural record of deformation along the hanging wall of a subduction interface.

The European Central Alps represent a remarkable natural laboratory giving the opportunity to (nearly) continuously document hanging-wall processes from shallow levels exposed in Arosa and Engadine regions (Bachmann et al., 2009a,b) down to deeper segments exposed in the Dent Blanche and Sesia complexes (Trümpy, 1975; Konrad-Schmolke et al., 2011; Angiboust et al., 2015; Jaeckel et al., 2018, Fig. 4.1). The subduction and accretion of continental slivers from the stretched Apulian margin over several millions of years against the Apulian buttress gave rise to the Austroalpine domain (Compagnoni et al., 1977; Dal Piaz et al., 2003). This composite nappe stack comprises individual slices separated by localized shear zones interpreted as transient slip interfaces and where local brittle and semi-brittle deformation patterns have been reported (Polino et al., 1990; Babist et al., 2006; Angiboust et al., 2014, 2015; Locatelli et al., 2018; Menant et al., 2018). While the Arosa-Engadine as well as Dent Blanche regions have been extensively investigated in the frame of the subduction interface model, the southern end of the Austroalpine complex in the Central Alps (Malenco region) remains unexplored despite its potential importance as the missing element linking the depths of the Arosa-Engadine (10-20 km) and Dent Blanche-Sesia massifs (40-60 km). We herein report field, pressure-temperature (P-T), and geochronological data from the aforementioned part of the Central Alps in order to study the processes taking place during subduction and underplating of the Margna and Sella nappes. We place particular emphasis on observing the deformation mechanisms in the plate interface zone(s) during subduction at the depth of the transition beneath the seismogenic zone as it is identified by instrumental observations to be below 350°C and recently found to exhibit a diversity of slip behaviours (e.g., Obara and Kato, 2016, and references therein).

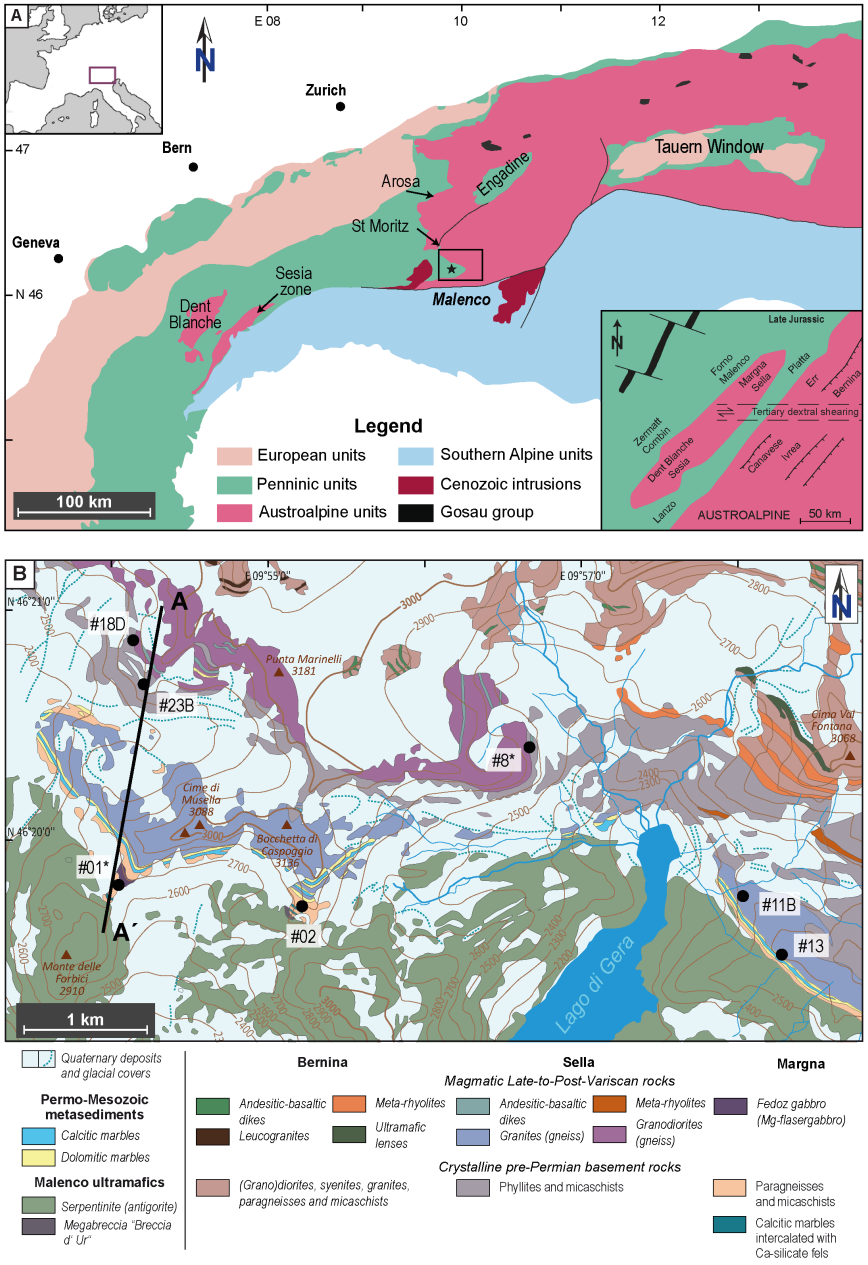

Figure 4.1: (A) Geological map of the Western and Central Alps showing the location of the Austroalpine nappes with respect to surrounding tectonic units. The studied area is located in the black box in the Val Malenco region. Inset: Paleogeographic reconstruction along the NW margin of the Apulian plate. Dent Blanche, Sesia, Margna, and Sella nappes are interpreted as extensional allochthons derived from the Apulian margin (modified from Froitzheim and Manatschal (1996)). (B) Geological map of the Val Malenco, modified from Montrasio et al. (2005). Shades of magenta colors represent units belonging to Sella nappe, beige to Margna nappe; also shown are the Malenco ultramafics (greenish) and the Bernina nappe (light brown). Black circles denote the sampling localities (e.g., #01* includes samples #01A, #01B, and #01F). For exact location, see also Table 4.1. Line A-A' shows the position of the cross section in Figure 4.2B.

4.2 Geological setting

The Central Alps are the result of the convergence between the European and the Adriatic plates and their subsequent collision during Tertiary times (Ring et al., 1988; Liniger and Nievergelt, 1990; Handy, 1996; Schmid et al., 2004). Two distinct tectonic phases affected the region during the evolution of the Alpine edifice: east to southeast subduction of the Penninic units during the Cretaceous, which formed an oceanic domain between the two continental plates, accompanied by top-W thrusting and a later shift to N-S shortening with top-N directions in the Paleogene (Ratschbacher, 1986; Ring et al., 1988; Durr, 1992; Handy, 1996).

The study area is located in Val Malenco, Central Alps, at the border of N Italy and SE Switzerland (Figs. 4.1A and 4.1B), precisely at the transition between the Austroalpine slice stack and the South Penninic oceanic domain. The major tectonic units in the study area are the Penninic Malenco-Forno unit, the overlying Austroalpine Margna and Sella nappes, both representing continental crust, and their sedimentary covers (e.g., Guntli and Liniger, 1989; Liniger and Nievergelt, 1990; Hermann and Müntener, 1992; Trommsdorff et al., 1993; Bissig and Hermann, 1999; Mohn et al., 2011).

4.2.1 Austroalpine units and their Permo-Mesozoic sedimentary covers

The continental Austroalpine units are represented in the study area by the Margna and the Sella nappes. Stratigraphic similarities between the Margna cover and sediments from the Lower Austroalpine Err nappe (Liniger and Guntli, 1988) suggest an Apulian affinity for the Margna nappe (Liniger, 1992). The Malenco and Platta nappes, which abut our studied units in the SW and NE, respectively, are former subcontinental mantle units exhumed during Jurassic rifting (Trommsdorff et al., 1993; Manatschal, 1995; Froitzheim and Manatschal, 1996). The position of Margna and Sella nappes between these two (ultra)mafic units reflects the primary complexity of the passive margin (Liniger, 1992; Spillmann, 1993). In this frame, Margna and Sella were extensional allochthons (e.g., Froitzheim and Manatschal, 1996), representing the transition from the Adria continental margin toward the South Penninic ocean basin during Jurassic,

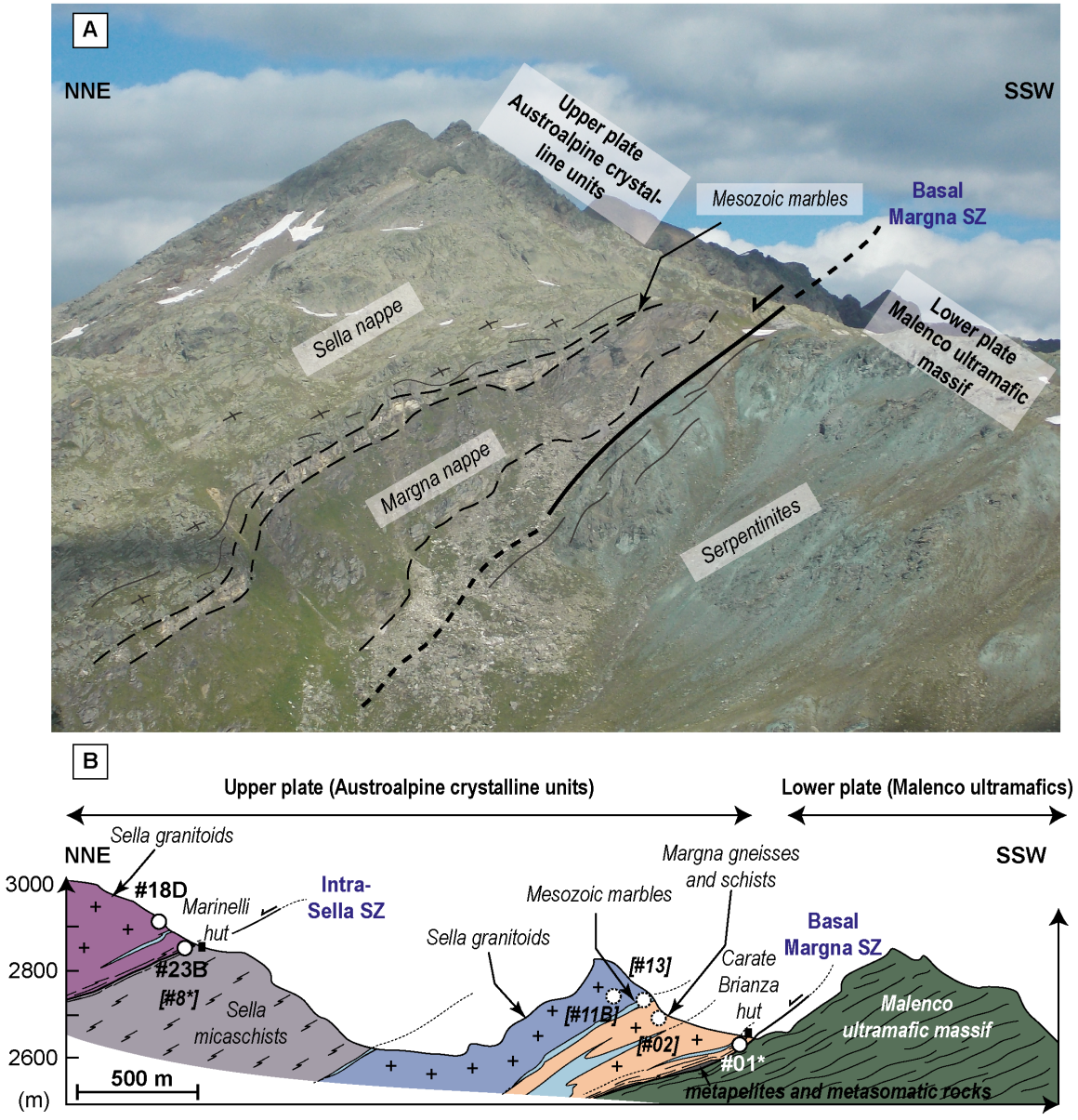

Figure 4.2: (A) Field picture showing the basal Margna shear zone (SZ) in the Pass d'Ur area; view from Rifugio Bignami. (B) Simplified cross section showing the structure of the studied area as well as sampling localities (#18 and #01). Star (*) refers to all three samples #01A, #01B, and #01F; samples in brackets and corresponding dotted circles denote localities that are not present in this cross section but in the equivalent units (see also map in Fig. 4.1B).

with Margna being the most distal part of the Adria continent (Hermann and Müntener, 1996; Hermann et al., 1997).

Both nappes encompass pre-Variscan continental rocks, mostly granodiorites and granites, which were later metamorphosed into orthogneisses (e.g., Staub, 1946; Liniger and Guntli, 1988; Guntli and Liniger, 1989; Hermann and Müntener, 1992). Occasionally, 2-3-m-thick andesitic and basaltic dikes crosscut the large igneous bodies for several hundreds of meters. A

sequence of Mesozoic, mostly Cretaceous, sediments is covering the Margna and Sella basement rocks (Hermann and Müntener, 1992; Trommsdorff et al., 2005). The Margna nappe also contains an association of gabbros and lower crustal granulites (Hermann et al., 1997). This association is absent in Sella and is identical to the one found within the Malenco ultramafic units (Trommsdorff et al., 2005).

The boundaries between the Margna (lower) and the Sella (upper) units are marked by thin slices of sedimentary rocks (Figs. 4.2A and 4.2B; Hermann and Müntener, 1992). They comprise Triassic pre-rift marine shelf dolomite marbles and presumably Lower Jurassic syn-rift quartz-calcschists that locally contain dolomite breccias (Hermann and Müntener, 1992; Trommsdorff et al., 2005). Their formation is connected to the rifting phase of the Austroalpine units during Mesozoic times. Both sedimentary units exhibit Alpine metamorphism.

The Dent Blanche and Sesia units are considered equivalent to the Margna and Sella nappes in the Central Alps (Froitzheim and Manatschal, 1996; Froitzheim et al., 1996; Schmid et al., 2004). Both units consist of a polymetamorphic continental basement that was intruded by pre-Alpine granitoids and mafic bodies (e.g., Rubatto et al., 1999; Monjoie et al., 2007). Together, all four nappes (Margna, Sella, Dent Blanche, and Sesia) are thought to have represented extensional allochthons between two denuded mantle units, the Malenco to the west and the Platta to the east (e.g., Beltrando et al., 2010, inset of Fig. 4.1A).

Another Austroalpine unit in the broader Val Malenco area, not further studied here, however, is the Bernina nappe comprising intrusive rocks slightly deformed and with local Alpine metamorphic overprint (Fig. 4.1B; Rageth, 1984; Spillmann and Büchi, 1993; Trommsdorff et al., 2005).

4.2.2 Malenco-Forno units

The Malenco unit, structurally beneath the Margna nappe (Figs. 4.2A and 4.2B), is mainly composed of ultramafic rocks (peridotite and spinel lherzolite) that are largely serpentinized and also retain ophicarbonates in various localities (Trommsdorff and Evans, 1977; Hermann and Müntener, 1992). A Jurassic crust-to-mantle transition is preserved near Mount Braccia, where gabbros and pelitic granulites are intermixed with the ultramafics as well as the Fedoz

gabbro intrusion, also observed in the Margna unit (Gautschi, 1979, 1980; Ulrich and Borsien, 1996; Hermann et al., 1997). According to Trommsdorff et al. (1993) and Hermann et al. (1997), the Malenco ultramafics were a denudated subcontinental fragment of the Adriatic lithospheric plate later exhumed during Jurassic rifting. Subsequent exhumation of the unit to the ocean floor (Trommsdorff et al., 1993) is supported by serpentinization of the ultramafic units, rodingitization, and the formation of ophicarbonates (Müntener et al., 2000). During the Upper Cretaceous, the Malenco ultramafics were overprinted by Alpine deformation and subsequently incorporated into the Alpine nappe stack (Müntener et al., 1997).

The Forno unit belongs tectonically to the same level as the Malenco unit and is a typical ocean floor sequence (Montrasio, 1973; Ferrario and Montrasio, 1976; Peretti, 1985) comprising volcanoclastic rocks and basalts. The whole oceanic crust sequence is overlain by middle Jurassic to late Cretaceous sediments (Peretti, 1985).

4.2.3 Alpine metamorphic ages in Val Malenco

The broader Val Malenco area and the three units that comprise it (Sella, Margna, and Malenco) have been the target of several petrological and structural studies focusing on the inherited, pre-Alpine structures and deformation observed in the nappes (e.g., Froitzheim and Manatschal, 1996; Hermann and Müntener, 1996; Bissig and Hermann, 1999; Müntener et al., 2000, 2010; Trommsdorff et al., 2005).

Only a few studies in the Val Malenco area have, so far, dealt with the timing of Alpine deformation and its imprint on older, preexisting structures (Fig. 4.3). Cretaceous greenschist-facies metamorphism in the southern Platta and Malenco units was initially recorded by Deutsch (1983), who obtained K-Ar amphibole ages spanning a range of 90-69 Ma. $^{40}Ar/^{39}Ar$ dating on riebeckite from Platta yielded apparent ages in the range of 89-70 Ma, while K-Ar dating on mica-bearing meta-radiolarites from the lower Austroalpine Err nappe yielded ages of 89-76 Ma for the first generation of white micas (parallel to S1 foliation; Handy, 1996) and 80-67 Ma for the second generation Handy (parallel to S2; 1996). Finally, Villa et al. (2000) recognized two amphibole generations related to Alpine deformation from the Malenco ultramafics, one pressure and one temperature dominated, at 91-83 and 73-67 Ma, respectively. Mohn et al. (2011) suggest that deformation observed in the rocks of the Malenco ultramafics, as well as

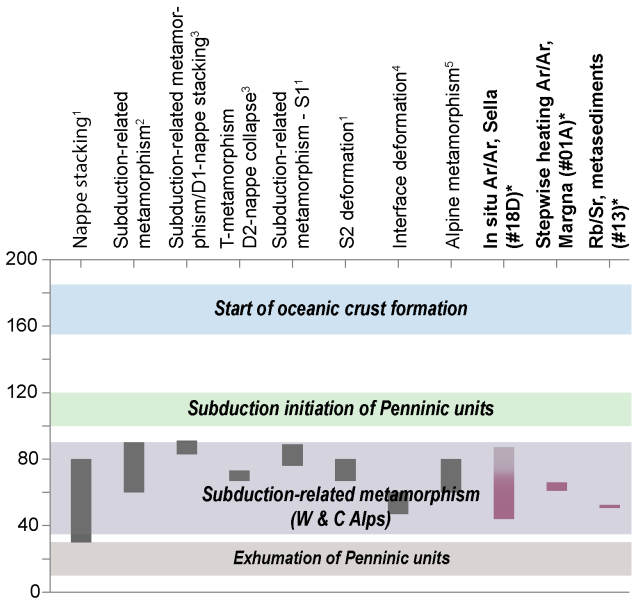

Figure 4.3: Published Alpine deformation age data for Val Malenco and Central Alps. Footnotes: (1) Handy (1996); (2) Handy and Oberhänsli (2004); (3) Villa et al. (2000); (4) Bachmann et al. (2009b); (5) Frey et al. (1974); (*) this study.

of S Platta, Margna, and Sella units, is possibly related to pressure-dominated metamorphism of P ∼0.5-0.6 GPa (Bissig and Hermann, 1999). Despite relatively large uncertainties, Picazo et al. (2019) recently obtained ages of 63.0 ± 3.0 Ma for pressure metamorphism associated with nappe stacking and 54.7 ± 4.1 Ma for possibly peak temperature Alpine metamorphism.

4.2.4 The subduction interface through time

Although the movement of the overriding plate has been systematically studied (Ratschbacher, 1986; Ring et al., 1988, 1989), and it was top-W during Cretaceous and top-N in Early Tertiary, the exact location of the subduction interface in the study area has long been disputed. Southward to south-eastward subduction started in the South Penninic ocean between 120 and 100 Ma (Handy and Oberhänsli, 2004, and references therein) and, based on $^{40}Ar/^{39}Ar$ dating of pseudotachylytes from the base of the Austroalpine nappe stack, was active between 90 and 60 Ma (Bachmann et al., 2009b). Recently, high-pressure (HP) subduction-related metamorphism was reported by Droop and Chavrit (2014) for the Lanzada-Santa Anna metagabbros, a unit structurally beneath the Malenco ultramafics and south of our study area (black star in Fig. 4.1A). According to the authors, these eclogitic metagabbros corroborate the existence

of a south-dipping subduction and place the interface beneath the Malenco unit, at some later stage during Alpine convergence history.

4.3 Analytical methods

4.3.1 Electron Probe Microanalyses

Electron probe microanalyses (EPMA) were performed with a JEOL-JXA 8230 probe at GFZ Potsdam, under common analytical conditions (15 kV, 20 nA, wavelength-dispersive spectroscopy mode), using a 10-μm-diameter beam. The following standards were used for calibration: orthoclase (Al, Si, K), fluorite (F), rutile (Ti), Cr_2O_3 (Cr), wollastonite (Ca), tugtupite (Cl), albite (Na), MgO (Mg), Fe_2O_3 (Fe), rhodonite (Mn). Samples of micaschists and (ortho- and para-)gneisses were analyzed from both the Margna and Sella units. The analyses focused on phengite and to a lesser extent on amphibole composition of eight samples. The Si content per formula unit (pfu) of phengites (Ph) and the related content of the celadonite (Cel) end-member, $K(Mg,Fe^{2+})AlSi_4O_{10}(OH)_2$, are used here as an indicator of relative pressure changes (Massonne and Schreyer, 1987). In other words, high-silica regions of phengite correlate with lower aluminum contents and can be an indicator of relatively higher pressure conditions. Mineral abbreviations are used as suggested by Whitney and Evans (2010).

4.3.2 Thermodynamic modeling

In order to estimate the P-T conditions under which micaschists and mica-rich gneisses from Magna shear zone (MSZ) and Intra-Sella shear zone (ISSZ) deformed, we calculated pseudosections, following a free-energy minimization approach using the software PerpleX (Connolly, 2005, version 6.7.7). The bulk rock composition in oxide weight percent was obtained by averaging for each sample conventional major elements X-ray fluorescence analyses on rock powders (made at the GFZ Potsdam) together with scanning electron microscope (SEM) surface estimates on thin sections (using an EVO MA-10 Zeiss microscope at the Institut de Physique du Globe de Paris [IPGP]). Synthetic bulk compositions used for the modeling as well as P-T pseudosection results are given in Supplemental Table A.2. The following solid solution models

Table 4.1: Overview of samples and locations.

Sample	Location	Latitude (°N)	Longitude (°E)	Rock	Minerals
Margna					
#01A	Rif. Carate Brianza	46°19'57.26"	09°54'14.05"	Gneiss	Qz-Ab-Wm-Ttn-Ap-Aln-Px-Zrn
#01B	Same as above	Same as above	Same as above	Micaschist	Qz-Wm-Chl-Grt-Bt-Hbl-Ap-Mag-Aln-Ep
#01F	Same as above	Same as above	Same as above	Micaschist	Qz-Wm-Fsp-Chl-Ep
#02	Forca di Fellaria	46°19'44.97"	09°55'10.42"	Micaschist	Qz-Fsp-Wm-Chl
Sella					
#11B	Alpe Gembre	46°19'42.50"	09°57'54.50"	Gneiss	Qz-Fsp-Wm-Chl
#18D	Rif. Marinelli	46°20'49.30"	09°54'11.70"	Micaschist	Qz-Wm-Chl-Ttn-Rt-Ilm
#23B	Same as above	Same as above	Same as above	Micaschist	Qz-Ab-Wm-Chl-Zrn-Ttn-Aln-Rt
#8.1	Rif. Bignami	46°20'27.97"	09°56'41.39"	Gneiss	Qz-Pl-Wm-Chl-Ap-Ep-Zrn
#8.2.1	Same as above	Same as above	Same as above	Gneiss	Qz-Pl-Wm-Rt
#8.2.2	Same as above	Same as above	Same as above	Gneiss	Qz-Fsp-Wm-Chl-Amp-Hem-Ttn-Ep-Bt
#8.3.2	Same as above	Same as above	Same as above	Gneiss	Qz-Pl-Ep-Ttn
Metasediments					
#13	Rif. Bignami	46°19'28.30"	09°58'08.40"	Marbles	Cal-Qz-Wm

have been used for the modeling: phengite, garnet, amphibole (Holland et al., 1998), feldspar (Fuhrman and Lindsley, 1988), and chlorite (Holland et al., 1998). MnO has been considered only for samples #01B and #23B. Ferric iron has been neglected as suggested by the low-Fe content of clinozoisite crystals in the main Alpine foliation. Water is considered as pure H_2O and in excess in the system based on microstructural observations (presence of veins and pressure solution fringes).

Best-fit P-T regions for each pseudosection have been estimated considering: (1) the field where we had the best agreement between observed and modeled paragenesis; (2) the microstructural mechanical behaviour of quartz and albite, which has been used as an approximate geothermometer; and (3) the phengite silica content isopleths.

4.3.3 Rb/Sr geochronology

Ages of metamorphism and ductile deformation are herein investigated by Rb/Sr multi-mineral isochron dating for four mica-rich mylonites and one impure meta-carbonate. In this study, white mica is the high Rb/Sr phase, largely determining the calculated age values. The Rb/Sr system of white mica is thermally stable at temperatures up to > 600°C (Glodny et al., 2008b) but may be fully reset by dynamic recrystallization even at lower temperature, down to 350°C.

Moreover, complete synkinematic recrystallization is often accompanied by inter-mineral isotopic re-equilibration (Inger and Cliff, 1994; Freeman et al., 1997; Villa, 1998; Müller et al., 1999, 2000; Cliff and Meffan-Main, 2003; Glodny et al., 2008a). Therefore, Rb/Sr isotopic data from penetratively deformed rocks can be used to date the waning stages of mylonitic deformation, given that deformation occurred below the temperature range for diffusional resetting and that no later substantial reheating or fluid-rock interaction occurred.

For Rb/Sr geochronology, mineral separates from three basement rock samples from the Margna nappe, one basement rock sample from the Sella nappe, and one from the meta-sediments covering the aforementioned pre-Alpine basement rocks have been prepared (see Table 4.1), with different mica grain-size fractions to identify possible presence of mixed mica populations (i.e., presence of unequilibrated, detrital, pre- or early deformational white mica relics; Müller et al., 1999). Isotopic data were generated at GFZ Potsdam using a Thermo Scientific TRITON thermal-ionization mass spectrometer. Sample processing, mineral separation, and data acquisition were performed following the procedures reported in (Glodny et al., 2008b). Uncertainties of Rb/Sr isotope and age data are quoted at the 2σ level throughout this work. The software Isoplot/Ex 3.71 (Ludwig, 2009) and the revised Rb decay constant of $1.3972 * 10^{-11} yr^{-1}$ (Villa, 2015) were used to calculate regression lines. The full Rb/Sr data set is presented in Supplemental Table A.1.

4.3.4 $^{40}Ar/^{39}Ar$ dating

$^{40}Ar/^{39}Ar$ dating was performed at the $^{40}Ar/^{39}Ar$ geochronology laboratory of Potsdam University. Bulk mineral separates $^{40}Ar/^{39}Ar$ dating and in situ $^{40}Ar/^{39}Ar$ UV laser ablation dating were performed on one mica-rich mylonitic sample from the Margna nappe and one foliated cataclastic micaschist sample from the Sella nappe, respectively. For the first technique, $^{40}Ar/^{39}Ar$ dating of bulk mineral separates by CO_2 laser stepwise heating, one hand specimen of micaschist was crushed and sieved. White mica fractions were obtained (handpicked fractions of 355-250 μm and mechanically prepared fractions of 500-355 and 355-250 μm; see also Wiederkehr et al. (2009) for fraction preparation) with a total of ∼10 mg of white mica. Scanning electron microscope investigations were performed for this sample, in order to make sure that no chemical zoning characterized white micas and hence the ages would reflect more

likely deformation-induced recrystallization. For in situ $^{40}Ar/^{39}Ar$ dating by UV laser ablation, a rock thick section (of ∼1 mm thickness and 5 mm diameter) was prepared and double polished. Before the laser experiment, the thick section was studied using the SEM in order to have an accurate reference frame during the $^{40}Ar/^{39}Ar$ experiment and a general control over mica zoning patterns.

The $^{40}Ar/^{39}Ar$ analytical system at the University of Potsdam has been described in detail in recent studies (Wiederkehr et al., 2009; Wilke et al., 2010; Halama et al., 2014). The Ar isotopic analytical system consists of (1) a New Wave Gantry Dual Wave laser ablation system with a 50 W continuous CO_2 laser (wavelength of 10.6 mm) for heating bulk samples and also Nd-YAG UV laser (frequency-quadrupled wavelength of 266 nm) for laser ablation of the thick section samples for extracting sample gases; (2) an ultra-high vacuum purification line equipped with two SAES getters and a cold trap used at -90°C; and (3) a high-sensitivity Micromass 5400 noble gas mass spectrometer equipped with an electron multiplier. The analysis with Micromass 5400 has been done with MassSpec software manufactured by Dr. Alan Deino in Berkeley Geochronology Center, California, USA.

Neutron activation of both samples was performed at the CLICIT Facility of the Oregon State University TRIGA Reactor, in Corvallis, Oregon, USA. All of the unknown samples were wrapped in commercial Al foil and were then contained in a 99.999% pure Al sample container (22.7 mm in diameter and 102.5 mm in height), together with the neutron flux monitoring mineral, Fish Canyon Tuff sanidine, prepared by the Geological Survey of Japan (Uto et al., 1997; Ishizuka, 1998, 27.5 Ma) and crystals of K_2SO_4 and CaF_2 for correction of interference by Ar isotopes produced from K and Ca other than those produced by $^{39}K(n,p)^{39}Ar$ reaction. The container had been irradiated for 4 h with the fast neutron flux of 2.5 x 10^{13} n/cm^2/s. After storage of the samples for several weeks at the reactor, they were finally brought back to Potsdam and then were analyzed for Ar isotopes. A K-Ar age standard biotite, HD-B1 biotite (Schwarz and Trieloff, 2007, 24.18 ± 0.09 Ma), which was also included in the same Al sample container as a routine procedure for every irradiation, was analyzed, and the accuracy of the system was confirmed.

4.4 Results

4.4.1 Field observations

The studied area comprises a series of several hectometer- to kilometer-thick continental slivers (pre-Alpine orthogneisses and micaschists) separated by greenschist-facies ductile shear zones. Some of these slices locally exhibit well-preserved magmatic fabrics, in particular in the Sella nappe. Anastomosing deformation networks are visible in the cliffs as well as in the landscape: they form 5-10-m-thick shear zones generally subparallel to the main Alpine shear zones. One of the major shear zones of the studied sequence lies within the lowermost 200 m at the base of the Margna nappe at the contact with the Malenco unit. Sheared metagranitic rocks exhibit a main foliation affected by a crenulation cleavage (Fig. 4.4A). Clasts of silica-rich domains (probably former pegmatitic veins in the orthogneiss) are observed wrapped by the main proto-mylonitic foliation (Fig. 4.4B). Semi-brittle deformation networks, marked in the field by broken feldspar clasts in a weakly oriented matrix are either found along the main thrust contacts or distributed within Margna and Sella slices (Fig. 4.4C). Along both the basal Margna shear zone (MSZ) and the Intra-Sella shear zone (ISSZ), foliated cataclasites (Fig. 4.4D) comprising submillimeter- to millimeter-sized clasts are exposed. Several generations of foliated cataclasites are recognized, striking parallel to the main N-plunging foliation or slightly oblique to it. They form centimeter- to decimeter-sized networks interleaved with domains where semi-brittle and ductile deformation prevails. Centimeter-thick quartz veins are locally observed within the regions more affected by Alpine deformation. Quartz veins are either found as en echelon vein sets cutting at high angle the main foliation (Fig. 4.4E) or as boudinaged lenses wrapped by the alpine foliation (Fig. 4.4F). A very strong flattening recorded in rock microfabrics contributed to the formation of numerous pressure-solution fringes visible from hand specimen to millimeter scale in both orthogneisses and Sella nappe micaschists (Fig. 4.4G).

Kinematic indicators, obscured by the strong flattening, indicate mixed top-N and top-SE tectonic transport directions. Previous studies in the broader Penninic/Austroalpine boundary report top-W kinematics during Cretaceous and a later shift to mainly top-N (e.g., Ratschbacher, 1986; Ring et al., 1988, 1989; Liniger and Nievergelt, 1990). However, it is possible that, lo-

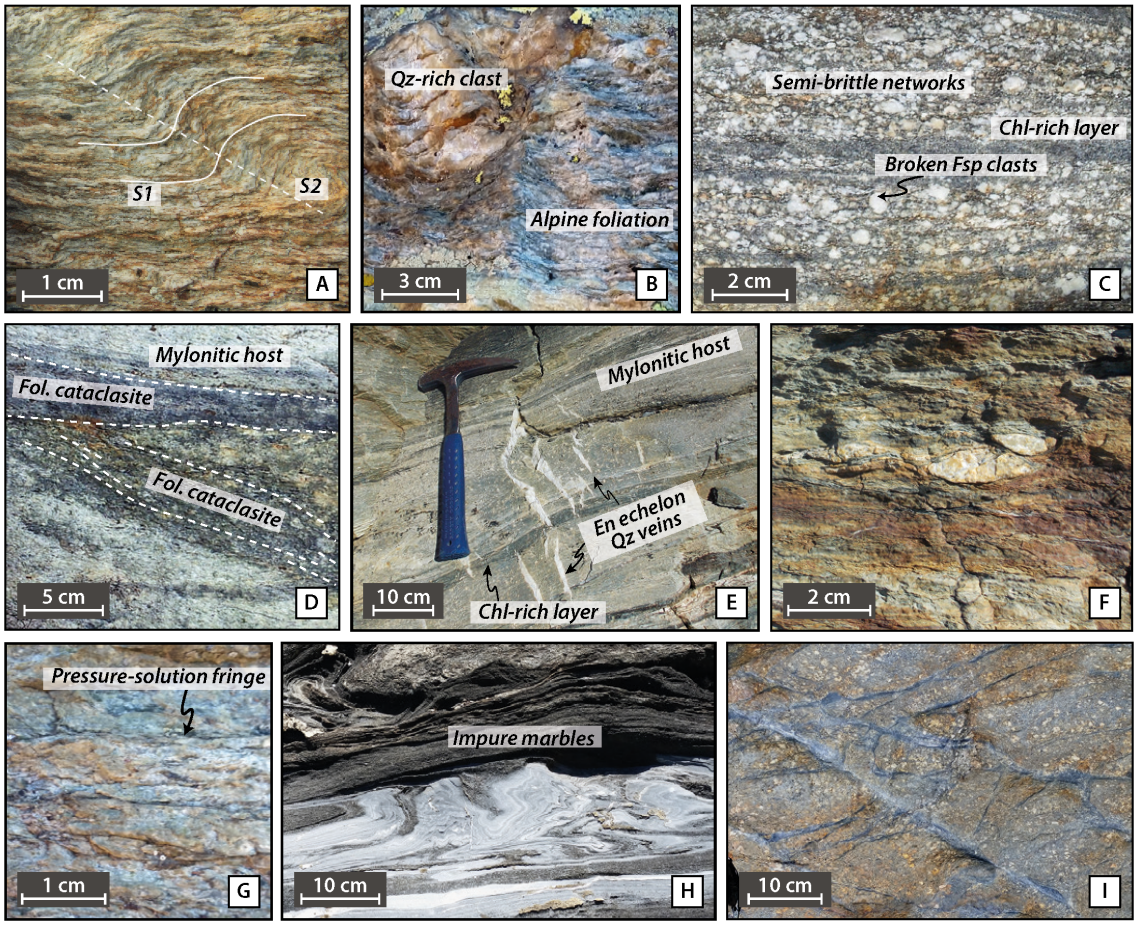

Figure 4.4: (A) Representative view of the Alpine imprint in Margna nappe gneisses showing a main foliation (S1) moderately imprinted by a crenulation plane (S2). (B) Field picture showing a silicic clast (former magmatic vein?) wrapped in the alpine foliation in the basal Margna shear zone. (C) Field picture showing a semi-brittle network comprising numerous finely crushed feldspar clasts moderately sheared along the main foliation (Sella nappe). (D) Picture showing two crosscutting generations of finely fractured orthogneisses (foliated cataclasites; Sella nappe). (E) Picture showing the mylonitic foliation from the Intra-Sella shear zone crosscut by en echelon quartz veins. (F) Picture showing centimeter-thick quartz vein as a boudinaged lens. (G) Close-up hand specimen picture showing the presence of darkish pressure solution planes, mostly parallel to the main thrust fault. (H) Layers of marbles and impure marbles showing tight folds (base of the Margna nappe). (I) Block deriving possibly from Sella or Bernina nappe, showing networks of pseudotachylytes (black veins) crosscutting a weakly deformed dioritic matrix.

cally, the old top-W structures are overprinted by the second phase; such is the case in Middle Austroalpine units of the Eastern Alps where transport directions are mainly top-N, although locally E-W stretching directions are observed (Ratschbacher, 1986). We recognized such top-W kinematic indicators in the Maloja gneiss NW of our study area, in Maloja pass, but not in the Val Malenco.

The top of the basal Margna shear zone is lined by an extremely sheared, nearly continuous ribbon lens of impure marbles forming mylonites and brecciated dolomitic limestones (Fig. 4.4H), while pseudotachylytes are commonly found in loose blocks falling from inaccessible cliffs that probably form the Sella and Bernina units (Fig. 4.4I).

Ductile deformation in the Malenco Massif led to pervasive mylonitic deformation of antigorite schists. The strong compositional and deformational gradient along the basal Margna shear zone between the crustal and mantle materials locally led to the formation of a metasomatized tectonic mixing zone comprising lenses of mafic tuffs, submetric to metric lenses of metasediments, as well as minor volumes of tremolite schists, and in parts deformed basement rocks exhibiting foliated cataclasites (named "breccias" in Picazo et al. (2019)).

4.4.2 Petrographic descriptions

Continental Austroalpine rocks for petrographic and geochronological studies were carefully selected based on the greatest intensity of Alpine overprint. In less mylonitized facies, few remnants of the pre-Alpine assemblages, namely albite porphyroclasts (Fig. 4.5A), garnet cores (Fig. 4.5E), biotite flakes, hornblende cores, and (possibly alpine prograde) muscovite cores can be observed. Alpine deformation led to the formation of a fine-grained foliation underlined by oriented phengite planes (Fig. 4.5A), tremolite around hornblende, clinozoisite, and titanite neoblasts (Fig. 4.5F). Pressure-solution fringes line up the main foliation. In one foliated cataclasite sample, two crosscutting foliations were observed (Figs. 4.5B and 4.5G), possibly associated with two stages of deformation, i.e., one that formed the main foliation and one that formed coevally with the crenulation cleavage. In quartz-rich lithologies, a strong apparent crystal-preferred orientation (CPO) denotes the existence of dynamic recrystallization during shearing (Figs. 4.5C and 4.5D). On the contrary, albite does not show clear evidence of intracrystalline deformation.

In samples identified as foliated cataclasites, all the mineral phases including albite and quartz exhibit microfracturing and alignment of crystal clasts along discrete shear planes. The semi-brittle networks differ from foliated cataclasites by the presence of coeval crystal-plastic deformation along shear planes (mostly underlined by phyllosilicates) and micro-cracking of stronger albite grains. Phengite planes are commonly closely associated with chlorite (Figs. 4.6A

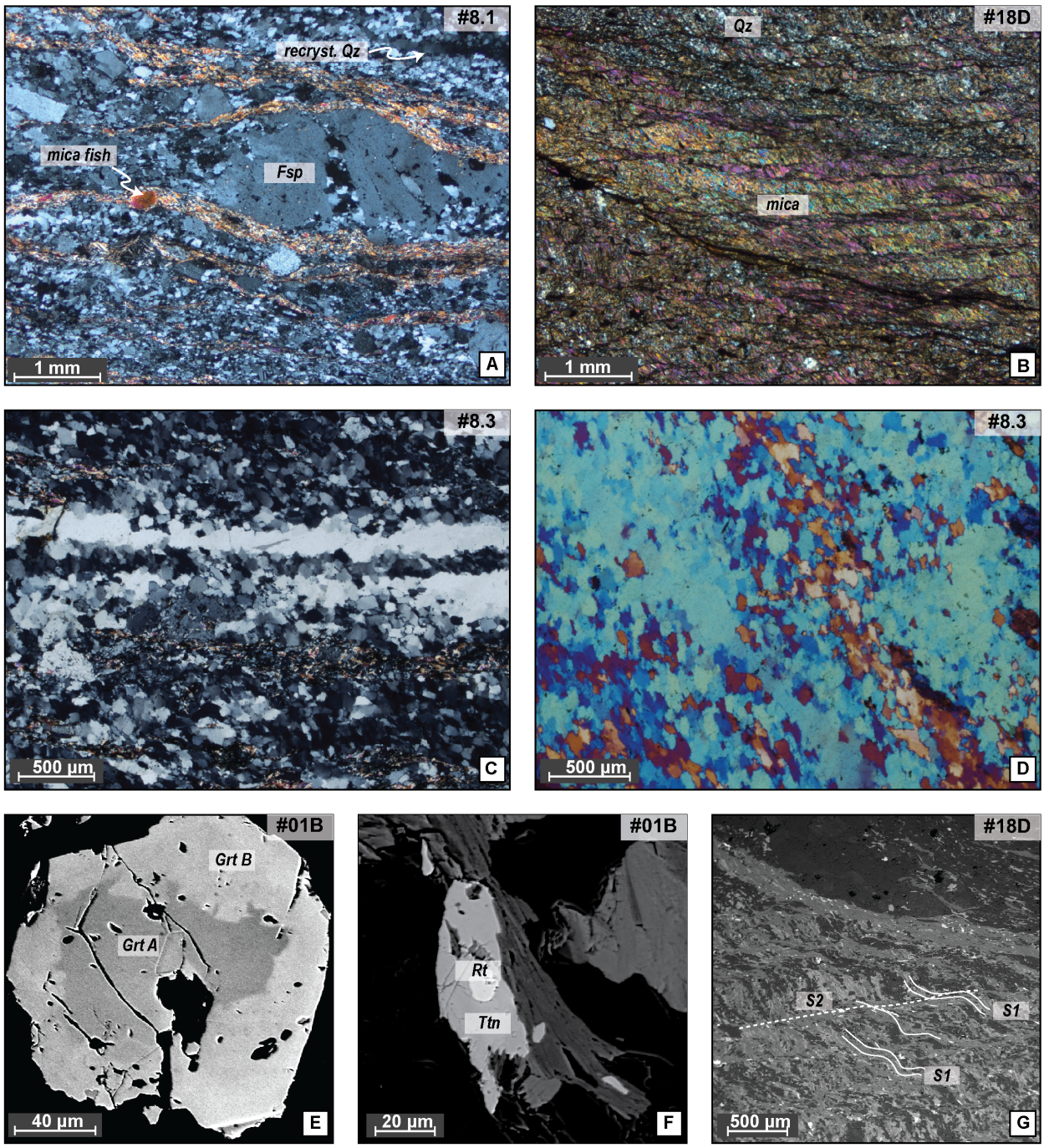

Figure 4.5: Optical microscope view (with polarized light) of a Sella mylonite showing a feldspar boudin, wrapped by micas, which mark the foliation. The feldspar grain has been partly replaced by quartz. A big white mica grain, within the fine mica foliation shows partial recrystallization of white micas. Quartz is recrystallized in the whole thin section. (B) Optical microscope view (with polarized light) of a Sella micaschist. The fine-grained micas form two foliations, S1 and S2 (see also picture G in the same figure). (C) Recrystallized quartz from a Sella mylonite, exhibiting recrystallization ribbons (with polarized light). (D) Crystal-preferred orientation (CPO) in recrystallized quartz from Sella mylonite (polarized light + gypsum plate). (E) Backscatter electron image of a garnet, with two distinct compositions; Margna mylonite. (F) Backscatter electron image showing titanite rimming around rutile in Sella micaschist. (G) Backscatter electron image of a Sella micaschist, showing the two different foliations, S1 and S2.

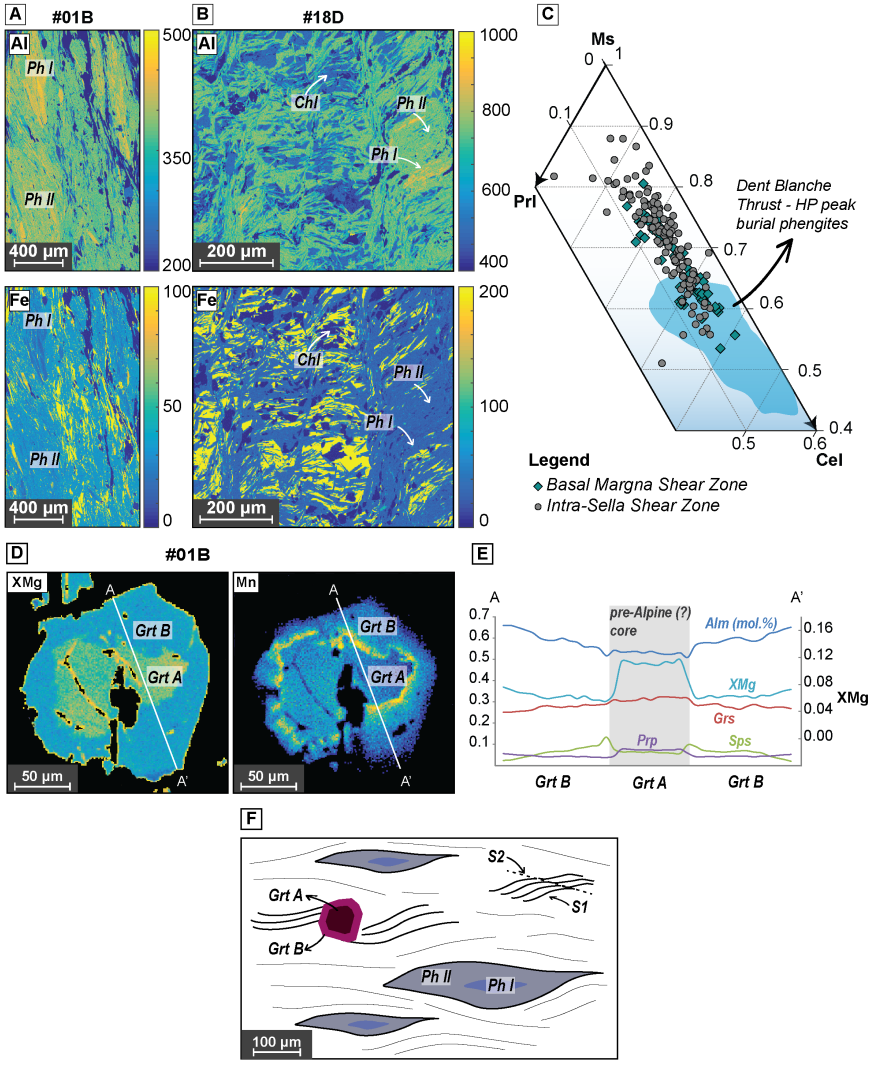

Figure 4.6: A) X-ray map of a mica-rich shear band from sample #01B showing that the matrix mainly composed of a high-pressure phengitic mica foliation (Ph II), locally contains 200-300 mm large remnants of higher aluminum clasts (Ph I). Chlorite flakes intergrown with phengite are best visible on the Fe map. (B) X-ray map of a mica-rich shear band from sample #18D showing chlorite-phengite domain. (C) Triangular plot of phengite composition in the celadonite-pyrophyllite-muscovite system for samples from the two shear zones studied here. The blue shaded domain shows, for comparison, the composition of peak burial phengite analyses from the Dent Blanche Massif (data from Angiboust et al., 2014, 2015). (D) X-ray map of a garnet crystal from sample #01B showing two distinct compositions: the core (Grt A) clearly evidences resorption and overgrowth by a newly formed generation (Grt B). The end-member compositions corresponding to the transect A-A' are shown in Figure 4.6E. (E) Composition profile across the garnet crystal shown in Figure 4.6D. Note the presence of a high Mn content at the contact between the (possibly) pre-Alpine and the alpine generation. (F) Schematic representation of the microstructures observed in sample #01B, showing the foliation, the two phengite generations, the core-rim structure of the garnet shown in Figure 4.6D and S1-S2 structures. Alm-almandine; Grs-grossular; Prp-pyrope; Sps-spessartine.

and 4.6B). Relicts of pre-Alpine origin exhibit micro-fracturing and resorption textures (Fig. 4.6D).

In some mylonitic samples, quartz exhibits marked grain size reduction.

Samples from both MSZ and ISSZ reveal the presence of Al-rich/Si-poor white mica cores (Si ∼3.2 pfu; Fig. 4.6A), surrounded by Al-poor/Si-rich phengitic mantles (Si between 3.3 and 3.4 pfu; Fig. 4.6C; Table 4.2). Phengite outer rims thus do not exhibit systematically lower Si contents as may be the case when phengite recrystallizes at lower pressure conditions during exhumation. The average Si content of the basal Margna shear zone is ∼3.22 pfu, and the maximum Si content is 3.32 pfu, both slightly lower than those of Guntli and Liniger (1989). The respective values for the Intra Sella shear zone are ∼3.31 pfu (average) and 3.46 pfu (maximum). Depending on the intensity of the Alpine overprint, the proportion of fully recrystallized phengite crystals ranges from 20 vol% (e.g., #01B; Fig. 4.6A) to nearly 90 vol% in #18D (Fig. 4.6B). Only one sample (#01B) exhibits thin Fe-rich garnet rims around a partly corroded, darker garnet core (Figs. 4.5E and 4.6D). The core of this garnet has a significantly higher XMg (Mg/(Fe + Mg)) content than its rims (Fig. 4.6E). A summary of our petrographic observations is presented in Figure 4.6F and Table 4.1; representative mineral analyses are shown in Table 4.2.

4.4.3 Thermodynamic modeling results

Best-fit region between observed parageneses and the modeled system is obtained at 0.9-1.0 GPa and 350°-375°C for sample #23B, while slightly lower pressures and higher temperatures correspond to sample #01A (0.65-0.9 GPa and 350°-400°C). The corresponding mineral assemblages predicted by the model are the following: Ab-Ph-Qz-Chl-Ep-Ttn-Pg and Ab-Ph-Qz-Chl-Ep-Ttn-Amp, for sample #23B and #01A, respectively. Even lower pressure and higher temperature conditions were obtained for #01B (0.6-0.9 GPa, ∼450°C; Fig. 4.7), corresponding to a paragenesis composed of Qz-Fs-Ph-Chl-Amp-Grt-Ep-Ttn. Detailed pseudosection plots are provided in Supplemental Figures A.1, A.2, and A.3. Modeled mineral modes are in agreement with observed modes in the samples. Note that the pressure estimates derived from the pseudosection modeling strongly depend on the position of the phengite silica isopleths, which represent the most reliable barometer for such an assemblage.

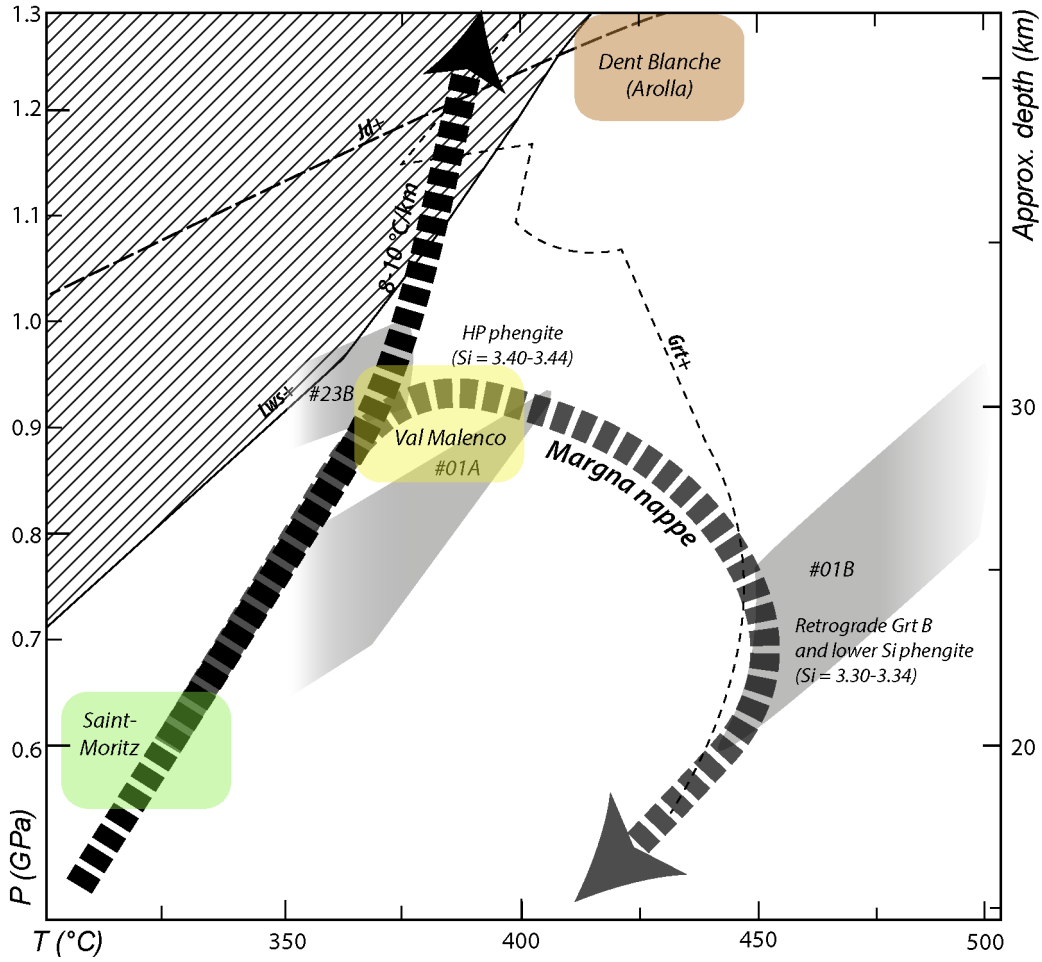

Figure 4.7: Summary of pseudosection modeling results comparing obtained results (gray shaded polygons) with peak burial estimates for the Arolla gneiss in Western Alps (brown rectangle: Angiboust et al., 2014) and the Austroalpine orthogneiss in St. Moritz (green rectangle: Bachmann et al., 2009b), both accreted along the same alpine paleo-interface (detailed pressure-temperature [P-T] pseudosections calculated for this work are provided in Supplemental Figures A.1, A.2, andA.3). Gray-shaded polygons correspond to the best-fit areas identified for each individual sample peak burial conditions. The shape of the retrograde path is controlled by the retrogressed sample #01B and by the presence of garnet in this sample. Jd-jadite; Lws-lawsonite; Ph-phengite.

4.4.4 Geochronological results

4.4.4.1 Rb/Sr dating

Determination of deformation ages from Margna and Sella basement rocks proved problematic because of Sr-isotope disequilibria in the mica populations. Smaller grains appear to be systematically younger than bigger grains (Figs. 4.8B and 4.8C). This pattern is a characteristic signature of incomplete recrystallization. Correspondingly, all basement rock samples show dis-

equilibria among the low-Rb/Sr phases (apatite, feldspar, and titanite). The issue of isotopic heterogeneity due to inheritance has been extensively addressed in Glodny et al. (2005) and highlighted in Bachmann et al. (2009b) and Angiboust et al. (2014). Full recrystallization of white mica during deformation together with Sr-bearing phases (such as apatite or albite) yields Sr isotopic re-equilibration, and ages calculated from equilibrated (sub)assemblages generally reflect the waning stages of deformation (e.g., Freeman et al., 1998; Inger and Cliff, 1994). In our samples, full recrystallization of pre-Alpine basement rocks was obviously not achieved, and Alpine, exhumation-related temperatures in our samples were too low for diffusional re-setting. The only geologically meaningful ages that could be calculated are ages of ca. 44 and 54 Ma, interpreted as maximum ages for the end of deformation for samples #01A and #01F, respectively (see also Discussion and Interpretation of age data sections for explanation of our observed data ranges).

Since dating of the pre-Alpine basement rocks did not produce conclusive results, we analyzed and dated a sample from the meta-sedimentary rocks found between the Margna and the Sella nappes. Despite small disequilibria between different calcite-dominated rock fragments, robust age information of 48.9 ± 0.9 Ma was acquired. Notably, for this sample, no correlation between mica grain size and apparent age is observed (Fig. 4.8A). Therefore, although the Alpine overprint in the study area cannot be precisely dated with Rb/Sr in white micas of pre-Alpine rocks, dating white micas from meta-sediments devoid of pre-Alpine history facilitates dating of the waning stages of ductile deformation. Analytical data on Rb/Sr geochronology are given in Supplemental Table A.1.

4.4.4.2 $^{40}Ar/^{39}Ar$ dating

Here we present the results acquired during stepwise heating as well as in situ $^{40}Ar/^{39}Ar$ dating on one mylonitic orthogneiss from Margna and one foliated cataclasite from Sella. The complete set of isotopic data is presented in Tables 4.3 and 4.4 for stepwise heating and in situ $^{40}Ar/^{39}Ar$ dating, respectively.

Stepwise heating. Stepwise-heating $^{40}Ar/^{39}Ar$ analysis was performed for mica fractions of mylonitic sample #01A (right column of Fig. 4.8B). Microscopically, the sample exhibits flattened quartz and mica flakes, the latter co-defining the foliation. There are no apparent

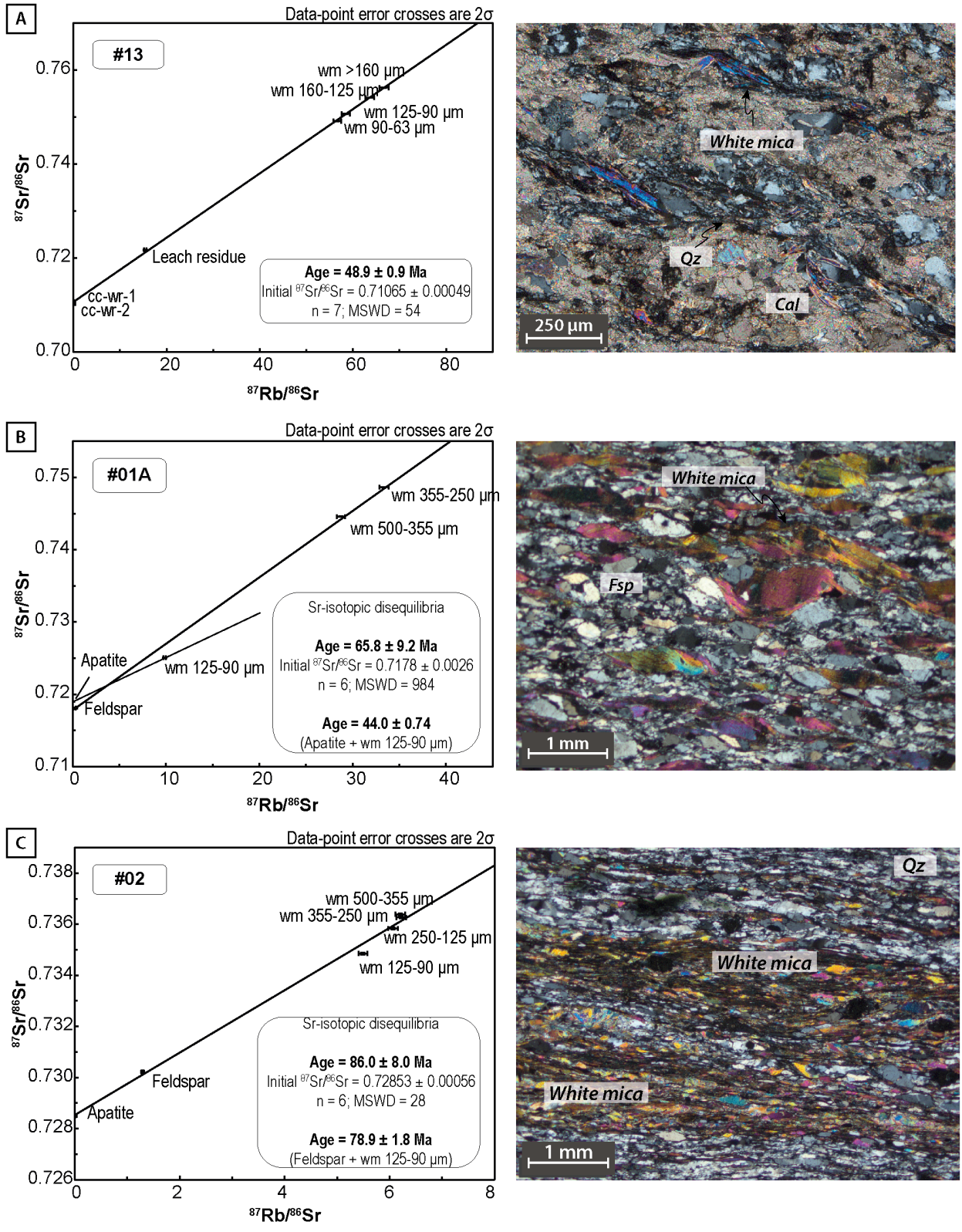

Figure 4.8: Rb/Sr mineral data (left column) and characteristic rock fabrics under optical microscope (right column) for three samples. (A) Sample #13 from Permo-Mesozoic metasediments. (B) Sample #01A. (C) Sample #02; B and C from the Margna nappe. Analytical data are given in Supplemental Table A.1. Grain size is indicated because different grain-size fractions were analyzed.

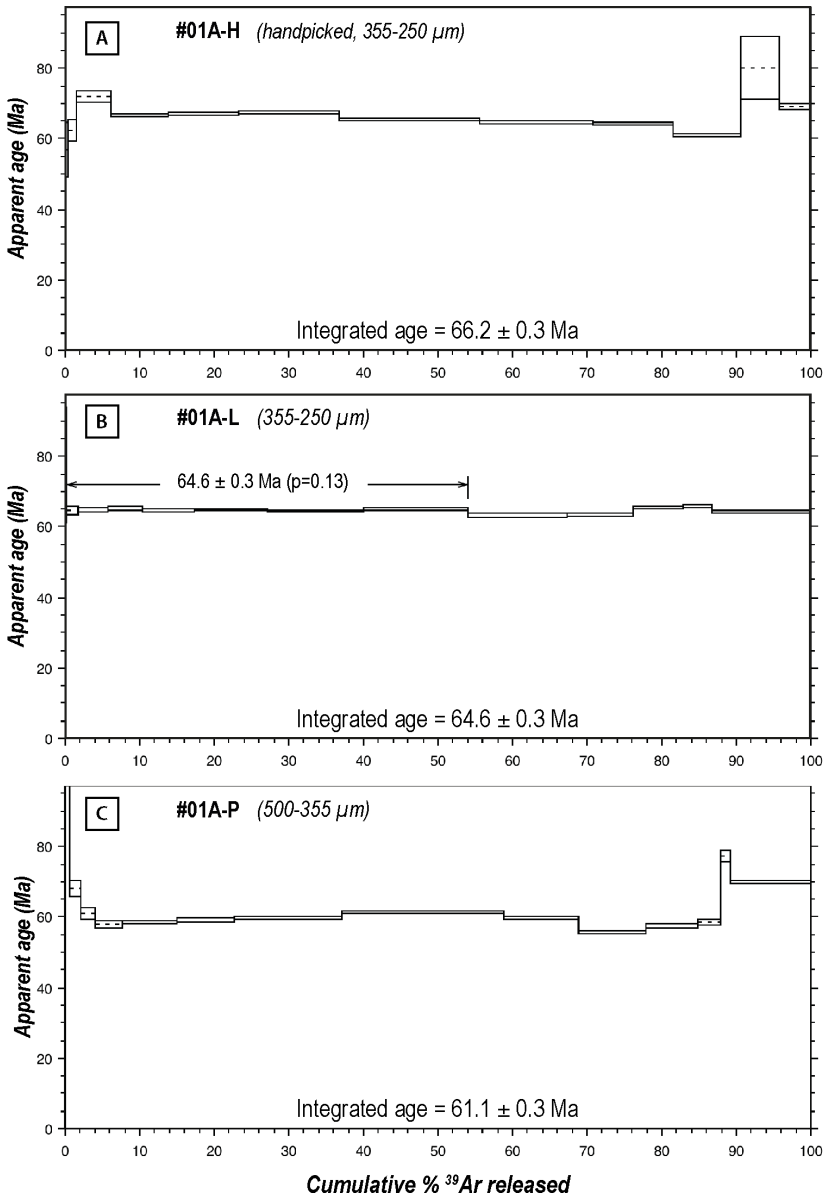

Figure 4.9: White mica $^{40}Ar/^{39}Ar$ age spectra obtained for sample #01A by stepwise- heating experiments. Total gas ages were determined by integrating over all steps. Steps attributed to the plateau are highlighted in black. Uncertainties are given in 2σ; H-handpicked fractions of 355-250 μm; L-fractions of (355-250 μm) obtained by the "tapping or shaking paper" method; P-fractions of (500-355 μm) obtained by the same method as L.

core-rim structures in the dated micas; therefore, deformation is thought to have affected them homogeneously. Dating of this sample yielded fairly homogeneous apparent ages for all grain sizes, namely a range of apparent deformation ages between 61.1 and 66.2 ($\pm$0.3) Ma (Figs. 4.9A - 4.9C). In particular, although an apparent plateau age for the handpicked small fractions (#01A-H, 355-250 μm) was not detected, most steps point to a meaningful age of ca. 66-64 Ma (Fig. 4.9A). A plateau age of 64.6 ($\pm$0.3) Ma was obtained for small fractions (#01A-L, 355-250 μm), collected by mechanical means (Fig. 4.9B). Finally, stepwise-heating dating of

large mica fractions collected by the same method (#01A-P, 500-355 μm) varies from ca. 55 Ma to ca. 61 Ma, therefore exhibiting an irregular pattern (Fig. 4.9C).

In situ dating. Macroscopically, sample #18D appears to be a foliated cataclasite, while its microstructure is characterized by the presence of S-C fabric in micas and large boudins of quartz. Foliation in the sample is marked by interconnected and synkinematic white micas and chlorite, coinciding with the S-fabric. Based on the microstructural observations, two different structures of white mica were systematically dated: along the S-plane (blue color in Figs. 4.10A - 4.10E) and along the C-plane (green color in Figs. 4.10A, 4.10B, 4.10E, and 4.10F). For the interpretation of the data, measurements with high Ca/K ratio were omitted, because Ca-derived ^{37}Ar was not produced in white micas but was derived from other Ca-rich minerals such as epidote and/or titanite, thus contamination of Ar from those Ca-rich minerals could be considered. Finally, we included only measurements that produced a total Ar of more than 40% of in situ radiogenic Ar and yielded an analytical uncertainty < 5 Ma.

Ages span a wide range for white micas along S-planes, including micas wrapping around quartz. However, measurements with the lowest uncertainties were obtained for ages between 44.0 $\pm$ 2.3 and 70.7 $\pm$ 2.7 Ma (Fig. 4.10G; Table 4.4). Due to their smaller extended length in the sample, fewer points were measured for micas forming the C-structures, which yielded intermediate ages from 56.0 $\pm$ 1.2-70.1 $\pm$ 3.0 Ma (Fig. 4.10G; Table 4.4). Since there is an overlap of ages for both structures, we cannot attribute them to separate kinematic or deformational events. It is interesting, however, to notice that the maximum ages obtained from Rb/Sr for the end of Alpine deformation (44.0 $\pm$ 0.7 and 54.3 $\pm$ 1.1 Ma) coincide with the youngest ages obtained by in situ $^{40}Ar/^{39}Ar$ dating.

4.5 Discussion

4.5.1 Interpretation of P-T data

We herein provide a first attempt to quantify the pressure-temperature history for the Alpine overprint event in Austroalpine rocks from the Malenco region. Synkinematic growth of chlorite and white mica and the recrystallization of quartz place a lower limit on temperatures at

Table 4.2: Mineral chemical analyses for garnet, amphibole and phengites from Margna and Sella nappes.

	Grt	Grt	Amp	Ph						(nOx=11)			
Sample	#01B	#01B	#8.2.2	#01B	#01B	#02	#02	#11B	#11B	#18D	#18D	#23B	#23B
Ref.	Z1-1-L18	Z1-1-L34	Z1-19	All (23)	Z2-8	All (16)	Z3-1	All (38)	Z1-5	All (51)	Z1-2	All (34)	Z2-7
Structure	Core	Rim	Core	Avg.	Max.*	Avg.	Max.*	Avg.	Max.*	Avg.	Max.*	Avg.	Max.*
SiO_2	37.38	37.28	45.01	48.00	49.74	47.79	48.13	48.7	46.7	48.73	49.63	49.94	52.61
TiO_2	0.09	0.19	1.2	0.44	0.36	0.29	0.33	0.27	0.25	0.19	0.12	0.31	0.38
Al_2O_3	20.79	20.70	9.63	29.69	29.10	32.28	31.49	29.76	29.85	30.29	29.29	27.38	26.49
FeO	24.88	26.97	18.62	3.18	2.74	2.29	2.42	2.49	2.69	2.82	2.64	3.68	1.99
MnO	2.97	3.15	0.66	0.01	0.02	0.00	0.01	0.01	0.01	0.02	0.01	0.03	0.01
MgO	2.01	1.13	9.13	2.41	2.58	1.58	1.81	2.59	2.45	2.31	2.72	3.23	3.77
CaO	11.06	9.9	11.62	0.02	0.03	0.01	0.00	0.01	0.01	0.03	0.03	0.03	0.01
Na_2O	0.00	0.00	1.43	0.65	0.5	0.72	0.82	0.53	0.47	0.27	0.19	0.14	0.19
K_2O	0.00	0.00	0.72	9.91	10.26	9.74	9.70	10.22	10.30	10.41	10.79	10.78	10.78
Sum	99.18	99.33	98.03	94.32	95.33	94.70	94.70	94.58	94.73	95.07	95.43	95.52	96.26
Si	2.99	3.00	6.74	3.25	3.32	3.20	3.23	3.30	3.39	3.27	3.32	3.35	3.46
Ti	0.01	0.01	0.14	0.02	0.02	0.01	0.02	0.01	0.02	0.01	0.01	0.02	0.02
Al	1.96	1.97	1.70 (tot)	2.37	2.29	2.55	2.49	2.32	2.17	2.39	2.31	2.17	2.06
Fe_{tot}	1.67	1.82	2.30	0.18	0.15	0.13	0.14	0.16	0.16	0.16	0.15	0.20	0.11
Mn	0.20	0.21	0.08	0.00	0.00	0.00	0.00	0.00	0.00	0.00	0.00	0.00	0.00
Mg	0.24	0.14	2.04	0.24	0.26	0.16	0.18	0.27	0.30	0.23	0.27	0.32	0.37
Ca	0.95	0.85	1.86	0.00	0.00	0.00	0.00	0.00	0.00	0.00	0.00	0.00	0.00
Na	0.00	0.00	0.42	0.08	0.06	0.09	0.11	0.06	0.02	0.03	0.03	0.02	0.02
K	0.00	0.00	0.14	0.86	0.87	0.83	0.83	0.89	0.92	0.89	0.92	0.92	0.91
XPrp	8.00	4.00	XMg	0.60	0.62	0.55	0.57	0.64	0.65	0.59	0.65	0.62	0.77
XAlm	54.00	59.00	Ms	0.72	0.65	0.78	0.75	0.69	0.61	0.72	0.67	0.64	0.52
XSps	7.00	7.00	Cel	0.22	0.28	0.14	0.18	0.25	0.34	0.20	0.27	0.31	0.41
XGrs	31.00	28.00	Prl	0.06	0.07	0.08	0.07	0.06	0.06	0.08	0.06	0.05	0.07

* Chemical analysis with the maximum Si content (pfu) in the analyzes sample.

Table 4.3: Full results of white mica $^{40}Ar/^{39}Ar$ stepwise-heating analysis.

Run ID	$^{40}Ar/^{39}Ar$ ± (1σ)	$^{38}Ar/^{39}Ar$ ± (1σ)	$^{37}Ar/^{39}Ar$ ± (1σ)	$^{36}Ar/^{39}Ar$ (10-3 ± (1σ))	^{40}Ar* (%)	^{39}Ar* (%)	$^{40}Ar^*/^{39}Ar$ ± (1σ)	Age ± (1σ) (Ma)
01A-H								
1043-01	164.819± 4.718	0.157 ± 0.018	1.841 ± 0.685	449.936 ± 14.033	19.4	0.4	32.046 ± 2.250	56.7 ± 3.9
1043-02	51.087 ± 0.852	0.036 ± 0.004	0.844 ± 0.217	53.965 ± 2.002	68.9	1.3	35.223 ± 0.867	62.3 ± 1.5
1043-03	42.588 ± 0.285	0.016 ± 0.001	0.000 ± 0.024	6.178 ± 1.345	95.7	4.6	40.755 ± 0.487	71.9 ± 0.8
1043-04	38.898 ± 0.154	0.015 ± 0.001	0.000 ± 0.016	4.339 ± 0.118	96.7	7.6	37.608 ± 0.155	66.4 ± 0.3
1043-05	38.859 ± 0.120	0.013 ± 0.001	0.001 ± 0.014	3.421 ± 0.097	97.4	9.4	37.843 ± 0.122	66.8 ± 0.2
1043-06	38.742 ± 0.109	0.013 ± 0.000	0.002 ± 0.010	2.043 ± 0.081	98.4	13.6	38.134 ± 0.111	67.3 ± 0.2
1043-07	37.364 ± 0.096	0.013 ± 0.000	0.012 ± 0.008	1.627 ± 0.061	98.7	18.7	36.879 ± 0.098	65.1 ± 0.2
1043-08	36.824 ± 0.115	0.013 ± 0.000	0.011 ± 0.009	1.170 ± 0.057	99.1	15.2	36.474 ± 0.115	64.4 ± 0.2
1043-09	36.579 ± 0.128	0.013 ± 0.001	0.000 ± 0.014	0.939 ± 0.097	99.2	10.8	36.295 ± 0.131	64.1 ± 0.2
1043-10	34.711 ± 0.119	0.012 ± 0.000	0.000 ± 0.014	1.428 ± 0.115	98.8	9.2	34.283 ± 0.124	60.6 ± 0.2
1043-11	46.318 ± 2.641	0.019 ± 0.001	0.065 ± 0.026	3.020 ± 0.257	98.1	5.0	45.428 ± 2.591	79.9 ± 4.5
1043-12	40.014 ± 0.204	0.013 ± 0.000	0.049 ± 0.036	3.029 ± 0.219	97.8	4.2	39.119 ± 0.212	69.0 ± 0.4
01A-L								
1042-01	224.501 ± 3.376	0.133 ± 0.004	0.126 ± 0.156	587.686 ± 9.082	22.6	0.4	50.849 ± 1.572	88.4 ± 2.7
1042-02	51.076 ± 0.321	0.023 ± 0.001	0.084 ± 0.030	48.325 ± 0.590	72.1	1.5	36.800 ± 0.305	64.4 ± 0.5
1042-03	44.919 ± 0.172	0.018 ± 0.001	0.020 ± 0.013	26.888 ± 0.231	82.3	4.0	36.971 ± 0.169	64.7 ± 0.3
1042-04	39.601 ± 0.186	0.014 ± 0.000	0.007 ± 0.020	8.049 ± 0.134	94.0	4.7	37.218 ± 0.181	65.1 ± 0.3
1042-05	38.325 ± 0.112	0.014 ± 0.000	0.000 ± 0.013	5.153 ± 0.100	96.0	6.8	36.796 ± 0.114	64.4 ± 0.2
1042-06	37.706 ± 0.091	0.013 ± 0.000	0.016 ± 0.009	2.668 ± 0.064	97.9	9.9	36.914 ± 0.092	64.6 ± 0.2
1042-07	37.394 ± 0.112	0.012 ± 0.000	0.000 ± 0.006	2.391 ± 0.050	98.1	12.8	36.682 ± 0.112	64.2 ± 0.2
1042-08	37.836 ± 0.122	0.012 ± 0.000	0.000 ± 0.005	2.595 ± 0.048	98.0	14.2	37.063 ± 0.122	64.9 ± 0.2
1042-09	36.498 ± 0.140	0.012 ± 0.000	0.000 ± 0.005	1.893 ± 0.056	98.5	13.2	35.934 ± 0.140	62.9 ± 0.2
1042-10	36.535 ± 0.127	0.013 ± 0.001	0.012 ± 0.012	1.301 ± 0.069	99.0	8.8	36.146 ± 0.128	63.3 ± 0.2
1042-11	37.631 ± 0.122	0.013 ± 0.000	0.000 ± 0.008	1.312 ± 0.088	99.0	6.7	37.236 ± 0.124	65.2 ± 0.2
1042-12	37.816 ± 0.152	0.017 ± 0.001	0.000 ± 0.019	1.127 ± 0.173	99.1	3.9	37.477 ± 0.160	65.6 ± 0.3
1042-13	37.010 ± 0.138	0.012 ± 0.000	0.026 ± 0.009	1.508 ± 0.055	98.8	13.2	36.562 ± 0.138	64.0 ± 0.2
01A-P								
1035-01	297.763 ± 3.950	0.167 ± 0.003	0.120 ± 0.127	747.150 ± 10.311	25.9	0.8	76.991 ± 1.820	132.0 ± 3.0
1035-02	79.382 ± 0.893	0.029 ± 0.005	0.052 ± 0.085	136.867 ± 1.806	49.1	1.4	38.938 ± 0.649	68.1 ± 1.1
1035-03	58.068 ± 0.570	0.035 ± 0.002	0.054 ± 0.054	79.440 ± 1.083	59.6	2.0	34.594 ± 0.468	60.6 ± 0.8
1035-04	48.525 ± 0.310	0.023 ± 0.001	0.084 ± 0.036	52.819 ± 0.565	67.8	3.7	32.920 ± 0.284	57.7 ± 0.5
1035-05	35.954 ± 0.164	0.016 ± 0.001	0.028 ± 0.019	9.110 ± 0.187	92.5	7.3	33.259 ± 0.165	58.3 ± 0.3
1035-06	35.620 ± 0.187	0.016 ± 0.001	0.036 ± 0.018	6.987 ± 0.196	94.2	7.6	33.554 ± 0.189	58.8 ± 0.3
1035-07	34.939 ± 0.151	0.013 ± 0.001	0.000 ± 0.011	3.316 ± 0.111	97.2	14.4	33.954 ± 0.153	59.5 ± 0.3
1035-08	35.565 ± 0.091	0.013 ± 0.000	0.000 ± 0.009	2.259 ± 0.073	98.1	21.8	34.893 ± 0.093	61.1 ± 0.2
1035-09	34.875 ± 0.119	0.013 ± 0.001	0.000 ± 0.015	3.083 ± 0.138	97.4	10.0	33.958 ± 0.124	59.5 ± 0.2
1035-10	33.033 ± 0.155	0.014 ± 0.000	0.001 ± 0.014	4.650 ± 0.146	95.8	8.9	31.654 ± 0.156	55.5 ± 0.3
1035-11	33.844 ± 0.174	0.012 ± 0.001	0.040 ± 0.016	3.700 ± 0.199	96.8	7.0	32.750 ± 0.180	57.4 ± 0.3
1035-12	34.386 ± 0.219	0.013 ± 0.001	0.006 ± 0.034	3.582 ± 0.434	96.9	3.1	33.323 ± 0.249	58.4 ± 0.4
1035-13	45.331 ± 0.407	0.014 ± 0.001	0.000 ± 0.083	3.855 ± 0.970	97.5	1.3	44.180 ± 0.491	77.0 ± 0.8
1035-14	41.862 ± 0.167	0.014 ± 0.001	0.362 ± 0.016	6.736 ± 0.142	95.3	10.7	39.905 ± 0.168	69.7 ± 0.3

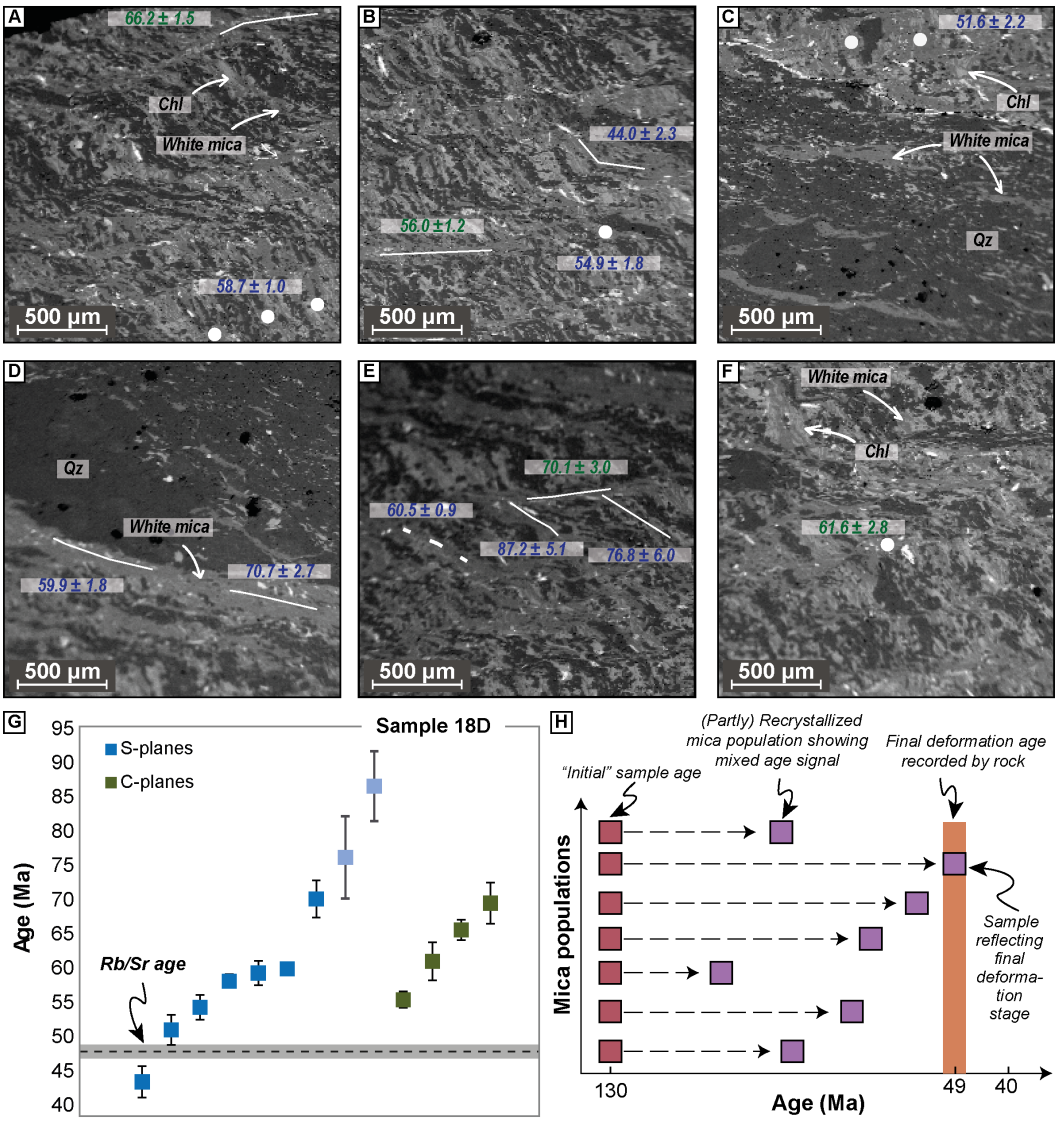

Figure 4.10: (A-F) Scanning electron microscope (SEM) backscattered electron photomicrographs of studied white mica-bearing sample #18D and the location of the analyzed domains during laser ablation in white micas; blue colors correspond to analyses of S-planes in micas, green colors to C-planes. (G) Summary of apparent ages obtained on white mica by in situ laser analyses; the two transparent age points correspond to measurements with large analytical uncertainty (>5 Ma), which are not taken into consideration for the interpretation of the in situ age data; dashed line corresponds to the age obtained by Rb/Sr on metasediments, and shaded area shows uncertainty at 2σ level. Uncertainties of $^{40}Ar/^{39}Ar$ analyses are given in 1σ. (H) Interpretation of a hypothetical span of both Rb/Sr and $^{40}Ar/^{39}Ar$ measurements; x-axis shows age (Ma), y-axis the different mica populations dated. The older ages (red squares) would correspond either to age of formation of the rock or complete pre-Alpine deformation. Full isotope resetting and re-equilibration of the rock would give ages clearly clustered around the last event of deformation (orange bar, e.g., at ca. 49 Ma). A geochronological signal similar to the purple squares, namely scattered deformation ages, would reflect mixed ages due to incomplete recrystallization and/or only partial isotopic resetting. The youngest age can, therefore, only be interpreted as the maximum age for the end of deformation.

Table 4.4: Full results of white mica $^{40}Ar/^{39}Ar$ in-situ UV laser ablation probe analysis.

Run ID	$^{40}Ar/^{39}Ar$ ($\pm1\sigma$)	$^{38}Ar/^{39}Ar$ ($\pm1\sigma$)	$^{37}Ar/^{39}Ar$ ($\pm1\sigma$)	$^{36}Ar/^{39}Ar$ (10-3 $\pm$) 1σ	$^{40}Ar*$ %	$^{40}Ar*/^{39}Ar$ ($\pm1\sigma$)	Age ($\pm1\sigma$) (Ma)
S-planes							
1049-09	60.786 ± 1.149	0.023 ± 0.005	0.000 ± 0.666	71.470 ± 4.470	65.1	39.503 ± 1.558	70.7 ± 2.7
1049-10	86.312 ± 2.446	0.061 ± 0.011	0.028 ± 1.412	126.557 ± 8.745	56.7	48.912 ± 2.943	87.2 ± 5.1
1049-12	74.229 ± 2.317	0.000 ± 0.0127	0.000 ± 1.373	10.467 ± 1.035	58.0	42.956 ± 3.411	76.8 ± 6.0
1049-20	40.893 ± 0.772	0.024 ± 0.005	0.104 ± 0.646	55.916 ± 3.776	59.6	24.375 ± 1.281	44.0 ± 2.3
1049-21	37.481 ± 0.710	0.022 ± 0.004	0.533 ± 0.557	23.640 ± 2.737	81.5	30.544 ± 1.034	54.9 ± 1.8
1049-23	35.848 ± 0.617	0.023 ± 0.002	0.316 ± 0.448	24.323 ± 3.723	80.0	28.687 ± 1.227	51.6 ± 2.2
1049-24	40.354 ± 0.543	0.025 ± 0.002	0.262 ± 0.359	23.795 ± 2.909	82.6	33.344 ± 0.991	59.9 ± 1.8
1049-26	33.450 ± 0.417	0.017 ± 0.002	0.002 ± 0.278	2.523 ± 1.407	97.8	32.699 ± 0.587	58.7 ± 1.0
1049-28	34.225 ± 0.336	0.018 ± 0.002	0.081 ± 0.204	1.774 ± 1.185	98.5	33.704 ± 0.484	60.5 ± 0.9
C-planes							
1049-11	50.722 ±1.119	0.008 ±0.005	0.000 ± 0.788	38.901 ± 4.845	77.2	39.147 ± 1.713	70.1 ± 3.0
1049-16	36.612 ±0.815	0.019 ±0.006	0.039 ± 0.527	7.753 ± 4.644	93.8	34.320 ± 1.581	61.6 ± 2.8
1049-19	39.028 ±0.543	0.021 ±0.003	0.000 ± 0.277	26.518 ± 1.705	79.9	31.179 ± 0.686	56.0 ± 1.2
1049-29	36.245 ±0.589	0.017 ±0.003	0.000 ± 0.332	0.000 ± 2.132	102.0	36.960 ± 0.868	66.2 ± 1.5

$\sim$250°C. Brittle deformation of albite as well as absence of blue amphibole and jadeite set an upper limit for peak T (<500°C) and peak P conditions (<1.2 GPa). Moreover, our pseudosection results along with micro-fabrics analysis suggest that deformation during Alpine convergence took place at T > 350°C and pressures $\sim$0.9 GPa. This estimate plots along the burial gradient of 8°-10°/km commonly accepted for late Cretaceous Alpine metamorphism (e.g., Agard et al., 2001). These pressure-temperature estimates are in agreement with previous attempts to quantify the alpine metamorphism in the base of the Austroalpine stack farther to the NW in the Bivio region (Handy, 1996) and in the Piz de la Margna region (main Alpine foliation Guntli and Liniger, 1989) where 0.6-0.9 GPa and 300°-450°C were obtained. A later stage of lower-pressure conditions is also mentioned for deformation postkinematic to the main Alpine foliation (0.4-0.5 GPa, Guntli and Liniger, 1989). The growth of thin garnet rims in equilibrium with phengite and chlorite from the main foliation suggests heating during decompression (Fig. 4.7), since garnet commonly requires temperatures >450°C to form. This event may relate with the D2 postpeak stage reported by Handy (1996) and referred as "T-dominated" in Villa et al. (2000). We emphasize that some uncertainty exists on P-T estimates for the burial P-T conditions (at least several tens of degrees and possibly a few hundred MPa) due to their strong dependence on phengite solid solution model (and associated Si isopleths) as well as the

control of MnO concentration on the "Garnet-in" reaction location (e.g., Mahar et al., 1997).

4.5.2 Interpretation of age data

Calculating the Rb/Sr isochron for white micas from metasediments marking the boundaries between the crystalline nappes yielded an age of 48.9 ± 0.9 Ma. Since there is no correlation between mica grain size and apparent age for this sample, we consider this a robust age. Moreover, it is identical to the age obtained by Bachmann et al. (2009b) for the youngest movements at the plate interface farther north in southern Switzerland and relatively close to the ages obtained by Picazo et al. (2019). It has been particularly difficult to derive meaningful age information for the crystalline basement rocks, since the various mineral fractions separated reveal significant disequilibrium, including the low-Rb/Sr phases such as apatite, albite, or titanite. Large mica grains seem apparently older than younger grains, which is a characteristic signature for incomplete recrystallization (Figs. 4.8B and 4.8C). We interpret the Sr disequilibrium and the obvious evidence for much older isotopic signatures as an incomplete overprint of possibly Variscan ages during Alpine shearing. An analogous conclusion has been already drawn for similar rocks from the base of the Austroalpine nappe farther north Bachmann et al. (2009b) and west in the Dent Blanche massif Angiboust et al. (2014).

To test whether the K-Ar system of white mica was more equilibrated than Rb/Sr in the crystalline basement rocks and to potentially avoid the problem of contamination of the Alpine signal by pre-Alpine isotopic relics, we analyzed white micas derived from one mylonitic gneiss from Margna and one foliated cataclasite from Sella, by $^{40}Ar/^{39}Ar$ stepwise heating and in situ dating, respectively. We analyzed the samples with the least fraction of isotopic relics. This approach enabled the production of age data from regions of the samples most pervasively affected by mylonitization. Microscopically, the sample used for stepwise-heating dating did not exhibit core-rim structures in phengite crystals. Three mica fractions were dated, yielding an age of 61.1-66.2 ± 0.3 Ma, and a plateau age of 64.6 ± 0.3 Ma was calculated for one of the fractions. In situ $^{40}Ar/^{39}Ar$ age results for sample #18D (foliated cataclasite), however, yielded a large span of ages from 44.0 to 70.7 Ma (see Fig. 4.10G). Neither an apparent systematic relation was observed between S- and C-structures and their calculated ages nor a correlation of the two structures with different Si content (Fig. 4.6B; unlike for Agard et al. (2002)).

Table 4.5: Overview of age data acquired in this study.

Sample	Rb/Sr age	Ar/Ar age	Interpretation
Margna			
#01A	44	61-66 (stepwise)	Rb/Sr maximum age for end of deformation
#01F	54	n/a	same as above
#02	Disequilibria	n/a	Rb/Sr disequilibria
Sella			
#18D	n/a	44-87 (in-situ)	Age span covering most of P-dominated Alpine deformation
#23B	Disequilibria	n/a	Rb/Sr disequilibria
Metasediments			
#13	48.9 ± 0.9	n/a	Synkinematic metamorphic (re)crystallization: deformation age

n/a – not applicable

It is known that extraneous ^{40}Ar (including both excess and inherited argon) can be commonly found in HP and UHP basement rocks (Scaillet, 1996; Sherlock and Kelley, 2002; Di Vincenzo et al., 2006, and references therein) and that in its presence apparently older and meaningless geological ages can be obtained. Excess argon might be present due to diffusion through grain boundaries, whereas inherited argon can result from preexisting argon from older minerals whose isotopic signature did not get fully re-equilibrated by the metamorphic imprint that one aims to date.

In the present study, the mylonitic sample dated with ^{40}Ar/^{39}Ar stepwise heating (#01A) exhibits disequilibrium of its isotopic signature, as attested by the lack of plateau for two mica fractions and the different ages calculated for different mica fractions, especially since bigger fractions (#01A-P) yield younger ages than the finer ones (compare Fig. 4.9C with Figs. 4.9A and 4.9B). Furthermore, ages obtained by in situ dating on the foliated cataclasite (#18D) exhibit a wide range of values (44-87 Ma; Fig. 4.10G), which, however, fall within the range of published Alpine deformation ages in the Central Alps in general (K-Ar on phengite crystals, Handy (1996); ^{40}Ar/^{39}Ar on amphiboles, Villa et al. (2000); Fig. 4.3), as well as for the time window of active subduction as inferred from the spread of pseudotachylyte ages (Bachmann et al., 2009b) along the same contact. The aforementioned geochronological heterogeneities are also reflected in the petrochemical signature of the rocks: feldspar boudins, mica fish within recrystallized mica fibers (Fig. 4.5A), and multiple phengite generations (Figs. 4.6A and 4.6B). Based on the above heterogeneities and our previous interpretation of the age data as indicative of maximum ages for the cessation of deformation, we cannot exclude the presence of extraneous

^{40}Ar in our samples.

As already mentioned, the maximum Rb/Sr ages for the end of Alpine deformation (44.0 and 54.3 Ma) coincide with the youngest in situ ^{40}Ar/^{39}Ar ages (44.0 Ma; see Table 4.5). We interpret the older ages obtained as reflecting mixed ages, due to incomplete recrystallization and only partial isotopic resetting, while we interpret the youngest ones as maximum age for the end of deformation (see also Fig. 4.10H; Picazo et al., 2019). Finally, we emphasize that the seeming discrepancy with the studies of Handy (1996) and Mohn et al. (2011) is due to the terminology used and not to the processes themselves: what these authors refer to as collision/D3 deformation is considered in our study a stage of "subduction of continental Austroalpine sliver(s)."

4.5.3 Alpine deformation along the base of the Austroalpine stack

The base of the Austroalpine nappes in Central and Western Alps (Dent Blanche) has been proposed by Bachmann et al. (2009b) and Angiboust et al. (2015), respectively, as a field analogue for the roof of an ancient subduction interface (see also Froitzheim and Manatschal, 1996; Froitzheim et al., 1996; Schmid et al., 2004, for paleogeographic reconstructions). Although the presence of a metamorphic gradient along the Arosa - St. Moritz - Malenco transect is well known (e.g., Trommsdorff, 1983; Guntli and Liniger, 1989), up to now this part of the Austroalpine-Penninic boundary has not been studied in the frame of the subduction interface.

The Val Malenco setting is a plate interface zone characterized by abundant underplated continental slivers (such as the Sella and Margna nappes), which likely represent extensional allochthons of the Apulian upper plate, sheared off early in the subduction history and transported toward depth. Hence, the Margna and Intra Sella shear zones (MSZ and ISSZ, respectively) correspond to parts of a shear zone network forming the plate interface zone in their entirety. As suggested by Beltrando et al. (2010) and Mohn et al. (2011), it is conceivable, but not easily tested, that preexisting extensional faults, active during Jurassic rifting, could have facilitated the detachment from the downgoing slab during the subduction event.

The shear zones studied here were, at least kinematically, at one point in their lifetime part of the plate interface shear-zone network. Since these shear zones are interface-parallel and none

of them ends blindly high up (nor crosses the units at an angle), we exclude the possibility that they represent splay faults into the upper plate. We rather assume that they formed part of a network belonging to the plate interface as long as they were active. This would make the system kinematically similar to the finding by Angiboust et al. (2014) on the evolution and stacking of interfaces through progressive underplating of duplex units. Unfortunately, our dating results do not resolve whether they were sequentially active - as in the Dent Blanche area - or active simultaneously. We stress that exhumation and collision have left an imprint in the present-day structures. However, our sampling and observations were limited to areas with minimum reworking, as shown by the white mica zoning pattern, which exhibits only minor exhumation-related zoning and by the moderate back-shearing observed in the kinematic indicators along main thrust contacts. In addition, the youngest ages near 44 Ma that we obtained are older than the late Eocene-Oligocene collisional event that started at ca. 40 Ma and continued until ca. 25 Ma (e.g., Becker, 1993; Markley et al., 1998; Price et al., 2018) related to the entrance of the European continental margin in the Alpine subduction zone and associated with a kinematic inversion of subduction-related structures.

Despite some uncertainties due to the scarcity of pressure indicators, our estimates plot deeper than for Arosa and St. Moritz, for which peak burial temperatures of 200°-250°C and 300°-350°C have been estimated, respectively (Fig. 4.7; Bachmann et al., 2009b). On a microstructural point of view, the Alpine deformation and the associated mylonitic deformation are much more extensively expressed in the Malenco region than along shallower equivalents (see fabric description from Bachmann et al. (2009a,b); Fig. 4.11). In fact, large mylonitic corridors are commonly observed in Margna and Sella nappes, unlike Arosa and St. Moritz, where deformation of the Austroalpine units is mostly expressed by microscale fractures in shallower parts and recrystallization of sheet silicates deeper. The larger amount of ductile imprint is likely a consequence of increasingly higher peak burial temperatures from Arosa, through Malenco down to Dent Blanche regions at also slower strain rates. Veining and mineralization within the Austroalpine units of the study area are not pervasive, which agrees with observations for the shallower basal parts of the Austroalpine, in the Arosa-St. Moritz region (Bachmann et al., 2009b).

One of the main differences between Arosa-St. Moritz and Malenco is the absence of in situ

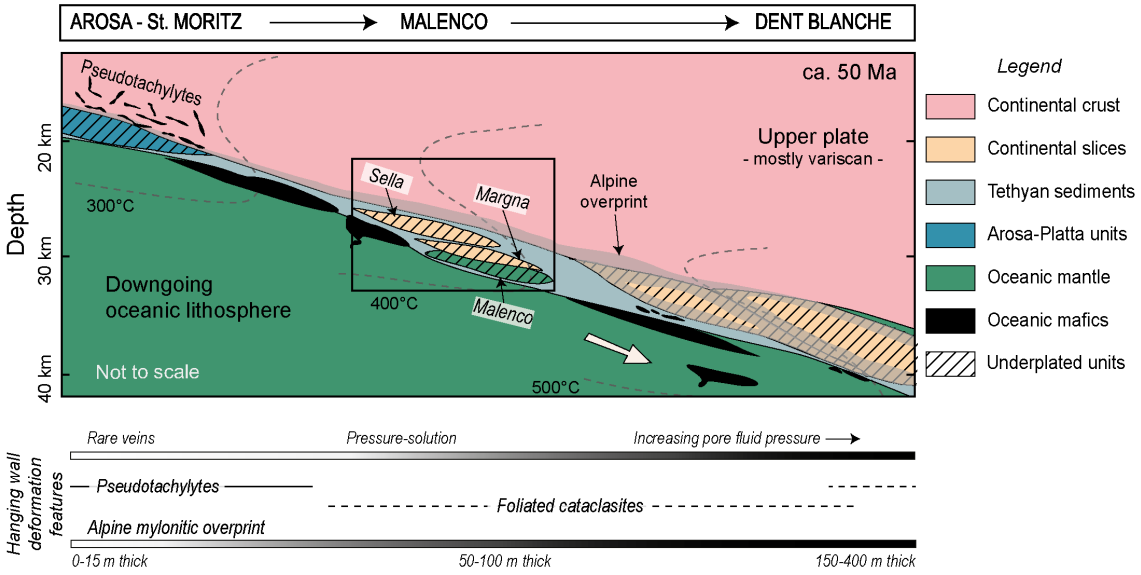

Figure 4.11: Synthetic sketch summarizing the structure of the paleo-Alpine interface at ca. 50 Ma, when Margna and Sella nappes were already basally accreted to the Austroalpine tectonic edifice. Val Malenco deformation patterns are compared in this figure with features reported by Bachmann et al. (2009a,b) for the shallower region and by Angiboust et al. (2014) and Menant et al. (2018) for the deeper regions.

pseudotachylytes along the base of the Austroalpine units of the latter. In the study area of Bachmann et al. (2009b), pseudotachylytes are abundant in the northern part of the transect, providing evidence for high strain rates at seismic slip velocities; the southernmost (and hence deepest) locality where pseudotachylytes along the plate interface zone are mentioned is SW of St. Moritz, where peak temperatures of ∼350°C were reached. In our study area, a significant number of pseudotachylytes was observed only in the form of fallen blocks along streams; but based on their abundance and location in which they were found, we hypothesize they derive from the hanging wall, i.e., higher Austroalpine units, such as Upper Sella and/or Bernina nappes (Fig. 4.4I). The rocks studied in the Val Malenco region accommodated shearing predominantly by ductile flow with limited cataclastic networks (Fig. 4.11). While this observation, along with the evidence for repeated hydrofracturing, is indicative of variations in creep velocity by at least several orders of magnitude, there is no clear evidence as to whether they are related to slip at seismic velocities, i.e., at 1 m/s. Along the base of the Dent Blanche basal thrust, the close genetic link between foliated cataclasites with metamorphic veins led Angiboust et al. (2015) to propose their association with semi-brittle and brittle-ductile switches, potentially the record of transient slow slip events that take place near the base of the seismogenic zone. Some

pseudotachylytes found in the core of Dent Blanche massif (Valpelline unit) were interpreted as the consequences of the accumulation of high stresses in very stiff rocks that were not prone to breaking (Menant et al., 2018). Their age is coeval with peak burial conditions, pointing to heterogeneous deformation patterns at depth in accreted continental slivers in the Alpine channel. They may or may not be coeval with the pseudotachylytes found as fallen blocks in our study area. It has yet to be shown whether the Bernina pseudotachylytes formed during the rifting phase (e.g., Bissig and Hermann, 1999; Mohn et al., 2011), or if they formed in a similar manner as for the Valpelline unit in the Dent Blanche massif. With the absence of distinct fabrics that may be related to seismogenic deformation and temperatures of ∼400°C, we, therefore, hypothesize that this part of the Alpine subduction zone represents the deformation styles of the transition zone, found globally to characterize the downdip end of seismicity toward aseismic creep at similar temperatures (e.g., Hyndman et al., 1997; Oleskevich et al., 1999). Moreover, the findings corroborate repeated switches between slower and faster creep velocities and near-lithostatic pore-fluid pressure conditions characterizing this depth domain, similar to findings in this depth region found instrumentally in many active subduction settings.

4.6 Conclusions

The Lower Austroalpine units in the Malenco region were subducted, underplated, and partly re-crystallized during the long history of Alpine convergence. The dominant deformation pattern along Alpine shear zones affecting the Austroalpine bodies during peak burial (at ∼400°C and 0.9 GPa) is ductile with widespread pressure-solution as well as local semi-brittle (fractured albite) and brittle, cataclastic networks. Rb/Sr geochronology on mica-rich metasediments deposited during Jurassic rifting and later metamorphosed during Alpine convergence yields a robust age of deformation and (re)crystallization of 48.9 ± 0.9 Ma. However, our Rb/Sr as well as $^{40}Ar/^{39}Ar$ dating of some Alpine, seemingly recrystallized white micas from mylonites and one foliated cataclasite of the crystalline basement reveal a wide range of ages, which, despite falling within the range obtained by previous studies (Handy, 1996; Villa et al., 2000; Picazo et al., 2019), can only be considered as mixed ages due to partial resetting of the isotopic signature of the system.

Putting together recent findings in the broader Val Malenco area (e.g., Droop and Chavrit, 2014; Picazo et al., 2019) and the P-T-t results of this study, we highlight the existence, during the geodynamic evolution of the Central Alps, of a continuous subduction and underplating process along the active subduction interface, from the upper nappes (Austroalpine) toward the deeper ones (Malenco). The Val Malenco area sheds light onto a region below the seismogenic depths exposed in Arosa-St. Moritz and displays subduction-related deformation at a depth range in the transition zone, which is globally found to host both slow creep as well as more rapid silent slip events.

Acknowledgements

This research was funded by the People Programme (Marie Curie Actions) of the European Union's Seventh Framework Programme FP7/2017-2013/under REA grant agreement no. 604713, "Zooming in between Plates (ZIP)" and by a USPC-IDEX grant to S.A. O. Müntener is acknowledged for fruitful scientific discussion. C. Pranger and S. Olivotos are thanked for assistance during fieldwork and M. Locatelli for useful discussions. M. Dziggel is also acknowledged for helping with the digitization of the geological map. We thank U. Ring, an anonymous reviewer, and the Associate Editor, G. Bebout for their constructive reviews. This is Institut de Physique du Globe de Paris (IPGP) contribution #4094.

Chapter 5

Effective rheology of a two-phase subduction shear zone: Insights from numerical simple shear experiments and implications for subduction zone interfaces

Note

This chapter is a reformatted version of a paper with the same title, which has been submitted to *EPSL*.

Abstract

The physical nature and the rheology of the subduction interface play an important role in the deformation and the degree of locking. Inspired by exhumed subduction shear zones that exhibit block-in-matrix characteristics (mélanges), synthetic models are created with different proportions of strong clasts within a weak matrix and compared to natural mélange outcrops.

Using 2D Finite Element visco-plastic numerical simulations in simple shear kinematic conditions, the effective rheological parameters of such a two-phase medium, comprising blocks of basalt embedded within a wet quartzitic matrix are determined. Models and their structures are treated as scale-independent and self-similar and published field geometries are upscaled to km-scale models, compatible with large-scale far-field observations. Exhumed subduction mélanges suggest that deformation is mainly taken up by dissolution-precipitation creep. However, such flow laws are neither well-established yet experimentally nor of ample use in numerical modelling studies. In order to make the results comparable to and usable by numerical studies, dislocation creep is assumed as the governing flow law for both basalt and wet quartz. By using different confining pressures, temperatures and strain rates, effective rheological estimates for a natural subduction interface are provided. The results suggest that the block-in-matrix ratio affects deformation and strain localization, with the effective dislocation creep parameters (A, n, and Q) varying between the values of the strong and the weak phase, in cases where deformation of both materials is purely viscous. As the contribution of brittle deformation of the strong blocks increases, however, the value of the stress exponent, n, can exceed that of the purely strong phase.

5.1 Introduction

Subduction zones are regions where large portions of plate convergence are accommodated and much of the Earth's geologic activity occurs (Peacock, 2009; Stern, 2002). They undergo strong interplate coupling along their interface and exhibit large magnitude earthquakes in their seismogenic zone (e.g. Hyndman et al., 1997; Conrad et al., 2004; Heuret and Lallemand, 2005), as well as a plethora of recently discovered slip behaviours, such as slow slip events and episodic tremor and slip (e.g. Rogers and Dragert, 2003; Obara et al., 2004; Peng and Gomberg, 2010; Gao and Wang, 2017). Modern views of a subduction zone interface suggest a broad range of mixed kinematic (e.g., Audet et al., 2009; Obara and Kato, 2016) and rheological properties along the subduction interface (e.g., Bachmann et al., 2009b; Fagereng and Cooper, 2010; Rowe et al., 2013; Wassmann and Stöckhert, 2013b), the result of which is mechanical segmentation of the interface.

Investigating the different scales at which these deformation processes are manifested can shed light on the effective rheology along the interface (e.g. Stöckhert, 2002; Herrendörfer et al., 2015; Agard et al., 2018). Exhumed suture zones constitute a pivotal target of this multi-scale investigation, since they enable direct insight on fossil subduction interfaces and provide opportunities to access the long-term record of subduction zone deformation (e.g., Ernst and Dal Piaz, 1978; Platt, 1986; Stöckhert, 2002; Agard et al., 2009, 2018). One specific case of a subduction interface is a bi-modal aggregate of finite thickness consisting of a weak, often sedimentary matrix with embedded strong "exotic" blocks of upper and/or lower plate rocks, termed subduction or tectonic mélange (e.g. Shreve and Cloos, 1986; Ring et al., 1990). Recently, field observations have emphasized the existence of subduction mélanges with varying concentrations of blocks (Festa et al., 2012, 2019), in e.g. Western and Central Alps (Ring et al., 1990; Bachmann et al., 2009b; Angiboust et al., 2014), New Zealand (Fagereng and Cooper, 2010) and SW Japan (Kimura et al., 2012), the bulk deformation of which suggests a mixed brittle-ductile behaviour (Fagereng and Den Hartog, 2017). One question that arises is how strongly the bulk rheology of such a complex aggregate is affected by the block-in-matrix ratio and if this rheological behaviour can be used for refining the rheology often used in lithospheric-scale simulations (Grigull et al., 2012; Beall et al., 2019).

Since large-scale geodynamic models cannot resolve such fine structures (Fig. 5.1), numerical studies have recently focused on small-scale processes and how they relate to large-scale aseismic and/or slow slip deformation (Fagereng and Den Hartog, 2017; Webber et al., 2018; Beall et al., 2019; French and Condit, 2019). Using as a proxy for the subduction interface a high block-in-matrix outcrop of the Chrystalls Beach mélange, New Zealand, Webber et al. (2018) investigated stress and strain transients and suggested that SSEs can be represented, amongst others, by alternating clast-supported and matrix-supported bulk rheology. Beall et al. (2019), studying different generalized mélanges, found that the block concentration can affect the type of creep, with $\geq 50\%$ weak matrix accommodating steady creep at low stress and $\leq 50\%$ weak matrix promoting transient slow slip. Moreover, French and Condit (2019) investigated strain partitioning and the conditions under which aseismic creep and SSEs might occur in different lithological units that constitute part of the subduction interface.

All the aforementioned studies provide important insight concerning how deformation is taken

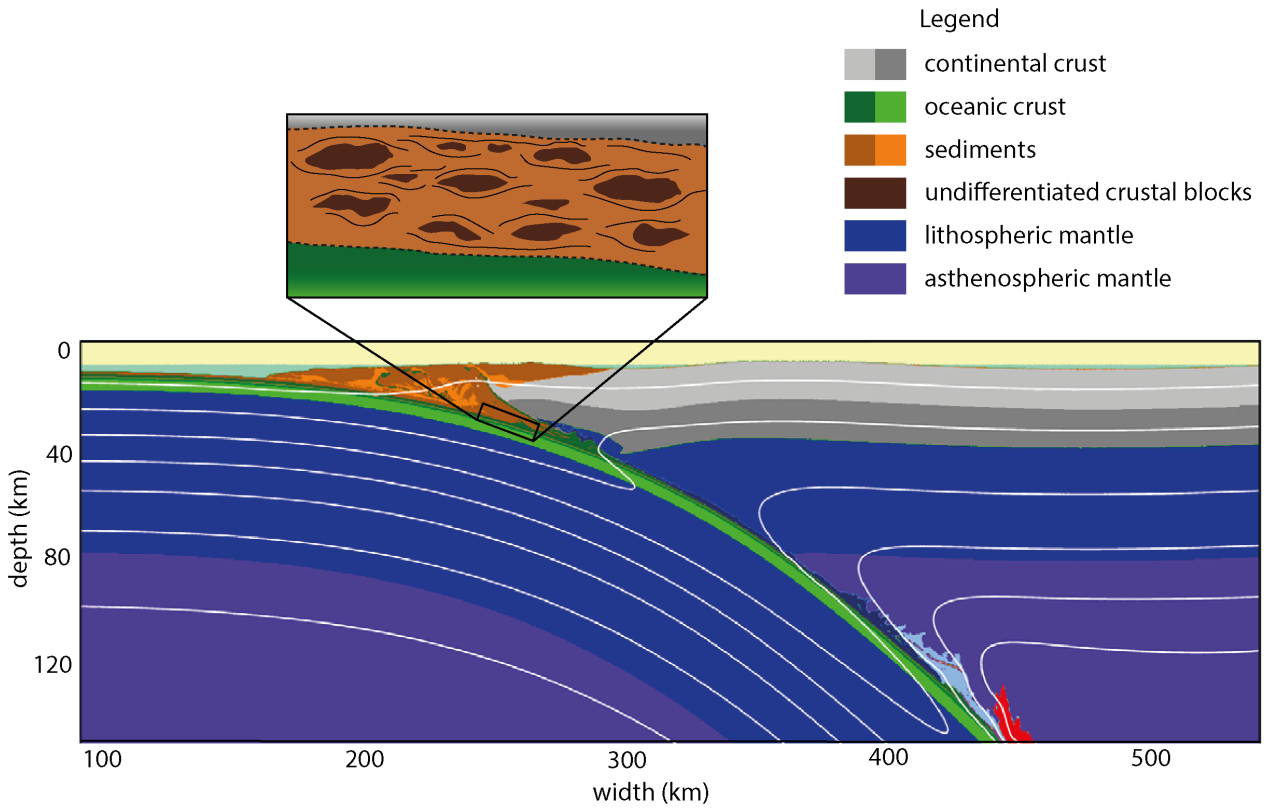

Figure 5.1: Example of a large-scale geodynamic subduction zone model (from Ruh et al., 2015). Inset shows that in the outcrop-scale the interface is not always a homogeneous medium, as considered in large-scale models. Instead, it may be rather heterogenous, comprising two (or even more) phases. Since the mesh of large-scale models cannot resolve such small, outcop-scale structures, using an effective viscosity that takes into account these structures may help refine the rheology of the interface.

up by the different units/materials along the subduction interface and what the potential macroscopic kinematics are. This study acts complementary to the aforementioned works since it focuses on calculating the effective viscous creep parameters of a subduction mélange, as a function of the concentrations of blocks. First, using synthetic 2D maps of circles and ellipses with distinct block-in-matrix ratios (Fig. 5.2) and assuming dislocation creep as the dominant deformation mechanism, the effective creep parameters are calculated, i.e. the pre-exponential term, A, the stress sensitivity, n and the activation energy, Q. These synthetic models are then compared with natural observations from exhumed subduction mélanges. It is emphasized that the scope of this study is to examine the effective rheology of complex subduction interface in a snapshot in time and at different depths, irrespective of whether it formed during subduction or it was a pre-existing structure.

5.2 Mélange rheology and deformation

The proportions of the strong phase play an essential role in the bulk deformation of the polyphase aggregate. Handy (1990) identified three distinct classes of polyphase aggregates: 1) a load-bearing framework, characterized by a dominant strong phase ($> 75\%$) with a relatively small volume proportion of the weak phase ($< 25\%$), in which the bulk strength approaches that of the strong material; 2) isolated clasts within a substantially weaker matrix, in which the bulk strength is that of the deforming matrix, and 3) two phases with a relatively low strength contrast, in which the bulk strength is between that of the end-members.

For proportions of the strong phase $> 70\%$, the strength of the aggregate is thought to be governed by the rheology of this strong material (e.g. Shelton and Tullis, 1981). However, more recent studies show that a concentration of $> 50\%$ of blocks may be a more realistic threshold and can lead to an increase of the bulk viscosity of the assemblage (Grigull et al., 2012; Beall et al., 2019). Grigull et al. (2012), in particular, did a comprehensive study on exhumed subduction mélanges and suggested that most of the deformation is taken up by the matrix for outcrops consisting of up to 50% of blocks. Factors influencing the type of bulk deformation are the dominant deformation mechanisms of the matrix, the volume fraction of blocks suspended in the matrix and the geometry of the blocks.

For this study, first 2D synthetic maps are considered, consisting of different percentages of circular and elliptical strong blocks within a matrix. These shapes are chosen to account for the geometries of blocks outlined by Grigull et al. (2012). These synthetic models are then compared with "natural" models based on published mélange data around the world that record brittle and ductile deformation patterns. The block proportions of the synthetic models range between 10% and 66% (Fig. 5.2). For the "natural" models, block distributions are used from mélange outcrops from the Chrystalls Beach in New Zealand, from the Mugi Mélange in Japan and from the Schistes Lustrés in the European Alps. The corresponding block-in matrix ratios range between 6% and 69% (Fig. 5.3).

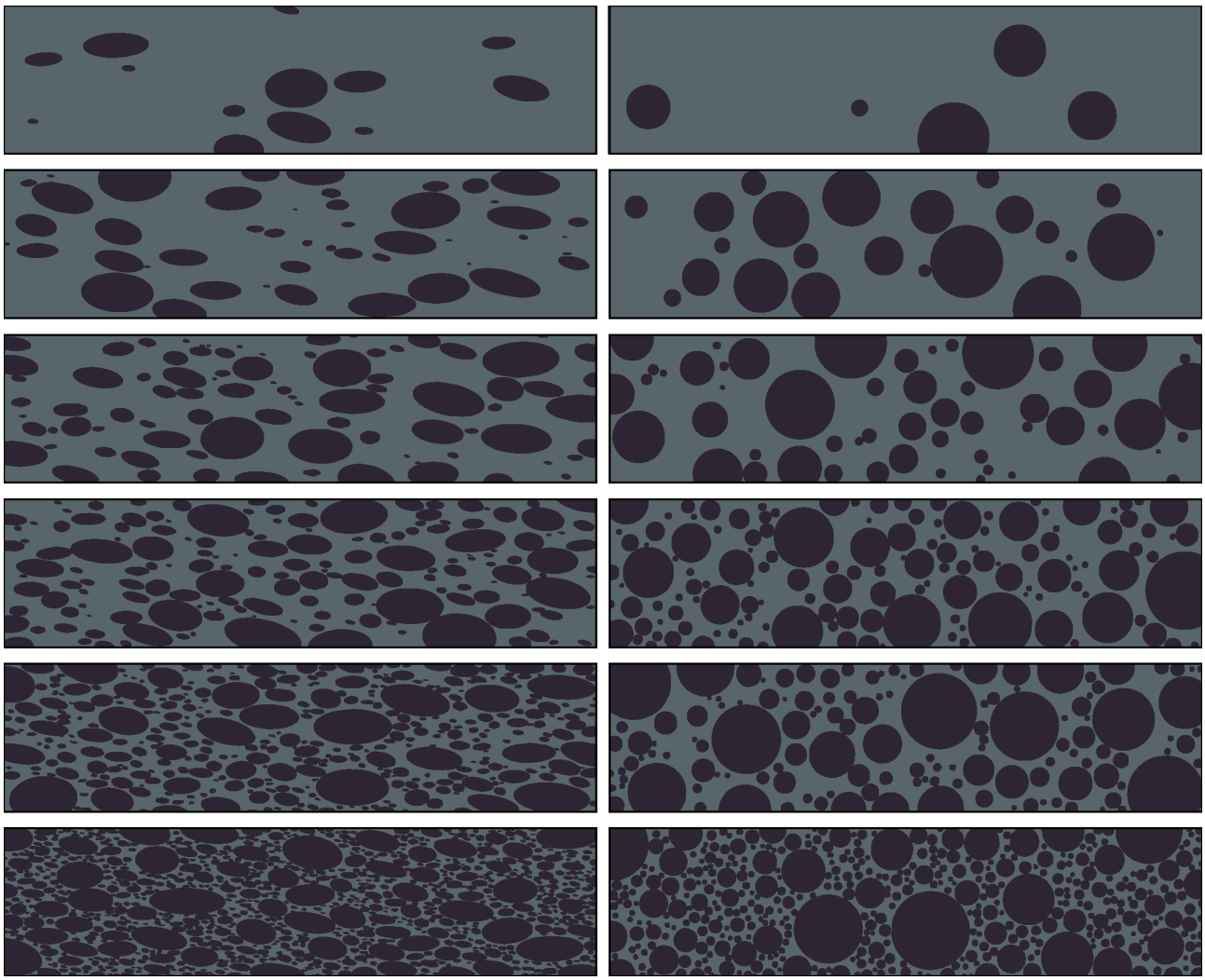

Figure 5.2: Synthetic 2D elliptical (left) and circular (right) models. Percentages from top to bottom are ca. 10, 20, 30, 50, 60 and 65%.

5.2.1 Models after natural examples

5.2.1.1 Chrystalls Beach Complex, New Zealand

The Chrystalls Beach Complex, an accretionary mélange within the Otago Schist in New Zealand, formerly occupied part of the seismogenic zone and formed under peak metamorphic conditions of > 550 MPa and $\sim 300°C$ (Fagereng and Cooper, 2010; Fagereng, 2011). Within this mélange, bi-modal deformation fabrics are observed: chert and basalt blocks exhibit brittle structures while the phyllitic matrix shows evidence of viscous shearing. The overall deformation points to a mixed continuous-discontinuous behaviour: continuous matrix fabrics accounting for aseismic flow abut on more competent areas of localized seismic and/or aseismic slip (Fagereng and Cooper, 2010). Different deformation mechanisms described at the

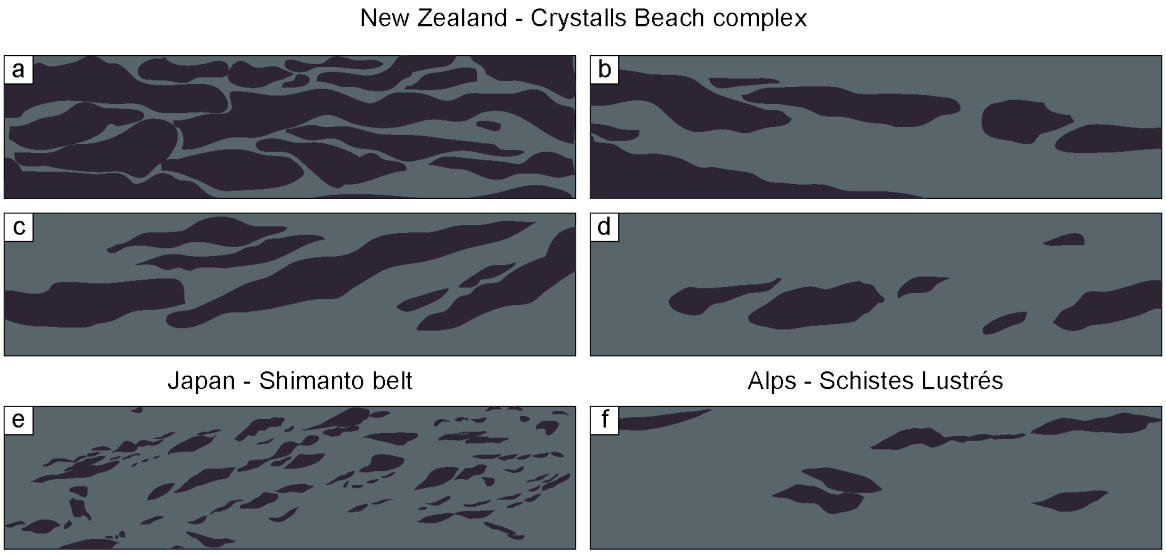

Figure 5.3: Field outcrops used as the "natural models". (a-d) digitized outcrops from the Chrystalls Beach complex (Fagereng and Cooper, 2010). (e) digitized outcrop from Mugi Mélange in the Shimanto Belt, Japan (Kimura et al., 2012). (f) digitized outcrop from the Schistes Lustrés, in the Alps.

microscale by Fagereng (2011) imply transient, locally elevated fluid pressures.

5.2.1.2 Mugi mélange, SW Japan

The Mugi mélange, part of the Shimanto Belt in SW Japan, consists of a mixture of basalt, chert and shale slivers wrapped within a highly sheared black shale matrix. The inferred maximum temperature of $> 150°C$ (Kimura et al., 2012, and references therein) corresponds to the upper thermal limit of the seismogenic zone (Oleskevich et al., 1999). The fabrics differ between the sheared matrix and the basaltic blocks: pressure-solution, mineral preferred orientation and flattening during shear characterize the matrix while (ultra)cataclastic deformation prevails in the competent basaltic blocks, with only scarce evidence of pressure-solution. The co-existence of mineralized veins and relatively pervasive viscous fabrics implies locally elevated fluid pressures and increased viscous strains, respectively.

5.2.1.3 Schistes Lustrés, W Alps

The Schistes Lustrés in Western Alps comprise sheared calcschists (Lemoine et al., 1984; Agard et al., 2001) with embedded metabasaltic and serpentinitic slivers resulting from the deep

juxtaposition of the various elements forming the Tethyan seafloor (Lagabrielle and Lemoine, 1997; Schwartz et al., 2013). The aggregation of competent mafic blocks and weak matrix reached a depth of 40-65 km during Alpine subduction in the Cretaceous and the early Tertiary Agard et al. (2002). Most tectonic slices forming the Schistes Lustrés complex exhibit strong flattening, pervasive shearing, as well as marked metamorphic gradients among sub-units from 350°C to the west up to 500°C along the eastern margin of the unit (Agard et al., 2001; Beyssac et al., 2002; Plunder et al., 2012; Angiboust et al., 2014). In the higher-grade segments of the Schistes Lustrés complex (e.g. Fenestrelle region, Agard et al., 2002) the greatest part of the matrix is composed of sheared metapelites comprising dismembered fragments of prograde veinsets filled mostly by quartz and albite (Fig. 5.3c).

5.2.2 Digitizing field outcrops

This study focuses on the block-matrix ratios, the blocks shape and orientation as documented by field observations. Models and their structures (i.e. the relative block size distribution) are treated as scale-independent and self-similar, as suggested by Medley (2002); Grigull et al. (2012); Fagereng (2011); Le Pourhiet et al. (2013). Therefore, fractal distribution of the structures is assumed and models are upscaled to subduction shear zone dimensions. Using a constant field exposure ∼1 m wide and a similar aspect ratio (here 4:1), the distribution is upscaled to create a digital map of 3x0.5 km. In order to avoid boundary effects, 2/6 of the models are filled by extra matrix on the left and the right boundaries (Fig. 5.4).

5.3 Numerical modelling and parametrization

5.3.1 Numerical approach

The visco-plastic 2D version of the code pTatin3D (May et al., 2014, 2015), a highly scalable, massively parallel implementation of the Finite Element Method is used, which employs an Arbitrary Lagrangian Eulerian discretisation, together with the material point method. The code is solving the Stokes equation for incompressible flow that describes the changes in momentum (force) in response to pressure and viscosity. The equations governing viscous flow are accu-

rately resolved through the use of high order stable elements ($Q_2 - P_1$). Material properties and history variables are assigned to material points contained within the computational domain.

Since I am interested in the steady-state long-term deformation in the models, elasticity is neglected and the code solves for conservation of mass, which is approximated by enforcing incompressibility of the flow, v:

$$\nabla \cdot \mathbf{v} = 0 \tag{5.1}$$

and conservation of momentum:

$$\frac{\partial \boldsymbol{\sigma}}{\partial \boldsymbol{x}} = 0 \tag{5.2}$$

Then the full stress tensor is:

$$\boldsymbol{\sigma} = \boldsymbol{\sigma^d} - \boldsymbol{I}P \tag{5.3}$$

where $\boldsymbol{\sigma}^d$ is the deviatoric stress tensor, $\mathbf{I}$ the identity matrix and P the isotropic pressure. Then,

$$\boldsymbol{\sigma^d} = 2\eta_{eff}\dot{\boldsymbol{\varepsilon}} \tag{5.4}$$

Due to the small size of the models, we neglect gravity. The temperature is constant in each models, but assigned according to a geothermal gradient to mimic different depths. Effective material viscosity is defined by the typical dislocation creep law as:

$$\eta^v_{eff} = \frac{1}{2}(\dot{\varepsilon}_{II}^{\frac{1}{n}-1} A^{\frac{-1}{n}} exp(\frac{Q}{RT})) \tag{5.5}$$

where A, n and Q are the dislocation creep coefficients commonly obtained by deformation experiments.

Pressure dependent Drucker-Prager (DP) yield criterion is used as a stress limiter

$$\tau_y = P\sin\phi - Co\cos\phi \tag{5.6}$$

using the internal friction angle ϕ, and cohesive strength, Co, as input parameters. If the deviatoric stresses predicted by dislocation creep (Eq. 5.5) exceed the DP yield criterion (Eq. 5.6),

the effective viscosity is re-evaluated as follows:

$$\eta_{eff}^{p} = \frac{\tau_y}{\varepsilon_{II}} \tag{5.7}$$

$$\eta_{eff} = min[\eta_{eff}^{v}, \eta_{eff}^{p}] \tag{5.8}$$

Since models are viscoplastic, the deformation of the bodies is irreversible. Depending upon material properties and P-T-conditions, they deform either in a viscous or in a plastic way, both of which can lead either to localized or distributed deformation. Based on a continuum mechanics approach, when the rocks yield in a brittle way, no discrete frictional interface is developed; instead, faults in the form of shear bands develop, with lower pressure and plastic viscosity and higher strain rate than in the surrounding material. Effective viscosity is calculated for the shear band, based on the shear stresses given by the Drucker-Prager criterion (see eq. 5.6).

5.3.2 Parameterization of pore fluid pressure

Pore fluid pressures act opposite to the direction of the normal stresses exerted on a body and therefore strongly affect the shear stresses upon it. In my models I do not have an explicit formulation for pore fluid pressures; instead the effective pressure, P_{eff}, changes according to the pore fluid ratio, λ, which is defined as:

$$P_{eff} = P(1 - \lambda) \tag{5.9}$$

and λ is igiven by:

$$\lambda = P_f / P_{lith} \tag{5.10}$$

where the subscripts f and $lith$ denote the fluid and lithostatic pressure, respectively. It takes the values of 0 for dry, ~ 0.4 for hydrostatic and 1 for lithostatic conditions.

5.3.3 Parametrization of high stress plasticity

At low temperatures and high stresses, glide assisted dislocation deformation occurs without recovery, referred to as low-temperature plasticity or Peierls mechanism (e.g. Frost and Ashby, 1982; Kameyama et al., 1999). Mechanisms such as Peierls and GBS creep limit rock strength to $400 - 700$ MPa (Kameyama et al., 1999; Precigout et al., 2007; Popov and Sobolev, 2008; Burov, 2011; Watremez et al., 2013) and are only weakly pressure dependent. To avoid unrealistically high stresses in the models, dislocation glide is approximated by von Mises stresses. Consequently, material strength is limited by frictional brittle failure (see Eq. 5.6) up to a maximum constant plastic yield strength (see also "stress limiter" in Van Hunen et al., 2002). In the model domains where this limit is reached, the material is perfectly plastic and shows no localization.

5.3.4 Tests and boundary conditions

Different boundary conditions in simple shear were tested, and the ones that mimic the best simple shear experiments performed on Griggs apparatuses were chosen (see Supplementary Fig. B.1): confining pressure is applied perpendicular to the y-axis on the vertical borders of the model (see Fig. 5.4); at the top and bottom boundaries, horizontal, x-parallel velocities are imposed (v_x), determining the amount of shearing/strain rate the model undergoes, while vertical velocities are forced to be zero at the bottom ($v_y = 0$).

For the sake of simplicity, a geotherm of $10°C/km$ is used, slightly warmer than the one inferred for the Schistes Lustrés ($\sim 8°C/km$; Agard et al. (2001)), or proposed by Gerya et al. (2002) and Syracuse et al. (2010). While the latter numerical models were suspected to underestimate temperatures of exhumed metamorphic rocks for depths <70 km (Penniston-dorland et al., 2015; van Keken et al., 2019), a quite good match with natural data seems in fact to exist for the former, as shown by Agard et al. (2018). Confining pressure is calculated by:

$$P = \rho_m g z, \tag{5.11}$$

where ρ_m is the average density of the rocks from the surface until the depth, z of the particular

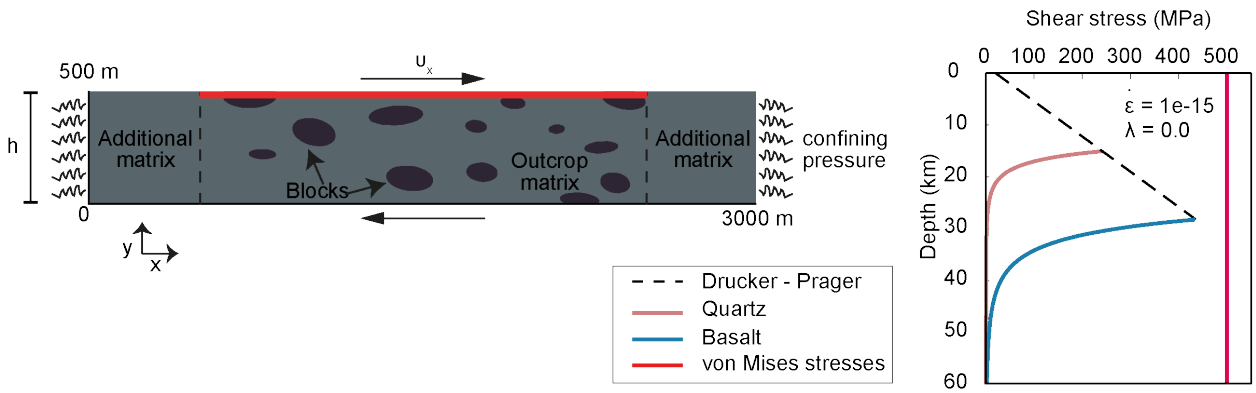

Figure 5.4: Left: Boundary conditions implemented for all model geometries; dark colour is used for the blocks and light for the matrix. The red line at the top of the model denotes the interface values used for computing different rheological parameters. Right: schematic representation of the rheology used in the models.

model, and g is the acceleration of gravity. Finally, different shearing velocities are implemented on the upper and the lower part of the models (see Fig. 5.4) ranging from 10^{-3} cm/year to 10^{3} cm/year.

Additionally, resolution tests for the x- and y-directions were performed, varying them from 60 to 600 and from 10 to 100 Q_2 elements, respectively (see Supplementary Fig. B.2). The preferred resolution was 450x75 Q_2 elements, allowing both for faster calculation times and no loss of information/structures.

As mentioned before, a fractal distribution of the models and their structures is assumed (see Section 5.2.2) in order to upscale the models to km-scales. However, to test this assumption, outcrop-scale models were run (same geometry with 100-times smaller dimensions in $x-$ and $y-$directions). These outcrop-scale models compare well with the larger, km-scale ones; this way, the results are comparable both to field structures as well as large-scale geodynamic models.

5.3.5 Material parameters

Brittle strength in both basalt and quartz in models is described by Byerlee's law: a cohesion of 20 MPa and an initial angle of friction, ϕ, of 30° are considered. I use 500 MPa as the cutoff von Mises stresses, based on the calculations of Kameyama et al. (1999) for the onset of Peierls mechanism in olivine. The von Mises stresses play the role of stress limiter when deviatoric

stresses exceed this pre-described value (see also Section 5.3.3). However, since the effective coefficient of friction in our subduction setup is low due to the presence of water (hydrostatic conditions), the Peierls cutoff stress is almost never reached. Accordingly, to avoid negative tensile stresses, a lower tensile cutoff is imposed at 10 MPa. Thus, no tensile hydrofractures can form, but the domains where they could have occurred can be assessed.

For the viscous deformation of both matrix and blocks, dislocation creep is used, with values for each material given in Table 5.1. Weak wet quartz is chosen as a proxy for the weak sedimentary matrix, which is often quartz- and phyllosilicate-rich in field outcrops. The competent blocks are usually either of continental or oceanic origin; here, I investigate the case in which only oceanic rocks comprise the strong blocks. Therefore, the composition of oceanic crust is assumed to be roughly basaltic, similar to Hacker et al. (2003a), although estimating accurately the bulk composition is more complex (see e.g. Perfit, 2018). Material points contained within the mesh are used to locate regions with different mechanical behaviours.

Table 5.1: Dislocation creep parameters used in this study.

Material	Density (kg/m^3)	A ($MPa^{-n}s^{-1}$)	n	Q (kJ/mol)	V (cm^3)	Reference	Proxy for
Wet quartz	2650	3.2e-4	2.3	154	-	Ranalli, 1997	matrix
Basalt	3000	1.0e-4	3.5	250	-	Shelton & Tullis, 1981 Hacker & Christie, 1990	blocks

5.3.6 Evaluating the degree of localization

To evaluate the degree of localization, the normalized shear strain rate ($\dot{\gamma}_{norm}$) is used. To compute this parameter, first the background strain rate of each model is calculated by dividing the implemented v_x velocity by the width of the model (v_x/h; Fig. 5.4). Then each value of the computed strain rates of a model ($\dot{\gamma}_{comp}$) is divided by the background strain rate ($\dot{\gamma}_{background}$; Eq. 5.12),

$$\dot{\gamma}_{norm} = \frac{\dot{\gamma}_{comp}}{\dot{\gamma}_{background}} \tag{5.12}$$

in order to evaluate the degree of localization in the whole model.

5.4 Results and Discussion

5.4.1 Effect of temperature/depth and strain rate

The primary effect of depth in the models is related to the temperature with increasing depth. In shallow/cold models with $T = 200°C$, both matrix and blocks are brittle (Fig. 5.5), as seen also in the strength envelopes of Figure 5.4. However, at temperatures $\geq 300°$C (models starting from 30 km depth), quartz deforms viscously by dislocation creep, while basalt deformation falls within the brittle regime. In such cases, the co-existence of basalt and quartz can lead to semi-brittle behaviour of the model, characterized by a network of connecting shear bands cutting through both phases (models denoted with *SB* in Figure 5.5). For the same strain rate at different depths (one row in Fig. 5.5), the transition from brittle models (noted as B; uniform localization along the shear band,) to viscous flow (noted as V; heterogeneous localization due to different viscous strengths of the materials) occurs at greater depth/temperatures. If a steady-state convergence rate is assumed, then each row of Figure 5.5 can be considered as the evolution of the models with depth or time. On the other hand, for a constant depth (one column in Fig. 5.5) this transition depends on the strain rates: as the temperature (hence the depth) increases, higher background strain rates are required to shift from the viscous to the (semi-)brittle regime. It is, therefore, evident that the type of failure a model or field outcrop exhibits is a trade-off between temperature and strain rate; other similarly important parameters, not investigated here, include the pore fluid pressures, grain size evolution etc.

5.4.2 Calculating effective parameters of viscosity

For calculating the effective viscosity for each block content, only models for which the bulk deformation is governed by viscous flow can be considered. In the case of homogeneous models (either pure quartz or pure basalt), this is straight-forward, since brittle deformation is obvious: in brittle models a shear band forms in the middle of the domain with an angle of ca. 24° (the small change of the friction angle, with respect to the initial one of 30°, is due to the hydrostatic pore fluid pressure considered).

In two-phase models, however, the characterization of the bulk rheology as brittle or viscous

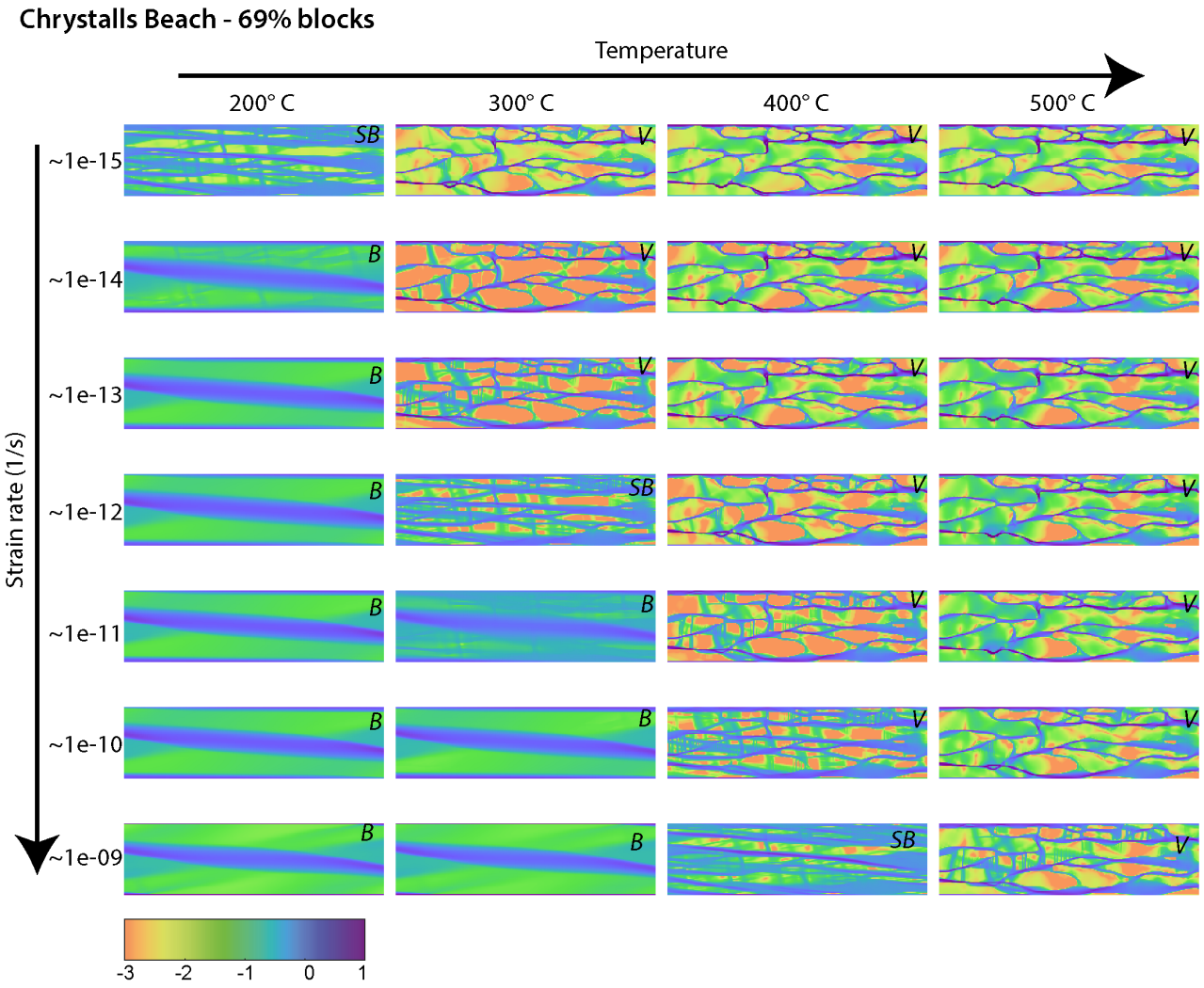

Figure 5.5: Models colour-coded based on their normalized strain rates (in log) for the Chrystalls Beach geometry of 69% blocks. Each row has the same background strain rate, while each column has the same temperature.

is not so obvious, because of the bi-modal deformation observed simultaneously. Therefore, to categorize the bulk deformation of the models as brittle or viscous, the mean value of the second invariant of the normal stress vs. the second invariant of the shear stress is plotted (τ_{II} vs. σ_{II}), which gives the Mohr-Coulomb yield criterion. All frictional models plot along the same line (yield line), whereas all non-frictional models lie below this line Fig. 5.4.2.

In order to estimate the effective viscosity of the two-phase geometries, the effective parameters (n, Q, pre-exponential term A) are computed for all models plotting below the frictional yield line. Details on how these parameters are calculated are given in B.3.

Figure 5.7 shows the effective parameters calculated for a range of depths, from 30 to 60 km,

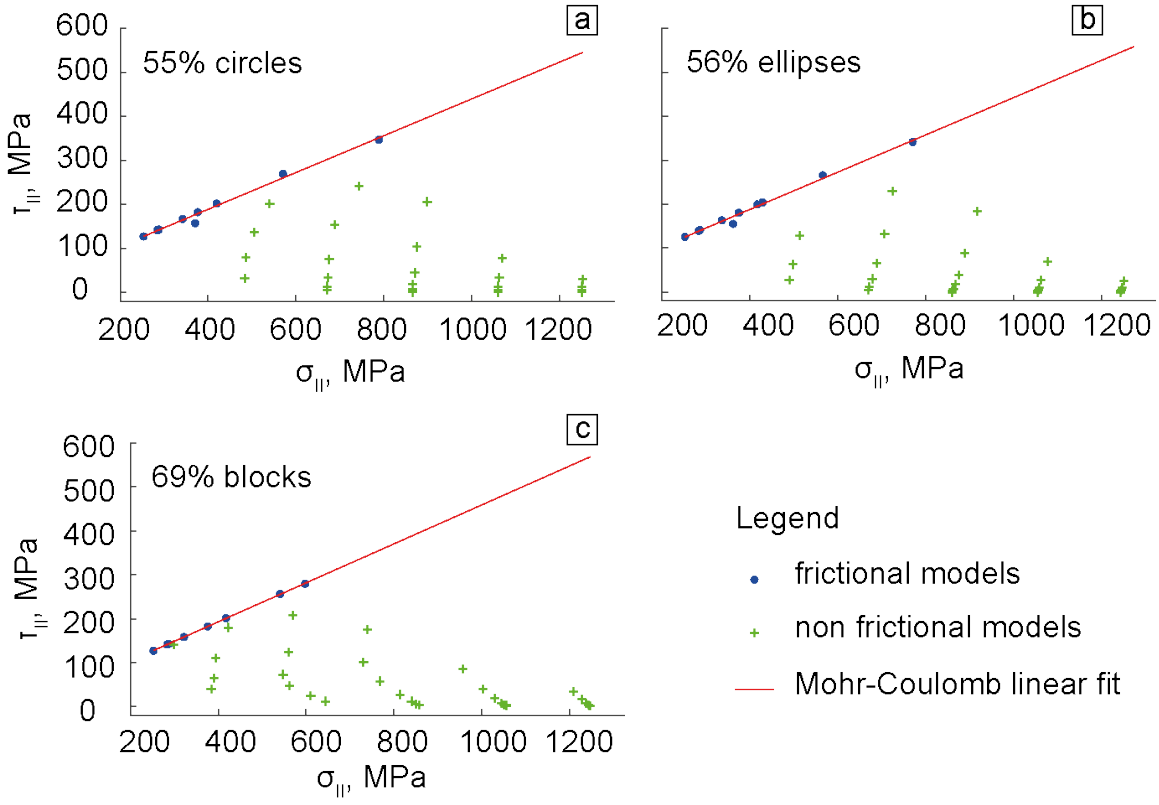

Figure 5.6: Mohr-Coulomb failure criterion (red straight line) for different block shapes in high block percentage models. Green crosses denote all non-frictional models used for deducing effective creep parameters; blue circles are frictional models used for calculating the effective coefficient of friction.

and for the different percentages of blocks for all three sets of models (from left to right for circular, elliptical and natural blocks). Both the percentage of the blocks and the temperature exert a major control on the effective dislocation creep parameters (Fig. 5.7a-c, Fig. 5.7e-g and Fig. 5.7i-k) and hence the viscosity (Fig. 5.7d,h,l).

The effect of depth reflects the influence of temperature on the type of failure: at 30 km, basalt is brittle within an already viscously deforming matrix (from now on mentioned as "semi-brittle" behaviour, denoted as *SB* in models in Fig. 5.5). The values of the effective dislocation creep parameters decrease with increasing temperature, marking the transition of basalt from brittle to viscous. However, such a behaviour in the models is only evident for a percentage of the strong phase $\geq 40\%$, where the existence of a load-bearing framework controls the bulk viscosity of the mélange (see also Handy, 1990). This is observed for all shapes of blocks tested, whether circles, ellipses or natural ones.

At temperatures where both phases are viscous (500° and 600°C), the effective creep parameters

fall within the rage of initial values. For example, n lies between 2.3 and 3.5, showing an increase with increasing percentage of the strong phase. Interestingly, the value of n is larger as we go from circular to elliptical and natural blocks. This might be the result of the increasing anisotropy of the blocks' shapes, from circles (with aspect ratio, AR, of 1) to ellipses (AR between 1.5 and 3) and finally to natural blocks (AR between 2 and 8). Increasing anisotropy indeed means larger stress concentrations due to geometrical effects, hence an increase in the stress exponent, n.

However, for $> 30\%$ of strong blocks and cold temperatures (300°-400°C), where basalt is still frictional, n can reach higher values than the one of the purely strong phase (Fig. 5.7a,e,i). It has been suggested that frictional and linear viscous deformation are functionally end-members of the power-law case, the former being characterized by $1/n \rightarrow \infty$, the latter by $1/n \rightarrow 1$ (Montési, 2004). Moreover, the modified Omori law for the decay of aftershocks can be derived either from the Dietrich-Ruina rate-and-state friction (Ruina, 1983; Guillet and Guillet, 2004; Dieterich, 1994; Savage, 2007; Perfettini and Avouac, 2004; Langbein et al., 2006), or from the equations of ductile flow (Montési, 2004). In the presented models, with increasing contribution of frictional deformation in the bulk rheology, the value of n also increases. This large contribution of frictional stresses is seen in all three shapes of blocks, from circular to natural, with values of n increasing with anisotropy/aspect ratio. The higher stress exponents of the cold, block-dominated models are interpreted to reflect the effect of this high degree of frictional localization within the fault/mélange zone (see also Fig. 5.8).

5.4.3 General mixing models and bound theory

Mixing models for estimating the elastic properties of single-phase polycrystalline materials have been developed based on the assumption of either uniform strain rate or uniform stress. The former gives the iso-strain upper or Voigt bound (Voigt, 1928), whereas the latter gives the lower or Reuss bound (Reuss, 1929). In analogy to the behaviour of linear elastic aggregates (e.g. Hashin, 1963), the viscous parameters (n, Q and A) of a two-phase aggregate can be given by an upper bound during uniform strain rate experiments and by a lower bound during uniform stress experiments. They depend on the volume fraction of the weak and strong phase of the aggregate and it has been shown that although they represent unrealistic cases, they can

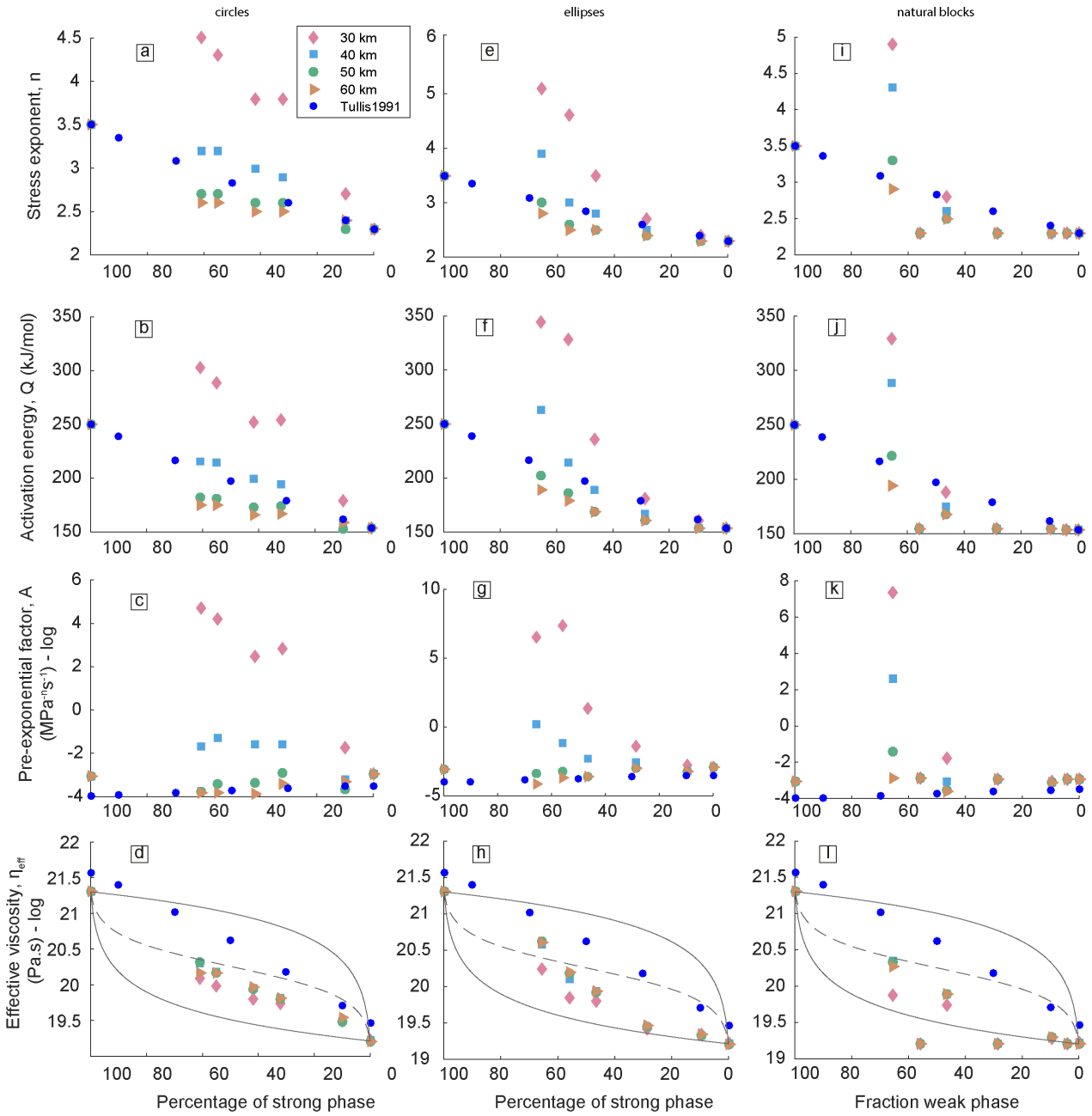

Figure 5.7: Summary of effective creep parameters. X-axis: percentage of strong phase; Y-axis: Calculated effective parameters n, Q, A and viscosity, η from top to bottom, for circular (a-d), elliptical (e-h) and natural (i-l) models.

be regarded as upper and lower bounds for the linear elastic situation (Hill, 1965).

Tullis et al. (1991) followed a numerical approach for an aggregate of monomineralic pyroxene and plagioclase, both of which exhibited power law rheology. Based on the volume-weighted geometric mean of the end-members, the authors proposed simple expressions for calculating the effective rheological parameters (stress exponent, n_a, activation energy, Q_a and pre-exponential

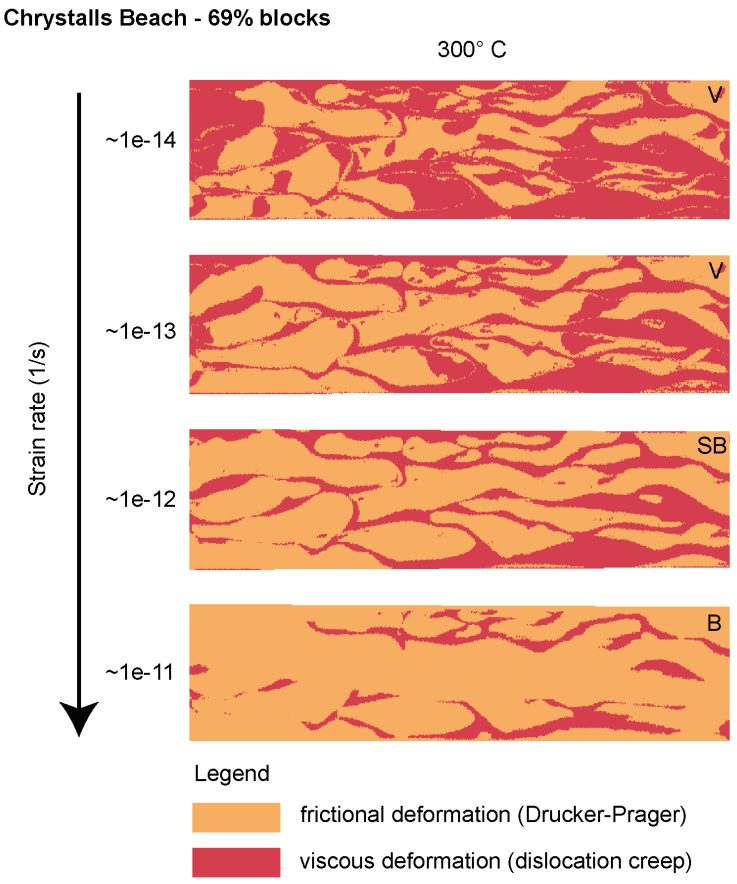

Figure 5.8: Type of yielding for the Chrystalls Beach models, at 300°C and for different strain rates. Note the increasing contribution of frictional deformation as strain rates increase.

term, A) for an aggregate, a of any material containing two or more phases:

$$n_a = 10^{(f_1 \log n_1 + f_2 \log n_2)} \tag{5.13}$$

$$Q_a = \frac{Q_2(n_a - n_1) - Q_1(n_a - n_2)}{n_2 - n_1} \tag{5.14}$$

$$A_a = 10^{[\log A_2(n_2 - n_1) - \log A_1(n_a - n_2)]/[n_2 - n_1]} \tag{5.15}$$

where the subscripts 1 and 2 are the fractions of the two phases. The bulk parameters calculated with this approach using the values in Table 5.1 for basalt and quartz, are shown in blue full circles in Figure 5.7.

Further generalization of the bound theories of Voigt and Reuss, led Ji et al. (2004) to derive a

phenomenological formula, called general mixture rule (GMR), which is appropriate to describe bulk mechanical properties (including viscosity) of various isotropic polyphase rocks. Their GMR is given by:

$$M_C^J = \sum_{i=1}^{N} (V_i M_i^J), \tag{5.16}$$

where M is the mechanical property of interest (e.g. the viscosity), V is the volume fraction of each phase and c and i represent the i-th phase and a composite (c) consisting of N phases. J is a microstructural or scaling parameter taking values between -1 and 1, with $J = 1$ representing the Voigt bound and $J = -1$ representing the Reuss bound. For the experimentally derived ductile flow strength of nonporous two-phase aggregates, values of $J = -0.25$ corresponds to the end-member case where the weak phase forms a continuous stress-supported structure; on the other hand, $J = 0.25$ corresponds to the end-member case where the strong phase is the continuously stress-supported structure. In both cases, the shape of the inclusions is somewhat random and the volume percentage of the strong phase is between 40% and 70% (Ji et al., 2004).

Another theoretical mixing rule for estimating the bulk rheology of a multi-phase aggregate deforming viscously was given by Huet et al. (2014). Their models are based on geometric averaging and the bulk creep parameters, as well as the calculated viscosities provide a good fit with two-phase experimental data. The differences to the work presented here are: 1) the assumption of a homogeneous, isotropic distribution of the two phases and the absence of (shape- or crystallograpic-)preferred orientation; and 2) the absence of a brittle failure mechanism, which is considered to play an important role in the large increase of the creep parameter values in the present models.

5.4.4 Limitations - Effect of flow law

In the present work, dislocation creep is considered as the only viscous deformation mechanism of both the matrix and the blocks. To the best of the my knowledge, diffusion creep has not been reported for basalt, hence this assumption is consider realistic. For the case of quartz, though, field observations of subduction mélange units show that at shallow depths (up to 20-30 km), viscous deformation is taken up mostly by solution-precipitation creep (e.g., Stöckhert,

2002; Bachmann et al., 2009b; Fagereng and Cooper, 2010; Gratier et al., 2013; Wassmann and Stöckhert, 2013b; Fagereng and Den Hartog, 2017). The detailed processes of this deformation mechanism are up to now not well constrained (see also Wallace et al., 2012). Since dislocation creep is a mechanism that is active at higher stresses, these models can be considered as calculating an upper limit for the stresses (Stöckhert, 2002), or alternatively, the minimum depth at which our given viscosity estimates are expected for a specific strain rate. In addition, the uncertainties of the extrapolation of experimental flow laws as well as the elusive physical meaning of the pre-exponential factor, A and the activation energy also pose limitations to the interpretation of the models (see also discussion in Platt, 2015).

Furthermore, modelling the mélange matrix as a monomineralic body consisting of only wet quartz is a simplification. If the matrix is a composite of e.g quartz, feldspar and/or micas, the bulk flow strength of the matrix will be underestimated by the present approach (see also Ji et al., 2000). It is evident that the creep parameters of each rock play a significant role in the deformation regimes, since each combination of A, n and Q gives significantly different results. However, the specific flow laws are chosen based on the general behaviour of basalt and quartz, as commonly observed in nature: quartz becomes viscous at shallower depths, or colder temperatures, than basalt (ca. 300°C and ca. 450°C, respectively).

Finally, the initial conditions of the model, such as the geotherm, the confining pressure and extrapolation of viscous creep parameters are also assumptions/generalizations. This extrapolation, though, of the creep parameters from experimental data to natural conditions is valid as long as the deformation mechanisms acting at both scales are similar (Dimanov and Dresen, 2005).

5.4.5 Comparison to other studies

The present approach resembles the one undertaken by Tullis et al. (1991), in which they modelled the bulk rheology of two materials deforming by dislocation creep (see Eqs. 5.13 - 5.15 and the resulting blue circles in Figure 5.7). The discrepancy between their study and the present estimates lies in the fact that their models do not include any pressure dependent failure mechanism, such as the Drucker Prager, which leads to values of n higher than the initial ones.

In a more recent study that dealt also with bulk rheology of a subduction mélange, Beall et al. (2019) concluded that deformation within a mélange unit is governed by that of the weak matrix in cases where clasts constitute $< 50\%$ of the total volume; for higher concentrations of the strong phase, viscosity can increase up to more than 10 times due to clast interactions. The purely viscous models of this study agree with these observations, except that the threshold seems to be somewhat higher ($\sim$55-60%; Fig. 5.7). Importantly, their models have constant stress boundary conditions (instead of our kinematic conditions) and a substantially different implementation of the viscosity (viscosity ratios instead of a flow law). This agreement outlines the fact that effective rheology averaging is not affected by boundary conditions: it is comparable whether estimated under constant simple shear kinematic conditions (this study), or constant stress conditions (Beall et al., 2019).

However, in the semi-brittle models (those calculated for 300° and 400°C), a different bulk behaviour emerges and this affects the estimates for the bulk viscosity of this study. Computed effective n values become greater than the largest input value of 3.5 (used for basalt); as already mentioned, this increase of nonlinearity reflects the increasing contribution of frictional strain rates/deformation.

Mixing rules have been applied to several experimental studies in the dislocation creep regime. For instance, Dimanov and Dresen (2005) experimentally studied the bulk rheology of a two-phase mixture of anorthite-diopside (in which the latter constitutes the strong phase). They found that different viscous mechanisms participate in the deformation of the aggregate, depending on values of the stresses. At low stresses, microstructures suggest load transfer from a weak anorthite matrix to stronger diopside particles; at higher stresses, where dislocation creep is active, the stress sensitivity, n, of the aggregate lies between that calculated for the pure phases, the values of which are mainly controlled by the diopside content. Similarly, creep activation energies of the composite are within the range of, and close to, those for the pure end-members.

5.5 Conclusions and implications for subduction interface rheology

This study investigates the effective rheology and type of deformation in subduction mélanges, with respect to the concentration of strong blocks. A dependency of deformation and strain localization upon the block-in-matrix ratio is reported: in models dominated by the weak phase, the effective stress exponent, n, is similar to that of the purely weak phase ($n = 2.3$); when blocks constitute more than 50% of the total area, n exhibits a gradual increase towards the value of the n for the strong phase ($n = 3.5$). However, at moderate depths ($30 - 40$ km) where basalt is brittle and sediment (quartz) is ductile, although the bulk deformation of the model exhibits power-law rheology (dislocation creep), the bulk type of failure is semi-brittle. This is reflected upon the n, which exhibits even larger values than in the strong phase, and in the consequent increase of the effective viscosity. With increasing strain rates, the depth of the brittle-ductile-transition increases, allowing brittle failure to localize where viscous creep should be expected. However, utilizing dislocation creep for viscous deformation of blocks and matrix suggests that the results can be considered as reflecting the maximum viscous strength of the bulk model.

Since models are scale independent, the results can be applied from grain to map scales. This renders the effective rheology calculations of subduction mélanges suitable for use in larger-scale geodynamic models; in particular, in some conditions, considering a larger n may be important. Moreover, the reported brittle-ductile behaviour of the high block-concentration models can potentially contribute to understanding mechanical aspects of episodic tremor and slip (ETS; Rogers and Dragert, 2003). For example, Hayman and Lavier (2014) suggested that episodic fracture and viscous creep of strong blocks within weak viscously deforming rocks can cause tremor and slow slip. A mélange occurring along a plate interface might record diverse types of seismic slip along the interface, such as aftershocks or VLFs (Kimura et al., 2012), while matrix dominated mélanges tend to diffuse strain and accommodate it in a steadily creeping way (Fagereng and Cooper, 2010).

Finally, the most important aspect in the bulk rheology of a two-phase aggregate is not the

unilateral effect of each of the aforementioned parameters, but rather the interplay between them. The same deformation pattern can be observed for a combination of conditions, e.g., higher pore fluid pressure and slower strain rates. It is, therefore, crucial to assess the combined effect of the studied parameters on the deformation of rocks.

Chapter 6

Conclusions and Outlook

Note

This chapter contains results from Chapters 3, 4, and 5, in relation to the research aims highlighted in Chapter 1.6.

6.1 Re-cap of aims and objectives

In Chapter 1, the reasons for addressing the following research questions were presented in detail, along three main lines:

- What are the characteristic deformation mechanisms, along a subduction interface, as these are reported at exhumed suture zones? Can these mechanisms be connected with seismic and aseismic slip patterns remotely recorded along active subduction zones? How is the rheology of a subduction interface commonly simulated in geodynamic models?
- What is the characteristic deformation along the subduction interface during subduction of continental slivers and what is its timing? Can deformation fabrics and their timing elucidate active deformation conditions of the transition zone, at the downdip end of the seismogenic zone?
- What is the effective rheology of a subduction interface, in the special case that it is not a homogeneous medium, but rather characterized by a block-in-matrix geometry? How

does the concentration of blocks affect the bulk deformation of the mélange? Can the effective rheology of a mixed material reflect small-scale complexities, rendering it thus useful for implementation in large-scale geodynamic models?

The following section summarizes the findings of this work, with respect to these questions.

6.2 Conclusions

The main messages of the thesis can be summed up in the following list:

- The dominant viscous deformation mechanisms observed at exhumed rocks deformed along the subduction interface are dissolution-precipitation creep and, to a lesser extent, dislocation creep. From the rock record it is evident that there exists a rheological segmentation along the interface.

- A continuous spectrum from aseismic to seismic slip along the subduction interface has emerged from far-field records, which coincides, spatially, with the geological record of deformation patterns.

- Field studies point to a close relationship between fabrics on exhumed rocks and remotely recorded kinematic deformation along active subduction zones. Switches of brittle and ductile deformation, slip partitioning between blocks and matrix, and rheological contrasts have been invoked for explaining these transient slip events.

- Although dissolution-precipitation creep is the dominant mechanism and, together with frictional sliding, it could potentially explain part of the transients recorded in active subduction zones, it is not commonly implemented in numerical studies, largely due to resolution limitations.

- The first case study, in Val Malenco, confirms the deformation mechanisms expected: field and petrological observations on the continental, Lower Austroalpine units indicate that, during their subduction and consequent underplating, they deformed predominantly in a ductile way. Pressure-solution and locally semi-brittle and brittle networks are widespread.

- Rb/Sr geochronology on mica-rich metasediments metamorphosed during Alpine convergence yields a robust age of deformation and (re)crystallization of 48.9 ± 0.9 Ma. However, Rb/Sr and $^{40}Ar/^{39}Ar$ dating of Alpine, seemingly recrystallized white micas yielded mixed ages of deformation, due to partial resetting of the isotopic signature of the system.

- Presented P-T-t data, along with recent studies (Droop and Chavrit, 2014; Picazo et al., 2019), point to continuous subduction and underplating processes along the active subduction interface during the geodynamic evolution of the Central Alps. The Val Malenco area sheds light onto a region below the seismogenic depths exposed in Arosa - St. Moritz and displays subduction-related deformation at a depth range in the transition zone, which is globally found to host both slow creep, as well as more rapid silent slip events.

- In the second case study, deformation and strain localization in two-phase media (mélanges) depend on the block-in-matrix ratios. For matrix dominated assemblages, the bulk rheology is similar to that of the purely weak phase; however, when blocks constitute more than 50% of the total area, viscosity increases due to clast interactions.

- At depths where basalt is brittle and quartz is ductile ($30 - 40$ km), the bulk rheology of the model follows a dislocation creep law; however, the bulk type of failure is semi-brittle, as attested by the large values of the stress exponent, n (even larger values than in the strong phase), and by the consequent increase of the effective viscosity.

- The use of dislocation creep for viscous deformation of blocks and matrix suggests that presented results should be considered as reflecting the maximum viscous strength of the bulk model. Scale-independency of the models renders the effective rheology calculations of subduction mélanges suitable for use in larger-scale geodynamic models. The reported brittle-ductile behaviour of high block-concentration models can potentially contribute to understanding mechanical aspects of episodic tremor and slip (ETS), as the latter are partially caused by brittle-viscous switches in their deformation mode.

6.3 Future Work

This study demonstrated that constraining the rheological parameters of polyphase rocks or polyphase aggregates (such as mélanges) is important for understanding the deformation of the Earth's lithosphere. Numerical models provide a good link between the deformation occurring on Earth (long term, large scale) and the deformation documented in laboratory experiments (short term, small scale). However, research has mainly focused on properties of monomineralic, homogeneous rocks and their deformation. A future goal is to link numerical simulations to experimental deformation of polyphase rock aggregates via mathematical/scaling relationships and provide an effective rheology for large-scale models, able to encompass, indirectly, some of the complexity we observe in nature. One way to do that is by studying the rheology of experimentally deformed polyphase rock aggregates (e.g., quartz-feldspar or quartz-basalt) and deriving empirical mixing flow laws and numerically testing the rheology of the above mixing flow laws. First in the small scales for which these parameters were deduced and then extrapolating, numerically and mathematically, to geologically significant lengths and time-scales. This would enable upscaling the effective viscosity of complex (two-phase) media for use in lithospheric scale numerical simulations.

Bibliography

P. Agard, O. Vidal, and B. Goffé. Interlayer and Si content of phengites in high-pressure carpholite-bearing metapelites. *Journal of Metamorphic Geology*, 19:479–495, 2001.

P. Agard, P. Monié, L. Jolivet, and B. Goffé. Exhumation of the Schistes Lustrés complex: in situ laser probe 40Ar/39Ar constraints and implications for the Western Alps. *Journal of Metamorphic Geology*, 20(6):599–618, 2002. doi: 10.1046/j.1525-1314.2002.00391.x.

P. Agard, P. Yamato, L. Jolivet, and E. Burov. Exhumation of oceanic blueschists and eclogites in subduction zones: Timing and mechanisms, 2009.

P. Agard, P. Yamato, M. Soret, C. Prigent, S. Guillot, A. Plunder, B. Dubacq, A. Chauvet, and P. Monié. Plate interface rheological switches during subduction infancy: Control on slab penetration and metamorphic sole formation. *Earth and Planetary Science Letters*, 451: 208–220, 2016. doi: 10.1016/j.epsl.2016.06.054.

P. Agard, A. Plunder, S. Angiboust, G. Bonnet, and J. Ruh. The subduction plate interface: rock record and mechanical coupling (from long to short timescales). *Lithos*, 320-321:537–566, 2018. doi: 10.1016/j.lithos.2018.09.029.

I. Allison, R. L. Barnett, and R. Kerrich. Superplastic flow and changes in crystal chemistry of feldspars. *Tectonophysics*, 53(1-2), 1979. doi: 10.1016/0040-1951(79)90351-2.

R. W. Allmendinger and T. Gubbels. Pure and simple shear plateau uplift, Altiplano-Puna, Argentina and Bolivia. *Tectonophysics*, 1996. doi: 10.1016/0040-1951(96)00024-8.

R. W. Allmendinger, T. E. Jordan, S. M. Kay, and B. L. Isacks. the Evolution of the Altiplano-Puna Plateau of the Central Andes. *Annual Review of Earth and Planetary Sciences*, 25(1): 139–174, 1997. doi: 10.1146/annurev.earth.25.1.139.

R. Ando, R. Nakata, and T. Hori. A slip pulse model with fault heterogeneity for low-frequency earthquakes and tremor along plate interfaces. *Geophysical Research Letters*, 37(10), 2010. doi: 10.1029/2010GL043056.

S. Angiboust, P. Agard, H. Raimbourg, P. Yamato, and B. Huet. Subduction interface processes recorded by eclogite-facies shear zones (Monviso, W. Alps). *Lithos*, 127(1-2):222–238, 2011. doi: 10.1016/j.lithos.2011.09.004.

S. Angiboust, S. Wolf, P. Agard, E. Burov, and P. Yamato. Effect of fluid release on intermediate depth subduction processes : Insights from fully-coupled numerical modelling. *Earth and Planetary Science Letters*, 14:4826, 2012.

S. Angiboust, J. Glodny, O. Oncken, and C. Chopin. In search of transient subduction interfaces in the Dent Blanche-sesia tectonic system (W. Alps). *Lithos*, 205:298–321, 2014. doi: 10.1016/j.lithos.2014.07.001.

S. Angiboust, J. Kirsch, O. Oncken, J. Glodny, P. Monié, and E. Rybacki. Probing the transition between seismically coupled and decoupled segments along an ancient subduction interface. *Geochemistry, Geophysics, Geosystems*, 16(6):1905–1922, 2015. doi: 10.1002/2015GC005776.

M. F. Ashby and C. G. Sammis. The damage mechanics of brittle solids in compression. *Pure and Applied Geophysics PAGEOPH*, 133(3):489–521, 1990. doi: 10.1007/BF00878002.

P. Audet and Y. H. Kim. Teleseismic constraints on the geological environment of deep episodic slow earthquakes in subduction zone forearcs: A review. *Tectonophysics*, 670:1–15, 2016. doi: 10.1016/j.tecto.2016.01.005.

P. Audet and A. J. Schaeffer. Fluid pressure and shear zone development over the locked to slow slip region in Cascadia. *Science Advances*, 4(3):1–7, 2018. doi: 10.1126/sciadv.aar2982.

P. Audet, M. G. Bostock, N. I. Christensen, and S. M. Peacock. Seismic evidence for overpressured subducted oceanic crust and megathrust fault sealing. *Nature*, 457:76–78, 2009. doi: 10.1038/nature07650.

H. Austrheim and T. B. Andersen. Pseudotachylytes from Corsica: Fossil earthquakes from a

subduction complex. *Terra Nova*, 16(4):193–197, 2004. doi: 10.1111/j.1365-3121.2004.00551.x.

A. Y. Babeyko and S. V. Sobolev. High-resolution numerical modeling of stress distribution in visco-elasto-plastic subducting slabs. *LITHOS*, 103(1-2):205–216, 2008. doi: 10.1016/j.lithos.2007.09.015.

J. Babist, M. R. Handy, M. Konrad-Schmolke, and K. Hammerschmidt. Precollisional, multistage exhumation of subducted continental crust: The Sesia Zone, western Alps. *Tectonics*, 25(6):1–25, 2006. doi: 10.1029/2005TC001927.

R. Bachmann, J. Glodny, O. Oncken, and W. Seifert. Abandonment of the South Penninic-Austroalpine palaeosubduction zone, Central Alps, and shift from subduction erosion to accretion: constraints from Rb/Sr geochronology. *Journal of the Geological Society, London*, 166(2):217–231, 2009a. doi: 10.1144/0016-76492008-024.

R. Bachmann, O. Oncken, J. Glodny, W. Seifert, V. Georgieva, and M. Sudo. Exposed plate interface in the European Alps reveals fabric styles and gradients related to an ancient seismogenic coupling zone. *Journal of Geophysical Research: Solid Earth*, 114(5):1–23, 2009b. doi: 10.1029/2008JB005927.

E. H. Bailey, W. P. Irwin, and D. L. Jones. Franciscan and related rocks and their significance in the geology of western California. *California Division of Mines and Geology Bulletin*, page 177, 1964.

J. B. Barnes and T. A. Ehlers. End member models for Andean Plateau uplift, 2009.

A. Barnhoorn, M. Bystricky, L. Burlini, and K. Kunze. The role of recrystallisation on the deformation behaviour of calcite rocks: Large strain torsion experiments on Carrara marble. *Journal of Structural Geology*, 26(5):885–903, 2004. doi: 10.1016/j.jsg.2003.11.024.

P. Baud and P. G. Meredith. Damage accumulation during triaxial creep of Darley Dale sandstone from pore volumometry and acoustic emission. *International journal of rock mechanics and mining sciences & geomechanics abstracts*, 34(3-4):371, 1997. doi: 10.1016/S1365-1609(97)00060-9.

A. Beall, Å. Fagereng, and S. Ellis. Strength of Strained Two-Phase Mixtures: Application to Rapid Creep and Stress Amplification in Subduction Zone Mélange. *Geophysical Research Letters*, 46(1):169–178, 2019. doi: 10.1029/2018GL081252.

G. E. Bebout and S. C. Penniston-Dorland. Fluid and mass transfer at subduction interfaces-The field metamorphic record. *Lithos*, 240-243:228–258, 2016. doi: 10.1016/J.LITHOS.2015.10.007.

H. Becker. Garnet peridotite and eclogite Sm-Nd mineral ages from the Lepontine dome (Swiss Alps): new evidence for Eocene high-pressure metamorphism in the central Alps. *Geology*, 21(7):599–602, 1993. doi: 10.1130/0091-7613(1993)021<0599:GPAESN>2.3.CO;2.

J. Bedford, M. Moreno, J. C. Baez, D. Lange, F. Tilmann, M. Rosenau, O. Heidbach, O. Oncken, M. Bartsch, A. Rietbrock, A. Tassara, M. Bevis, and C. Vigny. A high-resolution, time-variable afterslip model for the 2010 Maule Mw = 8.8, Chile megathrust earthquake. *Earth and Planetary Science Letters*, 383:26–36, 2013. doi: 10.1016/j.epsl.2013.09.020.

W. M. Behr and J. P. Platt. A naturally constrained stress profile through the middle crust in an extensional terrane. *Earth and Planetary Science Letters*, 303(3-4):181–192, 2011. doi: 10.1016/j.epsl.2010.11.044.

W. M. Behr, A. J. Kotowski, and K. T. Ashley. Dehydration-induced rheological heterogeneity and the deep tremor source in warm subduction zones. *Geology*, 46(5):475–478, 2018. doi: 10.1130/G40105.1.

J. H. Behrmann. Microstructure and fabric transitions in calcite tectonites from the Sierra Alhamilla (Spain). *Geologische Rundschau*, 72(2):605–618, 1983. doi: 10.1007/BF01822084.

B. Bekins, A. M. McCaffrey, and S. J. Dreiss. Influence of kinetics on the smectite to illite transition in the Barbados accretionary prism. *Journal of Geophysical Research*, 99(B9), 1994. doi: 10.1029/94jb01187.

M. Beltrando, R. Compagnoni, and B. Lombardo. (Ultra-) High-pressure metamorphism and orogenesis: An Alpine perspective. *Gondwana Research*, 18(1):147–166, 2010. doi: 10.1016/j.gr.2010.01.009.

M. Bernaudin and F. Gueydan. Episodic Tremor and Slip Explained by Fluid-Enhanced Microfracturing and Sealing. *Geophysical Research Letters*, 45(8):3471–3480, 2018. doi: 10.1029/2018GL077586.

C. M. Bethke. Inverse hydrologic analysis of the distribution and origin of Gulf Coast-type geopressured zones. *Journal of Geophysical Research*, 91(B6):6535, 1986. doi: 10.1029/jb091ib06p06535.

O. Beyssac, B. Goffé, C. Chopin, and J. N. Rouzaud. Raman spectra of carbonaceous material in metasediments: A new geothermometer. *Journal of Metamorphic Geology*, 20(9):859–871, 2002. doi: 10.1046/j.1525-1314.2002.00408.x.

R. W. Bialas, F. Funiciello, and C. Faccenna. Subduction and exhumation of continental crust: Insights from laboratory models. *Geophysical Journal International*, 184(1):43–64, 2011. doi: 10.1111/j.1365-246X.2010.04824.x.

P. Bird. Stress and temperature in subduction shear zones: Tonga and Mariana. *Geophysical Journal of the Royal Astronomical Society*, 55(2):411–434, 1978. doi: 10.1111/j.1365-246X.1978.tb04280.x.

T. Bissig and J. Hermann. From pre-Alpine extension to Alpine convergence: The example of the southwestern margin of the Margna nappe (Val Malenco, N-Italy). *Schweizerische Mineralogische und Petrographische Mitteilungen*, 79(3):363–380, 1999.

M. Bjørnerud. Rethinking conditions necessary for pseudotachylyte formation: Observations from the Otago schists, South Island, New Zealand. *Tectonophysics*, 490(1-2):69–80, 2010. doi: 10.1016/j.tecto.2010.04.028.

M. C. Blake and D. L. Jones. Origin of Franciscan Melanges in Northern California. *Modern and Ancient Geosynclinal Sedimentation*, pages 345–357, 1974. doi: 10.2110/pec.74.19.0345.

A. Boullier and Y. Gueguen. Peridotite mylonite produced by superplastic flow. *Fault related rocks-a photographic atlas. Princeton Unversity Press, New Jersey*, pages 592–593, 1998.

A. M. Boullier and Y. Gueguen. SP-Mylonites: Origin of some mylonites by superplastic flow. *Contributions to Mineralogy and Petrology*, 50(2):93–104, 1975. doi: 10.1007/BF00373329.

N. Brantut, P. Baud, M. J. Heap, and P. G. Meredith. Micromechanics of brittle creep in rocks. *Journal of Geophysical Research: Solid Earth*, 117(8):1–12, 2012. doi: 10.1029/2012JB009299.

K. S. Broadwell, M. Locatelli, A. Verlaguet, P. Agard, and M. J. Caddick. Transient and periodic brittle deformation of eclogites during intermediate-depth subduction. *Earth and Planetary Science Letters*, 521:91–102, 2019. doi: 10.1016/j.epsl.2019.06.008.

C. H. Bruce. Smectite dehydration-its relation to structural development and hydrocarbon accumulation in Northern Gulf of Mexico Basin. *Bulletin of the American Association of Petroleum Geologists*, 68(6):673–683, 1984. doi: 10.1306/ad461363-16f7-11d7-8645000102c1865d.

R. Bürgmann and G. Dresen. Rheology of the Lower Crust and Upper Mantle: Evidence from Rock Mechanics, Geodesy, and Field Observations. *Annual Review of Earth and Planetary Sciences*, 36(1):531–567, 2008. doi: 10.1146/annurev.earth.36.031207.124326.

E. B. Burov. Rheology and strength of the lithosphere. *Marine and Petroleum Geology*, 28(8):1402–1443, 2011. doi: 10.1016/j.marpetgeo.2011.05.008.

M. Cannat. Thin crust, ultramafic exposures, and rugged faulting patterns at the Mid-Atlantic Ridge (22°-24°N). *Geology*, 23(1):49–52, 1995. doi: 10.1130/0091-7613(1995)023<0049:TCUEAR>2.3.CO;2.

B. Carrapa, J. D. Trimble, and D. F. Stockli. Patterns and timing of exhumation and deformation in the Eastern Cordillera of NW Argentina revealed by (U-Th)/He thermochronology. *Tectonics*, 30(3):n/a–n/a, 2011. doi: 10.1029/2010tc002707.

N. L. Carter, D. A. Anderson, F. D. Hansen, and R. L. Kranz. *Creep and Creep Rupture of Granitic Rocks*, pages 61–82. American Geophysical Union (AGU), 1981. ISBN 9781118663806. doi: 10.1029/GM024p0061.

C. Chopin. Coesite and pure pyrope in high-grade blueschists of the Western Alps: a first record and some consequences. *Contributions to Mineralogy and Petrology*, 86(2):107–118, 1984. doi: 10.1007/BF00381838.

C. Chopin. Ultrahigh-pressure metamorphism: Tracing continental crust into the mantle. *Earth and Planetary Science Letters*, 212(1-2):1–14, 2003. doi: 10.1016/S0012-821X(03)00261-9.

R. A. Cliff and S. Meffan-Main. Evidence from Rb-Sr microsampling geochronology for the timing of Alpine deformation in the Sonnblick Dome, SE Tauern Window, Austria. *Geological Society, London, Special Publications*, 220(1):159–172, 2003. doi: 10.1144/GSL.SP.2003.220.01.09.

M. Cloos. Flow mélanges: Numerical modeling and geologic constraints on their origin in the Franciscan subduction complex, California: Reply. *Bulletin of the Geological Society of America*, 94(10):1243–1244, 1983. doi: 10.1130/0016-7606(1983)94<1243:FMNMAG>2.0.CO;2.

R. L. Coble. A Model for Boundary Diffusion Controlled Creep in Polycrystalline Materials. *Journal of Applied Physics*, 34(6):1679–1682, 1963. doi: 10.1063/1.1702656.

S. C. Cohen. Numerical Models of Crustal Deformation in Seismic Zones. *Advances in Geophysics*, 41(C):133–231, 1999. doi: 10.1016/S0065-2687(08)60027-8.

R. G. Coleman and X. Wang. Overview of the geology and tectonics of UHPM. In *Ultrahigh Pressure Metamorphism*, pages 1–32. 1995. doi: 10.1017/cbo9780511573088.002.

R. Compagnoni, G. V. Dal Piaz, J. C. Hunziker, G. Gosso, B. Lombardo, and P. F. Williams. The Sesia-Lanzo zone, a slice of continental crust with alpine high pressure-low temperature assemblages in the Western Italian Alps. *Rendiconti Società Italiana di Mineralogia e Petrologia*, 33(I):281–334, 1977.

J. A. Connolly. Computation of phase equilibria by linear programming: A tool for geodynamic modeling and its application to subduction zone decarbonation. *Earth and Planetary Science Letters*, 236(1-2):524–541, 2005. doi: 10.1016/j.epsl.2005.04.033.

C. P. Conrad, S. Bilek, and C. Lithgow-Bertelloni. Great earthquakes and slab pull: Interaction between seismic coupling and plate-slab coupling. *Earth and Planetary Science Letters*, 218 (1-2):109–122, 2004. doi: 10.1016/S0012-821X(03)00643-5.

D. S. Cowan. Origin of blueschist-bearing chaotic rocks in the Franciscan Complex, San Simeon, California. *Bulletin of the Geological Society of America*, 89(9):1415–1423, 1978. doi: 10.1130/0016-7606(1978)89<1415:OOBCRI>2.0.CO;2.

A. J. Cross and P. Skemer. Ultramylonite generation via phase mixing in high-strain experiments. *Journal of Geophysical Research: Solid Earth*, 122(3):1744–1759, 2017. doi: 10.1002/2016JB013801.

C. A. Currie, R. D. Hyndman, K. Wang, and V. Kostoglodov. Thermal models of the Mexico subduction zone: Implications for the megathrust seismogenic zone. *Journal of Geophysical Research: Solid Earth*, 107(B12):ETG 15–1–ETG 15–13, 2002. doi: 10.1029/2001jb000886.

G. V. Dal Piaz. History of tectonic interpretations of the Alps. *Journal of Geodynamics*, 32 (1-2):99–114, 2001. doi: 10.1016/S0264-3707(01)00019-9.

G. V. Dal Piaz, A. Bistacchi, and M. Massironi. Geological outline of the Alps. *Episodes*, 26 (3):175–180, 2003. doi: 10.18814/epiiugs/2003/v26i3/004.

P. Debat, J. C. Soula, L. Kubin, and J. L. Vidal. Optical studies of natural deformation microstructures in feldspars (gneiss and pegmatites from Occitania, southern France). *Lithos*, 11(2):133–145, 1978. doi: 10.1016/0024-4937(78)90004-X.

S. A. M. den Hartog, C. J. Spiers, S. A. M. D. Hartog, and C. J. Spiers. Influence of subduction zone conditions and gouge composition on frictional slip stability of megathrust faults. *Tectonophysics*, 600:75–90, 2013. doi: 10.1016/j.tecto.2012.11.006.

A. Deutsch. Datierungen an Alkaliamphibolen und Stilpnomelan aus der suedlichen Platta-Decke (Graubunden). *Eclogae geol. Helv.*, 76:295–308, 1983.

G. Di Vincenzo, S. Rocchi, F. Rossetti, and F. Storti. Dating brittle faulting: exploiting the complementarity of the step-heating and in situ 40Ar-39Ar laser techniques to solve the complexity of Cenozoic pseudotachylytes from the West Antarctic Rift System. *Terra Antartica Reports*, 12:49–56, 2006.

J. Dieterich. A constitutive law for rate of earthquake production and its application to

earthquake clustering. *Journal of Geophysical Research*, 99(B2):2601–2618, 1994. doi: 10.1029/93JB02581.

J. H. Dieterich. Time-dependent friction and the mechanics of stick-slip. *Pure and Applied Geophysics*, 116(4-5):790–806, 1978. doi: 10.1007/BF00876539.

A. Dimanov and G. Dresen. Rheology of synthetic anorthite-diopside aggregates: Implications for ductile shear zones. *Journal of Geophysical Research: Solid Earth*, 110(7):1–24, 2005. doi: 10.1029/2004JB003431.

H. Dragert, K. Wang, and G. Rogers. Geodetic and seismic signatures of episodic tremor and slip in the northern Cascadia subduction zone. *Earth, Planets and Space*, 2004. doi: 10.1186/BF03353333.

G. Dresen and B. Evans. Brittle and semibrittle deformation of synthetic marbles composed of two phases. *Journal of Geophysical Research: Solid Earth*, 98(B7):11921–11933, 2008. doi: 10.1029/93jb00697.

G. T. R. Droop and D. Chavrit. Eclogitic metagabbro from the Lanzada Window, eastern Central Alps: confirmation of subduction beneath the Malenco Unit. *Swiss Journal of Geosciences*, 107(1):113–128, 2014. doi: 10.1007/s00015-014-0162-z.

M. R. Drury. Dynamic recrystallization and strain softening of olivine aggregates in the laboratory and the lithosphere. *Geological Society Special Publication*, 243(2):143–158, 2005. doi: 10.1144/GSL.SP.2005.243.01.11.

M. R. Drury and J. L. Urai. Deformation-related recrystallization processes. *Tectonophysics*, 172(3-4):235–253, 1990. doi: 10.1016/0040-1951(90)90033-5.

J. C. Duarte, W. P. Schellart, and A. R. Cruden. How weak is the subduction zone interface? *Geophysical Research Letters*, 42(8):2664–2673, 2015. doi: 10.1002/2014GL062876.

S. B. Durr. Structural history of the Arosa Zone between Platta and Err nappes east of Marmorera (Grisons): multi-phase deformation at the Penninic- Austroalpine plate boundary. *Eclogae Geologicae Helvetiae*, 85(2):361–374, 1992.

G. Eberli. The evolution of the southern continental margin of the Jurassic Tethys Ocen as recorded in the Allgäu Formation of the Austroalpine Nappes of Graubünden (Switzerland). *Eclogae Geologicae Helvetiae*, 81(1):175–214, 1988.

K. Elger, O. Oncken, and J. Glodny. Plateau-style accumulation of deformation: Southern Altiplano. *Tectonics*, 24(4):1–19, 2005. doi: 10.1029/2004TC001675.

W. Ernst and G. V. Dal Piaz. Mineral parageneses of eclogitic rocks and related mafic schists of the Piemonte ophiolite nappe, Breuil-St. Jacques area, Italian Western Alps. *American Mineralogist*, 63:621–640, 1978.

W. G. Ernst. Metamorphic zonations on presumably subducted lithospheric plates from Japan, California and the Alps. *Contributions to Mineralogy and Petrology*, 34(1):43–59, 1971. doi: 10.1007/BF00376030.

W. G. Ernst and J. G. Liou. Overview of uhp metamorphism and tectonics in well-studied collisional orogens. *International Geology Review*, 41(6):477–493, 1999. doi: 10.1080/00206819909465153.

Å. Fagereng. Fractal vein distributions within a fault-fracture mesh in an exhumed accretionary mélange, Chrystalls Beach Complex, New Zealand. *Journal of Structural Geology*, 33(5):918–927, 2011. doi: 10.1016/j.jsg.2011.02.009.

Å. Fagereng and A. F. Cooper. Petrology of metabasalts from the Chrystalls Beach accretionary mélange - implications for tectonic setting and terrane origin. *New Zealand Journal of Geology and Geophysics*, 53(1):57–70, 2010. doi: 10.1080/00288301003631806.

Å. Fagereng and S. A. Den Hartog. Subduction megathrust creep governed by pressure solution and frictional-viscous flow. *Nature Geoscience*, 10(1):51–57, 2017. doi: 10.1038/ngeo2857.

A. Ferrario and A. Montrasio. Manganese Ore deposit of Monte del Forno. Its Stratigraphie and Structural Implications. *Schweizerische Mineralogische und Petrographische Mitteilungen*, 56: 377–385, 1976.

A. Festa, Y. Dilek, G. A. Pini, G. Codegone, and K. Ogata. Mechanisms and processes of stratal

disruption and mixing in the development of mélanges and broken formations: Redefining and classifying mélanges. *Tectonophysics*, 568-569:7–24, 2012. doi: 10.1016/j.tecto.2012.05.021.

A. Festa, G. A. Pini, K. Ogata, and Y. Dilek. Diagnostic features and field-criteria in recognition of tectonic, sedimentary and diapiric mélanges in orogenic belts and exhumed subduction-accretion complexes. *Gondwana Research*, 74:7–30, 2019. doi: 10.1016/j.gr.2019.01.003.

A. M. Freed and R. Bürgmann. Evidence of power-law flow in the Mojave desert mantle. *Nature*, 430(6999):548–551, 2004. doi: 10.1038/nature02784.

S. R. Freeman, S. Inger, R. W. Butler, and R. A. Cliff. Dating deformation using Rb-Sr in white mica: Greenschist facies deformation ages from the Entrelor shear zone, Italian Alps. *Tectonics*, 16(1):57–76, 1997. doi: 10.1029/96TC02477.

S. R. Freeman, R. W. H. Butler, R. A. Cliff, and D. C. Rex. Direct dating of mylonite evolution: a multi-disciplinary geochronological study from the Moine Thrust Zone, NW Scotland. *Journal of the Geological Society, London*, 155(5):745–758, 1998. doi: 10.1144/gsjgs.155.5.0745.

M. E. French and C. B. Condit. Slip partitioning along an idealized subduction plate boundary at deep slow slip conditions. *Earth and Planetary Science Letters*, 528:115828, 2019. doi: 10.1016/j.epsl.2019.115828.

H. Frey, J. C. Hunzicker, W. Frank, J. Bocquet, G. V. Dal Piaz, E. Jäger, and E. Niggli. Alpine metamorphism of the Alps : a review. *Schweizerische mineralogische und petrographische Mitteilungen*, 54:247–290, 1974.

M. Frey, J. C. Hunziker, E. Jäger, and W. B. Stern. Regional distribution of white K-mica polymorphs and their phengite content in the Central Alps. *Contributions to Mineralogy and Petrology*, 83(1-2):185–197, 1983. doi: 10.1007/BF00373092.

W. Frisch. Tectonic progradation and plate tectonic evolution of the Alps. *Tectonophysics*, 60 (3-4):121–139, 1979. doi: 10.1016/0040-1951(79)90155-0.

N. Froitzheim. Synsedimentary and synorogenic normal faults within a thrust sheet of the

Eastern Alps (Ortler zone, Graubunden, Switzerland). *Eclogae Geologicae Helvetiae*, 81(3): 593–610, 1988.

N. Froitzheim and G. Manatschal. Kinematics of Jurassic rifting, mantle exhumation, and passive-margin formation in the Austroalpine and Penninic nappes (eastern Switzerland). *Geological Society of America Bulletin*, 108(9):1120–1133, 1996. doi: 10.1130/0016-7606(1996)108<1120:KOJRME>2.3.CO;2.

N. Froitzheim, S. M. Schmid, and P. Conti. Repeated change from crustal shortening to orogen-parallel extension in the Austroalpine units of Graubünden. *Eclogae Geologicae Helvetiae*, (87):561–607, 1994. doi: 10.5169/seals-167471.

N. Froitzheim, S. M. Schmid, and M. Frey. Mesozoic paleogeography and the timing of eclogite-facies metamorphism in the Alps: a working hypothesis. *Eclogae Geologicae Helvetiae*, 89 (1):81–110, 1996. doi: 10.5169/seals-167895.

H. Frost and M. Ashby. *Deformation-mechanism maps; the plasticity and creep of metals and ceramics*. Pergammon Press, Oxford, 1982.

M. L. Fuhrman and D. H. Lindsley. Ternary-feldspar modeling and thermometry. *American Mineralogist*, 73:201–215, 1988. doi: 10.4052/tigg.24.13.

J.-i. Fukuda, C. W. Holyoke, and A. K. Kronenberg. Deformation of Fine-Grained Quartz Aggregates by Mixed Diffusion and Dislocation Creep. *Journal of Geophysical Research: Solid Earth*, 123(6):4676–4696, 2018. doi: 10.1029/2017JB015133.

W. Fyfe, N. Price, and Thompson AB. *Fluids in the Crust*. Elsevier, Amsterdam, 1978. ISBN 978-94-010-4536-0. doi: 10.1007/978-94-011-1226-0.

X. Gao and K. Wang. Rheological separation of the megathrust seismogenic zone and episodic tremor and slip. *Nature*, 543(7645):416–419, 2017. doi: 10.1038/nature21389.

A. Gautschi. Geologie und Petrologie des Fedozer Gabbros (Östliche Zentralalpen, Prov. Sondrio, N-Italien/Kt. Graubünden, Schweiz). *Abstr. Schweizerische Mineralogische und Petrographische Mitteilungen*, 59:423–427, 1979.

A. Gautschi. *Metamorphose und Geochemie der basischen Gesteine des Bergeller Ostrands*. Phd thesis, ETH Zürich, 1980.

T. V. Gerya, B. Stöckhert, A. L. Perchuk, and B. Sto. Exhumation of high-pressure metamorphic rocks in a subduction channel: A numerical simulation. *Tectonics*, 21(6):6–1–6–19, 2002. doi: 10.1029/2002TC001406.

J. Glodny, U. Ring, A. Kühn, P. Gleissner, and G. Franz. Crystallization and very rapid exhumation of the youngest Alpine eclogites (Tauern Window, Eastern Alps) from Rb/Sr mineral assemblage analysis. *Contributions to Mineralogy and Petrology*, 149(6):699–712, 2005. doi: 10.1007/s00410-005-0676-5.

J. Glodny, A. Kühn, and H. Austrheim. Geochronology of fluid-induced eclogite and amphibolite facies metamorphic reactions in a subduction-collision system, Bergen Arcs, Norway. *Contributions to Mineralogy and Petrology*, 156(1):27–48, 2008a. doi: 10.1007/s00410-007-0272-y.

J. Glodny, U. Ring, and A. Kühn. Coeval high-pressure metamorphism, thrusting, strike-slip, and extensional shearing in the Tauern Window, Eastern Alps. *Tectonics*, 27(4), 2008b. doi: 10.1029/2007TC002193.

A. M. Goryaeva, P. Carrez, and P. Cordier. Modeling defects and plasticity in MgSiO3 post-perovskite: Part 2-screw and edge [100] dislocations. *Physics and Chemistry of Minerals*, 42 (10):793–803, 2015. doi: 10.1007/s00269-015-0763-8.

J. P. Gratier, J. Richard, F. Renard, S. Mittempergher, M. L. Doan, G. Di Toro, J. Hadizadeh, and A. M. Boullier. Aseismic sliding of active faults by pressure solution creep: Evidence from the San Andreas fault observatory at Depth. *Geology*, 39(12):1131–1134, 2011. doi: 10.1130/G32073.1.

J.-p. P. Gratier, F. F. Renard, and P. Labaume. How pressure solution creep and fracturing processes interact in the upper crust to make it behave in both a brittle and viscous manner. *Journal of Structural Geology*, 21(8-9):1189–1197, 1999. doi: 10.1016/S0191-8141(99)00035-8.

J.-p. P. Gratier, D. K. Dysthe, and F. Renard. The role of pressure solution creep in the ductility of the earth's upper crust. *Advances in Geophysics*, 54:47–179, 2013. doi: 10.1016/B978-0-12-380940-7.00002-0.

I. Grevemeyer, J. L. Diaz-Naveas, C. R. Ranero, and H. W. Villinger. Heat flow over the descending Nazca plate in central Chile, 32°S to 41°S: Observations from ODP Leg 202 and the occurrence of natural gas hydrates. *Earth and Planetary Science Letters*, 213(3-4): 285–298, 2003. doi: 10.1016/S0012-821X(03)00303-0.

S. Grigull, A. Krohe, C. Moos, S. Wassmann, and B. Stöckhert. "Order from chaos": A field-based estimate on bulk rheology of tectonic mélanges formed in subduction zones. *Tectonophysics*, 568-569:86–101, 2012. doi: 10.1016/j.tecto.2011.11.004.

M.-H. Guillet and G. Guillet. Atopie et urticaire de contact au latex chez l'enfant: Etude chez 27 malades de moins de 15 ans. *Annales de Dermatologie et de Vénéréologie*, 131(1):35–37, 2004. doi: http://dx.doi.org/10.1016/S0151-9638(04)93539-9.

M. Guillope and J. P. Poirier. Dynamic recrystallization during creep of single-crystalline halite: an experimental study. *Journal of Geophysical Research*, 84(B10):5557–5567, 1979. doi: 10.1029/JB084iB10p05557.

S. Guillot, K. Hattori, P. Agard, S. Schwartz, and O. Vidal. Exhumation Processes in Oceanic and Continental Subduction Contexts: A Review. pages 175–205. 2009. doi: 10.1007/978-3-540-87974-9_10.

P. Guntli and M. Liniger. Metamorphose in der Margna-Decke im Bereich Piz de la Margna und Piz Fedoz (Oberengadin). *Schweiz. Mineral. Petrogr. Mitt.*, 69:289–301, 1989.

B. R. Hacker. H2O subduction beyond arcs. *Geochemistry, Geophysics, Geosystems*, 9(3), 2008. doi: 10.1029/2007GC001707.

B. R. Hacker, L. Ratschbacher, L. Webb, M. O. McWilliams, T. Ireland, A. Calvert, S. Dong, H.-R. Wenk, and D. Chateigner. Exhumation of ultrahigh-pressure continental crust in east central China: Late Triassic-Early Jurassic tectonic unroofing. *Journal of Geophysical Research: Solid Earth*, 105(B6):13339–13364, 2000. doi: 10.1029/2000jb900039.

B. R. Hacker, G. A. Abers, and S. M. Peacock. Subduction factory 1. Theoretical mineralogy, densities, seismic wave speeds, and H 2 O contents . *Journal of Geophysical Research: Solid Earth*, 108(B1):1–26, 2003a. doi: 10.1029/2001jb001127.

B. R. Hacker, S. M. Peacock, G. A. Abers, and S. D. Holloway. Subduction factory 2. Are intermediate-depth earthquakes in subducting slabs linked to metamorphic dehydration reactions? *Journal of Geophysical Research: Solid Earth*, 108(B1), 2003b. doi: 10.1029/2001jb001129.

R. Halama, M. Konrad-Schmolke, M. Sudo, H. R. Marschall, and M. Wiedenbeck. Effects of fluid-rock interaction on 40Ar/39Ar geochronology in high-pressure rocks (Sesia-Lanzo Zone, Western Alps). *Geochimica et Cosmochimica Acta*, 126:475–494, 2014. doi: 10.1016/j.gca.2013.10.023.

M. R. Handy. The Solid-State Flow of Polymineralic Rocks. *Journal of Geophysical Research*, 95(B6):8647–8661, 1990.

M. R. Handy. The transition from passive to active margin tectonics: a case study from the Zone of Samedan (eastern Switzerland). *Geologische Rundschau*, 85(4):832–851, 1996. doi: 10.1007/BF02440114.

M. R. Handy and R. Oberhänsli. Explanatory notes to the map: metamorphic structure of the Alps, age map of the metamorphic structure of the Alps - tectonic interpretation and outstanding problems. *Mitteilungen der Österreichischen Mineralogischen Gesellschaft*, 149: 201–225, 2004.

M. R. Handy, S. B. Wissing, and L. E. Streit. Frictional-viscous flow in mylonite with varied bimineralic composition and its effect on lithospheric strength. *Tectonophysics*, 303(1-4): 175–191, 1999. doi: 10.1016/S0040-1951(98)00251-0.

Z. Hashin. Theory of mechanical behavior of heterogeneous media. Technical report, 1963.

N. W. Hayman and L. L. Lavier. The geologic record of deep episodic tremor and slip. *Geology*, 42(3):195–198, 2014. doi: 10.1130/G34990.1.

M. J. Heap, P. Baud, P. G. Meredith, A. F. Bell, and I. G. Main. Time-dependent brittle creep in Darley Dale sandstone. *Journal of Geophysical Research*, 114(B7):B07203, 2009. doi: 10.1029/2008JB006212.

M. J. Heap, P. Baud, P. G. Meredith, S. Vinciguerra, A. F. Bell, and I. G. Main. Brittle creep in basalt and its application to time-dependent volcano deformation. *Earth and Planetary Science Letters*, 307(1-2):71–82, 2011. doi: 10.1016/j.epsl.2011.04.035.

J. Hermann and O. Müntener. Strukturelle Entwicklung im Grenzbereich zwischen dem penninischen Malenco-Ultramafitit und dem Unterostalpin (Margna- und Sella-Decke). *Schweizerische Mineralogische und Petrographische Mitteilungen*, 72:225–240, 1992. doi: 10.5169/seals-54909.

J. Hermann and O. Müntener. Extension-related structures in the Malenco-Margna-system: Implications for paleogeography and consequences for rifting and Alpine tectonics. *Schweizerische Mineralogische Und Petrographische Mitteilungen*, 76(3):501–519, 1996.

J. Hermann, O. Müntener, V. Trommsdorff, W. Hansmann, and G. B. Piccardo. Fossil crust-to-mantle transition, Val Malenco (Italian Alps). *Journal of Geophysical Research*, 102:123–132, 1997. doi: 10.1029/97jb01510.

R. Herrendörfer, Y. van Dinther, T. Gerya, and L. A. Dalguer. Earthquake supercycle in subduction zones controlled by the width of the seismogenic zone. *Nature Geoscience*, 8(6): 471–474, 2015. doi: 10.1038/ngeo2427.

J. Herrmann, E. Rybacki, H. Sone, and G. Dresen. Deformation Experiments on Bowland and Posidonia Shale-Part II: Creep Behavior at In Situ p c-T Conditions. *Rock Mechanics and Rock Engineering*, 2019. doi: 10.1007/s00603-019-01941-2.

M. Herwegh, J. de Bresser, and J. ter Heege. Combining natural microstructures with composite flow laws: an improved approach for the extrapolation of lab data to nature. *Journal of Structural Geology*, 27(3):503–521, 2005. doi: 10.1016/J.JSG.2004.10.010.

A. Heuret and S. Lallemand. Plate motions, slab dynamics and back-arc deformation. *Physics of the Earth and Planetary Interiors*, 149(1-2 SPEC. ISS.):31–51, 2005. doi: 10.1016/j.pepi.2004.08.022.

R. Hill. A self-consistent mechanics of composite materials. *Journal of Mechanics Physics Solids*, 13:213–222, 1965.

G. Hirth and J. Tullis. Dislocation creep regimes in quartz aggregates. *Journal of Structural Geology*, 14(2):145–159, 1992. doi: 10.1016/0191-8141(92)90053-Y.

T. Holland, J. Baker, and R. Powell. Mixing properties and activity-composition relationships of chlorites in the system MgO-FeO-Al2O3-SiO2-H2O. *European Journal of Mineralogy*, 10 (3):395–406, 1998. doi: 10.1127/ejm/10/3/0395.

A. Hoshikuma. Grain growth and superplasticity: their implication to earth science. *Journal - Geological Society of Japan*, 102:232–239, 1996.

K. J. Hsü. Principles of mélanges and their bearing on the franciscan-knoxville paradox. *Bulletin of the Geological Society of America*, 79(8):1063–1074, 1968. doi: 10.1130/0016-7606(1968) 79[1063:POMATB]2.0.CO;2.

B. Huet, P. Yamato, and B. Grasemann. The Minimized Power Geometric model: An analytical mixing model for calculating polyphase rock viscosities consistent with experimental data. *Journal of Geophysical Research: Solid Earth*, 119(4):3897–3924, 2014. doi: 10.1002/2013JB010453.

A. L. Husker, V. Kostoglodov, V. M. Cruz-Atienza, D. Legrand, N. M. Shapiro, J. S. Payero, M. Campillo, and E. Huesca-Pérez. Temporal variations of non-volcanic tremor (NVT) locations in the Mexican subduction zone: Finding the NVT sweet spot. *Geochemistry, Geophysics, Geosystems*, 13(3), 2012. doi: 10.1029/2011GC003916.

R. D. Hyndman, M. Yamano, and D. A. Oleskevich. The seismogenic zone of subduction thrust faults. *Island Arc*, 6(3):244–260, 1997. doi: 10.1111/j.1440-1738.1997.tb00175.x.

R. D. Hyndman, P. A. McCrory, A. Wech, H. Kao, and J. Ague. Cascadia subducting plate fluids channelled to fore-arc mantle corner: ETS and silica deposition. *Journal of Geophysical Research: Solid Earth*, 120(6):4344–4358, 2015. doi: 10.1002/2015JB011920.

S. Ilic and K. Hackl. Solution-precipitation creep - micromechanical modelling and numerical results. *Proc. Appl. Math. Mach.*, 278:277–278, 2005. doi: 10.1002/pamm.200510.

S. Inger and R. A. Cliff. Timing of metamorphism in the Tauern Window, Eastern Alps:

RbâĂŘSr ages and fabric formation. *Journal of Metamorphic Geology*, 12(5):695–707, 1994. doi: 10.1111/j.1525-1314.1994.tb00052.x.

P. I. Ioannidi, S. Angiboust, O. Oncken, P. Agard, J. Glodny, and M. Sudo. Deformation along the roof of a fossil subduction interface in the transition zone below seismogenic coupling: The Austroalpine case and new insights from the Malenco Massif (Central Alps). *Geosphere*, 15, 2020.

O. Ishizuka. Vertical and horizontal variations of the fast neutron flux in a single irradiation capsule and their significance in the laser-heating 40Ar/39Ar analysis: Case study for the hydraulic rabbit facility of the JMTR reactor, Japan. *Geochemical Journal*, 32(4):243–252, 1998. doi: 10.2343/geochemj.32.243.

Y. Ito and K. Obara. Very low frequency earthquakes within accretionary prisms are very low stress-drop earthquakes. *Geophysical Research Letters*, 33(9):1–4, 2006. doi: 10.1029/2006GL025883.

Y. Ito, K. Obara, K. Shiomi, S. Sekine, and H. Hirose. Slow Earthquakes Coincident with Episodic Tremors and Slow Slip Events. *Science*, 315(5811):503–506, 2007. doi: 10.1126/science.1134454.

Y. Ito, Y. Asano, and K. Obara. Very-low-frequency earthquakes indicate a transpressional stress regime in the Nankai accretionary prism. *Geophysical Research Letters*, 36(20), 2009. doi: 10.1029/2009GL039332.

K. Jaeckel, G. E. Bebout, and S. Angiboust. Deformation-enhanced fluid and mass transfer along Western and Central Alps paleo-subduction interfaces : Significance for carbon cycling models. *Geosphere*, 14(6):1–21, 2018. doi: 10.1130/GES01587.1/4530582/ges01587.pdf.

S. Jammes and L. L. Lavier. The effect of bimineralic composition on extensional processes at lithospheric scale. *Geochemistry, Geophysics, Geosystems*, 17(8):3375–3392, 2016. doi: 10.1002/2016GC006399.

S. Jammes, L. L. Lavier, and J. E. Reber. Localization and delocalization of deformation in a bimineralic material. *Journal of Geophysical Research: Solid Earth*, 120(5):3649–3663, 2015. doi: 10.1002/2015JB011890.

S. Ji and P. Zhao. Strength of two-phase rocks: A model based on fiber-loading theory. *Journal of Structural Geology*, 16(2):253–262, 1994. doi: 10.1016/0191-8141(94)90108-2.

S. Ji, R. Wirth, E. Rybacki, and Z. Jiang. High-temperature plastic deformation of quartz-plagioclase multilayers by layer-normal compression. *Journal of Geophysical Research: Solid Earth*, 105(B7):16651–16664, 2000. doi: 10.1029/2000jb900130.

S. Ji, Q. Wang, B. Xia, and D. Marcotte. Mechanical properties of multiphase materials and rocks: A phenomenological approach using generalized means. *Journal of Structural Geology*, 26(8):1377–1390, 2004. doi: 10.1016/j.jsg.2003.12.004.

T. John, N. Gussone, Y. Y. Podladchikov, G. E. Bebout, R. Dohmen, R. Halama, R. Klemd, T. Magna, and H. M. Seitz. Volcanic arcs fed by rapid pulsed fluid flow through subducting slabs. *Nature Geoscience*, 5(7):489–492, 2012. doi: 10.1038/ngeo1482.

K. M. Johnson, D. R. Shelly, and A. M. Bradley. Simulations of tremor-related creep reveal a weak crustal root of the San Andreas Fault. *Geophysical Research Letters*, 40(7):1300–1305, 2013. doi: 10.1002/grl.50216.

P. G. Jordan. The deformational behaviour of bimineralic limestone-halite aggregates. *Tectonophysics*, 135(1-3):185–197, 1987. doi: 10.1016/0040-1951(87)90160-0.

H. Jung and S. I. Karato. Effects of water on dynamically recrystallized grain-size of olivine. *Journal of Structural Geology*, 23(9):1337–1344, 2001a. doi: 10.1016/S0191-8141(01)00005-0.

H. Jung and S. I. Karato. Water-induced fabric transitions in olivine. *Science*, 293(5534): 1460–1463, 2001b. doi: 10.1126/science.1062235.

O. A. Kaibyshev, A. I. Pshenichniuk, and V. V. Astanin. Superplasticity resulting from cooperative grain boundary sliding. *Acta Materialia*, 1998. doi: 10.1016/S1359-6454(98)00197-9.

M. Kameyama, D. A. Yuen, and S.-i. I. Karato. Thermal-mechanical effects of low-temperature plasticity (the Peierls mechanism) on the deformation of a viscoelastic shear zone. *Earth and Planetary Science Letters*, 168(1-2):159–172, 1999. doi: 10.1016/S0012-821X(99)00040-0.

S.-i. Karato. *Deformation of Earth Materials*, volume 9780521844. Cambridge University Press, Cambridge, 2008. ISBN 9780511804892. doi: 10.1017/CBO9780511804892.

S.-i. Karato. Rheological Properties of Minerals and Rocks. In *Physics and Chemistry of the Deep Earth*, pages 94–144. John Wiley & Sons, Ltd, Chichester, UK, 2013. ISBN 9780470659144. doi: 10.1002/9781118529492.ch4.

A. Katsumata and N. Kamaya. Low-frequency continuous tremor around the Moho discontinuity away from volcanoes in the southwest Japan. *Geophysical Research Letters*, 30(1): 20–1–20–4, 2003. doi: 10.1029/2002gl015981.

B. J. P. Kaus and Y. Y. Podladchikov. Initiation of localized shear zones in viscoelastoplastic rocks. *Journal of Geophysical Research*, 111(January 2005):1–18, 2006. doi: 10.1029/2005JB003652.

D. M. Kerrick and J. A. Connelly. Metamorphic devolatilization of subducted marine sediments and the transport of volatiles into the Earth's mantle. *Nature*, 411(6835):293–296, 2001. doi: 10.1038/35077056.

D. M. Kerrick and J. A. Connolly. Metamorphic devolatilization of subducted oceanic metabasalts: Implications for seismicity, arc magmatism and volatile recycling. *Earth and Planetary Science Letters*, 189(1-2):19–29, 2001. doi: 10.1016/S0012-821X(01)00347-8.

G. Kimura and A. Mukai. Underplated units in an accretionary complex: Melange of the Shimanto Belt of eastern Shikoku, southwest Japan. *Tectonics*, 10(1):31–50, 1991. doi: 10.1029/90TC00799.

G. Kimura, A. Yamaguchi, M. Hojo, Y. Kitamura, J. Kameda, K. Ujiie, Y. Hamada, M. Hamahashi, and S. Hina. Tectonic mélange as fault rock of subduction plate boundary. *Tectonophysics*, 568-569:25–38, 2012. doi: 10.1016/j.tecto.2011.08.025.

S. H. Kirby. Rheology of the lithosphere. *Reviews of Geophysics*, 21(6):1458–1487, 1983. doi: 10.1029/RG021i006p01458.

Y. Kitamura, K. Sato, E. Ikesawa, K. Ikehara-Ohmori, G. Kimura, H. Kondo, K. Ujiie, C. T. Onishi, K. Kawabata, Y. Hashimoto, H. Mukoyoshi, and H. Masago. Mélange and its seismogenic roof décollement: A plate boundary fault rock in the subduction zone - An example from the Shimanto Belt, Japan. *Tectonics*, 24(5):1–15, 2005. doi: 10.1029/2004TC001635.

S. Klinge, K. Hackl, and J. Renner. A mechanical model for dissolution-precipitation creep based on the minimum principle of the dissipation potential. *Proceedings of the Royal Society A: Mathematical, Physical and Engineering Sciences*, 471(2180):20140994, 2015. doi: 10.1098/rspa.2014.0994.

R. J. Knipe. Deformation mechanisms - recognition from natural tectonites. *Journal of Structural Geology*, 11(1-2):127–146, 1989. doi: 10.1016/0191-8141(89)90039-4.

S. Kodaira, T. Iidaka, A. Kato, J. O. Park, T. Iwasaki, and Y. Kaneda. High pore fluid pressure may cause silent slip in the Nankai Trough. *Science*, 304(5675):1295–1298, 2004. doi: 10.1126/science.1096535.

D. L. Kohlstedt and M. S. Weathers. Deformation-induced microstructures, paleopiezometers, and differential stresses in deeply eroded fault zones. *Journal of Geophysical Research*, 85 (B11):6269–6285, 1980. doi: 10.1029/JB085iB11p06269.

M. Konrad-Schmolke, T. Zack, P. J. O'Brien, and M. Barth. Fluid migration above a subducted slab - Thermodynamic and trace element modelling of fluid-rock interaction in partially overprinted eclogite-facies rocks (Sesia Zone, Western Alps). *Earth and Planetary Science Letters*, 311(3-4):287–298, 2011. doi: 10.1016/j.epsl.2011.09.025.

M. Krabbendam, J. L. Urai, and L. J. van Vliet. Grain size stabilisation by dispersed graphite in a high-grade quartz mylonite: An example from Naxos (Greece). *Journal of Structural Geology*, 25(6):855–866, 2003. doi: 10.1016/S0191-8141(02)00086-X.

R. L. Kranz. Crack growth and development during creep of Barre granite. *International Journal of Rock Mechanics and Mining Sciences & Geomechanics Abstracts*, 16(1):23–35, 1979. doi: 10.1016/0148-9062(79)90772-1.

R. L. Kranz, W. J. Harris, and N. L. Carter. Static fatigue of granite at 200°C. *Geophysical Research Letters*, 9(1):1–4, 1982. doi: 10.1029/GL009i001p00001.

R. Kruse and H. Stünitz. Deformation mechanisms and phase distribution in mafic high-temperature mylonites from the Jotun Nappe, southern Norway. *Tectonophysics*, 303(1-4): 223–249, 1999. doi: 10.1016/S0040-1951(98)00255-8.

F. Kumon. Shimanto Supergroup in the southern part of Tokushima Prefecture, SouthwestJapan. *The Journal of the Geological Society of Japan*, 87(5):277–295_1, 1981. doi: 10.5575/geosoc.87.277.

Y. Lagabrielle and M. Lemoine. Alpine, Corsican and Apennine ophiolites: the slow-spreading ridge model. *Comptes Rendus de l'Académie des Sciences - Series IIA - Earth and Planetary Science*, 325(12):909–920, 1997. doi: 10.1016/s1251-8050(97)82369-5.

S. Lamb and L. Hoke. Origin of the high plateau in the Central Andes, Bolivia, South America. *Tectonics*, 16(4):623–649, 1997. doi: 10.1029/97TC00495.

J. Langbein, J. R. Murray, and H. A. Snyder. Coseismic and initial postseismic deformation from the 2004 Parkfield, California, earthquake, observed by global positioning system, electronic distance meter, creepmeters, and borehole strainmeters. *Bulletin of the Seismological Society of America*, 96(4 B), 2006. doi: 10.1785/0120050823.

H. Laubscher and D. Bernoulli. Mediterranean and Tethys. In *The Ocean Basins and Margins*, pages 1–28. 1977. doi: 10.1007/978-1-4684-3036-3_1.

L. Le Pourhiet, B. Huet, L. Labrousse, K. Yao, P. Agard, and L. Jolivet. Strain localisation in mechanically layered rocks beneath detachment zones: Insights from numerical modelling. *Solid Earth*, 4(1):135–152, 2013. doi: 10.5194/se-4-135-2013.

J. Y. Lee, K. Marti, J. P. Severinghaus, K. Kawamura, H. S. Yoo, J. B. Lee, and J. S. Kim. A redetermination of the isotopic abundances of atmospheric Ar. *Geochimica et Cosmochimica Acta*, 70(17):4507–4512, 2006. doi: 10.1016/j.gca.2006.06.1563.

M. Lemoine, M. Marthaler, Caron J.M., M. Sartori, S. Amaudric Du Chaffaut, T. Dumont, A. Escher, H. Masson, R. Polino, and T. P. Découverte de foraminifères planctoniques du Crétacé supérieur dans les schistes lustrés du Queyras (Alpes occidentales). Conséquences paléogéographiques et tectoniques. *Comptes Rendus de l'Academie des Sciences*, 229:727–732, 1984.

A. Lin, Z. Sun, and Z. Yang. Multiple generations of pseudotachylyte in the brittle to ductile regimes, Qinling-Dabie Shan ultrahigh-pressure metamorphic complex, central China. *Island Arc*, 12(4):423–435, 2003. doi: 10.1046/j.1440-1738.2003.00407.x.

A. Lin, T. Maruyama, S. Aaron, K. Michibayashi, A. Camacho, and K. I. Kano. Propagation of seismic slip from brittle to ductile crust: Evidence from pseudotachylyte of the Woodroffe thrust, central Australia. *Tectonophysics*, 402(1-4 SPEC. ISS):21–35, 2005. doi: 10.1016/j.tecto.2004.10.016.

M. Liniger and P. Guntli. Bau und Geschichte des zentralen Teils der Margna-Decke. *Schweizerische Mineralogische Petrographische Mitteilungen*, 68(1):41–54, 1988.

M. Liniger and P. Nievergelt. Stockwerk-Tektonik im suÌĺdlichen GraubuÌĺnden. *Schweizerische Mineralogische Petrographische Mitteilungen*, 70:95–101, 1990.

M. H. Liniger. *Der ostalpin-penninische Grenzbereich im Gebiet der nördlichen Margna-Decke (Graubünden, Schweiz)*. PhD thesis, ETH, 1992.

J. G. Liou, R. Zhang, and W. G. Ernst. An introduction to ultrahigh-pressure metamorphism. *Island Arc*, 3(1):1–24, 1994. doi: 10.1111/j.1440-1738.1994.tb00001.x.

Y. Liu and J. R. Rice. Aseismic slip transients emerge spontaneously in three-dimensional rate and state modeling of subduction earthquake sequences. *Journal of Geophysical Research: Solid Earth*, 110(8):1–14, 2005. doi: 10.1029/2004JB003424.

Y. Liu and J. R. Rice. Spontaneous and triggered aseismic deformation transients in a subduction fault model. *Journal of Geophysical Research: Solid Earth*, 112(9):B09404, 2007. doi: 10.1029/2007JB004930.

Y. Liu and J. R. Rice. Slow slip predictions based on granite and gabbro friction data compared to GPS measurements in northern Cascadia. *Journal of Geophysical Research: Solid Earth*, 114(9):1–19, 2009. doi: 10.1029/2008JB006142.

M. Locatelli, A. Verlaguet, P. Agard, L. Federico, and S. Angiboust. Intermediate-depth brecciation along the subduction plate interface (Monviso eclogite, W. Alps). *Lithos*, 320-321: 378–402, 2018. doi: 10.1016/j.lithos.2018.09.028.

M. Locatelli, A. Verlaguet, P. Agard, T. Pettke, and L. Federico. *Fluid Pulses During Stepwise Brecciation at Intermediate Subduction Depths (Monviso Eclogites, W. Alps):*

First Internally Then Externally Sourced, volume 20. 2019. ISBN 0000000287531. doi: 10.1029/2019GC008549.

K. Ludwig. Isoplot v. 3.71: A Geochronological Toolkit for Microsoft Excel. *Berkeley Geochronology Center, Berkeley, California, Special Publication*, 4:(70 pp.), 2009.

K. M. Luttrell, X. Tong, D. T. Sandwell, B. A. Brooks, and M. G. Bevis. Estimates of stress drop and crustal tectonic stress from the 27 February 2010 Maule, Chile, earthquake: Implications for fault strength. *Journal of Geophysical Research: Solid Earth*, 116(11), 2011. doi: 10.1029/2011JB008509.

M. E. Magee and M. D. Zoback. Evidence for a weak interplate thrust fault along the northern Japan subduction zone and implications for the mechanics of thrust faulting and fluid expulsion. *Geology*, 21(9):809–812, 1993. doi: 10.1130/0091-7613(1993)021<0809:EFAWIT>2.3.CO;2.

E. M. Mahar, J. M. Baker, R. Powell, T. J. B. Holland, and N. Howell. The effect of Mn on mineral stability in metapelites. *Journal of Metamorphic Geology*, 15(2):223–238, 1997. doi: 10.1111/j.1525-1314.1997.00011.x.

G. Manatschal. *Jurassic rifting and formation of a passive continental margin (Platta and Err nappes, Eastern Switzerland): geometry, kinematics and geochemestry of fault rocks and a comparision with the Galicia margin.* PhD thesis, ETH Zürich, 1995.

C. E. Manning. The solubility of quartz in H2O in the lower crust and upper mantle. *Geochimica et Cosmochimica Acta*, 58(22):4831–4839, 1994. doi: 10.1016/0016-7037(94)90214-3.

R. H. Marchant and G. M. Stampfli. Subduction of continental crust in the Western Alps. *Tectonophysics*, 269(3-4):217–235, 1997. doi: 10.1016/S0040-1951(96)00170-9.

M. J. Markley, C. Teyssier, M. A. Cosca, R. Caby, J. C. Hunziker, and M. Sartori. Alpine deformation and 40Ar/39Ar geochronology of synkinematic white mica in the Siviez-Mischabel Nappe, western Pennine Alps, Switzerland. *Tectonics*, 17(3):407–425, 1998. doi: 10.1029/98TC00560.

C. Marone and E. Richardson. Learning to read fault-slip behavior from fault-zone structure. *Geology*, 38(8):767–768, 2010. doi: 10.1130/focus082010.1.

H.-J. J. Massonne and W. Schreyer. Phengite geobarometry based on the limiting assemblage with K-feldspar, phlogopite, and quartz. *Contributions to Mineralogy and Petrology*, 96(2): 212–224, 1987. doi: 10.1007/BF00375235.

T. Matsuzawa, H. Hirose, B. Shibazaki, and K. Obara. Modeling short- and long-term slow slip events in the seismic cycles of large subduction earthquakes. *Journal of Geophysical Research: Solid Earth*, 115(12), 2010. doi: 10.1029/2010JB007566.

D. A. May, J. Brown, and L. Le Pourhiet. PTatin3D: High-Performance Methods for Long-Term Lithospheric Dynamics. *International Conference for High Performance Computing, Networking, Storage and Analysis, SC*, 2015(January):274–284, 2014. doi: 10.1109/SC.2014.28.

D. A. May, J. Brown, and L. Le Pourhiet. A scalable, matrix-free multigrid preconditioner for finite element discretizations of heterogeneous Stokes flow. *Computer Methods in Applied Mechanics and Engineering*, 290(June):496–523, 2015. doi: 10.1016/j.cma.2015.03.014.

D. P. McKenzie and R. L. Parker. The North Pacific: An example of tectonics on a sphere. *Nature*, 216(5122):1276–1280, 1967. doi: 10.1038/2161276a0.

E. Medley. Estimating Block Size Distributions of Melanges and Similar Block-in-Matrix Rocks (Bimrocks). *Proceedings of 5th North American Rock Mechanics Symposium (NARMS)*, pages 509–606, 2002.

A. Menant, S. Angiboust, P. Monié, O. Oncken, and J.-M. M. Guigner. Brittle deformation during Alpine basal accretion and the origin of seismicity nests above the subduction interface. *Earth and Planetary Science Letters*, 487:84–93, 2018. doi: 10.1016/j.epsl.2018.01.029.

F. Meneghini, G. Di Toro, C. D. Rowe, J. C. Moore, A. Tsutsumi, and A. Yamaguchi. Record of mega-earthquakes in subduction thrusts: The black fault rocks of pasagshak point (Kodiak Island, Alaska). *Bulletin of the Geological Society of America*, 122(7-8):1280–1297, 2010. doi: 10.1130/B30049.1.

T. A. Michalske and S. W. Freiman. A molecular interpretation of stress corrosion in silica. *Nature*, 295(5849):511–512, 1982. doi: 10.1038/295511a0.

G. Mohn, G. Manatschal, E. Masini, and O. Müntener. Rift-related inheritance in orogens: A case study from the Austroalpine nappes in Central Alps (SE-Switzerland and N-Italy). *International Journal of Earth Sciences (Geol Rundsch)*, 100(5):937–961, 2011. doi: 10.1007/s00531-010-0630-2.

P. Monjoie, F. Bussy, U. Schaltegger, A. Mulch, H. Lapierre, and H.-R. Pfeifer. Contrasting magma types and timing of intrusion in the Permian layered mafic complex of Mont Collon (Western Alps, Valais, Switzerland): evidence from U/Pb zircon and 40Ar/39Ar amphibole dating. *Swiss Journal of Geosciences*, 100(1):125–135, 2007. doi: 10.1007/s00015-007-1210-8.

L. G. Montési. Controls of shear zone rheology and tectonic loading on postseismic creep. *Journal of Geophysical Research: Solid Earth*, 109(10), 2004. doi: 10.1029/2003JB002925.

A. Montrasio. Strutture a pillow nelle anfiboliti del M. Forno (Penninico medio-Alpi Retichi). *Rendiconti Accademia Nazionale Lincei, Scienzia Fisica Matematica Naturali*, 54:114–123, 1973.

A. Montrasio, V. Trommsdorff, V. Hermann, O. Müntener, and P. Spillmann. Carta Geologica della Valmalenco. *Supplement to Scheizerische Mineralogische und Petrographische Mitteilungen*, 85:1, 2005.

M. Moreno, C. Haberland, O. Oncken, A. Rietbrock, S. Angiboust, and O. Heidbach. Locking of the Chile subduction zone controlled by fluid pressure before the 2010 earthquake. *Nature Geoscience*, 7(4):292–296, 2014. doi: 10.1038/ngeo2102.

W. J. Morgan. Rises, Trenches, Great Faults and Crustal Blocks. *Journal of Geophysical Research*, 73:1959–82, 1968.

V. S. Mount and J. Suppe. State of stress near the San Andreas fault: Implications for wrench tectonics. *Geology*, 15(12):1143–1146, 1987. doi: 10.1130/0091-7613(1987)15<1143:SOSNTS>2.0.CO;2.

W. Müller, R. D. Dallmeyer, F. Neubauer, and M. Thöni. Deformation-induced resetting of Rb/Sr and 40Ar/39Ar mineral systems in a low-grade, polymetamorphic terrane (Eastern Alps, Austria). *Journal of the Geological Society*, 156(2):261–278, 1999. doi: 10.1144/gsjgs.156.2.0261.

W. Müller, N. S. Mancktelow, and M. Meier. Rb-Sr microchrons of synkinematic mica in mylonites: An example from the DAV fault of the Eastern Alps. *Earth and Planetary Science Letters*, 180(3-4):385–397, 2000. doi: 10.1016/S0012-821X(00)00167-9.

O. Müntener, J. Hermann, I. M. Villa, and V. Trommsdorff. From Jurassic rifting to Cretaceous nappe formation: a combined 39Ar/40Ar and microprobe study on amphiboles. *Terra Abstracts*, 1:489, 1997.

O. Müntener, J. Hermann, and V. Trommsdorff. Cooling History and Exhumation of Lower-Crustal Granulite and Upper Mantle (Malenco, Eastern Central Alps). *Journal of Petrology*, 41(2):175–200, 2000. doi: 10.1093/petrology/41.2.175.

O. Müntener, G. Manatschal, L. Desmurs, and T. Pettke. Plagioclase peridotites in ocean-continent transitions: Refertilized mantle domains generated by melt stagnation in the shallow mantle lithosphere. *Journal of Petrology*, 51(1-2):255–294, 2010. doi: 10.1093/petrology/egp087.

R. Nakata, R. Ando, T. Hori, and S. Ide. Generation mechanism of slow earthquakes: Numerical analysis based on a dynamic model with brittle-ductile mixed fault heterogeneity. *Journal of Geophysical Research: Solid Earth*, 116(8):B08308, 2011. doi: 10.1029/2010JB008188.

K. D. Nelson. A suggestion for the origin of mesoscopic fabric in accretionary melange, based on features observed in the Chrystalls Beach Complex, South Island, New Zealand. *Geological Society of America Bulletin*, 93(7):625–634, 1982. doi: 10.1130/0016-7606(1982)93<625:ASFTOO>2.0.CO;2.

J. Newman, W. M. Lamb, M. R. Drury, and R. L. Vissers. Deformation processes in a peridotite shear zone: Reaction-softening by an H2O-deficient, continuous net transfer reaction. *Tectonophysics*, 303(1-4):193–222, 1999. doi: 10.1016/S0040-1951(98)00259-5.

A. Niemeijer, G. Di Toro, A. W. Griffith, A. Bistacchi, S. A. F. Smith, S. Nielsen, G. Di, W. A. Grif, A. Bistacchi, S. A. F. Smith, and S. Nielsen. Inferring earthquake physics and chemistry using an integrated fi eld and laboratory approach. *Journal of Structural Geology*, 39:2–36, 2012. doi: 10.1016/j.jsg.2012.02.018.

A. R. Niemeijer and C. J. Spiers. Influence of phyllosilicates on fault strength in the brittle-ductile transition: Insights from rock analogue experiments. *Geological Society Special Publication*, 245:303–327, 2005. doi: 10.1144/GSL.SP.2005.245.01.15.

H. Noda and N. Lapusta. Stable creeping fault segments can become destructive as a result of dynamic weakening. *Nature*, 493(7433):518–521, 2013. doi: 10.1038/nature11703.

K. Obana and S. Kodaira. Low-frequency tremors associated with reverse faults in a shallow accretionary prism. *Earth and Planetary Science Letters*, 287(1-2):168–174, 2009. doi: 10.1016/j.epsl.2009.08.005.

K. Obara. Nonvolcanic deep tremor associated with subduction in southwest Japan. *Science*, 296(5573):1679–1681, 2002. doi: 10.1126/science.1070378.

K. Obara. Characteristics and interactions between non-volcanic tremor and related slow earthquakes in the Nankai subduction zone, southwest Japan, 2011.

K. Obara and Y. Ito. Very low frequency earthquakes excited by the 2004 off Kii peninsula earthquakes: A dynamic deformation process in the large accretionary prism. *Earth, Planets and Space*, 57(4):321–326, 2005. doi: 10.1186/BF03352570.

K. Obara and A. Kato. Connecting slow earthquakes to huge earthquakes. *Science*, 353(6296):253–258, 2016. doi: 10.1126/science.aaf1512.

K. Obara, H. Hirose, F. Yamamizu, and K. Kasahara. Episodic slow slip events accompanied by non-volcanic tremors in southwest Japan subduction zone. *Geophysical Research Letters*, 31(23):4–7, 2004. doi: 10.1029/2004GL020848.

D. A. Oleskevich, R. D. Hyndman, and K. Wang. The updip and downdip limits to great subduction earthquakes: Thermal and structural models of Cascadia, south Alaska, SW

Japan, and Chile. *Journal of Geophysical Research: Solid Earth*, 104(B7):14965–14991, 1999. doi: 10.1029/1999JB900060.

O. Oncken, D. Hindle, J. Kley, K. Elger, P. Victor, and K. Schemmann. Deformation of the Central Andean Upper Plate System âĂŤ Facts, Fiction, and Constraints for Plateau Models. In *The Andes*, pages 3–27. 2006. doi: 10.1007/978-3-540-48684-8_1.

A. Ord and J. M. Christie. Flow stresses from microstructures in mylonitic quartzites of the Moine Thrust zone, Assynt area, Scotland. *Journal of Structural Geology*, 6(6):639–654, 1984. doi: 10.1016/0191-8141(84)90002-6.

C. W. C. Passchier and R. A. R. Trouw. *Microtectonics*. Springer, Berlin, 2005. ISBN 3540640037. doi: 10.1007/3-540-29359-0.

S. M. Peacock. Thermal and metamorphic environment of subduction zone episodic tremor and slip. *Journal of Geophysical Research: Solid Earth*, 114(8):1–9, 2009. doi: 10.1029/2008JB005978.

S. M. Peacock and R. D. Hyndman. Hydrous minerals in the mantle wedge and the maximum depth of subduction thrust earthquakes. *Geophysical Research Letters*, 26(16):2517–2520, 1999. doi: 10.1029/1999GL900558.

S. M. Peacock, N. I. Christensen, M. G. Bostock, and P. Audet. High pore pressures and porosity at 35 km depth in the Cascadia subduction zone. *Geology*, 2011. doi: 10.1130/G31649.1.

Z. Peng and J. Gomberg. An integrated perspective of the continuum between earthquakes and slow-slip phenomena. *Nature Geoscience*, 3(9):599–607, 2010. doi: 10.1038/ngeo940.

S. C. Penniston-dorland, M. J. Kohn, and C. E. Manning. The global range of subduction zone thermal structures from exhumed blueschists and eclogites : Rocks are hotter than models. *Earth and Planetary Science Letters*, 428:243–254, 2015. doi: 10.1016/j.epsl.2015.07.031.

A. Peretti. Der Monte-del-Forno-Komplex am Bergell-Ostrand: Seine Lithostratigraphie, alpine Tektonik und Metamorphose. *Eclogae Geologicae Helvetiae*, 78(1):23–48, 1985.

M. Pérez-Gussinyé, J. P. Morgan, T. J. Reston, and C. R. Ranero. The rift to drift transition at non-volcanic margins: Insights from numerical modelling. *Earth and Planetary Science Letters*, 244(1-2):458–473, 2006. doi: 10.1016/j.epsl.2006.01.059.

H. Perfettini and J.-P. Avouac. Postseismic relaxation driven by brittle creep: A possible mechanism to reconcile geodetic measurements and the decay rate of aftershocks, application to the Chi-Chi earthquake, Taiwan. *Journal of Geophysical Research: Solid Earth*, 109(B2), 2004. doi: 10.1029/2003jb002488.

M. Perfit. Earth's Oceanic Crust. In W. White, editor, *Encyclopedia of Earth Sciences Series*, volume 15, pages 430–439. Springer International Publishing, 2018. ISBN 9783319391939. doi: 10.1007/978-3-319-39312-4_266.

P. Philippot. Opposite vergence of Nappes and crustal extension in the FrenchâĂŘItalian western Alps. *Tectonics*, 9(5):1143–1164, 1990. doi: 10.1029/TC009i005p01143.

P. Philippot. Fluid-melt-rock interaction in mafic eclogites and coesite-bearing metasediments: Constraints on volatile recycling during subduction. *Chemical Geology*, 108(1-4):93–112, 1993. doi: 10.1016/0009-2541(93)90319-E.

S. M. Picazo, T. A. Ewing, and O. Müntener. Paleocene metamorphism along the Pennine-Austroalpine suture constrained by U-Pb dating of titanite and rutile (Malenco, Alps). *Swiss Journal of Geosciences*, 2019. doi: 10.1007/s00015-019-00346-1.

J. P. Platt. Dynamics of orogenic wedges and the uplift of high-pressure metamorphic rocks. *Geological Society of America Bulletin*, 97(9):1037–1053, 1986. doi: 10.1130/0016-7606(1986)97<1037:DOOWAT>2.0.CO;2.

J. P. Platt. Rheology of two-phase systems: A microphysical and observational approach. *Journal of Structural Geology*, 77:213–227, 2015. doi: 10.1016/j.jsg.2015.05.003.

A. Plunder, P. Agard, B. Dubacq, C. Chopin, and M. Bellanger. How continuous and precise is the record of P-T paths? Insights from combined thermobarometry and thermodynamic modelling into subduction dynamics (Schistes Lustrés, W. Alps). *Journal of Metamorphic Geology*, 30(3):323–346, 2012. doi: 10.1111/j.1525-1314.2011.00969.x.

J. P. Poirier. Creep of crystals: high-temperature deformation processes in metals, ceramics and minerals. *Creep of crystals: high-temperature deformation processes in metals, ceramics and minerals.*, 1985. doi: 10.1016/0191-8141(86)90116-1.

R. Polino, G. V. Dal Piaz, and G. Gosso. Tectonic erosion at the Adria margin and accretionary processes for the Cretaceous orogeny of the Alps. *Mémoires de la Société Géologique de France*, 156:345–367, 1990.

F. F. Pollitz. Transient rheology of the uppermost mantle beneath the Mojave Desert, California. *Earth and Planetary Science Letters*, 215(1-2):89–104, 2003. doi: 10.1016/S0012-821X(03)00432-1.

A. A. Popov and S. V. Sobolev. SLIM3D: A tool for three-dimensional thermomechanical modeling of lithospheric deformation with elasto-visco-plastic rheology. *Physics of the Earth and Planetary Interiors*, 171(1-4):55–75, 2008. doi: 10.1016/j.pepi.2008.03.007.

A. Post and J. Tullis. A recrystallized grain size piezometer for experimentally deformed feldspar aggregates. *Tectonophysics*, 303(1-4):159–173, 1999. doi: 10.1016/S0040-1951(98)00260-1.

J. Precigout, F. Gueydan, D. Gapais, C. J. Garrido, and A. Essaifi. Strain localisation in the subcontinental mantle - a ductile alternative to the brittle mantle. *Tectonophysics*, 445(3-4):318–336, 2007. doi: 10.1016/j.tecto.2007.09.002.

J. B. Price, B. P. Wernicke, M. A. Cosca, and K. A. Farley. Thermochronometry Across the Austroalpine-Pennine Boundary, Central Alps, Switzerland: Orogen-Perpendicular Normal Fault Slip on a Major "Overthrust" and Its Implications for Orogenesis. *Tectonics*, 37(3):724–757, 2018. doi: 10.1002/2017TC004619.

R. Rageth. Intrusiva und Extrusiva der Bernina-Decke zwischen Morteratsch und Berninapass (Graubunden). *Schweizerische Mineralogische und Petrographische Mitteilungen*, 64:83–109, 1984.

R. Raj. Creep in polycrystalline aggregates by matter transport through a liquid phase. *Journal of Geophysical Research: Solid Earth*, 87(B6):4731–4739, 1982. doi: 10.1029/JB087iB06p04731.

R. Raj and M. F. Ashby. On grain boundary sliding and diffusional creep. *Metallurgical Transactions*, 2(4):1113–1127, 1971. doi: 10.1007/BF02664244.

R. Raj and C. K. Chyung. Solution-precipitation creep in glass ceramics. *Acta Metallurgica*, 29(1):159–166, 1981. doi: 10.1016/0001-6160(81)90096-1.

G. Ranalli. *Rheology of the Earth*. Chapman & Hall, London, UK, 2nd edition, 1995. ISBN 978-0-412-54670-9.

L. Ratschbacher. Kinematics of Asutro-Alpine cover nappes: changing translation path due to transpression. *Tectonophysics*, 125:335–356, 1986. doi: 10.1016/0040-1951(86)90170-8.

J. E. Reber and M. Pec. Comparison of brittle- and viscous creep in quartzites: Implications for semi-brittle flow of rocks. *Journal of Structural Geology*, 113(May):90–99, 2018. doi: 10.1016/j.jsg.2018.05.022.

J. E. Reber, N. W. Hayman, and L. L. Lavier. Stick-slip and creep behavior in lubricated granular material: Insights into the brittle-ductile transition. *Geophysical Research Letters*, 41(10):3471–3477, 2014. doi: 10.1002/2014GL059832.

J. E. Reber, L. L. Lavier, and N. W. Hayman. Experimental demonstration of a semi-brittle origin for crustal strain transients. *Nature Geoscience*, 8(9):712–715, 2015. doi: 10.1038/ngeo2496.

K. Regenauer-Lieb, D. A. Yuen, and J. Branlund. The initiation of subduction: Criticality by addition of water? *Science*, 294(5542):578–580, 2001. doi: 10.1126/science.1063891.

H. F. Reid. The Elastic-Rebound Theory of Earthquakes. *Bulletin of the Department of Geology, University of California Publications*, vol. 6, no:413–444, 1911.

A. Reuss. Berechnung der Fließgrenze von Mischkristallen auf Grund der Plastizitätsbedingung für Einkristalle. *ZAMM - Journal of Applied Mathematics and Mechanics / Zeitschrift für Angewandte Mathematik und Mechanik*, 9(1):49–58, 1929. doi: 10.1002/zamm.19290090104.

J. R. Rice, N. Lapusta, and K. Ranjith. Rate and state dependent friction and the stability of sliding between elastically deformable solids. *Journal of the Mechanics and Physics of Solids*, 49(9):1865–1898, 2001. doi: 10.1016/S0022-5096(01)00042-4.

U. Ring, L. Ratschbacher, and W. Frisch. Plate-boundary kinematics in the Alps: motion in the Arosa suture zone. *Geology*, 16(8):696–698, 1988. doi: 10.1130/0091-7613(1988)016<0696:PBKITA>2.3.CO;2.

U. Ring, L. Ratschbacher, W. Frisch, D. Biehler, and M. Kralik. Kinematics of the Alpine plate-margin: structural styles, strain and motion along the Penninic-Austroalpine boundary in the Swiss-Austrian Alps. *Journal of the Geological Society, London*, 146:835–849, 1989. doi: 10.1038/341576c0.

U. Ring, L. Ratschbacher, W. Frisch, S. DÜrr, and S. Borchert. The internal structure of the Arosa Zone (Swiss-Austrian Alps). *Geologische Rundschau*, 79(3):725–739, 1990. doi: 10.1007/BF01879211.

P. Y. F. Robin. Pressure solution at grain-to-grain contacts. *Geochimica et Cosmochimica Acta*, 42(9):1383–1389, 1978. doi: 10.1016/0016-7037(78)90043-1.

G. Rogers and H. Dragert. Episodic tremor and slip on the Cascadia subduction zone: The chatter of silent slip. *Science*, 300(5627):1942–1943, 2003. doi: 10.1126/science.1084783.

C. D. Rowe, J. C. Moore, F. Meneghini, and A. W. McKeirnan. Large-scale pseudotachylytes and fluidized cataclasites from an ancient subduction thrust fault. *Geology*, 33(12):937–940, 2005. doi: 10.1130/G21856.1.

C. D. Rowe, J. C. Moore, and F. Remitti. The thickness of subduction plate boundary faults from the seafloor into the seismogenic zone. *Geology*, 41(9):991–994, 2013. doi: 10.1130/G34556.1.

C. D. Rowe, W. A. Griffith, and W. A. Grif. Do faults preserve a record of seismic slip: A second opinion. *Journal of Structural Geology*, 78:1–26, 2015. doi: 10.1016/j.jsg.2015.06.006.

D. Rubatto, Gebauer D., and C. R. Dating of low-temperature and high-pressure metamorphic zircoons: the age of Alpine metamorphism in the Sesia-Lanzo zone (Western Alps). *Earth and Planetary Science Letters*, 167:141–158, 1999.

A. M. Rubin. Episodic slow slip events and rate-and-state friction. *Journal of Geophysical Research: Solid Earth*, 113(July):1–18, 2008. doi: 10.1029/2008JB005642.

J. B. Ruh, L. Le Pourhiet, P. Agard, E. Burov, and T. Gerya. Tectonic slicing of subducting oceanic crust along plate interfaces: Numerical modeling. *Geochemistry, Geophysics, Geosystems*, 16(10):3505–3531, 2015. doi: 10.1002/2015GC005998.

A. Ruina. Slip instability and state variable friction laws. *Journal of Geophysical Research*, 88 (B12):10359–10370, 1983. doi: 10.1029/JB088iB12p10359.

E. H. Rutter. Experimental study of the influence of stress, temperature, and strain on the dynamic recrystallization of Carrara marble. *Journal of Geophysical Research*, 100(B12), 1995. doi: 10.1029/95jb02500.

E. H. Rutter and K. H. Brodie. Experimental intracrystalline plastic flow in hot-pressed synthetic quartzite prepared from Brazilian quartz crystals. *Journal of Structural Geology*, 26 (2):259–270, 2004a. doi: 10.1016/S0191-8141(03)00096-8.

E. H. Rutter and K. H. Brodie. Experimental grain size-sensitive flow of hot-pressed Brazilian quartz aggregates. *Journal of Structural Geology*, 26(11):2011–2023, 2004b. doi: 10.1016/j.jsg.2004.04.006.

E. H. Rutter, M. Casey, and L. Burlini. Preferred crystallographic orientation development during the plastic and superplastic flow of calcite rocks. *Journal of Structural Geology*, 16 (10):1431–1446, 1994. doi: 10.1016/0191-8141(94)90007-8.

D. M. Saffer and H. J. Tobin. Hydrogeology and Mechanics of Subduction Zone Forearcs: Fluid Flow and Pore Pressure. *Annual Review of Earth and Planetary Sciences*, 39(1):157–186, 2011. doi: 10.1146/annurev-earth-040610-133408.

D. M. Saffer and L. M. Wallace. The frictional, hydrologic, metamorphic and thermal habitat of shallow slow earthquakes. *Nature Geoscience*, 8(8):594–600, 2015. doi: 10.1038/ngeo2490.

J. C. Savage. Postseismic relaxation associated with transient creep rheology. *Journal of Geophysical Research: Solid Earth*, 112(5), 2007. doi: 10.1029/2006JB004688.

S. Scaillet. Excess 40Ar transport scale and mechanism in high-pressure phengites: A case study from an eclogitized metabasite of the Dora-Maira nappe, western Alps. *Geochimica et Cosmochimica Acta*, 60(6):1075–1090, 1996. doi: 10.1016/0016-7037(95)00440-8.

M. Scambelluri and P. Philippot. Deep fluids in subduction zones. *Lithos*, 55(1-4):213–227, 2001. doi: 10.1016/S0024-4937(00)00046-3.

M. Scambelluri, J. Fiebig, N. Malaspina, O. Müntener, and T. Pettke. Serpentinite Subduction: Implications for Fluid Processes and Trace-Element Recycling. *International Geology Review*, 46(7):595–613, 2004. doi: 10.2747/0020-6814.46.7.595.

S. Schmid, J. Boland, and M. Paterson. Superplastic flow in finegrained limestone. *Tectonophysics*, 43(3-4):257–291, 1977.

S. M. Schmid. Microfabric studies as indicators of deformation mechanisms and flow laws operative in mountain building. *Mountain building processes*, pages 95–110, 1982.

S. M. Schmid, M. S. Paterson, and J. N. Boland. High temperature flow and dynamic recrystallization in carrara marble. *Tectonophysics*, 65(3-4):245–280, 1980. doi: 10.1016/0040-1951(80)90077-3.

S. M. Schmid, O. A. Pfiffner, N. Froitzheim, G. Schönborn, and E. Kissling. Geophysical-geological transect and tectonic evolution of the Swiss-Italian Alps. *Tectonics*, 15(5):1036–1064, 1996. doi: 10.1029/96TC00433.

S. M. Schmid, B. Fügenschuh, E. Kissling, and R. Schuster. Tectonic map and overall architecture of the Alpine orogen. *Eclogae Geologicae Helvetiae*, 97(1):93–117, 2004. doi: 10.1007/s00015-004-1113-x.

C. H. Scholz. Earthquakes and friction laws. *Nature*, 391(6662):37–42, 1998. doi: 10.1038/34097.

C. H. Scholz. *The Mechanics of Earthquakes and Faulting*. Cambridge University Press, 2002. ISBN 9780521652230. doi: 10.1017/CBO9780511818516.

S. Schwartz, S. Guillot, B. Reynard, R. Lafay, B. Debret, C. Nicollet, P. Lanari, and A. L. Auzende. Pressure-temperature estimates of the lizardite/antigorite transition in high pressure serpentinites. *Lithos*, 178:197–210, 2013. doi: 10.1016/j.lithos.2012.11.023.

W. H. Schwarz and M. Trieloff. Intercalibration of 40Ar-39Ar age standards NL-25, HB3gr hornblende, GA1550, SB-3, HD-B1 biotite and BMus/2 muscovite. *Chemical Geology*, 242 (1-2):218–231, 2007. doi: 10.1016/j.chemgeo.2007.03.016.

P. Segall and A. M. Bradley. Slow-slip evolves into megathrust earthquakes in 2D numerical simulations. *Geophysical Research Letters*, 39(17), 2012. doi: 10.1029/2012GL052811.

T. Seno. Determination of the pore fluid pressure ratio at seismogenic megathrusts in subduction zones: Implications for strength of asperities and Andean-type mountain building. *Journal of Geophysical Research: Solid Earth*, 114(5):1–25, 2009. doi: 10.1029/2008JB005889.

D. R. Shelly, G. C. Beroza, S. Ide, and S. Nakamula. Low-frequency earthquakes in Shikoku, Japan, and their relationship to episodic tremor and slip. *Nature*, 442(7099):188–191, 2006. doi: 10.1038/nature04931.

G. Shelton and J. Tullis. Shelton: Experimental flow laws for crustal rocks. *Eos Trans AGU*, 1981.

A. H. Shen and H. Keppler. Direct observation of complete miscibility in the albite-H2O system. *Nature*, 385(6618):710–712, 1997. doi: 10.1038/385710a0.

S. Sherlock and S. Kelley. Excess argon evolution in HP-LT rocks: A UVLAMP study of phengite and K-free minerals, NW Turkey. *Chemical Geology*, 182(2-4):619–636, 2002. doi: 10.1016/S0009-2541(01)00345-X.

I. Shimizu. Kinetics of pressure solution creep in quartz: theoretical considerations. *Tectonophysics*, 245(3-4):121–134, 1995. doi: 10.1016/0040-1951(94)00230-7.

R. L. Shreve and M. Cloos. Dynamics of sediment subduction, melange formation, and prism accretion. *Journal of Geophysical Research*, 91(B10):10229, 1986. doi: 10.1029/jb091ib10p10229.

R. H. Sibson. Roughness at the base of the seismogenic zone: contributing factors. *Journal of Geophysical Research*, 89(B7):5791–5799, 1984. doi: 10.1029/JB089iB07p05791.

R. H. Sibson. Stress switching in subduction forearcs: Implications for overpressure containment and strength cycling on megathrusts. *Tectonophysics*, 600:142–152, 2013. doi: 10.1016/j.tecto.2013.02.035.

C. Simpson. Deformation of granitic rocks across the brittle-ductile transition. *Journal of Structural Geology*, 7(5):503–511, 1985. doi: 10.1016/0191-8141(85)90023-9.

S. V. Sobolev and I. A. Muldashev. Modeling Seismic Cycles of Great Megathrust Earthquakes Across the Scales With Focus at Postseismic Phase. *Geochemistry, Geophysics, Geosystems*, 18(12):4387–4408, 2017. doi: 10.1002/2017GC007230.

P. Spillmann. *Die Geologie des Grenzbereichs im penninisch-ostalpinen südlichen Berninagebirge*. Phd thesis, ETH Zürich, 1993.

P. Spillmann and H. Büchi. The Pre-Alpine Basement of the Lower Austro-Alpine Nappes in the Bernina Massif (Grisons, Switzerland; Valtellina, Italy). In *von Raumer J.F., Neubauer F (eds) The Pre-Mesozoic Geology in the Alps*, pages 457–467. Springer, 1993. ISBN 978-3-642-84642-7. doi: 10.1007/978-3-642-84640-3_27.

G. A. Spinelli and D. M. Saffer. Along-strike variations in underthrust sediment dewatering on the Nicoya margin, Costa Rica related to the updip limit of seismicity. *Geophysical Research Letters*, 31(4), 2004. doi: 10.1029/2003GL018863.

M. Springer. Interpretation of heat-flow density in the Central Andes. In *Tectonophysics*, volume 306, pages 377–395, 1999. doi: 10.1016/S0040-1951(99)00067-0.

R. Staub. Geologische Karte der Berninagruppe 1:50'000. *Spez.-Karte Nr. 118, Scheiz. Geol. Kommission*, 1946.

R. J. Stern. Subduction zones. *Reviews of Geophysics*, 40(4):1395–1406, 2002. doi: 10.1029/2001RG000108.

R. N. Stevens. Grain boundary sliding and diffusion creep. *Surface Science*, 31(C):543–565, 1972. doi: 10.1016/0039-6028(72)90274-9.

M. Stipp, H. Stünitz, R. Heilbronner, and S. M. Schmid. The eastern Tonale fault zone : a 'natural laboratory' for crystal plastic deformation of quartz over a temperature range from 250 to 700°C. *Journal of Structural Geology*, 24:1861–1884, 2002. doi: 10.1016/j.scienta.2018.04.053.

M. Stipp, J. Tullis, M. Scherwath, and J. H. Behrmann. A new perspective on paleopiezometry: Dynamically recrystallized grain size distributions indicate mechanism changes. *Geology*, 38 (8):759–762, 2010. doi: 10.1130/G31162.1.

B. Stöckhert. Stress and deformation in subduction zones: insight from the re- cord of exhumed metamorphic rocks. In *Deformation Mechanisms, Rheology and Tectonics." Current Status and Future Perspectives*, volume 1, pages 162–164. 2002. ISBN 4444444444444. doi: 10.1144/GSL.SP.2001.200.01.15.

A. G. Sylvester. Strike-slip faults. *Bulletin of the Geological Society of America*, 100(11): 1666–1703, 1988. doi: 10.1130/0016-7606(1988)100<1666:SSF>2.3.CO;2.

E. M. Syracuse, P. E. van Keken, G. A. Abers, D. Suetsugu, C. Bina, T. Inoue, D. Wiens, M. Jellinek, P. E. V. Keken, and G. A. Abers. The global range of subduction zone thermal models. *Physics of the Earth and Planetary Interiors*, 183(1-2):73–90, 2010. doi: 10.1016/j.pepi.2010.02.004.

P. J. Tackley. Self-consistent generation of tectonic plates in three-dimensional mantle convection. *Earth and Planetary Science Letters*, 157(1-2):9–22, 1998. doi: 10.1016/S0012-821X(98)00029-6.

Y. Tatsumi. Migration of fluid phases and genesis of basalt magmas in subduction zones. *Journal of Geophysical Research*, 94(B4):4697–4707, 1989. doi: 10.1029/JB094iB04p04697.

C. Teyssier and B. Tikoff. Strike-slip partitioned transpression of the San Andreas fault system: a lithospheric-scale approach. *Geological Society Special Publication*, 135(1):143–158, 1998. doi: 10.1144/GSL.SP.1998.135.01.10.

B. W. Tichelaar and L. J. Ruff. Depth of seismic coupling along subduction zones. *Journal of Geophysical Research*, 1993. doi: 10.1029/92JB02045.

L. Tokle, G. Hirth, and W. Behr. Flow laws and fabric transitions in wet quartzite. *Earth and Planetary Science Letters*, 505:152–161, 2019. doi: 10.1016/j.epsl.2018.10.017.

V. Trommsdorff. Metamorphose magnesiumreicher Gesteine: Kritischer Vergleich von Natur, Experiments und thermodynamischer Datenbasis. *Fortschritte Der Mineralogie*, 61(2):283–308, 1983.

V. Trommsdorff and B. W. Evans. Antigorite-ophicarbonates: Contact metamorphism in

Valmalenco, Italy. *Contributions to Mineralogy and Petrology*, 62(3):301–312, 1977. doi: 10.1007/BF00371017.

V. Trommsdorff, G. B. Piccardo, and A. Montrasio. From magmatism through metamorphism to sea floor emplacement of subcontinental Adria lithosphere during pre-Alpine rifting. *Schweizerische Mineralogische Petrographische Mitteilungen*, 73:191–204, 1993.

V. Trommsdorff, A. Montrasio, J. Hermann, O. Müntener, P. Spillmann, and R. Gieré. The Geological Map of Valmalenco. *Schweizerische Mineralogische Und Petrographische Mitteilungen*, 85:1–13, 2005. doi: 10.1542/peds.2009-2791.

R. Trümpy. Penninic-Austroalpine Boundary in the Swiss Alps: A presumed Former Continental Margin and its Problems. *American Journal of Science*, 275-A:209–238, 1975.

J. A. Tullis. High temperature deformation of rocks and minerals, 1979.

T. E. Tullis, F. G. Horowitz, and J. Tullis. Flow laws of polyphase aggregates from end-member flow laws. *Journal of Geophysical Research*, 96(90):8081–8096, 1991. doi: 10.1029/90JB02491.

R. J. Twiss. Theory and applicability of a recrystallized grain size paleopiezometer. *Pure and Applied Geophysics*, 115(1-2):227–244, 1977. doi: 10.1007/BF01637105.

K. Ujiie, H. Saishu, Å. Fagereng, N. Nishiyama, M. Otsubo, H. Masuyama, and H. Kagi. An Explanation of Episodic Tremor and Slow Slip Constrained by Crack-Seal Veins and Viscous Shear in Subduction Mélange. *Geophysical Research Letters*, 45(11):5371–5379, 2018. doi: 10.1029/2018GL078374.

T. Ulrich and G. R. Borsien. Fedozer Metagabbro und Forno-Metabasalt (Val Malenco, Norditalien): Vergleichende Petrographische und Geochemische Untersuchungen. *Schweizerische mineralogische und petrographische Mitteilungen*, 76(3):521–535, 1996.

K. Uto, O. Ishizuka, A. Matsumoto, H. Kamioka, T. S, and S. Togashi. Laser-heating 40Ar/39Ar dating system of the Geological Survey of Japan: System outline and preliminary results. *Bulletin of the Geological Survey of Japan*, 48:23–46, 1997.

B. A. Van Der Pluijm. Marble mylonites in the Bancroft shear zone, Ontario, Canada: microstructures and deformation mechanisms. *Journal of Structural Geology*, 13(10):1125–1135, 1991. doi: 10.1016/0191-8141(91)90073-R.

D. Van der Wal, P. Chopra, M. Drury, and J. F. Gerald. Relationships between dynamically recrystallized grain size and deformation conditions in experimentally deformed olivine rocks. *Geophysical Research Letters*, 20(14):1479–1482, 1993. doi: 10.1029/93GL01382.

Y. Van Dinther, T. V. Gerya, L. A. Dalguer, P. M. Mai, G. Morra, and D. Giardini. The seismic cycle at subduction thrusts: Insights from seismo-thermo- mechanical models. *Journal of Geophysical Research: Solid Earth*, 118(12):6183–6202, 2013. doi: 10.1002/2013JB010380.

J. Van Hunen, A. P. Van Den Berg, and N. J. Vlaar. On the role of subducting oceanic plateaus in the development of shallow flat subduction. *Tectonophysics*, 352(3-4):317–333, 2002. doi: 10.1016/S0040-1951(02)00263-9.

P. E. van Keken, I. Wada, N. Sime, and G. A. Abers. Thermal Structure of the Forearc in Subduction Zones: A Comparison of Methodologies. *Geochemistry, Geophysics, Geosystems*, 20(7):3268–3288, 2019. doi: 10.1029/2019GC008334.

P. Vannucchi, F. Remitti, and G. Bettelli. Geological record of fluid flow and seismogenesis along an erosive subducting plate boundary. *Nature*, 451(February):699–703, 2008. doi: 10.1038/nature06486.

P. Vannucchi, F. Remitti, G. Bettelli, C. Boschi, and L. Dallai. Fluid history related to the early Eocene-middle Miocene convergent system of the Northern Apennines (Italy): Constraints from structural and isotopic studies. *Journal of Geophysical Research: Solid Earth*, 2010. doi: 10.1029/2009JB006590.

P. Vannucchi, F. Sage, J. Phipps Morgan, F. Remitti, and J. Y. Collot. Toward a dynamic concept of the subduction channel at erosive convergent margins with implications for interplate material transfer. *Geochemistry, Geophysics, Geosystems*, 13(1):1–24, 2012. doi: 10.1029/2011GC003846.

B. Velde. Phengite micas; synthesis, stability, and natural occurrence. *American Journal of Science*, 263(10):886–913, 1965. doi: 10.2475/ajs.263.10.886.

I. M. Villa. Isotopic closure. *Terra Nova*, 10(1):42–47, 1998. doi: 10.1046/j.1365-3121.1998.00156.x.

I. M. Villa. Ar geochronology of mono-and polymetamorphic basement rocks. *An International Journal of MINERALOGY*, 84:615–632, 2015. doi: 10.2451/2015PM0454.

I. M. Villa, J. Hermann, O. Müntener, and V. Trommsdorff. 39Ar-40Ar dating of multiply zoned amphibole generations (Malenco, Italian Alps). *Contributions to Mineralogy and Petrology*, 140(3):363–381, 2000. doi: 10.1007/s004100000197.

F. J. Vine and D. H. Matthews. Magnetic anomalies over oceanic ridges. *Nature*, 199(4897):947–949, 1963. doi: 10.1038/199947a0.

W. Voigt. *Lehrbuch der Kristallphysik*. Teubner, Leipzig, Germany, 1928.

R. von Huene and D. W. Scholl. Observations at convergent margins concerning sediment subduction, subduction erosion, and the growth of continental crust, 1991.

I. Wada, K. Wang, J. He, and R. D. Hyndman. Weakening of the subduction interface and its effects on surface heat flow, slab dehydration, and mantle wedge serpentinization. *Journal of Geophysical Research: Solid Earth*, 113(4):B04402, 2008. doi: 10.1029/2007JB005190.

J. Wakabayashi. Nappes, tectonics of oblique plate convergence, and metamorphic evolution related to 140 million years of continuous subduction, Franciscan Complex, California. *Journal of Geology*, 100(1):19–40, 1992. doi: 10.1086/629569.

L. M. Wallace, Å. Fagereng, and S. Ellis. Upper plate tectonic stress state may influence interseismic coupling on subduction megathrusts. *Geology*, 40(10):895–898, 2012. doi: 10.1130/G33373.1.

J. G. Wang and R. Raj. Mechanism of superplastic flow in a finegrained ceramic containing some liquid phase. *Journal of the American Ceramic Society*, 67:399–409, 1984.

J. N. Wang and T. G. Nieh. Role of Peierls stress in power law dislocation creep. *Materials Science and Engineering A*, 202(1-2):52–56, 1995. doi: 10.1016/0921-5093(95)09789-9.

K. Wang. Elastic and viscoelastic models of crustal deformation in subduction earthquake cycles. *The seismogenic zone of subduction thrust faults*, pages 540–575, 2007. doi: 10.7312/dixo13866-017.

K. Wang and Y. Hu. Accretionary prisms in subduction earthquake cycles: The theory of dynamic Coulomb wedge. *Journal of Geophysical Research: Solid Earth*, 111(6), 2006. doi: 10.1029/2005JB004094.

K. Wang and A. M. Tréhu. Invited review paper: Some outstanding issues in the study of great megathrust earthquakes-The Cascadia example, 2016.

K. Wang, Y. Hu, and J. He. Deformation cycles of subduction earthquakes in a viscoelastic Earth. *Nature*, 484(7394):327–332, 2012. doi: 10.1038/nature11032.

S. Wassmann and B. Stöckhert. Low stress deformation of garnet by incongruent dissolution precipitation creep. *Journal of Structural Geology*, 46:200–219, 2013a.

S. Wassmann and B. Stöckhert. Rheology of the plate interface - Dissolution precipitation creep in high pressure metamorphic rocks. *Tectonophysics*, 608:1–29, 2013b. doi: 10.1016/j.tecto.2013.09.030.

L. Watremez, E. Burov, E. D'Acremont, S. Leroy, B. Huet, L. Le Pourhiet, and N. Bellahsen. Buoyancy and localizing properties of continental mantle lithosphere: Insights from thermo-mechanical models of the eastern Gulf of Aden. *Geochemistry, Geophysics, Geosystems*, 14 (8):2800–2817, 2013. doi: 10.1002/ggge.20179.

S. Webber, S. Ellis, and Å. Fagereng. "Virtual shear box" experiments of stress and slip cycling within a subduction interface mélange. *Earth and Planetary Science Letters*, 488:27–35, 2018. doi: 10.1016/j.epsl.2018.01.035.

H. Wellman and R. Willett. The geology of the west coast from Abut Head to Milford Sound. *Transactions of the Royal Society of New Zealand. 199-219.*, pages 199–219, 1942.

J. Wheeler. Structural evolution of a subducted continental sliver: The northern Dora Maira massif, Italian Alps. *Journal of the Geological Society*, 148(6):1101–1113, 1991. doi: 10.1144/gsjgs.148.6.1101.

J. Wheeler. Importance of pressure solution and coble creep in the deformation of polymineralic rocks. *Journal of Geophysical Research*, 97(B4):4579–4586, 1992. doi: 10.1029/91JB02476.

J. C. White. Paradoxical pseudotachylyte - Fault melt outside the seismogenic zone. *Journal of Structural Geology*, 38:11–20, 2012. doi: 10.1016/j.jsg.2011.11.016.

R. S. White. Atlantic oceanic crust: Seismic structure of a slow-spreading ridge. *Geological Society Special Publication*, 13:101–111, 1984. doi: 10.1144/GSL.SP.1984.013.01.09.

S. H. White, S. E. Burrows, J. Carreras, N. D. Shaw, and F. J. Humphreys. On mylonites in ductile shear zones. *Journal of Structural Geology*, 2(1-2):175–187, 1980. doi: 10.1016/0191-8141(80)90048-6.

D. L. Whitney and B. W. Evans. Abbreviations for names of rock-forming minerals. *American Mineralogist*, 95(1):185–187, 2010. doi: 10.2138/am.2010.3371.

M. Wiederkehr, M. Sudo, R. Bousquet, A. Berger, and S. M. Schmid. Alpine orogenic evolution from subduction to collisional thermal overprint: The 40Ar/39Ar age constraints from the Valaisan Ocean , central Alps. *Tectonics*, 28(6), 2009. doi: 10.1029/2009TC002496.

F. D. Wilke, P. J. O'Brien, A. Gerdes, M. J. Timmerman, M. Sudo, and M. A. Khan. The multistage exhumation history of the Kaghan Valley UHP series, NW Himalaya, Pakistan from U-Pb and 40Ar/39Ar ages. *European Journal of Mineralogy*, 22(5):703–719, 2010. doi: 10.1127/0935-1221/2010/0022-2051.

J. T. Wilson. A new class of faults and their bearing on continental drift. *Nature*, 207(4995):343–347, 1965. doi: 10.1038/207343a0.

X. Xiao, R. Wirth, and G. Dresen. Diffusion creep of anorthite-quartz aggregates. *Journal of Geophysical Research: Solid Earth*, 107(B11):ECV 6–1–ECV 6–15, 2002. doi: 10.1029/2001JB000789.

A. Yamaguchi, T. Ishikawa, Y. Kato, T. Nozaki, F. Meneghini, C. D. Rowe, J. C. Moore, A. Tsutsumi, and G. Kimura. Fluid-rock interaction recorded in black fault rocks in the Kodiak accretionary complex, Alaska. *Earth, Planets and Space*, 66(1):58, 2014. doi: 10.1186/1880-5981-66-58.

P. Yamato, P. Agard, E. Burov, L. Le Pourhiet, L. Jolivet, and C. Tiberi. Burial and exhumation in a subduction wedge: Mutual constraints from thermomechanical modeling and natural P-T-t data (Schistes Lustrés, western Alps). *Journal of Geophysical Research: Solid Earth*, 112 (7):1–28, 2007. doi: 10.1029/2006JB004441.

K. Ye, Y. Yao, I. Katayama, B. Cong, Q. Wang, and S. Maruyama. Large areal extent of ultrahigh-pressure metamorphism in the Sulu ultrahigh-pressure terrane of East China: New implications from coesite and omphacite inclusions in zircon of granitic gneiss. *Lithos*, 52 (1-4):157–164, 2000a. doi: 10.1016/S0024-4937(99)00089-4.

K. Ye, Y. Yao, I. Katayama, B. Cong, Q. Wang, and S. Maruyama. Large areal extent of ultrahigh-pressure metamorphism in the Sulu ultrahigh-pressure terrane of East China: New implications from coesite and omphacite inclusions in zircon of granitic gneiss. *Lithos*, 52 (1-4):157–164, 2000b. doi: 10.1016/S0024-4937(99)00089-4.

T. Zack and T. John. An evaluation of reactive fluid flow and trace element mobility in subducting slabs. *Chemical Geology*, 239(3-4):199–216, 2007. doi: 10.1016/j.chemgeo.2006.10.020.

M. G. Zelin and A. K. Mukherjee. Superplasticity at different microstructural scales. *Materials Science Forum*, 170-172:29–38, 1994. doi: 10.4028/www.scientific.net/msf.170-172.29.

D. Zhao, O. P. Mishra, and R. Sanda. Influence of fluids and magma on earthquakes: Seismological evidence. *Physics of the Earth and Planetary Interiors*, 132(4):249–267, 2002. doi: 10.1016/S0031-9201(02)00082-1.

Zhong, Shijie and M. Gurnis. Controls on trench topography from dynamic models of subducted slabs. *Journal of Geophysical Research*, 99(B8), 1994. doi: 10.1029/94jb00809.

Appendix A

Appendix: Petrological data

A.1 Rb/Sr geochronology

Table A.1: Analytical data of Rb/Sr geochronology.

Sample no.	Material	Rb (ppm)	Sr (ppm)	$^{87}Rb/^{86}Sr$	$^{87}Sr/^{86}Sr$	$^{87}Sr/^{86}Sr$ $2\sigma_m$ (%)
Analysis no.						
#01A (disequilibria; max. age* = 44.0 ± 0.74 Ma)						
PS2840	wm 125-90 μm	209	61.5	9.86	0.725047	0.0018
PS2838	apatite	5.88	2410	0.00706	0.718988	0.0011
PS2839	feldspar	9.33	82.5	0.328	0.718093	0.0025
PS2840	wm 125-90 μm	209	61.5	9.86	0.725047	0.0018
PS2841	wm 355-250 μm	307	26.7	33.3	0.748662	0.0016
PS2842	wm 500-355 μm	306	30.9	28.8	0.744595	0.0022
#01F (disequilibria; max. age* = 54.3 ± 1.1 Ma)						
PS2825	feldspar	2.9	65.1	0.129	0.71305	0.0027
PS2826	wm 355-250 μm	347	218	4.6	0.716726	0.0018
PS2827	wm 500-355 μm	350	213	4.75	0.716893	0.002
PS2828	wm 125-90 μm	296	175	4.9	0.716674	0.0022
PS2829	wm 250-125 μm	331	203	4.73	0.716662	0.0014
PS2830	apatite	0.48	1652	0.00085	0.712138	0.0013
PS2831	titanite	1.43	66.7	0.062	0.710473	0.001
#02 (disequilibria; max. age* = 78.9 ± 1.8 Ma)						
PS2832	feldspar	13.6	30.6	1.29	0.730217	0.0014
PS2833	wm 125-90 μm	299	158	5.49	0.734855	0.0018
PS2834	wm 500-355 μm	355	166	6.2	0.736391	0.0012
PS2835	apatite	1.89	1479	0.0037	0.728496	0.0023
PS2836	wm 355-250 μm	364	170	6.22	0.736267	0.0012
PS2837	wm 250-125 μm	360	172	6.06	0.735831	0.0016
#23B (disequilibria; 184 ± 71 Ma)						
PS2819	wm 500-355 μm	359	69.9	14.9	0.766369	0.0018
PS2820	wm 250-125 μm	338	57.9	17	0.765286	0.0015
PS2821	feldspar	9.67	45.6	0.615	0.72684	0.0014
PS2822	apatite	8.74	1602	0.0158	0.71926	0.0015
PS2823	wm 355-250 μm	352	62	16.5	0.772152	0.0022
PS2824	wm 125-90 μm	318	52.4	17.7	0.758682	0.002
#13 (48.9 ± 0.9 Ma)						
PS3130	white leach residue	4.09	0.77	15.4	0.721748	0.0014
PS3131	wm 125-90 μm	333	16.5	58.5	0.7507	0.0009
PS3132	wm 160-125 μm	348	15.9	63.7	0.754162	0.0022
PS3133	cc-wr-1	3.07	116	0.0764	0.710336	0.002
PS3136	wm 90-63 μm	335	17.2	56.7	0.749142	0.0016
PS3137	cc-wr-2	3.68	157	0.0677	0.710694	0.0017
PS3139	wm >160 μm	341	14.9	66.7	0.756282	0.0026

* max. age refers to the maximum age for the end of deformation.

A.2 XRF data

Table A.2: XRF bulk rock chemical analyses.

Sample	SiO_2	TiO_2	Al_2O_3	Fe_2O_3	MnO	MgO	CaO	Na2O	K_2O	P_2O_5	LOI Tiegel	Sum
	(%)	(%)	(%)	(%)	(%)	(%)	(%)	(%)	(%)	(%)	(%)	(%)
#01A	68.5	0.45	15.7	3.00	0.031	1.00	0.71	4.35	3.91	0.221	1.84	99.70
#01B	80.5	0.364	7.9	3.35	0.038	1.36	1.04	0.16	2.14	0.215	2.62	99.61
#23B	59.1	0.794	18.2	8.19	0.108	3.16	0.65	2.52	3.67	0.152	2.68	99.28
	Ba	Cr	Ga	Nb	Ni	Rb	Sr	V	Y	Zn	Zr	
	(ppm)	(ppm)	(ppm)	(ppm)	(ppm)	(ppm)	(ppm)	(ppm)	(ppm)	(ppm)	(ppm)	
#01A	922	23	19	14	<10	123	94	37	42	27	202	
#01B	385	458	12	<10	19	85	165	609	54	51	88	
#23B	2697	98	22	13	32	121	72	124	33	123	138	

A.3 P-T pseudosections

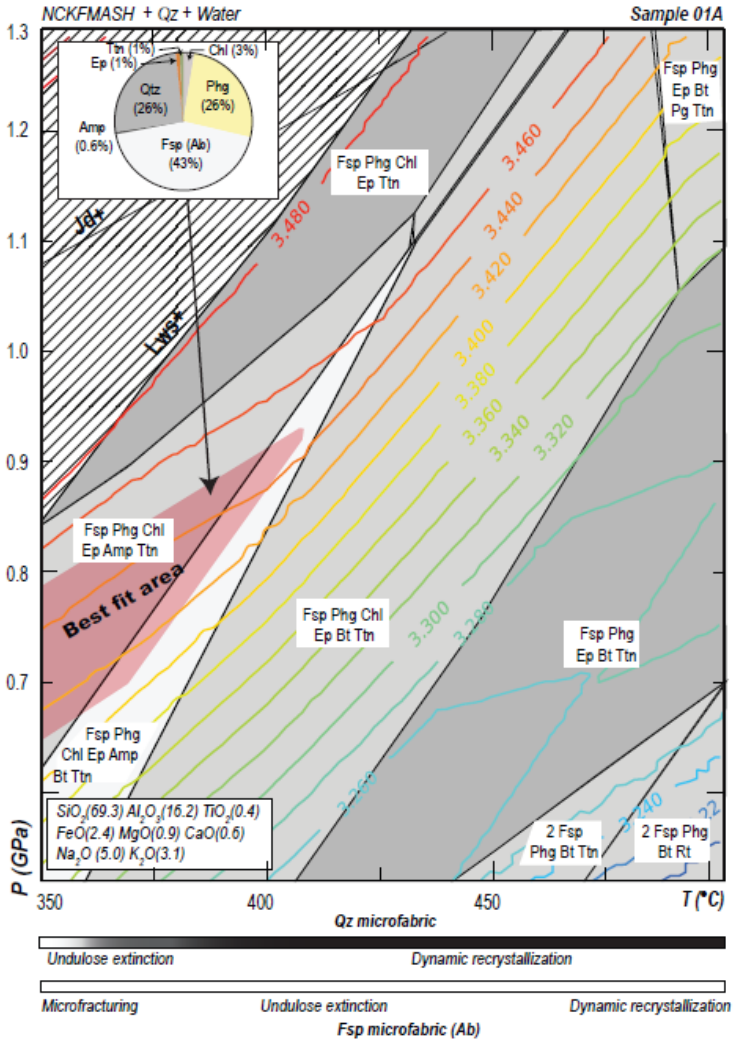

Figure A.1: P-T pseudosection in the NCKFMASH system (plus Qz and water) for sample #01A, showing the phase relationships and the best-fit area (red polygon). The colored lines are the phengite silica content isopleths, each corresponding to the annotated silica content.

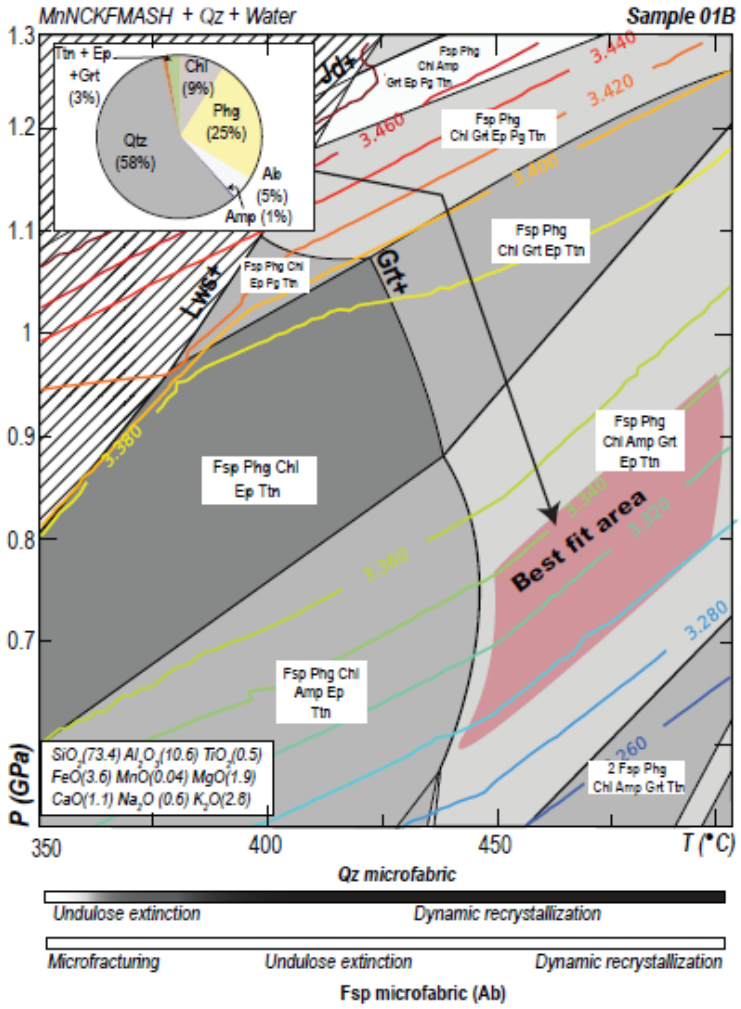

Figure A.2: P-T pseudosection in the NCKFMASH system (plus Qz and water) for sample #01B, showing the phase relationships and the best-fit area (red polygon). The colored lines are the phengite silica content isopleths, each corresponding to the annotated silica content.

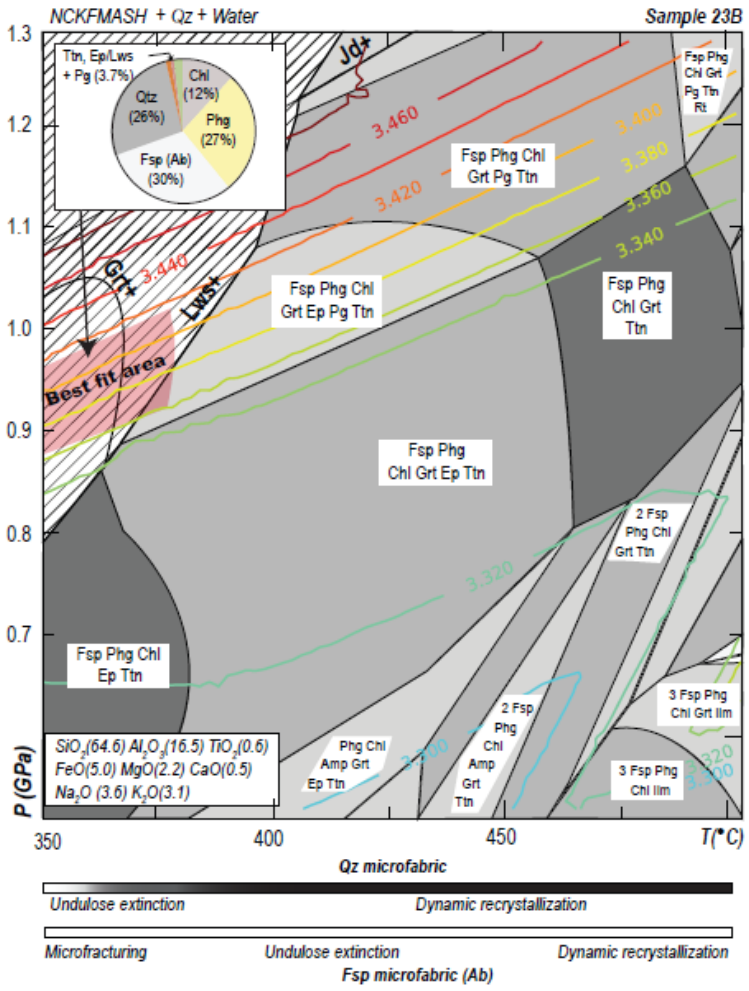

Figure A.3: P-T pseudosection in the NCKFMASH system (plus Qz and water) for sample #23B, showing the phase relationships and the best-fit area (red polygon). The colored lines are the phengite silica content isopleths, each corresponding to the annotated silica content.

Appendix B

Appendix: Numerical modelling data

B.1 Synthetic maps

I created two sets of synthetic maps, one consisting of ellipses, the other of circles. The blocks were allowed to be generated randomly within the model domain and the generation stopped when a specific amount of blocks was reached in each model (e.g. $\sim 10\%$ of ellipses or circles). In an effort to mimic the block size distribution observed by Grigull et al. (2012), the radius of the semi-major axis of the ellipses as well as the radius of the circles was allowed to vary between 15 and 265 units, in a total domain of 3000 units (or km). Finally, an aspect ratio between 1.5 and 3 was chosen for the ellipses, based on natural observations and the work of Grigull et al. (2012) and the orientation of the ellipses varied $\pm 15^{\circ}$ with respect to the the interface.

Table B.1: Percentages of strong and weak phases in synthetic and natural maps used in this study. SL: Schistes Lustrés, MU: Mugi Mélange, CL: Chrystalls Beach - low concentration, CA: Chrystalls Beach - medium concentration (A), CB: Chrystalls Beach - medium concentration (B), Chrystalls Beach - high concentration.

Circles	blocks	matrix
10	10.0%	90.0%
30	32.2%	67.8%
50	42.2%	57.8%
60	55.1%	44.9%
70	60.7%	39.3%
75	65.8%	34.2%
Ellipses	blocks	matrix
10	9.7%	90.3%
30	28.7%	71.3%
50	46.4%	53.6%
60	56.0%	44.0%
70	65.5%	34.5%
Natural	blocks	matrix
SL	6.0%	94.0%
MU	9.8%	90.2%
CL	12.6%	87.4%
CA	32.2%	67.8%
CB	33.5%	66.5%
CH	68.6%	31.4%

B.2 Tests

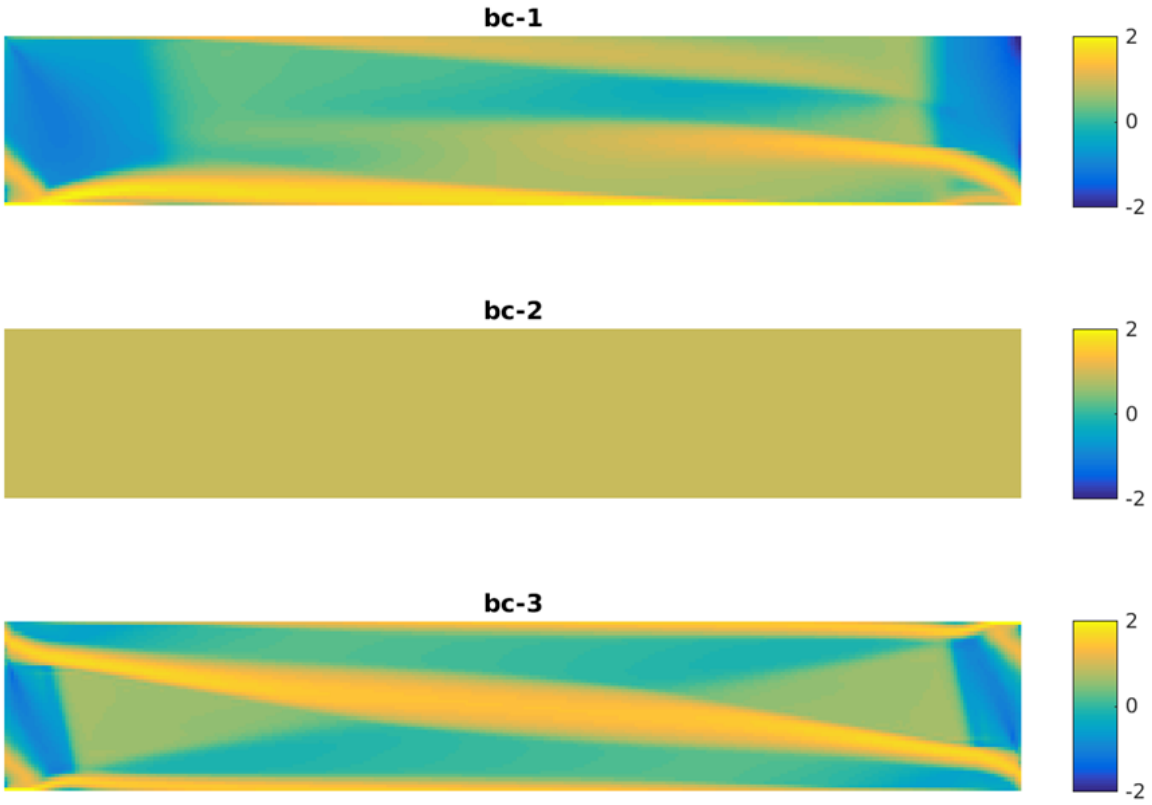

Figure B.1: Testing different boundary conditions for simple shear. Preferred boundary conditions are shown in the last row (*bc-3*). Colour bar shows the log of the normalized strain rate for each model.

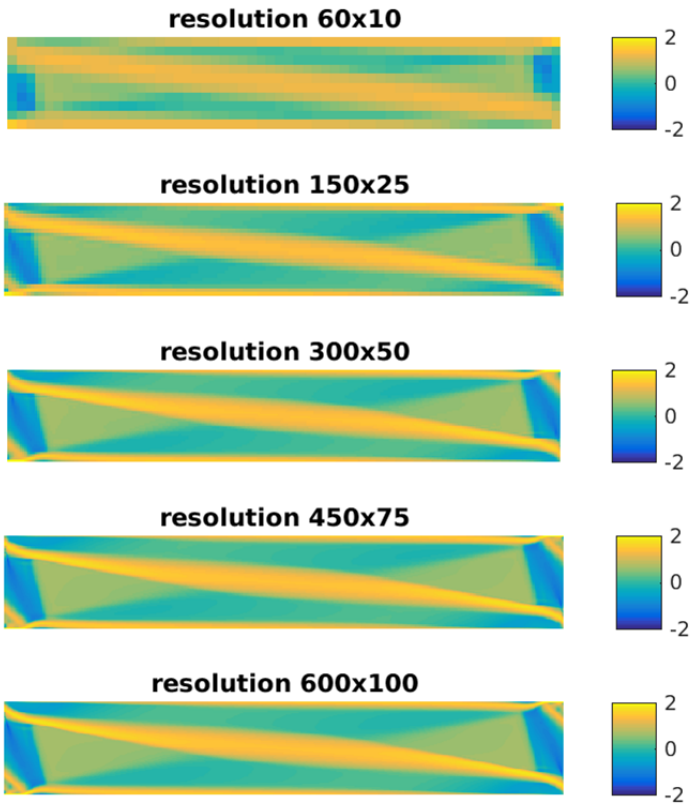

Figure B.2: Testing the resolution of the models. Preferred resolution is 450x75 Q_2 elements (second from the bottom). Colour bar shows the log of the normalized strain rate for each model.

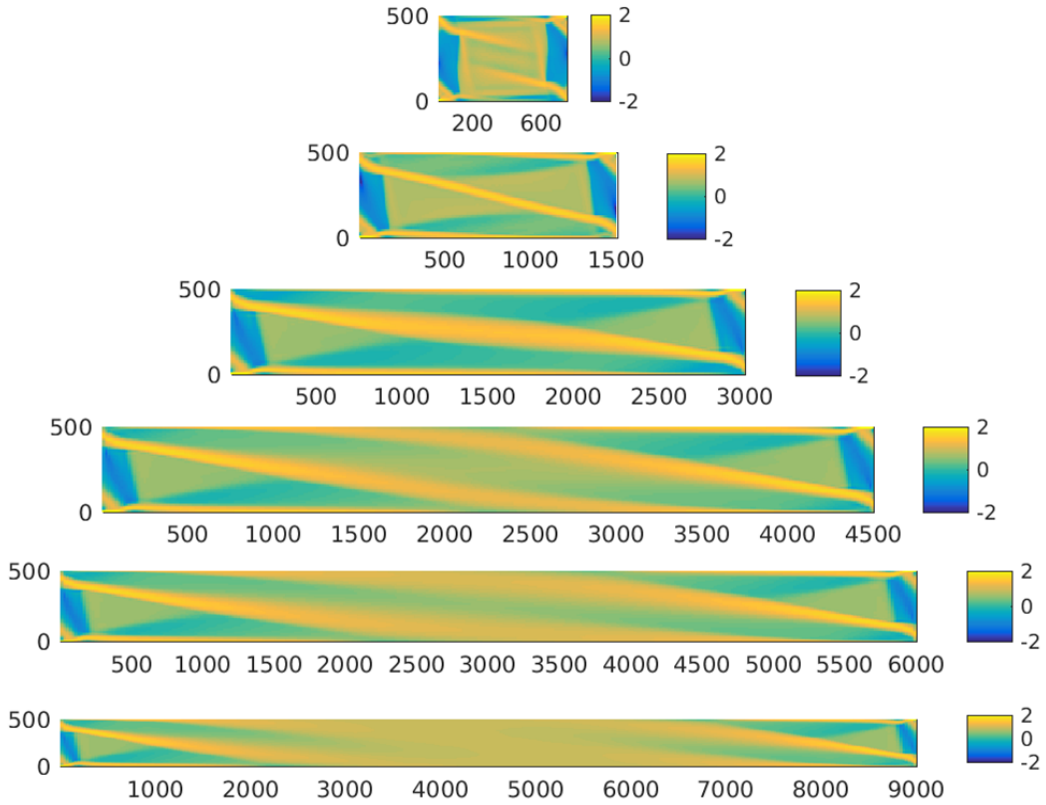

Figure B.3: Testing the length of the models. Preferred length is 3000x500 m (third from the top). Colour bar shows the log of the normalized strain rate for each model.

B.3 Calculating effective rheology

To calculate the parameters for the effective rheology of our models, I first examined which law described the bulk deformation of each one: I represented each model with the average of the second invariant of the shear stress and the average of the second invariant of the normal stress; each model falling on the straight line representing the yield surface in a 2D plot was considered frictional and hence excluded from the calculation of the effective viscous parameters, A, n and Q. All the remaining, non-frictional models were considered for calculating the viscous parameters. Dislocation creep is given by an equation of the form:

$$\dot{\varepsilon_{II}} = A\tau_{II}^{n} e^{\frac{-Q}{RT}}. \tag{B.1}$$

Taking the logarithm of Eq. B.1 gives:

$$log(\dot{\varepsilon_{II}}) = log(A) + nlog(\tau_{II}) - \frac{Q}{RT}log(e). \tag{B.2}$$

In a bi-logarithmic plot, the second invariant of the strain rate tensor, $\dot{\varepsilon_{II}}$, and the second invariant of the shear stress, τ_{II}, plot as a straight line, the slope of which provides the value of the effective stress exponent, n. Using this value and re-arranging Eq. B.1 gives:

$$ln(\dot{\varepsilon_{II}}) = ln(A) + nln(\tau_{II}) - \frac{Q}{RT}. \tag{B.3}$$

Thus, plotting the natural logarithm of $\dot{\varepsilon_{II}}$ over $(-1/RT)$ gives the value of the activation energy, Q. Finally, by substituting the calculated values of n and Q back into Eq. B.1, the pre-exponential factor, A, can be obtained.

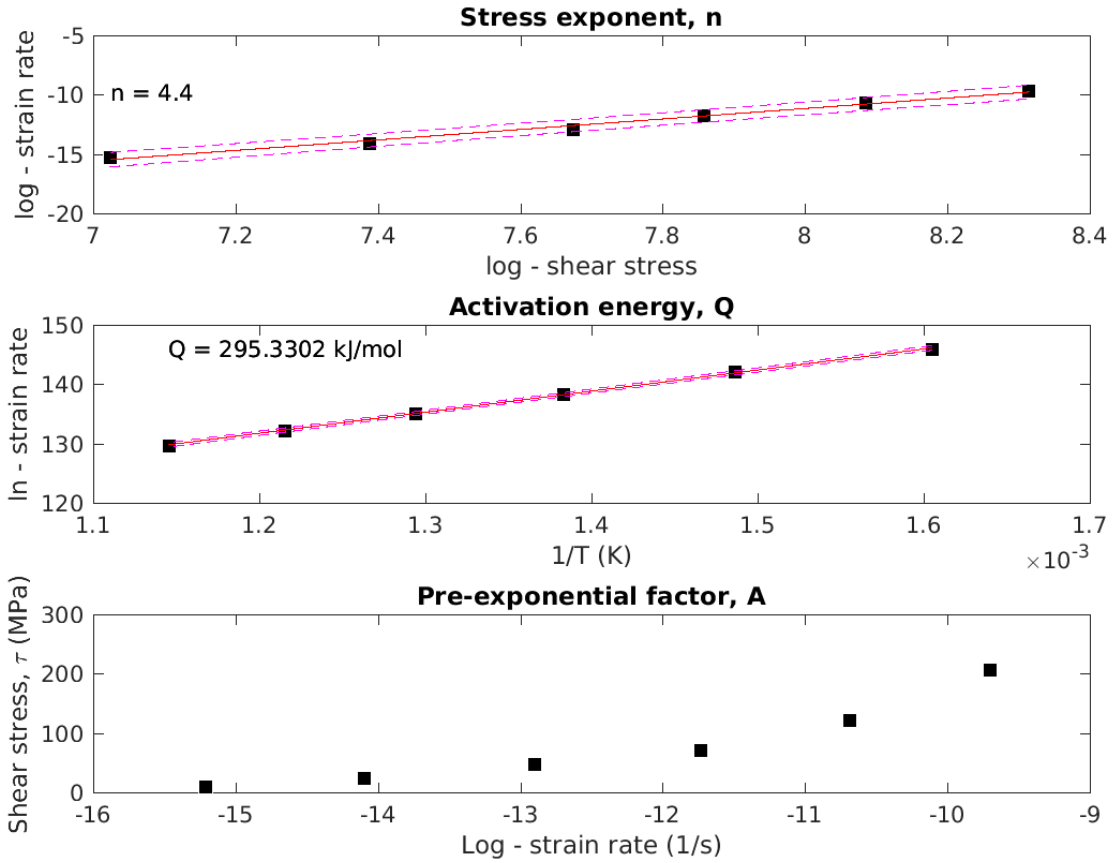

Figure B.4: Example of the plots used for calculating the effective dislocation creep parameters of our models. Showing the case of 60% ellipses.

Appendix C

Zusammenfassung

Subduktionszonen sind komplexe Systeme, in denen ein großer Teil der Deformation an der Grenzfläche beider Lithosphärenplatten lokalisiert ist. Folglich spielen die physischen Eigenschaften und die Rheologie dieser Grenzfläche eine entscheidende Rolle sowohl hinsichtlich der Deformation, des Grads der Verhakung und der Gleitprozesse während der Konvergenz als auch mit Blick auf großskalige Subduktionsprozesse. Im Laufe der letzten beiden Jahrzehnte wurden durch geodätische und geophysikalische Untersuchungen verschiedene Gleitmuster wie langsame Gleitvorgänge, episodische Tremore und episodisches Gleiten erkannt, deren grundlegende Prozesse sich uns jedoch noch nicht erschließen.

Da direkte Beobachtungen entlang aktiver Subduktionsgrenzflächen nicht möglich sind, ermöglichen Geländeuntersuchungen exhumierter Subduktionszonen wichtige Einblicke in die Art dieser transienten Vorgänge. Übereinstimmend legen die meisten Aufschlüsse nahe, dass die Subduktionsgrenzfläche relativ heterogen ist und verschiedene Einheiten umfasst, die während der Deformation unterschiedliches Verhalten zeigen. Jedoch sind diese Einheiten oft zu klein, um in einem großskaligen geodynamischen Model dargestellt zu werden und werden folglich in diesen auch nicht berücksichtigt. Aufschlussskalige numerische Experimente können in Verbindung mit Strukturbeobachtungen im Gelände zur Verfeinerung der in großskaligen geodynamischen Modellen genutzten Rheologien verwendet werden. Das für diese Arbeit verwendete Methodenspektrum umfasst Gelände-, petrologische und geochronologische Beobachtungen exhumierter Gesteine und aufschlussskalige numerische Berechnungen, die dazu dienen, die Rheologie der Plattengrenze, die wirkenden Deformationsmechanismen und deren zeitliche Abfolge

zu untersuchen.

Die europäischen Alpen sind ein großartiges natürliches Labor, in dem eine Subduktionsgrenzfläche fast vollständig aufgeschlossen ist, wodurch es möglich ist Deformationsprozesse in flachen bis tiefen Abschnitten einer Subduktionszone (von etwa 10 km bis etwa 45 km Tiefe) zu untersuchen. In dieser Arbeit wird ein Netzwerk fossiler Subduktionsgrenzflächen, das in den Zentralalpen (Val Malenco, Norditalien) aufgeschlossen ist, untersucht. Dies soll es ermöglichen, Prozesse an abtauchenden kontinentalen Krustenblöcken (die Margna Decke und die Sella Decke) in Tiefen, die denen des spröd-duktil Übergangs entsprechen, zu verstehen. Dieses Netzwerk umfasst Mylonite und Schiefer, aber auch vereinzelt Kataklasite mit Foliation. Zudem enthält es unterschiedliche Generationen von Glimmern und Granat, die lokal resorbierte prä-Alpine Bereiche Überwachsen. Thermodynamische Modellierung deutet auf eine maximale Versenkungstiefe von ca. 30 km mit einem Druck von $\sim$ 0.9 GPa und einer Temperatur von 350-400°C hin. Während geochronologische Untersuchungen des Rb/Sr-Systems an Marmoren ein Alter von 48.9 $\pm$ 0.9 Ma offenbaren, führt unvollständige Rekristallisation in deformierten Orthogneisen und Glimmerschiefern zu einer großen Spanne scheinbarer Rb/Sr- und $^{40}Ar/^{39}Ar$-Alter von 87-44 Ma. Basierend auf Druck-, Temperatur-, strukturellen und geochronologischen Untersuchungen kann angenommen werden, dass die untersuchte Scherzone das letzte Mal unterhalb der seismogenen Zone in einer aktiven Subduktionszone im Gleichgewicht war. Mikrostrukturen zeigen, dass Fluide die Rheologie dieser Schnittstelle durch Drucklösungskriechen beeinflussen. Diese Studie legt nahe, dass in dieser Scherzone Deformationsbedingungen festgehalten wurden, wie sie entlang einer Subduktionszone unterhalb der seismogenen Zone in einem Bereich, in dem transientes Gleiten auftritt, während aktiver Subduktion anzutreffen sind.

Andere aufgeschlossene Subduktionsgrenzflächen zeigen "block-in-matrix" Charakteristika, die als Mélange bezeichnet werden, und deren Gehalt von Blöcken die Gesamtrheologie beeinflussen können. Um dies zu untersuchen, wurden synthetische Modelle erstellt, die unterschiedliche Anteile kompetenter, in eine weiche Matrix eingebetteter Blöcke enthalten. Diese wurden mit exhumierten natürlichen Mélange-Aufschlüssen verglichen. 2D Finete-Elemente visco-plastische Modelle mit nicht-koaxialer Scherung erlaubten die Bestimmung der effektiven rheologischen Paramter solcher Zwei-Phasen-Medien, die aus Basaltblöcken innerhalb einer nassen quarzi-

tischen Matrix bestehen. Diese Modelle und ihre Strukturen werden als skaleninvariant und selbstähnlich betrachtet. Darüber hinaus werden Geländebeziehungen auf km-skalige Modelle, die mit großskaligen geodätischen und geophysikalischen Beobachtungen vergleichbar sind, hochskaliert. Aufschlüsse von Mélanges sowie anderer Einheiten, die während der Subduktion deformiert wurden, legen nahe, dass der wesentliche Deformationsmechanismus Lösungs-Fällungs-Kriechen ist. Jedoch sind Fließgesetze für Lösungs-Fällungs-Kriechen experimentell nicht gut bestimmt und werden in großskaligen numerischen Modellen nur selten verwendet. Um diese Ergebnisse vergleichbar mit und nutzbar für numerische Untersuchungen zu machen, nehmen wir Lösungskriechen als bestimmendes Fließgesetz unserer beiden Phasen (Basalt und nasser Quarz) an und ermöglichen damit die Abschätzung tatsächlicher Rheologien für eine natürliche Subduktionszone. Unsere Ergebnisse legen nahe, dass die Konzentration der Blöcke die Deformation und die Lokalisierung der Verformung beeinflusst. Die Parameter für das effektive Versetzungskriechen (A, n und Q) variieren und nehmen Werte an, die zwischen denen der kompetenten und der schwachen Phase liegen, wenn beide Phasen viskos deformiert werden. Allerdings kann mit Zunahme des Anteils spröder Deformation der Basaltblöcke der Wert des Spannungsexponenten, n, denjenigen der kompetenten Phase Überschreiten. Das Verwenden dieser effektiven Parameter in Modellen des seismischen Zyklus könnte dabei helfen den möglichen Einfluss von Heterogenitäten auf das Gleitverhalten der Plattengrenze zu untersuchen.

Zusammenfassend kann festgehalten werden, dass die Heterogenität der Subduktionszone eine wichtige Rolle mit Blick auf den Grad der Lokalisierung der Verformung und der Rheologie der Plattengrenze spielt. Gleichzeitiges Auftreten von spröder und duktiler Deformation tritt in Subduktionszonen häufig auf und könnte unterschiedliches kinematisches Verhalten hervorrufen. Eine erneute Untersuchung der Gefüge exhumierter Gesteine hinsichtlich der (relevanten) absoluten und relativen Entstehungsabfolge und der räumlichen Verteilung einzelner Gefügeelemente ist unbedingt erforderlich, um die kinematischen Beobachtung geodätischer und geophysikalischer Untersuchungen mit den auf der Grenzfläche wirkenden Deformationsmechansimen zusammen zu führen. Schließlich kann die Integration der Ergebnisse kleinskaliger numerischer Untersuchungen in großskalige geodynamische Modelle helfen, unser Verständnis des mechanischen Verhaltens der Plattengrenze zu verbessern. Dies umfasst auch transiente

und aseismische Phänomene, die die Wiederkehrzeit von Megathrust-Beben in aktiven Subduktionszonen kontrollieren könnten.